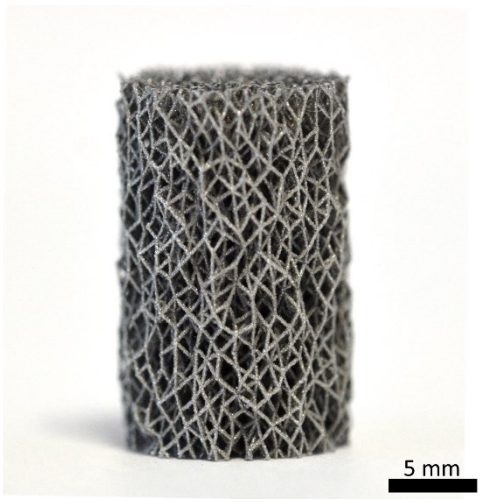
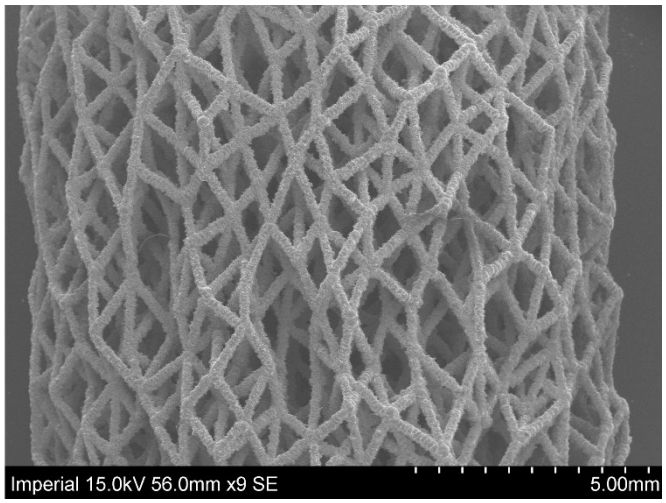
Optimizing Additive Manufactured Porous Structures for Orthopaedics





Shaaz Ghouse

Department of Mechanical Engineering

Imperial College London

A thesis in fulfilment of the requirements for the degree of Doctor of Philosophy

September 28, 2018

Declaration of Authorship

I, Shaaz Ghouse, hereby declare that all the work contained in this thesis is my own and is based on testing and results generated by me during my time as a PhD student at Imperial College London. All other work has been referenced appropriately.

Copyright Declaration

The copyright of this thesis rests with the author and is made available under a Creative Commons Attribution Non-Commercial No Derivatives licence. Researchers are free to copy, distribute or transmit the thesis on the condition that they attribute it, that they do not use it for commercial purposes and that they do not alter, transform or build upon it. For any reuse or redistribution, researchers must make clear to others the licence terms of this work

Abstract

To accelerate bone regeneration, porous scaffolds in orthopaedics should have a stiffness less than the bone being replaced, due to the mechanobiology of bone, whilst maintaining maximum yield and fatigue strength to combat implant failure. This PhD explored optimising additively manufactured (AM) porous structures for application as bone ingrowth scaffolds.

The effect laser parameters and laser scanning strategies have on the strut thickness, yield strength, and fatigue strength of porous structures was investigated. The yield and fatigue strength of a porous structure for a given stiffness could be increased up to 10%, mostly due to changes in internal porosity and microstructure. Optimisation of laser power was material specific, whilst scan strategy optimisation was material independent.

Porous structures were manufactured from various biocompatible metals. Trends observed during fatigue testing for monolithic metals and statically for solid and porous AM structures were not always indicative of the fatigue behaviour of porous AM structures. Unlike their solid counterparts and as porous structures, tantalum and a titanium-tantalum alloy outperformed titanium grade 23 and commercially pure titanium in fatigue-strength:stiffness.

I*n vivo* testing of a heterogeneous porous scaffold, intended to maintain mechanical homeostasis in the medial femoral condyle of ewes, was performed. Bone ingrowth into the scaffold was 10.73±2.97% after 6 weeks. Fine woven bone, in the interior of the scaffold, and intense formations of developed woven bone overlaid with lamellar bone at the implant periphery were observed.

This research will allow manufacturers, particularly in orthopaedics, to improve their additive manufacturing processes to build stronger porous structures that last longer. The *in vivo* portion of this study and the emphasis on understanding the mechanical environment implants are in, should allow for more accurate testing of the mechanobiology of bone in response to implanted porous scaffolds and for better translation from *in vivo* studies to commercial implants.

Acknowledgements

First and foremost I would like to thank my supervisor Dr Jonathan Jeffers for providing me with the opportunity and freedom to research in a field I find so interesting. Your guidance and support has been integral to this work. I would also like to thank my associate supervisor Dr Paul Hooper for his technical support and for constantly challenging me throughout this PhD.

I would like to acknowledge the Engineering and Physical Research Council and Renishaw PLC, my industrial sponsor, for their financial and technical support through grant number EP/K027549/1. Thank you, in particular, to my industrial contact at Renishaw, Dr Ken Nai, for facilitating much of this research and for your continued help. I must also acknowledge Sarat Babu and the team at Betatype for providing me the software tools and help necessary to achieve my goals during this work.

I would like to gratefully acknowledge all the Imperial College London technicians and support staff that have aided me throughout my PhD.

To all my fellow collaborators, co-authors and colleagues in the Biomechanics group, in the Department of Mechanical Engineering and in Imperial College London it has been a pleasure to work with all of you.

Finally to all my friends and family, thank you so much for all the support over the years, I would not have accomplished all that I have without you.

Table of Contents

1 Chapter 1 – Introduction 1

1.1 Introduction 1

1.2 Motivation 3

1.3 Aims and Objectives 6

1.4 Structure 6

1.5 References 9

2 Chapter 2 – Background 13

2.1 Clinical Background 13

2.1.1 Characteristics of Bone and Bone Remodelling 13

2.1.2 Mechanical Properties of Bone and Stress-Shielding 16

2.1.3 Clinical Applications of Porous Metals 19

2.1.4 Requirements for Bone In-Growth 21

2.2 Additive Manufacturing 24

2.2.1 Fundamentals of Additive Manufacturing 25

2.2.2 AM of Porous Biomaterials 32

2.2.3 Mechanical and Material Properties of Porous Structures 33

2.2.4 Parameter Optimisation on AM Material Properties 37

2.3 Biomaterials 40

2.3.1 Stainless Steel 40

2.3.2 Titanium 41

2.3.3 Tantalum 45

2.3.4 Titanium – Tantalum 46

2.4 Summary 48

2.5 References 49

3 Chapter 3 – Materials and Methods 59

3.1 Specimen Design 59

3.1.1 Characterisation Structure 59

3.1.2 Electron Backscatter Diffraction Specimen 60

3.1.3 Stochastic Architectured Structure 61

3.1.4 Locally Stiffness Matched Porous Scaffold 62

3.2 Build File Generation 63

3.2.1 Contour Strategy 63

3.2.2 Points Strategy 64

3.2.3 Pulsing Strategy 67

3.3 Materials and Manufacturing 69
3.4 Porous Structure Testing 72
3.4.1 Morphological Analysis 72
3.4.2 Quasi – Static Testing 73
3.4.3 Fatigue Testing 75
3.4.4 Build Time Measuring 77
3.5 *In Vivo* Testing 78
3.5.1 Surgical Procedure 78
3.5.2 Explant Analysis 80
3.6 References 83
4 Chapter 4 – Influence of Laser Parameters and Scanning Strategies on the Mechanical and Material Properties of Porous structures 85
4.1 Materials and Methods 86
4.1.1 Evaluation of Characterisation Structures 86
4.1.2 Evaluation of Stochastic Architectured Porous Structures 86
4.2 Results 89
4.2.1 Evaluation of Characterization Structures 89
4.2.2 Mechanical Testing of Stochastic Porous Structures 92
4.2.3 Effect of Laser Parameters and Scanning Strategies on High Cycle Fatigue Strength 97
4.2.4 Effect of Laser Parameters and Scanning Strategies on Microstructure 99
4.3 Discussion 107
4.3.1 Optimisation of the mechanical properties of architectured structures 107
4.3.2 Effect of laser parameters and scanning strategies on material properties 108
4.3.3 Effect of Laser Parameters and Scanning Strategies on High Cycle Fatigue Strength 110
4.3.4 Validity of the Specific Enthalpy Model 111
4.3.5 Limitations 113
4.4 Summary 114
4.5 References 115
5 Chapter 5 – Influence of Material on the Static and High Cycle Fatigue Strength of a Stochastic Porous Structure 119
5.1 Material and Methods 120
5.1.1 The Effect of Laser Parameters and Material on Strut Thickness 120
5.1.2 The Effect of Material on Static and Fatigue Strength 120

5.2 Results 122
5.2.1 Evaluation of Characterisation Structures 122
5.2.2 Evaluation of Stochastic Porous Structures 125
5.3 Discussion 136
5.3.1 Material Optimisation of Porous Structures 136
5.3.2 Modelling the Mechanical Behaviour of Stochastic Porous structures 138
5.3.3 Limitations 139
5.4 Summary 140
5.5 References 141
6 Chapter 6 – The Design and *In Vivo* Testing of a Locally Stiffness Matched Porous Scaffold 143
6.1 Material and Methods 144
6.1.1 Specimen Design 144
6.1.2 Specimen Manufacture 148
6.2 Results 149
6.2.1 Bone Core Testing 149
6.2.2 Locally Stiffness-Matched Scaffold 151
6.2.3 *In Vivo* Results 154
6.3 Discussion 161
6.3.1 Mechanical Response of Trabecular Bone and AM Porous Materials 161
6.3.2 *In Vivo* Performance of Stiffness-matched Scaffolds 163
6.3.3 Limitations 164
6.4 Summary 166
6.5 References 168
7 Chapter 7 – Conclusion and Future Work 171
7.1 Conclusions 171
7.2 Future Work 173
7.2.1 Microstructure and Cooling Rates 173
7.2.2 Thermal Post-Processing 173
7.2.3 Mechanical Post-Processing 174
7.2.4 Structural Optimization 174
7.2.5 Titanium – Tantalum Alloys 175
7.2.6 Fatigue Strength 175
7.2.7 *In Vivo* Testing 175
7.3 List of Publications 177

8 Appendix A – Specific Enthalpy Models Raw Data 179

9 Appendix B – Stochastic Porous Structure Raw Data & Further Optimisation Graphs 195

10 Appendix C – EBSD Data 211

11 Appendix D – Ex-vivo Sheep Bone Raw Data 217

12 Appendix E – Rights and Permissions 221

List of Figures

Figure 1.1 – Line vs 3D representation of porous architectures 4

Figure 2.1 – Hierarchical structural organization of bone 14

Figure 2.2 – Hypothesis on the relationship between bone strain history rate and the net rate of bone volume change 15

Figure 2.3 – A mechanical model of bone remodelling 16

Figure 2.4 – Variation of Elastic Modulus (MPa) as a function of location in the proximal tibia of humans 17

Figure 2.5 – Stress-Strain Curves for human cancellous bone. As relative density increases modulus and compressive strength increases and the strain at which densification occurs decreases. Low density cancellous bone is pictured inset 17

Figure 2.6 – Mechanical properties (Left: Young's Modulus and Right: Compressive Strength) of bone versus bone density 18

Figure 2.7 – Progression of bone resorption (from left to right) due to stress shielding in the proximal tibia 19

Figure 2.8 – Reduction of stress shielding due to tailoring the properties of a porous structure 20

Figure 2.9 – Backscattered SEM imaging of bone ingrowth into a transcortical porous tantalum implant into the femoral diaphysis of skeletally mature mongrel dogs after two weeks (left) and three weeks (right) 22

Figure 2.10 – Schematic of a typical laser powder bed fusion machine (left) and some operating parameters (right) 25

Figure 2.11 – Melt-pool generation in laser powder bed fusion 26

Figure 2.12 – Staircase effect (left) and semi-fused particles (right) 26

Figure 2.13 – Laser parameter optimisation for maximum density 27

Figure 2.14 – (a) crack-like pores induced by effects like balled and unmolten particles (dashed circles) and spherical pores (b) 28

Figure 2.15 – SEM images of the balling characteristics of single scan tracks with increasing scan speed 29

Figure 2.16 – Localised thermally induced residual stress 30

Figure 2.17 – Cubic crystal system structures. Many porous AM materials are built with these types of repeating unit cells 34

Figure 2.18 – Compressive behaviour of porous structures: a) the struts bend under compression (bending dominant); b) under compression the horizontal strut will carry tension (stretch dominant); c) the structure is over-constrained and possibly in states of self-stress… 35

Figure 2.19 – Compressive Stress – Strain curve of a porous metal 36

Figure 2.20 – Fatigue failure curve (Strain vs. number of cycles to failure) of a porous metal under compression-compression fatigue 36

Figure 2.21 – Effect of a single laser parameter (laser scanning speed) on a porous AM material property (left: strut diameter, right: base material porosity). Shown for an aluminium alloy (AlSi10Mg) 38

Figure 2.22 – Porosity of titanium grade 5 samples built with varying laser powers (P) and scan speed. (a) P = 160 W. (b) P = 120 W. (c) P = 80 W. (d) P = 40 W. No relationship is observed between energy density and porosity 38

Figure 2.23 – Phase diagram for Ti-6Al-4V 42

Figure 2.24 – Typical LBPF Ti64 microstructure, columnar prior beta grains are seen filled with acicular α’ (Build direction is vertical) 43

Figure 2.25 - Effect of microstructure on tensile properties of LBPF titanium parts 44

Figure 2.26 – Fatigue strength comparison between porous structures manufactured from titanium alloys and tantalum. Left: Normalised maximum fatigue stress versus number of cycles to failure. Right: Fatigue strength at one million cycles versus overall structure porosity 46

Figure 2.27 – Effect of Ta content on Modulus, Strength and Elongation 47

Figure 3.1 – Characterisation Structure Manufacture Workflow 60

Figure 3.2 – EBSD Structure Manufacture Workflow 61

Figure 3.3 – Manufacturing Workflow from Specimen Design to Build File Generation to Manufacture. Note: 1-3 are simplified for clarity and not to scale. 62

Figure 3.4 – 3D Rendering of Locally Stiffness-Matched Scaffold 63

Figure 3.5 – Traditional Contour-Hatch Scanning Strategy 64

Figure 3.6 – Melt-pool video of a contour scan: Laser scans a specified diameter circle/ellipse (2-19). Upon completion scanners jump to the next location and the following contour scan occurs (not shown). 64

Figure 3.7 – Single Exposure Scanning Strategy 65

Figure 3.8 – Single Exposure issues for low angled struts: When building a strut at 30° at a 50 µm layer thickness and assuming a melt-pool width and depth of 100 µm, a typical single exposure strategy would likely not build a strut, as there are no overlapping melt-pools (for simplicity melt-pools are shown as spherical). 66

Figure 3.9 – Points Strategy: Projection of horizontal component of strut onto slice layer (green lines) 66

Figure 3.10 – Points Strategy for low angled struts: Exposures are fired along the projected horizontal component of the strut on a layer-by-layer basis 66

Figure 3.11 – Point Exposure (shown for a vertical strut): The laser is held at a fixed position and exposes (fires) for a specified time (2-17). Upon completion scanners jump to the next exposure point (18-34) and the following exposure occurs (34-35). Previous exposure point is circled during the scanners jump to the next point. 67

Figure 3.12 – Pulsing Strategy (shown for a vertical strut): The laser is held at fixed position and exposes (fires) for a specified time (e.g. 7-8) then the laser turns off for a specified time (e.g. 9-12); this point gets repeatedly pulsed with exposures (in this example 5x with a 50% duty cycle). Upon completion scanners jump to the next exposure point (27-34) and the following pulsed exposures occur (34-35). Previous exposure point is circled during the scanners jump to the next point. 68

Figure 3.13 – Renishaw AM250 69

Figure 3.14 – Diagram showing optical layout of the commercial LPBF machine and modification to allow coaxial imaging of the melt pool 70

Figure 3.15 – BSEM Images of Powder Feedstock. Note: All powder shown in recycled condition except Ta which is shown in virgin condition. In the TiTa images the large dark

spheres are CP-Ti powder whilst the small light particles are Ta powder (agglomerated due to being through the powder bed fusion process numerous times) 71

Figure 3.16 – Compression Stress-Strain curve of an AM stochastic porous structure (only shown to 10% Strain) 74

Figure 3.17 – Compression Test Setup 74

Figure 3.18 – Compression – Compression Fatigue Test Setup 75

Figure 3.19 – A 15 specimen example of the staircase method of fatigue testing and data collection from ISO 12107:2012 77

Figure 3.20 – Implant Placement 79

Figure 3.21 – Implant Placement during Surgery 79

Figure 3.22 – Specimen retrieval: A) Distal Femur removed. B) Specimen trimmed around scaffold and defect, mounted and sectioned. 80

Figure 4.1 – SEM images of characterization structure for increasing enthalpy. Top row: 90°, 60° and 45° struts. Bottom row: 90°, 30° and 15° struts. Orange arrows indicate vertical build direction 90

Figure 4.2 – SEM images of Characterization Structure Struts for increasing Enthalpy and different build angles. Orange arrows indicate vertical build direction 90

Figure 4.3 – Strut Thickness vs. Specific Enthalpy Plots for a) the Points Strategy in SS316 (also typical for the Pulsing Strategy) and b) the Contour Strategy in Ti64. Plots are typical for both materials. Due to high number of data points and for graphical clarity, error bars not shown. Average S.D. for strut thickness measurements was 0.018mm. The laser parameters associated with these specific enthalpy values can be found in Appendix A. 91

Figure 4.4 – Stochastic Porous Structure 92

Figure 4.5 – Typical Porous structure Stress-Strain Curves for Ti64 and SS316. Ti64 exhibits relatively brittle failure whilst SS316 exhibits more ductile failure. Curves shown for specimens with a 3.3 and a 3.5 GPa modulus respectively, and without hysteresis loops to 50% strain. 92

Figure 4.6 – Failed porous structures during quasi-static testing with a ~3.0 GPa modulus ... 93

Figure 4.7 – Compressive yield stress & internal porosity (Φ) vs. Modulus Plots for the Points Scan Strategy. For each material, two separate curves/points are seen, one for samples built at 50W and one for samples built at 200W, with increase in strut diameter and thus modulus/density being controlled by an increase in exposure time. 94

Figure 4.8 – Micro-CT slices of Ti64 stochastic porous structures built via the Points Strategy at Laser Powers of 50 W and 200 W. For a given Modulus (E) and Density (ρ), greater Internal Porosity (Φ) is observed (circled in red) in samples built at 200 W for both Ti64 and SS316. 95

Figure 4.9 – Scan Strategy Comparisons on Compressive Strength & Internal Porosity (Φ) vs Modulus Plots. At low modulus values scan strategy did not affect the σ_y:E ratio, but as modulus increases the contour strategy produced samples with the highest σ_y:E ratio.....96

Figure 4.10 – Typical Compressive Strain vs. Cycles-to-Failure Curves for specimens without (left) and with (right) failure. 97

Figure 4.11 – SEM Images of a fatigue failed Ti64 specimen. Extensive cracking and fracture was observed at or near nodes, as indicated by arrows. Plastic deformation of struts is not evident. Higher magnification of the circled area is also seen. Build direction for both images is vertical. 97

Figure 4.12 – Effect of Laser Parameters (a) and Scanning Strategy (b) on High Cycle Fatigue Strength (10^6 Cycles) for Ti6Al4V ELI. R^2 values for all curve fits were 0.99. For clarity error bars are not shown, however standard deviations for all values are given in Table 4.6. 99

Figure 4.13 – Microstructure of Ti64 specimens at varying laser parameters and scanning strategies parallel to build direction. Typical prior β grains indicated (Build direction is vertical in all images). 101

Figure 4.14 – Microstructure of Ti64 specimens at varying laser parameters and scanning strategies perpendicular to build direction. Typical prior β grains indicated, pores arrowed. 102

Figure 4.15 – SEM Microstructure of Ti64 specimens at varying laser parameters and scanning strategies parallel to build direction (Build direction is vertical in all images). 103

Figure 4.16 – SEM image of a single strut (left) and with an EBSD crystal orientation map overlaid (right) 104

Figure 4.17 – EBSD orientation maps (inverse pole figures) of Ti64 specimens at varying laser parameters and scanning strategies parallel to build direction. (Build Direction is vertical in all images). Columnar grains are seen for all 50 W specimens. Greater uniformity of colors reflects stronger texture whereas the 200 W sample is characterised by a greater variety of colour and grains in many orientations. Refer to Figure 4.19 for crystal orientation colour reference...105

Figure 4.18 – EBSD Pole figures for Ti64 specimens at varying laser parameters and scanning strategies parallel to build direction. 105

Figure 4.19 – Colour Code representing the crystal orientation for titanium 106

Figure 5.1 - Characterisation Structures in CP-Ti, Ta and TiTa....122

Figure 5.2 - Strut Thickness model for CP-Ti. Average S.D. for strut thickness measurements was 0.019 mm 123

Figure 5.3 - Strut Thickness model for Ta. Average S.D. for strut thickness measurements was 0.019 mm 124

Figure 5.4 - Strut Thickness Model for TiTa. Average S.D. for strut thickness measurements was 0.017 mm 124

Figure 5.5 – Stochastic Porous Structures 125

Figure 5.6 – Compressive Yield Stress vs. Modulus Plots for (a) CP-Ti, (b) TiTa, and (c) Ta. 50W is seen to produce specimens with a greater strength:stiffness ratio for CP-Ti and TiTa, whilst 200W produces specimens with a greater strength:stiffness ratio for Ta. Error bars are standard deviations....126

Figure 5.7 – Typical Porous structure Stress-Strain Curves. Curves shown for specimens with a ~3.1 – 3.4 GPa modulus and without hysteresis loops to 50% strain 127

Figure 5.8 – Failed porous structures during quasi-static testing with a ~3.1 – 3.4 GPa modulus crushed to ~50% strain....128

Figure 5.9 – Effect of Material on Static Compressive Properties. R^2 values for all curve fits were 0.99. Error bars are not shown, however standard deviations for all values are given in Table 5.3. 129

Figure 5.10 – Typical Compressive Strain vs. Cycles-to-Failure Curves per material for specimens without (left) and with (right) failure. 130

Figure 5.11 – Compression – compression fatigue failed Ti64, CP-Ti, TiTa and Ta specimens. Angled fatigue failure fracture planes (crush bands) are indicated, likely following the weakest planes of the stochastic porous structure. 131

Figure 5.12 – SEM Images of a fatigue fracture surfaces 131

Figure 5.13 – Effect of Material on Fatigue Strength at 10^6 Cycles. R^2 values for all curve fits were 0.99. Error bars are not shown, however standard deviations for all values are given in Table 5.3. 132

Figure 5.14 – SEM and Microscopy Images. Build direction in all images is vertical. Row a & b: SEM Images; build layer and/or melt-pool texture lines (white arrows) and semi sintered particles (yellow arrows) are evident. Row c: Microscopy Images where crack initiation sites (red arrows) are evident particularly on the Ti64 specimen. Row d & e: Microstructure Images. Manufacturing Parameters are listed in Appendix B. 134

Figure 5.15 – Polished microscopy Images for Ti64, CP-Ti, TiTa and Ta specimens. Build direction in all images is vertical. 135

Figure 5.16 – Microstructure parallel to build plate. Build direction in all images is into the image. 135

Figure 6.1 - Coarse Local Bone Property Quantification. Notation: Anterior (A), Posterior (P), Medial (M), Lateral (L), Inferior (I) and Superior (S). 145

Figure 6.2 – 10mm Thick bone slice. a) Four bone cores drilled out. b) CT reconstruction of slice and meshed cylinders registered for bone mineral densitometry. 146

Figure 6.3 - Fine Local Bone Property Quantification. Notation: Anterior (A), Posterior (P), Medial (M), Lateral (L), Inferior (I) and Superior (S). 147

Figure 6.4 – Design of a locally bone-stiffness matched porous scaffold. Notation: Anterior (A), Posterior (P), Medial (M), Lateral (L), Inferior (I) and Superior (S). 148

Figure 6.5 – Compression Stress – Strain Curves for Trabecular Bone Cores and uniform stiffness CP – Ti porous materials of ~500-600 MPa modulus and ~1700 MPa modulus. CP – Ti specimens tested in Chapter 5 149

Figure 6.6 – Apparent Density vs. Modulus; a) tested points and trend line for trabecular bone in the medial femoral condyle, b)trend line over entire bone range (trabecular + cortical) .. 150

Figure 6.7 – Yield Stress vs. Modulus for the trabecular bone cores 151

Figure 6.8 – Scaffold Location Notation (shown for a right leg) 153

Figure 6.9 – Scaffold SEM Images (Build Direction indicated). A) Medial End of Scaffold, B) Higher magnification of medial end, C) Scaffold Periphery, D) Higher magnification of scaffold periphery 154

Figure 6.10 – Scaffold Strut and Pore Size Distribution 154

Figure 6.11 – μ-CT Renderings of bone ingrowth into a locally stiffness matched porous scaffold (not shown) 155

Figure 6.12 – Distal Placement of Scaffold in Animal 5. 9.5 mm from the medial end of the scaffold. 156

Figure 6.13 – Bone bridging gap. From left to right: A) Bone ingrowth into the lateral end of the scaffold, B) bone almost bridging the entire defect diameter 2mm from the lateral end of the scaffold and the defect tunnel, c) end of the cylindrical defect tunnel, 5mm from the lateral end of the scaffold. 156

Figure 6.14 – Osteogenic activity at the bone-implant interface (top) and implant interior (bottom) 157

Figure 6.15 – Fluorescent Microscopy Images for animals 4 and 6. Islets of bone deep within the scaffold interior circled 158

Figure 6.16 – Histology Images for animals 4 and 6. A and B are magnified sections of the scaffold periphery and interior respectively. Osteoblasts are indicated by arrows, osteocytes are circled. 159

Figure 6.17 – BSEM Images of Animal 4. A and C) Scaffold periphery: older (brighter) woven bone is seen overlaid by lamellar bone. Both complete engulfing of strut elements and intimate contact between strut and bone are observed. B) Scaffold interior: new embryonic-looking woven bone is seen with a lower degree of mineralization thus a darker appearance 160

List of Tables

Table 2.1 – Constitutional phases and their morphologies of the Ti-Ta alloys 47

Table 3.1 – Scoring criteria for bone formation at the bone-implant interface (periphery of the defect) and within the interior of the implant and defect. 82

Table 4.1 – Evaluation of Characterisation Structures Study Design and Manufacturing Conditions 86

Table 4.2 – Stochastic Porous Structures quasi-static Testing Study Design and Manufacturing Conditions 87

Table 4.3 – Stochastic Porous Structures fatigue Testing Study Design and Manufacturing Conditions 88

Table 4.4 – Minimum Strut Thickness (Values are average Strut Thickness ± S.D). Superscripts refer to the Laser Parameters used to produce minimum strut thickness as detailed in Table 4.5. 89

Table 4.5 – Laser Parameters used to produce minimum Strut Thickness (minimum specific enthalpy) to build successful structures. 89

Table 4.6 – Effect of Laser Parameters and Scan Strategy on the Mechanical Properties of a Ti64 Stochastic Structure (Values are mean ± S.D.) 98

Table 5.1 – Effect of laser parameters and material on strut thickness study design and manufacturing conditions.....120

Table 5.2 – Effect of material on static and fatigue strength study design and manufacturing conditions 121

Table 5.3 – Effect of Material on the Mechanical Properties of a Stochastic Structure (Values are mean ± S.D.). Italicised values are mechanical properties for the solid material, these values are only given as a reference as mechanical properties are heavily dependent on the manufacturing method and thermal history of the material. 133

Table 6.1 – Localised Density and Modulus Variations of Bone at implant Site and Modulus variations of scaffold. Location notation: XYZ, X: Posterior-Anterior, Y: Medial-Lateral, Z: Inferior-Superior; all going 1-3 respectively. 152

Table 6.2 – Bone ingrowth results 155

Nomenclature

3D	Three Dimensional
2D	Two Dimensonal
α	Alpha-phase
α′	Hexagonal martensite phase
α″	Orthorhombic martensite phase
A	Absorptivity
AM	Additive Manufactured/Manufacturing
ASTM	American Society for Testing and Materials
β	Beta-phase
BCC	Body Centred Cubic
BMU	Basic Multicellular Unit
BV	Volume of bone ingrowth into scaffold
C	Celsius
CAD	Computer Aided Design
cm	Centimetre
CP-Ti	Commercially Pure Titanium (Grade 2)
CT	Computed Tomography
°	Degrees
D	Thermal Diffusivity
D_{50}	Diameter of powder particles that 50% are smaller than
ε	Apparent engineering compressive strain
ε_y	Apparent engineering compressive strain at σ_y
E	Apparent Modulus
E_0	Young's Modulus
E_D	Laser Energy Density
EBSD	Electron Backscatter Diffraction
EDM	Electro Discharge Machining
ELI	Extra Low Interstitials
g	grams
GPa	Gigapascal
ΔH	Specific Enthalpy
HRC	Rockwell Hardness
ISO	International Organisation for Standardisation
kN	Kilonewton
λ	Wavelength
LPBF	Laser Powder Bed Fusion
μ	Micro
m	metre
mbar	Millibar
mm	Millimetre
MPa	Megapascal
N	Newton

N_f	Cycles to failure
P	Laser Power
$\varnothing$	Diameter
Φ	Internal Porosity
ρ	Apparent density
ρ_0	Density
σ	Apparent engineering compressive stress/strength
σ_y	Apparent engineering compressive yield stress/strength
σ_0	Engineering compressive stress/strength
s	Seconds
SS316	Stainless Steel 316L
SV	Volume of scaffold
Ta	Commercially Pure Tantalum
Ti	Titanium
Ti64	Titanium 6-Aluminium 4-Vanadium ELI (Grade 23)
TiTa	Titanium – Tantalum (30% - 70% split respectively)
TV	Total Defect Volume
u	Laser scan speed
W	Watts

1 Chapter 1 – Introduction

Additive manufactured (AM) architectured porous structures are now viable choices for the engineer in a variety of fields [1-4]. In orthopaedics, implants have traditionally been machined, forged or cast solid pieces of metal, that are orders of magnitude stiffer than natural bone [5]. These implants, can now be composed of low stiffness architectured porous structures produced by AM [6], from established biocompatible metals like Titanium, Cobalt Chrome, and Tantalum [7-9]. Orthopaedic devices therefore now have the potential to match the stiffness of cancellous bone throughout the skeleton which may enable new and better treatment options in the management of osteoarthritis and other bone pathologies, particularly for early intervention in young patients. Bone repair and regeneration can be driven by strain response with respect to load, i.e. the more strain, bone experiences due to loading the greater the increase is in bone volume [10-12]. Thus, to accelerate bone regeneration, a porous scaffold or porous coating on an implant should have a stiffness less than the bone that is being replaced, to induce more strain at the defect site [13]. However, maximising strength (unless otherwise stated strength refers to compressive yield strength hereafter) of additively manufactured porous metals at low stiffness remains a challenge, particularly in applications under high cyclic loads [14-16]. Optimisation of the manufacturing process and selection of the base material provides opportunities to maximize the static and fatigue strength of AM porous structures.

The overriding research questions for this thesis are:

- How do the manufacturing parameters in powder bed fusion affect the mechanical and material (microstructure, morphologic and geometric) properties of porous structures?
- What materials should these porous structures be made from for low stiffness – high strength applications (such as for bone in-growth surfaces)?
- Can a pragmatic approach be developed for *in vivo* testing of porous structures taking into account the mechanobiology of bone and its local variations?

1.1 Introduction

Additive manufacturing (AM), the process of fabricating objects layer by layer from 3D computer models, provides new avenues for fabricating net-shaped parts and assemblies, with complex geometries that traditional manufacturing technologies are unable to produce. Developments in AM processes, along with innovations in advanced materials has seen AM move from rapid prototyping to rapid manufacturing and small-scale production over the past

30 years. Metal additive manufacturing, and its ability to produce functional parts is of great interest to both industry and the scientific community. The AM process of interest in this research is powder bed fusion and works by a laser selectively melting micro metal powder particles in a layer-wise fashion to build a component. As a tool-free and potentially cost-efficient digital approach to manufacturing, AM of metals offers many key benefits that could change the industrial paradigm in sectors such as aerospace, automotive, energy, medical, tooling and consumer goods [17]. Most importantly, in the case of this thesis, it affords the creation of complex 3D geometries, such as architectured porous structures, that are not possible to achieve with other traditional processes.

Architectured porous structures have become an area of high commercial interest and research activity particularly as AM allows the fabrication of these materials with a degree of control and at a scale not previously possible. Porous structures, also known as lattices, foams or cellular materials, are a new, currently imperfectly characterized, class of materials [18]. They are found both in nature as well as in numerous engineering applications, possessing unique properties compared to their solid material counterparts. Porous structures exhibit low density and therefore low mass along with high specific strength and stiffness, surface area, acoustic absorption as well as high gas permeability. Thus, they are well suited as lightweight structures with high stiffness-to-weight-ratios, as well as having outstanding kinetic energy absorption characteristics and exceptional heat transfer capabilities. Applications include mechanical damping, vibration control, acoustic absorption, thermal management, filters, electrical screening and many more [19]. They are also particularly relevant in orthopaedics.

In orthopaedics, joint degeneration due to osteoarthritis, fractures or other bone diseases are challenging issues for the regeneration ability of the body. If the defect or issue cannot be handled by the body's healing process alone, it requires therapeutic intervention, often a metal implant or joint replacement. Porous structures provide numerous advantages in the treatment of these pathologies. Their porous nature provides a framework for bone in-growth which is useful for the fixation of the implant to the surrounding bone, as stable fixation is a prerequisite to long term implant success [20, 21]. They also provide a framework for the body’s regeneration ability to bridge large bone defects. In addition, the porosity of the structure allows the effective modulus of the implant to be reduced. Thus, not only can stress-shielding be avoided (i.e. the stiffness mismatch between bone and solid monolithic metals which can cause bone resorption), the mechanobiology of bone can be taken advantage of to promote greater bone in-growth and regeneration [10-12, 18, 19, 22]. Whilst these materials have already had

commercial success, there remains scope for improvement and to understand how best to manufacture these structures.

1.2 Motivation

Despite the numerous applications of porous AM structures and the significant commercial and academic interest, there remains hurdles that need to be overcome before their widespread adoption. The primary applications in orthopaedics for porous structures are as porous coatings on joint replacements for bone ingrowth to ensure good fixation, stability and to avoid stress-shielding; as bone regeneration scaffolds to repair large segmental defects and as early intervention implants for local chondral defects. Ensuring that these porous structures can be of a stiffness similar to or less than the bone being replaced, in order to maximise bone regeneration, whilst still maintaining maximum yield and fatigue strength is of paramount importance and a challenge. These types of structures are under harsh cyclic loading environments and to ensure implant longevity and patient satisfaction, they must last as long as possible.

As AM can now produce functional parts, greater emphasis in both industry and in research is placed on performance and mechanical properties. This has consequently resulted in an increase in research into the underlying mechanics of the AM process. The main challenge facing the continued adoption of AM by industries is the uncertainty in structural properties of the fabricated parts. This uncertainty arises due to AM parts possessing microstructural heterogeneities and randomly dispersed defects. During manufacture, metallic AM parts experience a complex thermal history involving directional heat extraction, and repeated melting and rapid solidification. This contributes to microstructural evolution and properties not typically found in conventional processes. As the laser parameters (laser power, laser speed, layer thickness, etc.) and scanning strategies used during fabrication affect the thermal history (i.e. melt-pool temperature, thermal gradient, cooling rate, cyclic reheating) of the part [23], they consequently affect microstructural details (grain size/morphology, texture, defect type/size/distribution and residual stress, etc.) and therefore the mechanical behaviour [24]. Whilst research has been conducted on the effect of laser parameters and scan strategies on the material and mechanical properties of solid AM parts, their effects on porous structures have been under reported. In addition, there are also inconsistencies and issues with the mechanical testing of porous structures in literature.

Furthermore, it has been reported that the fatigue behaviour of AM porous structures is different from that of bulk materials and the relationships normally used for the fatigue design of continuous materials are not applicable when designing AM porous structures [25]. It therefore remains to be seen whether the rationale for use behind common orthopaedic biomaterials still stands and whether new alloys can be manufactured that are more fit for purpose. For engineers looking to maximize the yield and fatigue strength for a given stiffness of AM porous structures, there are hurdles still to overcome. Most studies have limited or no samples tested in the higher cycle fatigue region (10^6 or higher cycles) and these studies also tend to present mechanical properties with respect to relative density or cycles-to-failure and not with respect to stiffness [9, 26, 27]. Extracting and comparing stiffness data from these works can prove difficult due to issues and inconsistencies in the mechanical testing. Optimising the AM processing parameters and selecting the correct material to build porous structures will result in better, stronger and longer lasting implants for patients.

Another motivation for this work is that, solid 3D modelling of porous structures can become prohibitively computationally expensive. As the physical size of the model of the porous structure grows too large and/or the feature sizes grow too small, modern CAD packages struggle with the number of faces, features or surfaces present. To overcome this software packages are now available that model complex porous structures not as 3D solids or surfaces but rather as line – based or graph representations (Figure 1.1).

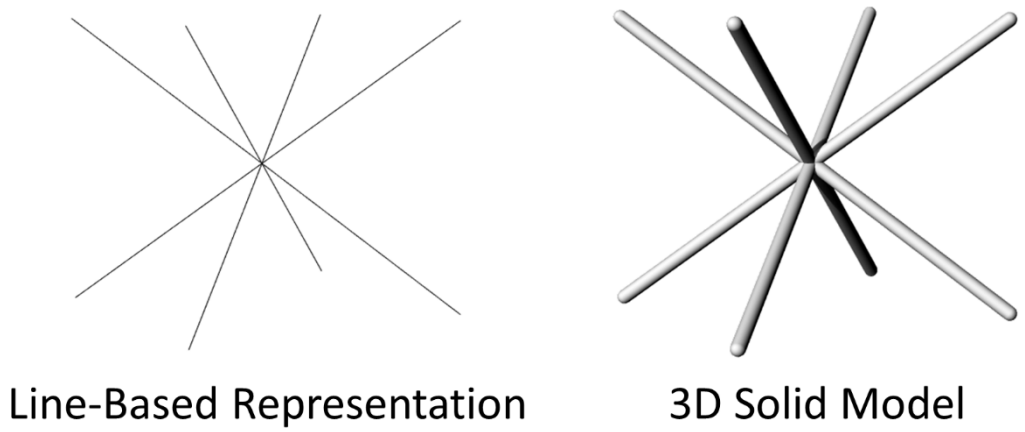


Figure 1.1 – Line vs 3D representation of porous architectures

This type of representation of porous structures creates new opportunities in terms of laser scanning strategies and laser parameter control particularly for micro features. Therefore, in order for line – based representations of porous structures to be adopted, the relationships

between laser parameters and scan strategy to strut thickness must be understood, including any effects due to build angle or material.

Finally, it is often stated that one of the requirements for bone in-growth into a porous scaffold or into a porous coating of an orthopaedic implant is that it should match the mechanical properties of the surrounding bone tissue [14, 28]. However, typically in *in vivo* testing of porous structures the mechanical properties of the bone being replaced are not quantified. Similarly, the mechanical properties of the patient's bone are unknown prior to surgery. Bone properties also vary significantly with age, anatomical site, bone quality [5, 14] and between animals, yet most research into porous scaffolds and porous commercial implants have ignored this variation. It is therefore difficult to compare in-growth results between studies and to translate *in vivo* animal testing to human subjects. Also, in *in vivo* testing of porous scaffolds in literature and in commercial porous scaffolds, the structure of the porous structure is generally homogenous. These scaffolds lack local variation in properties and are consistent regardless of skeletal location or animal used despite bone varying locally at the joint, globally through-out the skeleton and between species. Historically, *in vivo* testing of porous structures for bone in-growth has focused on morphological features, typically pore size and porosity, and have ignored the mechanobiological features of bone remodelling and the mechanical environment. As a result there are inconsistencies in the literature regarding 'optimum' pore size and porosity for bone ingrowth. Without understanding the mechanical properties of the tissue being replaced and the loading environment, it is difficult to make determinations regarding pore size and porosity for scaffolds.

Quantifying the mechanical environment a porous scaffold will be placed in and exploring how the mechanical properties of a scaffold will affect the quantity of bone in-growth, will ultimately lead to a better understanding of the mechanobiology of bone, will reduce ambiguity in the field regarding ideal characteristics of porous structures, will allow for comparisons to be made between *in vivo* studies and ultimately a better translation of these structures into commercial implants. Coupled with a more in-depth characterisation of how AM processing parameters and materials affect static and long term fatigue strength of porous structures should result in a more widespread adoption of porous structures and consequently better implants and patient outcomes.

1.3 Aims and Objectives

The aim of this research is to improve architectured porous structures produced by powder bed fusion for applications where bone ingrowth and regeneration is necessary such as in joint replacements, scaffolds and early intervention chondral implants. The focus will be on maximising the static and long term dynamic mechanical performance of these structures by altering the processing parameters and the materials used to manufacture them. As stated earlier, the mechanical environment, mechanical properties nor the mechanobiology of bone are often not properly characterised and considered during *in vivo* studies and during individual surgical operations. Therefore, another objective of this study is to develop a clinically applicable and pragmatic approach to the design and manufacture of a porous scaffold intended to invoke a desired mechanobiological response from bone and to analyse its performance *in vivo* in an animal model. This type of approach could lead to being able to produce site/joint-specific porous structures tuned to the local bone characteristics. As well as patient specific or cohort specific implants, for example implants that either, take advantage of the higher healing capacity of younger active patients and provide very low stiffness porous implants that accelerate bone regeneration or consider the poorer bone quality of older patients and provide more load bearing and durable implants.

1.4 Structure

The structure of this PhD is as follows:

- **Chapter 1 – Introduction**
    - An introduction to the study and the motivation behind the work. The aims and objectives of the study are presented as well as the structure of the thesis
- **Chapter 2 – Background**
    - The background chapter will cover the fundamental topics to understand the work presented and review relevant literature in the field. The clinical background for this work will be presented as well as and introduction into the characteristics of bone, bone remodelling and the requirements for osseointegration or bone ingrowth into porous structures. An introduction to powder bed fusion and important characteristics and phenomena behind its working will be given. Followed by an overview of research into porous structures, focusing on the role of manufacturing parameters and common biomaterials used as bone implants or scaffolds.
- **Chapter 3 – Materials and Methods**

  - The materials and methods in this research are presented. This will cover the design of all specimens and the testing and analysis procedures.

- **Chapter 4 – Influence of Laser Parameters and Scanning Strategies on the Mechanical and Material Properties of Porous structures**
  - This chapter begins with an investigation into the relationship between laser parameters and scanning strategies on strut thickness and explores minimum feature sizes and build angles.
  - This will be followed by an investigation into the influence laser parameters and scanning strategies have on the mechanical performance of a stochastic porous structure, both quasi-statically and in long term fatigue life. The focus is on maximizing the strength:stiffness and the fatigue-strength:stiffness of porous structures, in the stiffness range of trabecular bone.
- **Chapter 5 – Influence of Material on the Static and High Cycle Fatigue Strength of a Stochastic Porous structure**
  - The mechanical properties of stochastic porous structures manufactured from common biomaterials (CP-Ti, Ti64 and Ta) are characterised, looking to maximise the quasi-static and high cycle fatigue strength with respect to stiffness of the structures. It will be seen if their mechanical behaviour as porous structures follows the same trends as their monolithic solid counter parts.
  - A novel AM titanium-tantalum alloy will be developed and its mechanical performance characterised and compared to the other biomaterials investigated.
- **Chapter 6 – The design and *in vivo* testing of a stiffness matched porous scaffold**
  - The final study of this research looks to develop a pragmatic and clinically applicable approach to produce heterogeneous porous scaffolds or features for bone in-growth with a tailored strain or stiffness gradient that match the heterogeneity of the bone to be replaced.
  - *In vivo* testing in an ovine model of a locally-stiffness matched scaffold (i.e. is intended to maintain mechanical homeostasis) will be performed. The mechanical properties of trabecular bone in the medial condyle of the femur of skeletally mature ewes will be characterised and consequently a scaffold will be produced with local variations in stiffness equivalent to the bone it will be replacing. The newly formed bone in the scaffold will be quantified and analysed after 6 weeks *in vivo*.

- **Chapter 7 – Conclusions and Future Work**
    - Conclusions and summary of all the work in this study, as well as avenues for future work are presented in Chapter 7.

This thesis represents work from two published research articles (reproduced under the terms of the Creative Commons Attribution License (CC BY)) and 2 research articles currently under review. The following is a breakdown of these papers into the respective chapters and sections:

- **S. Ghouse**, S. Babu, R.J. Van Arkel, K. Nai, P.A. Hooper, J.R.T. Jeffers, The Influence of Laser Parameters and Scanning Strategies on the Mechanical Properties of a Stochastic Porous Material, Materials & Design 131 (2017) 498-508 [29]
    - Chapter 3 (3.1 – 3.1.3, 3.2 – 3.4) & Chapter 4 (4.1.1 – 4.1.2.1, 4.2.1, 4.2.2, 4.3.1, 4.3.2, 4.3.4, 4.3.5)
- **S. Ghouse**, S. Babu, K. Nai, P.A. Hooper, J.R.T. Jeffers, The influence of laser parameters, scanning strategies and material on the fatigue strength of a stochastic porous structure, Additive Manufacturing 22 (2018) 290-301 [30]
    - Chapter 3 (3.1.1, 3.1.3, 3.2 – 3.4), Chapter 4 (4.1.2.2, 4.2.3, 4.3.3) & Chapter 5
- **S. Ghouse**, N. Reznikov, O.R. Boughton, S. Babu, K.C.G. Ng, G. Blunn, J.P. Cobb, M.M. Stevens, J.R.T. Jeffers, The Design and in vivo testing of a locally stiffness-matched porous scaffold, Applied Materials Today (2019) [Under Review]
    - Chapter 3 (3.1.4, 3.4.2, 3.5) & Chapter 6
- N. Reznikov, O.R. Boughton, **S. Ghouse**, A. Weston, L. Collinson, G. Blunn, J.R.T. Jeffers, J.P. Cobb, M.M. Stevens, Individual response variations in scaffold-guided bone regeneration are determined by independent strain- and injury-induced mechanisms, Biomaterials 194 (2019) 183-194 [22]
    - Chapter 3 (3.5) & Chapter 6 (6.1.2, 6.1.3, 6.2.3, 6.3.2)

1.5 References

[1] L. Mullen, R.C. Stamp, W.K. Brooks, E. Jones, C.J. Sutcliffe, Selective Laser Melting: A regular unit cell approach for the manufacture of porous, titanium, bone in-growth constructs, suitable for orthopedic applications, Journal of Biomedical Materials Research Part B: Applied Biomaterials 89B(2) (2009) 325-334.

[2] M.J. Matthews, G. Guss, S.A. Khairallah, A.M. Rubenchik, P.J. Depond, W.E. King, Denudation of metal powder layers in laser powder bed fusion processes, Acta Materialia 114 (2016) 33-42.

[3] S. McKown, Y. Shen, W.K. Brookes, C.J. Sutcliffe, W.J. Cantwell, G.S. Langdon, G.N. Nurick, M.D. Theobald, The quasi-static and blast loading response of lattice structures, International Journal of Impact Engineering 35(8) (2008) 795-810.

[4] V.J. Challis, X. Xu, L.C. Zhang, A.P. Roberts, J.F. Grotowski, T.B. Sercombe, High specific strength and stiffness structures produced using selective laser melting, Materials & Design 63 (2014) 783-788.

[5] S.A. Goldstein, The mechanical properties of trabecular bone: Dependence on anatomic location and function, Journal of Biomechanics 20(11–12) (1987) 1055-1061.

[6] P. Heinl, L. Müller, C. Körner, R.F. Singer, F.A. Müller, Cellular Ti–6Al–4V structures with interconnected macro porosity for bone implants fabricated by selective electron beam melting, Acta Biomaterialia 4(5) (2008) 1536-1544.

[7] L. Mullen, R.C. Stamp, P. Fox, E. Jones, C. Ngo, C.J. Sutcliffe, Selective laser melting: A unit cell approach for the manufacture of porous, titanium, bone in-growth constructs, suitable for orthopedic applications. II. Randomized structures, Journal of Biomedical Materials Research Part B: Applied Biomaterials 92B(1) (2010) 178-188.

[8] S. Amin Yavari, R. Wauthle, J. van der Stok, A.C. Riemslag, M. Janssen, M. Mulier, J.P. Kruth, J. Schrooten, H. Weinans, A.A. Zadpoor, Fatigue behavior of porous biomaterials manufactured using selective laser melting, Materials Science and Engineering: C 33(8) (2013) 4849-4858.

[9] R. Wauthle, J. van der Stok, S. Amin Yavari, J. Van Humbeeck, J.-P. Kruth, A.A. Zadpoor, H. Weinans, M. Mulier, J. Schrooten, Additively manufactured porous tantalum implants, Acta Biomaterialia 14 (2015) 217-225.

[10] D.R. Carter, Mechanical loading histories and cortical bone remodeling, Calcified tissue international 36 Suppl 1 (1984) S19-24.

[11] A.-M. Pobloth, S. Checa, H. Razi, A. Petersen, J.C. Weaver, K. Schmidt-Bleek, M. Windolf, A.Á. Tatai, C.P. Roth, K.-D. Schaser, G.N. Duda, P. Schwabe, Mechanobiologically optimized 3D titanium-mesh scaffolds enhance bone regeneration in critical segmental defects in sheep, Science Translational Medicine 10(423) (2018).

[12] J. Van der Stok, O.P. Van der Jagt, S. Amin Yavari, M.F.P. De Haas, J.H. Waarsing, H. Jahr, E.M.M. Van Lieshout, P. Patka, J.A.N. Verhaar, A.A. Zadpoor, H. Weinans, Selective laser melting-produced porous titanium scaffolds regenerate bone in critical size cortical bone defects, Journal of Orthopaedic Research 31(5) (2013) 792-799.

[13] J. Henkel, M.A. Woodruff, D.R. Epari, R. Steck, V. Glatt, I.C. Dickinson, P.F.M. Choong, M.A. Schuetz, D.W. Hutmacher, Bone Regeneration Based on Tissue Engineering Conceptions — A 21st Century Perspective, Bone Research 1(3) (2013) 216-248.

[14] X. Wang, S. Xu, S. Zhou, W. Xu, M. Leary, P. Choong, M. Qian, M. Brandt, Y.M. Xie, Topological design and additive manufacturing of porous metals for bone scaffolds and orthopaedic implants: A review, Biomaterials 83 (2016) 127-141.

[15] F.S.L. Bobbert, K. Lietaert, A.A. Eftekhari, B. Pouran, S.M. Ahmadi, H. Weinans, A.A. Zadpoor, Additively manufactured metallic porous biomaterials based on minimal surfaces: A unique combination of topological, mechanical, and mass transport properties, Acta Biomaterialia 53 (2017) 572-584.

[16] R. Hedayati, H. Hosseini-Toudeshky, M. Sadighi, M. Mohammadi-Aghdam, A.A. Zadpoor, Computational prediction of the fatigue behavior of additively manufactured porous metallic biomaterials, International Journal of Fatigue 84 (2016) 67-79.

[17] S. Gorsse, C. Hutchinson, M. Gouné, R. Banerjee, Additive manufacturing of metals: a brief review of the characteristic microstructures and properties of steels, Ti-6Al-4V and high-entropy alloys, Science and Technology of Advanced Materials 18(1) (2017) 584-610.

[18] M.F. Ashby, A.G. Evans, N.A. Fleck, L.J. Gibson, J.W. Hutchinson, H.N.G. Wadley, Metal Foams: A Design Guide, Butterworth-Heinemann, Burlington, 2000.

[19] O. Rehme, Cellular Design for Laser Freeform Fabrication, Cuvillier2010.

[20] F. Matassi, A. Botti, L. Sirleo, C. Carulli, M. Innocenti, Porous metal for orthopedics implants, Clinical Cases in Mineral and Bone Metabolism 10(2) (2013) 111-115.

[21] D.Y.R. Chong, Biomechanical Analysis of Fixation and Bone Remodelling of Total Knee Replacement, (2009).

[22] N. Reznikov, O.R. Boughton, S. Ghouse, A.E. Weston, L. Collinson, G.W. Blunn, J. Jeffers, J.P. Cobb, M.M. Stevens, Individual response variations in scaffold-guided bone regeneration are determined by independent strain- and injury-induced mechanisms, Biomaterials 194 (2019) 183-194.

[23] W.E. Frazier, Metal Additive Manufacturing: A Review, Journal of Materials Engineering and Performance 23(6) (2014) 1917-1928.

[24] A. Yadollahi, N. Shamsaei, Additive manufacturing of fatigue resistant materials: Challenges and opportunities, International Journal of Fatigue 98 (2017) 14-31.

[25] S.M. Ahmadi, R. Hedayati, Y. Li, K. Lietaert, N. Tümer, A. Fatemi, C.D. Rans, B. Pouran, H. Weinans, A.A. Zadpoor, Fatigue performance of additively manufactured meta-biomaterials: The effects of topology and material type, Acta Biomaterialia 65 (2018) 292-304.

[26] R. Wauthle, S.M. Ahmadi, S. Amin Yavari, M. Mulier, A.A. Zadpoor, H. Weinans, J. Van Humbeeck, J.-P. Kruth, J. Schrooten, Revival of pure titanium for dynamically loaded porous implants using additive manufacturing, Materials Science and Engineering: C 54 (2015) 94-100.

[27] N.W. Hrabe, P. Heinl, B. Flinn, C. Körner, R.K. Bordia, Compression-compression fatigue of selective electron beam melted cellular titanium (Ti-6Al-4V), Journal of Biomedical Materials Research Part B: Applied Biomaterials 99B(2) (2011) 313-320.

[28] J. Wieding, T. Lindner, P. Bergschmidt, R. Bader, Biomechanical stability of novel mechanically adapted open-porous titanium scaffolds in metatarsal bone defects of sheep, Biomaterials 46 (2015) 35-47.

[29] S. Ghouse, S. Babu, R.J. Van Arkel, K. Nai, P.A. Hooper, J.R.T. Jeffers, The Influence of Laser Parameters and Scanning Strategies on the Mechanical Properties of a Stochastic Porous Material, Materials & Design 131 (2017) 498-508.

[30] S. Ghouse, S. Babu, K. Nai, P.A. Hooper, J.R.T. Jeffers, The influence of laser parameters, scanning strategies and material on the fatigue strength of a stochastic porous structure, Additive Manufacturing 22 (2018) 290-301.

2 Chapter 2 – Background

This chapter details the clinical relevance and application of this work along with a brief introduction into the mechanobiology of bone and bone ingrowth into porous scaffolds. An overview of how the powder bed fusion additive manufacturing process works and how processing parameters affect material properties will be provided. Theory regarding the behaviour of porous structures will be presented as well as a literature review regarding research into AM porous structures, focusing on how build or processing parameters affect mechanical strength. Finally, common orthopaedic biomaterials will be discussed, including research into low stiffness biocompatible metals.

2.1 Clinical Background

The volume of orthopaedic reconstruction procedures to combat osteoarthritis, inflammatory arthritis, metabolic bone disease and other musculoskeletal disorders have increased dramatically, resulting in high demand on the advancement of bone implant technology [1, 2]. Moreover, because of a prolonged life expectancy and an aging world population, there is a rapid increase in musculoskeletal pathologies such as fractures, low back pain, scoliosis, osteoporosis, bone infection or tumours, congenital defects and oral and maxillofacial pathologies, as well as rheumatic diseases like osteoarthritis. Large bone defects caused by severe fracture, tumour or infection are a challenging issue for the regeneration ability of the body. If the defect exceeds a critical size, bone regeneration cannot be handled by the body's healing process alone and requires supportive therapeutic intervention like autografts, allografts or a synthetic scaffold [3, 4]. Similarly, in the treatment of osteoarthritis of a joint, which is degeneration of cartilage and underlying bone, typically caused by injury, obesity, wear and tear, either a partial or full replacement of the joint by an implant is required. Joint replacements typically involve replacing the articulating surfaces of the joint by metal or ceramic materials, and sometimes with an additional bearing material (polyethylene) acting as the cartilage. Porous metals offer significant benefits in the treatment of these pathologies, due to the mechanisms of bone regeneration and adaptation.

2.1.1 Characteristics of Bone and Bone Remodelling

Bone is a complex three-dimensional porous composite structure with a highly organised internal architecture (Figure 2.1). It serves two critical mechanical functions, providing a rigid skeletal framework to support and protect the internal organs and body tissues

and forming a system of rigid levers that can be moved by forces from the attaching muscles. [5, 6]

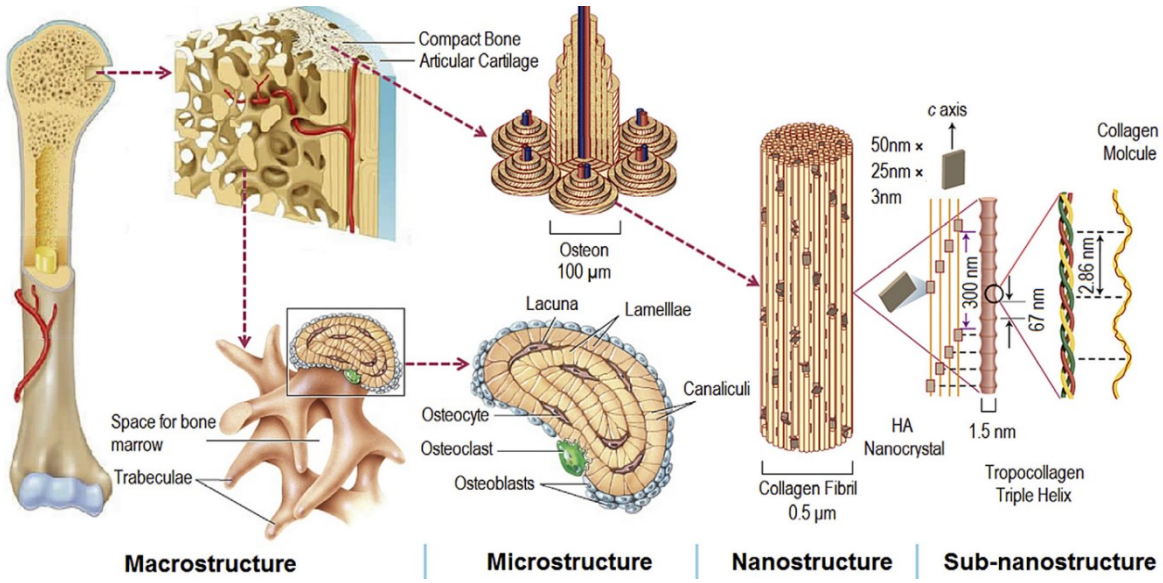


Figure 2.1 – Hierarchical structural organization of bone. Image reproduced with permission of the rights holder, Elsevier. [7]

An important function of trabecular or cancellous bone in human joints is to distribute the large contact stresses applied at the articular surfaces to the compact bone of the cortical shafts. Indeed, the trajectorial theory of bone architecture, states that the trabeculae are organised along the lines of principal stresses [8]; with the structure and strength of trabecular bone being a function of these stresses. Trabecular bone also possess very specific viscoelastic and anisotropic characteristics, both in morphology and mechanical properties. The unique mechanical performance of bone is characterised by high toughness, high specific strength, low stiffness and arguably most importantly, its ability to heal, i.e. bone remodelling and adaptation [9].

In 1892, Julius Wolff (a German scientist and anatomist) published his law on bone remodelling [5]. Although ‘‘Wolff’s law’’ was originally formulated in a strict mathematical sense that has since been discredited, the more general concept of ‘‘bone functional adaptation’’ to mechanical loading is supported by much experimental and observational data [10]. Bone continually undergoes dynamic biological remodelling, the coupled process whereby osteoclasts (bone-resorbing cells) remove mature or damaged bone tissue followed by osteoblasts (bone-forming cells) that generate new bone to maintain healthy homeostasis of bone [11, 12]. This unique feature of bone underpins its ability to remodel itself to repair damage, reducing the risk of fracture, whilst being able to adapt to its mechanical environment

[13]. Bone, therefore adapts to mechanical stimulus by apposition under high loading and by resorption under disuse (or less than habitual loading [14]).

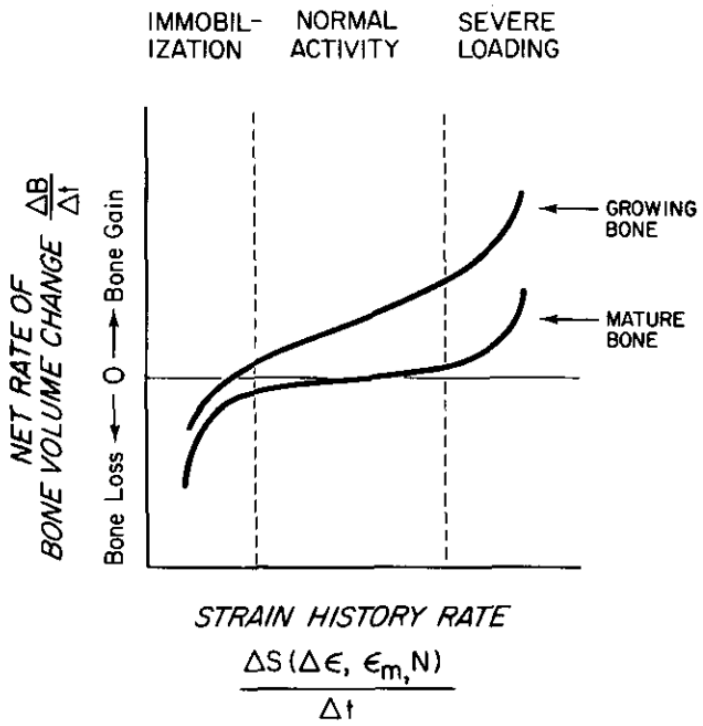


Figure 2.2 – Hypothesis on the relationship between bone strain history rate and the net rate of bone volume change. Image reproduced with permission of the rights holder, Springer Nature. [15]

It is likely that osteocytes (bone cells) respond to bone tissue strain by recruiting osteoclasts to sites where bone remodelling is required [16, 17]. Indeed, there are both theories (e.g. Wolff's Law, Perren's strain theory, Frost's "mechanostat" etc. [18]) and experiments that corroborate the effect of mechanical loads and strain on bone adaptation (Figure 2.2) [13, 19]. Adaptation and remodelling is hypothesised to optimise the stiffness and strength of bones, while minimising the metabolic cost of maintenance, ensuring that animal skeletons are continuously adjusted to control strain [13]. It must be noted that bone remodelling is a complex biological process not only dependent on functional (mechanical) requirements but also genetic, hormonal, metabolic and age-related factors as well (Figure 2.3).

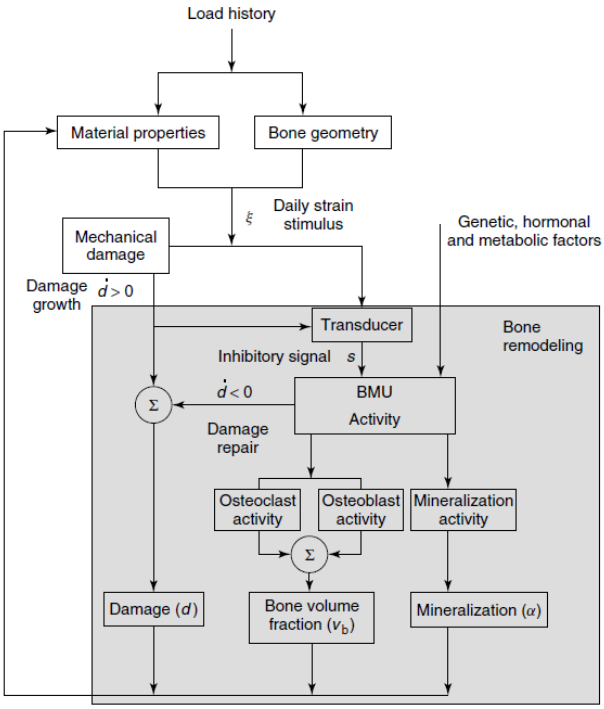


Figure 2.3 – A mechanical model of bone remodelling. Image reproduced with permission of the rights holder, John Wiley and Sons. [13]

2.1.2 Mechanical Properties of Bone and Stress-Shielding

Bone adaption and remodelling is one of the reasons why the mechanical properties and structure of bone vary both locally at joints and globally between joints. For humans, the modulus of cortical bone can vary between ~7 – 30 GPa whilst the modulus of trabecular bone varies between ~0.05 – 0.5 GPa [20]. The properties of bone not only vary between species and anatomical site but also due to age, sex, nutrition, activity level, bone health and diseases [1, 7, 8]. There is much published literature on the variation of modulus and strength of trabecular bone with anatomic site [21, 22], as well as how properties vary locally at joints [8]. An example of the modulus of trabecular bone varying locally is seen in Figure 2.4 for the proximal tibia.

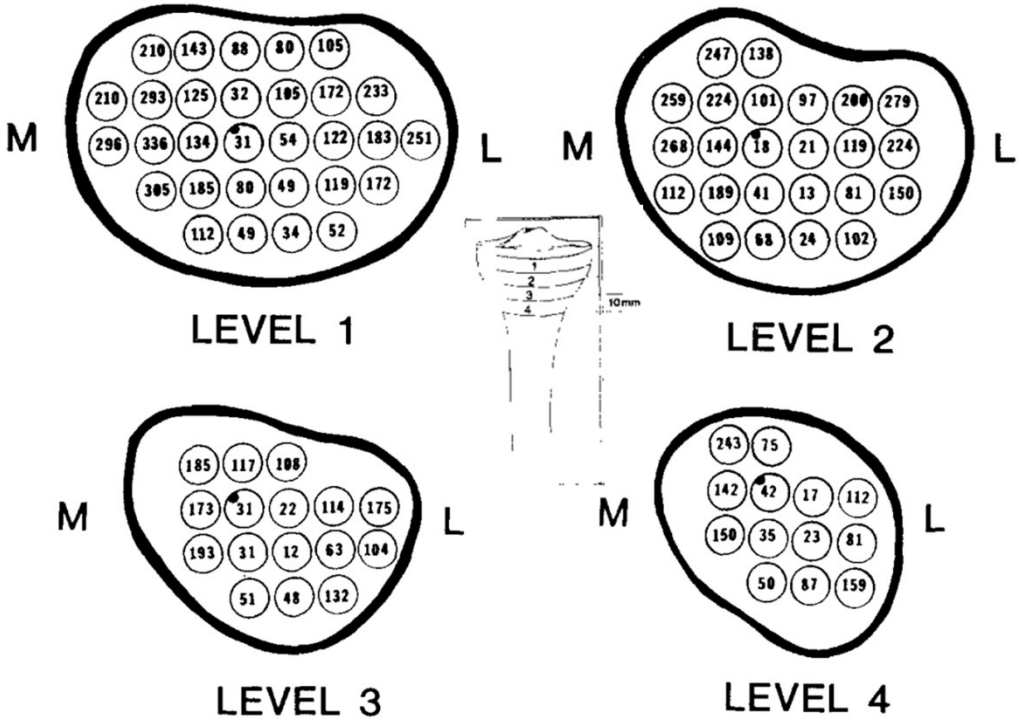


Figure 2.4 – Variation of Elastic Modulus (MPa) as a function of location in the proximal tibia of humans. Image reproduced with permission of the rights holder, Elsevier. [8]

The mechanical properties of bone are typically quantified by compression testing. The compressive stress-strain curve for cancellous bone is similar to those of a cellular solid or porous structure (Figure 2.5). There is an initial linear elastic portion, a plateau of almost constant stress (high energy absorption) and a final increasing steep region (densification).

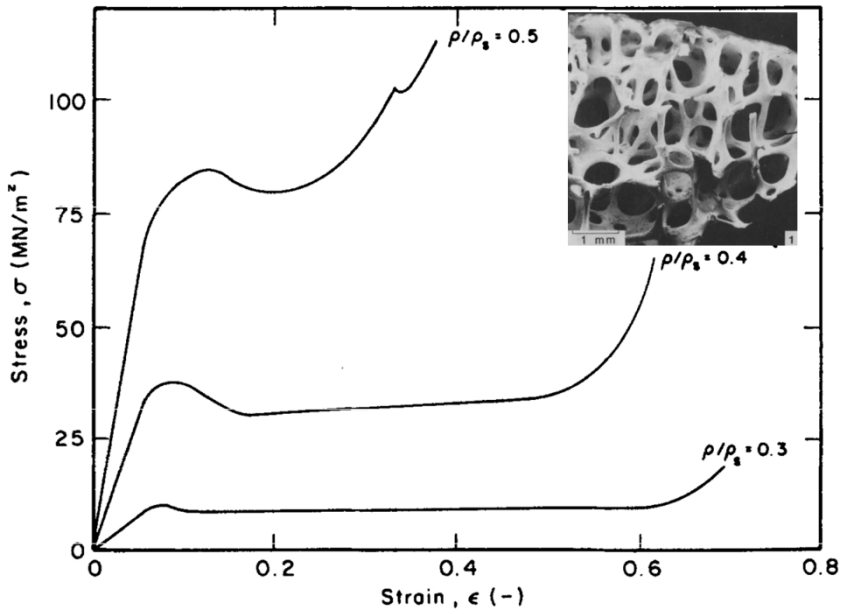


Figure 2.5 – Stress-Strain Curves for human cancellous bone. As relative density increases modulus and compressive strength increases and the strain at which densification occurs decreases. Low density cancellous bone is pictured inset. Image reproduced with permission of the rights holder, Elsevier. [23]

Gibson [23] published the fundamentals on behaviour of cellular materials, including trabecular bone, to mechanical loading. A power relationship between modulus and strength to the relative density of the material is described in these works. This will be discussed in more detail in section 2.2.3. A number of researchers have validated this experimentally and have shown the relationship between bone's mechanical properties to its mass, bone/apparent density, ash density, area fraction and Computed Tomography (CT) grayscale values [6, 23]. Figure 2.6 displays data from a variety of researchers who have tested an array of bone from different species as well as different cellular structures (open versus closed) and it is observed that both modulus and compressive strength are related to bone density by a power law.

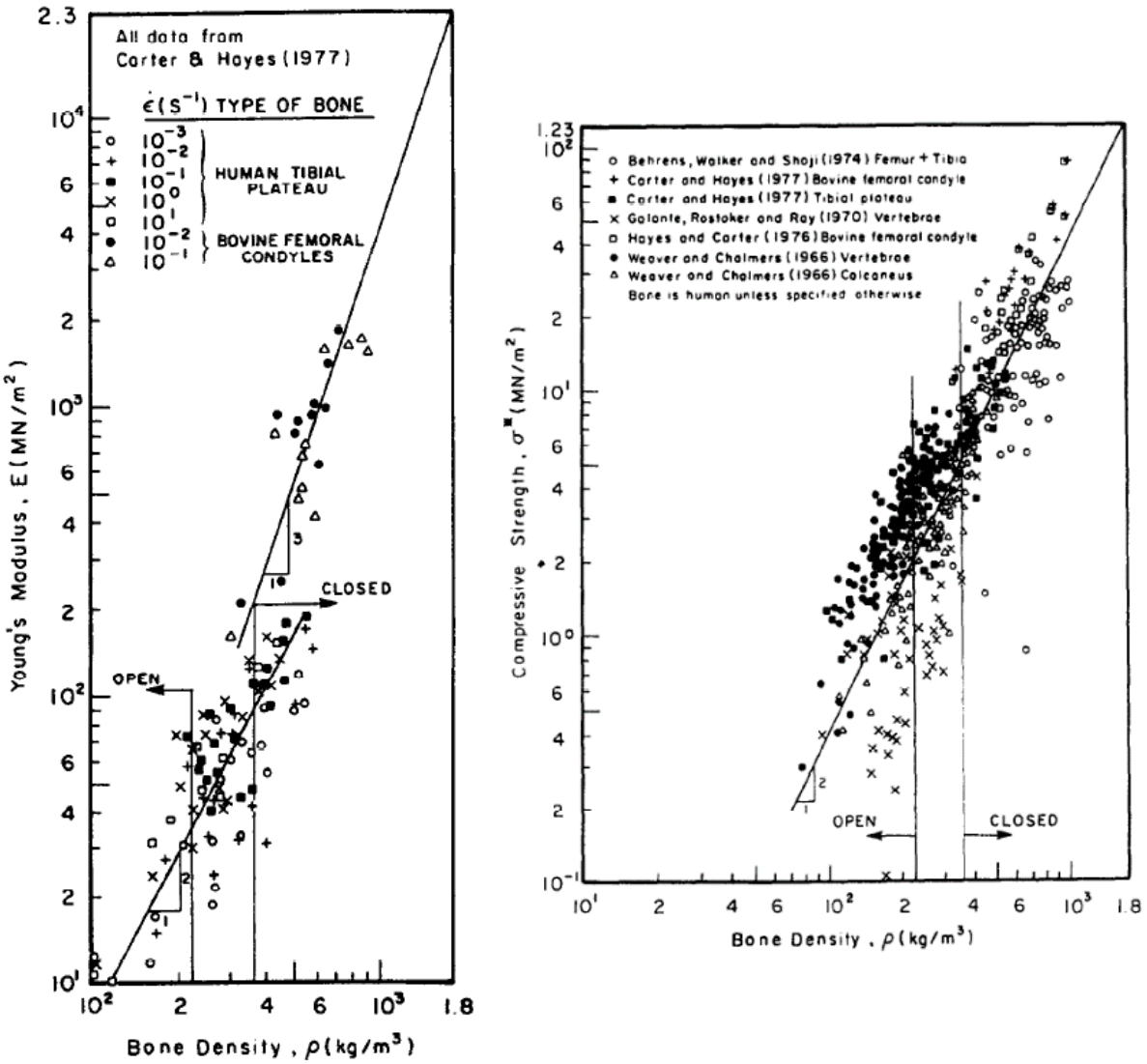


Figure 2.6 – Mechanical properties (Left: Young's Modulus and Right: Compressive Strength) of bone versus bone density. Image reproduced with permission of the rights holder, Elsevier. [23]

The order-of-magnitude(s) differences between the modulus of solid metal implants (~110 GPa for Titanium [24] and 210 GPa for Cobalt-Chrome [25]) and bone can result in localised reduction in bone density (osteopenia). This is due to a diversion of loads and thus strains from the bone to the implant. This is known as stress-shielding, which is a common cause of clinical failure of orthopaedic implants [26]. This unfavourable and altered stress distribution in the bone will cause some localised areas of bone to see a reduction in loading and strain. As there is no stimulus for continued remodelling required to maintain bone mass [27], this can lead to bone resorption (Figure 2.7) [7, 28]. Ultimately, this can result in aseptic loosening of the implant or fracture of the bone around the implant (peri-prosthetic fracture) [29].



Figure 2.7 – Progression of bone resorption (from left to right) due to stress shielding in the proximal tibia. Reproduced under Creative Commons Attribution-Non Commercial-No Derivatives License (CC BY NC ND). [30]

2.1.3 Clinical Applications of Porous Metals

Porous metals allow the effective modulus of the implant to closer match that of the bone it will be replacing whilst still maintaining mechanical competence. They also provide an interconnected structure, which allows bone tissue to grow deep into the implant to form a strong bone-implant interface and thus in addition to reducing stress-shielding have applications in repair of massive bone defects and fixation of cementless joint replacements. The three most common applications of porous metals in orthopaedics are:

- Repairing large segmental bone defects
- Reducing stress shielding
- Fixation of cementless joint replacements

In repairing large bone defects, autografts remain the gold standard, however donor site morbidity and limited supply are major concerns. Allografts and xenografts on the other hand may raise concerns in pathogen transmission and immunorejection respectively. Despite this,

more than 1 million bone grafting operations are performed in Europe and the United States annually, with the market size in the United States projected to exceed 2.2 billion by 2017 [1]. Due to the issues with auto and allografts, the development of synthetic materials for musculoskeletal tissue engineering is paramount. For large segmental defects within load-bearing areas, initially stable mechanical implants are indispensable. Porous metal materials can meet this requirement. These scaffolds offer advantages for numerous reasons: immediate weight-bearing with support of the osteosynthesis. As well as, long-term stability accompanied by its biocompatibility and bone ingrowth ability into the open-porous surface whilst maintaining a stiffness closer to the natural bone compared to a solid monolithic metallic implant [4].

With respect to joint replacements, in the past operations were commonly performed primarily on elderly patients, in view of the prosthesis survivorship. With the advances in surgical techniques and prosthesis technology, younger patients are undergoing surgeries for both local tissue defects and joint replacements. This patient group is now more active and functionally more demanding after surgery [5]. Today, implanted prostheses need to be more durable (load-bearing), they need to better match the patient's original biomechanics and be able to survive longer. Whilst both hip and knee replacements (the most common joints replaced) are well recognised as successful surgical procedures to treat osteoarthritis, implant failure is still a common problem resulting in revision operations [31].

As stated earlier, stress-shielding is a common cause of implant failure. By introducing architectured porosity into an implant, the effective modulus of the prosthesis can be significantly reduced and can better match the native bone (Figure 2.8).

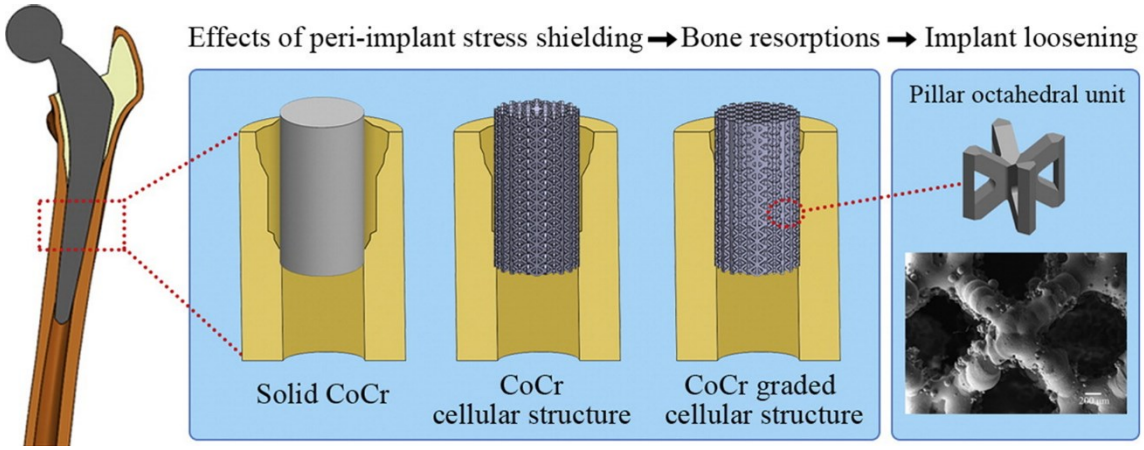


Figure 2.8 – Reduction of stress shielding due to tailoring the properties of a porous structure. Image reproduced with permission of the rights holder, Elsevier. [32]

For younger patients looking for solutions to local tissue defects, porous metals are able to take advantage of the healing capacity of a younger population. Traditionally implants can be fixed to the bone in several ways: by bone cement, by mechanical fixation devices (screws/interference fits) and by activated surfaces resulting in bone apposition. Stability is vital to the success and longevity of an implant *in vivo* and whilst these techniques have all been clinically successful and are still in practice, the recent trend in orthopaedics has been towards biological fixation by osseointegration or bone ingrowth [5, 33]. Porous metals, particularly manufactured by additive manufacturing, allow for an open interconnected structure to be designed. By taking advantage of the mechanobiology of bone, bone can grow deep into the structure achieving good long lasting levels of fixation.

2.1.4 Requirements for Bone In-Growth

The physiologic response to a porous implant or coating resembles the healing cascade of cancellous defects, with the newly formed tissues occupying the void spaces of the porous structure [34]. This is seen in Figure 2.9, which displays backscattered SEM images of bone ingrowth into a porous implant (seen as a bright white porous structure), where the thin dark grey speckles of bone occupy the voids in the implant and the new formed bone bridges the defect created in the cortical bone. The requirements of porous structures for bone in-growth in orthopaedics are that they [7, 9, 20, 34, 35]:

- Should be biocompatible/bio-inert
- Have a suitable surface for cell attachment, proliferation and differentiation,
- be porous with an open interconnected pore network for cell ingrowth and transport of nutrients and metabolic waste
- Have sufficient mechanical strength to avoid failure under load
- Provide a stiffness or strain gradient to encourage bone remodelling throughout the porous structure
- Have intimate contact with the bone and provide sufficient stability (i.e. minimum micro-motion between the scaffold and bone)

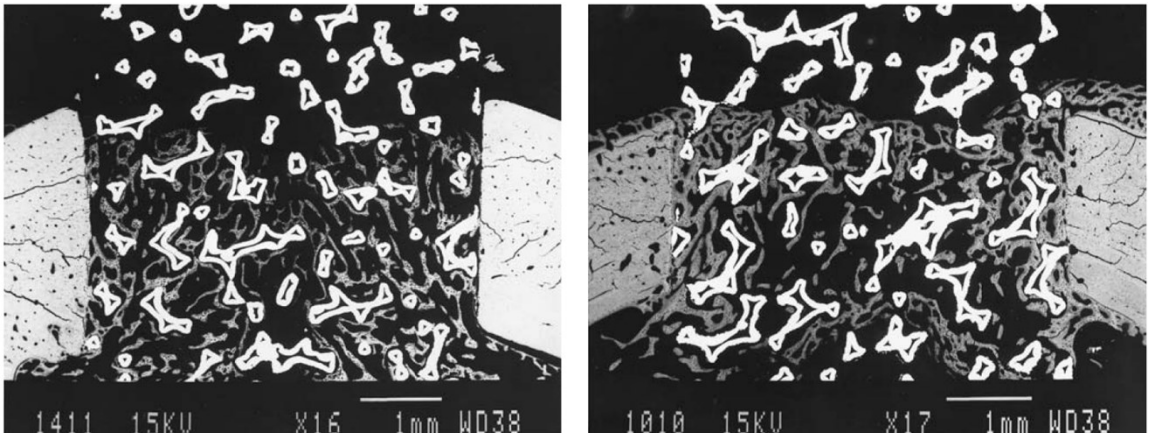


Figure 2.9 – Backscattered SEM imaging of bone ingrowth into a transcortical porous tantalum implant into the femoral diaphysis of skeletally mature mongrel dogs after two weeks (left) and three weeks (right). Reproduced under Creative Commons Attribution License (CC-BY-NC 4.0) [36].

Gaps at the bone-implant interface are known to decrease the volume fraction and extent of bone ingrowth. Although a 2 – 3mm gap may be bridged by bone in unloaded animal models, the ingrowth of human bone under load is less predictable. Intimate contact between the porous coating and bone has been shown to increase the amount of bone ingrowth in both human and animal models [34, 35]. In addition to this the motion between the implant and bone is vital, studies have shown 50 μm of micro-motion is the maximum to promote healthy bone ingrowth with ideally micro-motion being as small as possible. [35]

Historically it has been reported that one of the requirements for bone ingrowth into a porous scaffold or into a porous coating of an orthopaedic implant is that it should match the mechanical properties of the surrounding bone tissue [1, 4, 7]. However, an increasing volume of work supports taking advantage of the mechanobiology of bone and that the lower the stiffness of a porous scaffold is, relative to the bone it is replacing, the more bone ingrowth occurs [37, 38]. Therefore the challenges are to ensure porous structures retain sufficient mechanical competence at low stiffness, and to know the properties of the bone being replaced. However, not only are the mechanical properties of bone difficult to measure, resulting in variations in reported properties in literature [7, 39], but bone properties also vary between species, anatomical site and due to age, sex, nutrition, activity level, bone health and diseases [7, 9, 21]. Typically, when porous structures are tested *in vivo* or implanted during surgery the mechanical properties of the animal's or patient's bone being replaced are unknown and not quantified. It is therefore difficult to compare ingrowth results between studies and to translate *in vivo* animal testing to human subjects.

Most *in vivo* testing of porous structures for bone ingrowth has focused on structural features of the material, typically pore size and porosity. Implants have included solid titanium plates with holes of increasing diameter [40], porous sintered titanium coatings, hydroxyapatite scaffolds, conventionally manufactured [36] and additively manufactured [4, 37, 41] porous metal scaffolds. There has also been a wide array of animal models and implant locations (e.g. skeletal location, cortical versus trabecular bone) used [7, 9]. Consequently, the differences in mechanical environments and loading likely contribute to why inconsistencies in the literature exist regarding the 'optimal' scaffold pore size and porosity for bone ingrowth [9]. Some work has claimed 100 – 400 μm size pores to be ideal [34, 35], whereas other studies have found larger pore sizes of 600 – 1200 μm [42, 43] to be preferential for bone ingrowth [7], with some researchers even finding bone ingrowth to occur in pores of less than 100 μm [28, 40]. However, as bone fills in small sized pores, it may hinder the transportation of oxygen and nutrients to the centre of the scaffold, inhibiting cell proliferation and maturation, and resulting in poor bone-implant bonding [7]. There are also practical concerns about removing loose un-sintered powder from porous structures, particularly if the pore size is too small. Conversely, larger pore sizes are associated with a low short term bone ingrowth ratio, as during the initial stages of bone formation [44], only a small quantity of bone occupies the implant pores [1]. Similarly with regards to the role of scaffold porosity on bone ingrowth, typically higher porosity scaffolds (>70% porosity) have been shown to have better ingrowth than low porosity scaffolds (<70% porosity) [1, 28]; however in the porosity ranges of 70 – 90% researchers have found opposing results [28]. Without understanding the mechanical properties of the tissue being replaced and the loading environment, it is difficult to make determinations regarding "optimal" pore size and porosity for scaffolds.

Most commercial or research-grade porous scaffolds have a homogenous structure and are consistent regardless of skeletal location or animal used despite bone varying locally at joints, globally throughout the skeleton and between species. As an increasing volume of work indicates mechanobiology is an important factor in how bone responds to a scaffold or implant [37], there is a need for scaffolds and porous implants with stiffness gradients tailored to invoke the desired mechanobiological response from bone, specific to the site being investigated. More so, there is a need for a method to create such structures in a pragmatic way that can be deployed clinically in humans, additive manufacturing provides such an opportunity.

2.2 Additive Manufacturing

Additive manufacturing (AM), the process of joining materials to make objects from three-dimensional (3D) model data, typically layer-by-layer as opposed to traditional subtractive manufacturing methods, emerged in the late 1980s and has matured rapidly in recent years [45]. During the development stage in the 1990s, 3D printing was mostly used for rapid prototyping of polymer and thermoplastic materials. However, advancements in laser and electron beam technologies enabled the fabrication of metallic components. Over the years 3D printing progressed from rapid prototyping to rapid manufacturing of end-use and functional metallic parts [46].

The advantage of AM over conventional subtractive or forming methods is demonstrated by the design freedom that can be achieved, such as the possibility of producing geometries or topologically optimised lightweight components not possible by other means, or even consolidating assemblies into single parts. Whilst, AM is a common term used to describe a group of advanced manufacturing technologies that create objects in a layer-wise method [47], only a few of these technologies are appropriate for producing structural components. One of the dominant methods for producing functional metal parts with properties that can rival those of traditional processing techniques is via laser powder bed fusion (LPBF) [48, 49].

During the laser powder bed fusion process, micron sized powder particles (typ. 15-45 μm) are spread in very thin layers (typ. 25-60 μm) on a build platform and melted by the absorption of radiation from the thermal energy of a fibre laser beam under an inert atmosphere. The process begins by creating a computer-aided design (CAD) model of the object to be built and then geometrically slicing it into thin layers. Scan vectors are then generated to trace the contours of the cross-section with ‘hatch scans’ filling it in. This information is then transferred to a laser powder bed fusion system. For every layer, the laser beam exposes the relevant cross-sectional area of the part(s), thereby melting and re-solidifying the powder particles to each other and to the layer beneath, the build platform is then lowered, coated with a new layer of powder and the process repeats (Figure 2.10). In order to achieve this, a coating device, usually with a silicon wiper, spreads a new layer of powder onto the previous layer. The laser beam is directed and focused across the surface of the powder bed/build platform by scanner mirrors (galvanometers) and optics (typically an f – Theta lens) respectively in such a way that the powder particles can be melted where desired.

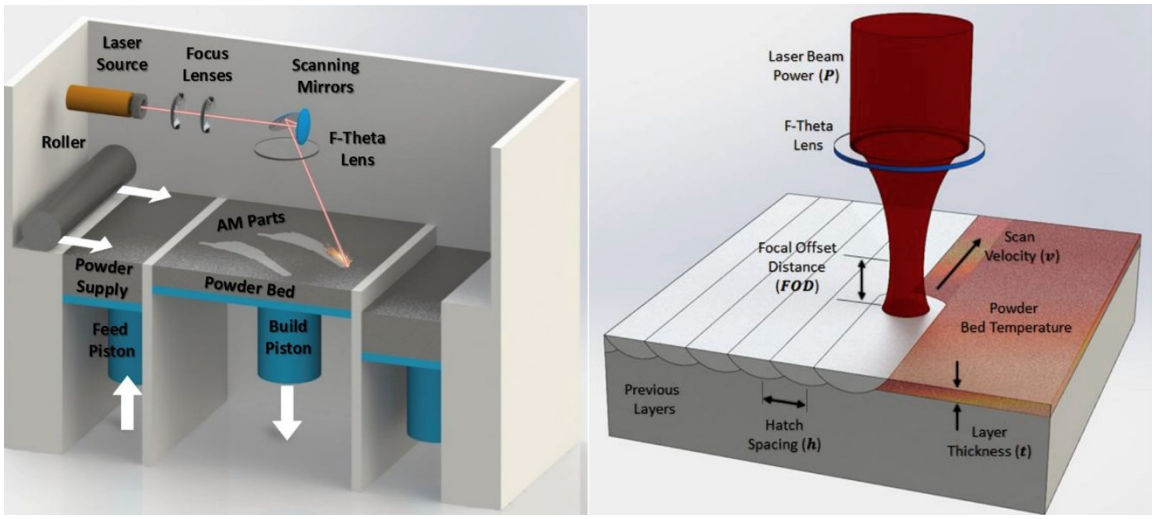


Figure 2.10 – Schematic of a typical laser powder bed fusion machine (left) and some operating parameters (right). Image reproduced with permission of the rights holder, Elsevier. [50]

At least 150 different parameters have been proposed that can affect the LPBF process and consequently the quality of produced parts, manufacturing cost and manufacturing time [51]. From these parameters, about 13 have been identified that are crucial to the resulting quality of manufactured parts; these parameters include the laser beam power, the laser beam speed across the powder bed, the build layer thickness and the scanning strategy (Figure 2.10). During fabrication, metallic AM parts experience a complex cyclic thermal history [47]. The rapid cooling rates and directional solidification in powder bed fusion causes the produced metal parts to have features and microstructures that differ from their cast and wrought counterparts. Heterogeneous microstructures, anisotropy, both elongated and fine grains as well as metallurgical defects (e.g. porosity and cracks) are examples of distinguishing material properties of AM metals [52]. The effect of the previously mentioned crucial process parameters on the thermal history of AM parts results in uncertainty and non-uniformity in the structural properties of the fabricated parts and consequently remains a barrier to the continued adoption of AM.

2.2.1 Fundamentals of Additive Manufacturing

In order to investigate the role of laser parameters, scanning strategies and different base materials on porous structures, some fundamentals of the laser powder bed fusion process must be understood. Understanding the laser interaction with metal powder beds is critical when obtaining optimum processing regimes. Upon irradiation of the laser to the powder bed, the powder material is heated and melts to form a liquid pool, known as the melt-pool, which solidifies and cools down rapidly (Figure 2.11).

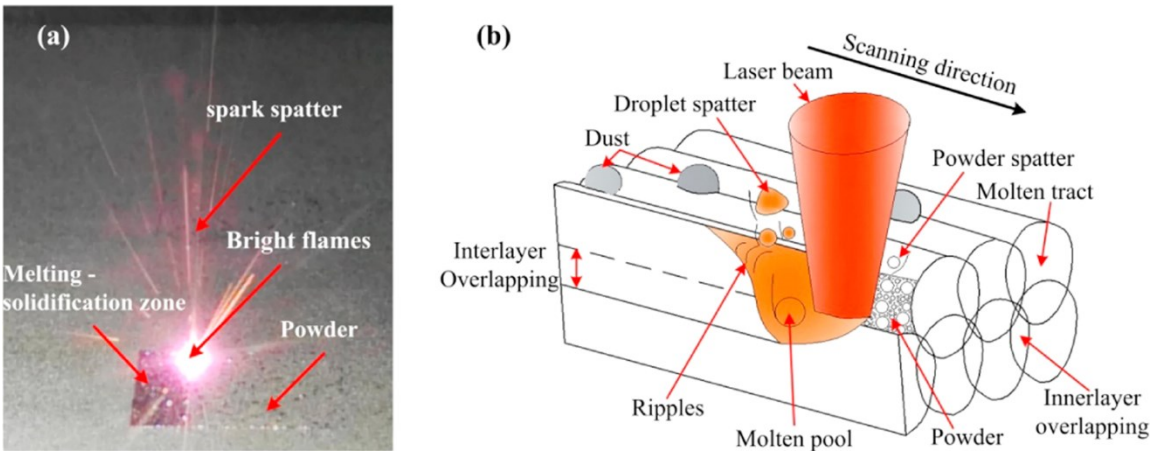


Figure 2.11 – Melt-pool generation in laser powder bed fusion. Image reproduced with permission of the rights holder, Elsevier. [53]

The size and shape of the melt-pool are dictated by the process parameters listed earlier, such as laser power, laser speed, layer thickness, hatch spacing etc. [54] The size of the melt-pool must be large enough to wet (attach to) the layer beneath it as well as be large enough to overlap with nearby scan vectors. Upon solidification, the upper surface of the melt-pool must also be flat enough to enable a next layer of powder to be spread over it. Residual heat from the melt-pool, particularly when scanning the outer contour of a part, can also have the undesired effect of having semi-fused particles attached to the surface thereby increasing the surface roughness. Poor surface roughness is exacerbated by the layer-wise manufacturing method of LPBF and the so called stair case effect (Figure 2.12).

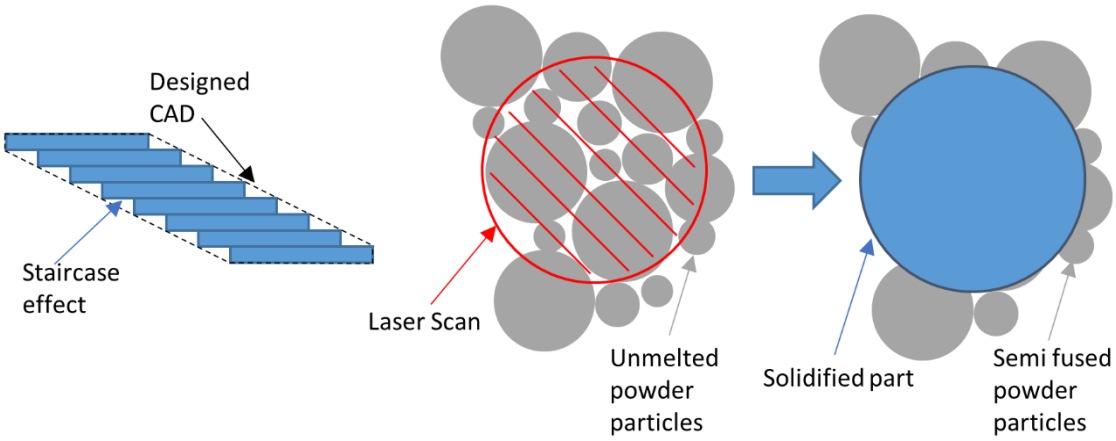


Figure 2.12 – Staircase effect (left) and semi-fused particles (right)

Typically the initial goal of optimisation of laser and process parameters is to achieve near 100% density (Figure 2.13). However the complex thermo-fluid process of laser powder bed fusion means this is difficult.

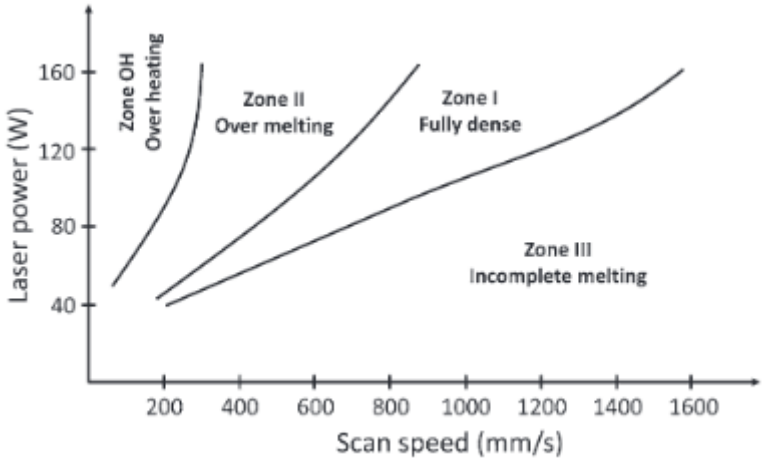


Figure 2.13 – Laser parameter optimisation for maximum density. Reproduced under Creative Commons Attribution License 4.0 [52]

Some of the key considerations of the LPBF process are as follows and will be discussed in detail:

- Defects
- Residual Stress
- Unique Microstructures and microstructural heterogeneity
- Anisotropy

2.2.1.1 Defects

There are a number of reasons for defects and porosity in AM parts which can be detrimental to the mechanical properties of the fabricated samples. They can simply be from insufficient or non-uniform powder spreading, from gas entrapment both in the metal powder particles or during solidification, or from more complex laser interactions with the powder bed and resulting melt-pool [55]. Porosity and defects can form due to both insufficient and excessive energy input from the laser. However, additional complexity arises from the fact that heat dissipation from the melt-pool is also a function of part geometry and part orientation. Thus, laser parameters that have been developed to produce fully dense test specimens (e.g. for a simple cylinder) may not be appropriate for the range of complex geometries capable via AM.

Insufficient energy from the laser to the powder bed and lack of overlap between scan vectors or build-layers (relative to the melt-pool size) produces un-melted or partially melted material and lack-of-fusion regions resulting in pores and cracks (Figure 2.14). The lack of fusion crack is one of the most serious defects in laser material processing especially in additive

manufacturing. It is directly connected to the mechanical behaviour and fatigue life of the final products in laser material processing. Conversely, excessive laser energy can cause a volatile and turbulent melt-pool leading to many different types of defects including spatter ejection, keyhole porosity and balling.

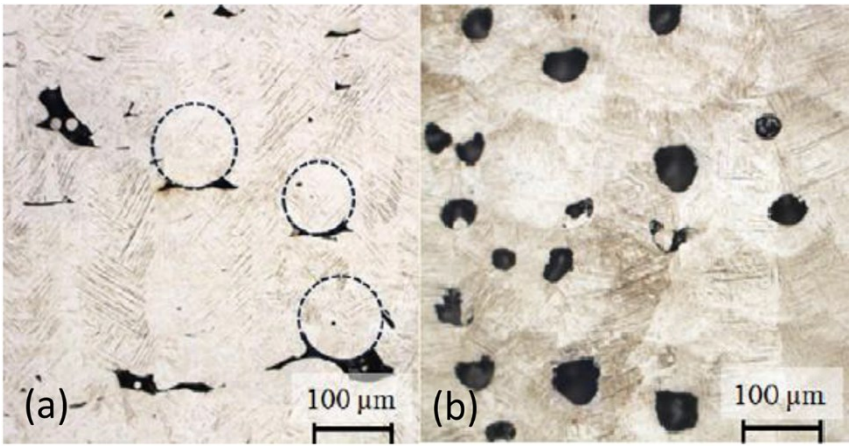


Figure 2.14 – (a) crack-like pores induced by effects like balled and unmolten particles (dashed circles) and spherical pores (b). Image reproduced with permission of the rights holder, Elsevier. [50]

Spatter ejection and keyhole welding occurs due to the overheating of the melt-pool as a result of the high energy beam-feedstock material interaction. It creates recoil pressure in the melt-pool due to convective transport of fluid (Marangoni Convection) which results in the spatter of metal droplets. Spatter ejection is found to contribute to the formation of oxide layers and also porosity, as the evaporated materials leave regions of molten pool with incomplete material solidification. This leads to formation of pores in the solidified structure. In keyhole-mode laser welding, the power density of the laser beam is sufficient to cause evaporation of the metal and formation of plasma. Metal evaporation causes the development of a vapour cavity that enhances the laser absorption. This enables the laser beam to "drill" to a far deeper depth than is possible than by just thermal conduction. Collapse of the cavity can leave voids in the wake of the laser beam [54].

Balling is observed most in AM processes and caused by the laser energy induced non-stabilised melt pool (Figure 2.15). Balling phenomenon is believed to happen for both low laser energy (incomplete wetting) and high laser energy (liquid splashes onto cohesive powder particles). Balling occurs as the result of limited liquid phase formation in the molten pool to initiate powder melting when the temperature becomes too high as the power of heat source increases. It is characterised by the development of rough, spherical structures on the surface of the 3D printed parts. The occurrence of balling is governed by various metallurgical

mechanisms including molten pool behaviour, Marangoni convection and wettability. Balling pores are typically larger than keyhole pores and they have a strong impact on the mechanical properties of the parts. Moreover, balling may result in the formation of discontinuous scan lines which will significantly affect the melt pool overlapping between scan lines and layers [46, 56, 57].

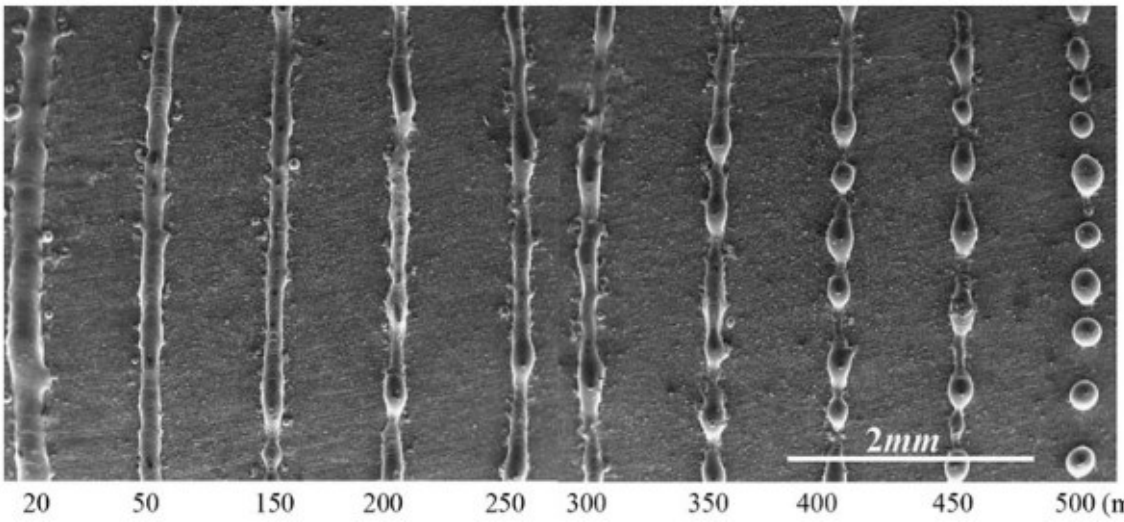


Figure 2.15 – SEM images of the balling characteristics of single scan tracks with increasing scan speed. Image reproduced with permission of the rights holder, Springer Nature. [56]

Other defects are lack of fusion at high energy, likely caused by thermal distortions, the formation of hot tears, a consequence of the material response to stress at elevated temperature and denudation zones [52]. Denudation zones are regions of displaced powders driven by the metal vapour ejection and entrainment of powder particles in the gas flow, which clears powders along the path of the laser towards the sides of the scan track [48]. This can contribute towards porosity as the available amount of powder along the laser scan route is reduced during subsequent scans [46].

In general the mechanical properties of LBPF parts under quasi static loading can be comparable to their conventionally fabricated alternatives, however, a major concern is their fatigue resistance. Contrary to failure under static loading, failure under fatigue is mostly driven by impurities and microstructural heterogeneity. In wrought materials, slip bands and microstructural weak points typically compete for initiating cracks by providing local plastic deformation under cyclic loading. However for LBPF parts fatigue failure typically is initiated by voids and defects close to the surface, which also act as stress concentrations [47]. Thus obtaining defect free parts, particularly by optimising the laser parameters, is vital to ensure long fatigue life of components. Particularly for fine porous structures it is imperative that they are as close to 100% dense as possible to maximise mechanical properties and fatigue life.

2.2.1.2 Residual Stress

As the laser selectively melts and fuses powder as it scans across a part there will be localised heating and cooling. Furthermore the melting and subsequent solidification of the thin layers creates significant thermal gradients resulting in the generation of residual stresses when the parts cool (Figure 2.16) [58]. Residual stresses can lead to deformation and failure of parts both within the AM process and in subsequent post processing steps [59]. Cracks that are accompanied with warping or distortion are normally caused by residual stress. These types of cracks are material dependent and maybe unavoidable [57]. Both the localised heating and cooling rate of melt-pool as well as the global thermal history of the part will affect the amount of residual stress generated, with a number of authors investigating the role of laser parameters and scan strategies on residual stress [45, 49, 57, 59], as well as the thermal post-processing required to relieve these stresses [60-62].

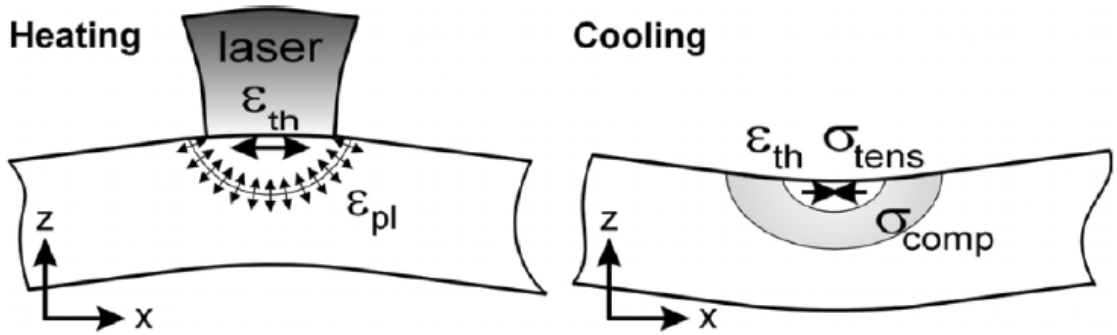


Figure 2.16 – Localised thermally induced residual stress. Image reproduced with permission of the rights holder, Elsevier. [50]

Residual stress is also one of the reasons why low angle features require support structures in powder bed fusion. Typically surfaces <30 – 45° relative to the build plate need to be built with supports which are manually removed post-build or post thermal heat treatment. However, when building complex geometries such as porous structures it can be exceedingly difficult to remove supports from deep within the structure. For this reason the majority of AM research into porous structures have tended to be on unit cell geometries with struts > 45° to the build plate [7, 63], whilst some research has looked at porous structures with low angle or even horizontal struts they tend to have poor morphology [64]. By developing novel scanning strategies and optimising the laser parameters (laser power, laser exposure time per point, etc.) during the build process, this research will also investigate whether thin mechanically competent struts can be built at low angles. This will allow for a better match to the architecture of trabecular bone, where individual trabeculae grow at all angles.

2.2.1.3 AM Microstructure

Mechanical properties of metals are highly dependent on the microstructure [50], the same is true of AM metal specimens. The high energy-material interaction cycle in LBPF causes rapid heating and melting of materials which eventually leads to rapid solidification upon cooling as well as directional heat extraction being present. Generally, the high heating/cooling rates in the rate of $10^3 – 10^8$ K s^{-1} contribute to the formation of non-equilibrium phases [46] and anisotropic and heterogeneous microstructures that intrinsically differ from metallic parts manufactured via conventional methods [65]. The laser parameters (laser power, laser speed, layer thickness, etc.) and scanning strategies affect the thermal history (i.e. melt pool temperature, thermal gradient, cooling rate, cyclic reheating) during fabrication, and consequently affect the microstructural details (grain size/morphology, texture, defect type/size/distribution and residual stress, etc.), and therefore the mechanical behaviour of fabricated parts [47].

A number of researchers have shown how different laser parameters and scanning strategies result in differences in phases present, grain morphology, grain size and texture in LBPF. LBPF specimens are characterised by a heterogeneous microstructure as a result of local differences during the melting and solidification process. These local differences occur both across a given layer and with respect to build height. Thus, the produced microstructure is affected by part geometry, size [66], orientation, build height and number of parts being built as they will all affect the thermal history of the melting and solidification process. Furthermore, differences in thermal conditions (thermal gradients, cooling rates etc.) can result in differences in phases present, their quantity and constitution. Naturally, changes in microstructure, both in terms of grain characteristics (size, morphology texture) and phases present and their quantities will affect the mechanical properties of the built part [67-72]. For example, the strength and yield stresses of a material depend on the grain size as described by the Hall-Petch relationship [72]. Locally in an AM part, as the melting and solidification occurs rapidly, there is insufficient time for grain development and grain growth, grain refinement is expected to occur. However for certain materials, the layer-by-layer nature of AM and the repeated melting and solidification of layers sometimes causes certain grains and phases to be elongated along the height of the part. Unfortunately, this work has almost exclusively investigated solid parts and there remains a lack of research regarding the role of laser parameters and scan strategies on microstructure and mechanical properties of porous specimens. Specific examples of the role of laser parameters on microstructure for selected biomaterials can be found in Section 2.3.

2.2.1.4 Anisotropy

As described above, there are constantly changing thermal conditions during the laser powder bed fusion process in addition to a directional heat flux and large thermal gradients. These features of AM metal microstructures also can contribute to significant anisotropy. A common microstructure feature observed is epitaxial columnar grain morphology aligned parallel to the build direction. Grain morphology along with differences in texture, due to the steep thermal gradients and re-melting of previous layers, alignment of grain boundaries, part orientation as well as location of defects, all contribute to significant anisotropy in mechanical properties. This is exacerbated in some materials if their atomic crystal structure is also anisotropic, for example in the hexagonal close packed (hcp) crystal structure [67] of commercially pure titanium.

Section 2.2.1 highlights the complexity behind the optimisation of process parameters for AM parts. Increasing research has highlighted the effect laser parameters and scan strategies can have on the material and mechanical properties of solid AM parts, but their effects on porous structures have been under reported. In addition to this there are also inconsistencies and issues with the mechanical testing of porous structures in literature. Before discussing relevant materials for the manufacture of porous structures, a review of research into porous structures will first be presented.

2.2.2 AM of Porous Biomaterials

Due to the technological developments in additive manufacturing, architectured porous structures are increasingly deployable for a range of applications including weight reduction, energy absorption and heat exchangers [48, 73-75]. In orthopaedics, implants which have traditionally been solid pieces of metal, that are significantly stiffer than the natural bone [21], can now be composed of low stiffness porous structures produced by AM [76], from biocompatible metals like stainless steel, titanium, cobalt chrome, and tantalum [41, 42, 77]. Bone repair and regeneration has been shown to be driven by strain response with respect to load [15, 37, 78]. Therefore, in order to accelerate bone regeneration, a porous scaffold or porous coating on an implant should have a stiffness less than the bone that is being replaced (0.05-0.5 GPa for trabecular bone and 7-30 GPa for cortical bone [20]). However, a challenge is to ensure that at low modulus, AM porous structures have maximum strength to guarantee implant survival in a high cyclic load environment.

Additive manufacturing of metals provides implant manufacturers numerous advantages when producing a porous biomaterial compared to conventional manufacturing techniques. The microarchitecture of porous biomaterials can be precisely controlled, namely the size, shape, distribution and interconnectivity of pores and struts can be finely tuned as well as the overall porosity and effective modulus. AM also allows for gradients or local variations in the structure and can provide a strong interface between porous features and solid monolithic geometries. As the mechanical characteristics of bone vary with skeletal location, both the local and global mechanical properties of porous biomaterials can be tuned by modifying its micro-architecture, thereby maximising the bone remodelling/ingrowth. Another important advantage is that patient specific implants can be produced more easily using additive manufacturing techniques [79]. The manufacturing methods, the architecture of the structure, the base material and thermal/mechanical post-processing all provide opportunities to maximise the static and fatigue strength of AM porous structures. This research will focus solely on the role of manufacturing methods and base materials on porous structures.

2.2.3 Mechanical and Material Properties of Porous Structures

The majority of research on AM porous structures has investigated different architectures (unit cell types), characterising the strength and stiffness of the structures at varying porosities (relative densities). Most structures investigated are non-stochastic architectures which include variations of cubic crystal system structures (Figure 2.17) [80-82], space filing polyhedrons [83] and triply periodic structures [84-87]. A few researchers have also looked at pseudo-randomised versions of crystal system structures [42] and fully stochastic architectures [88, 89] but in general stochastic architectures have received very little attention.

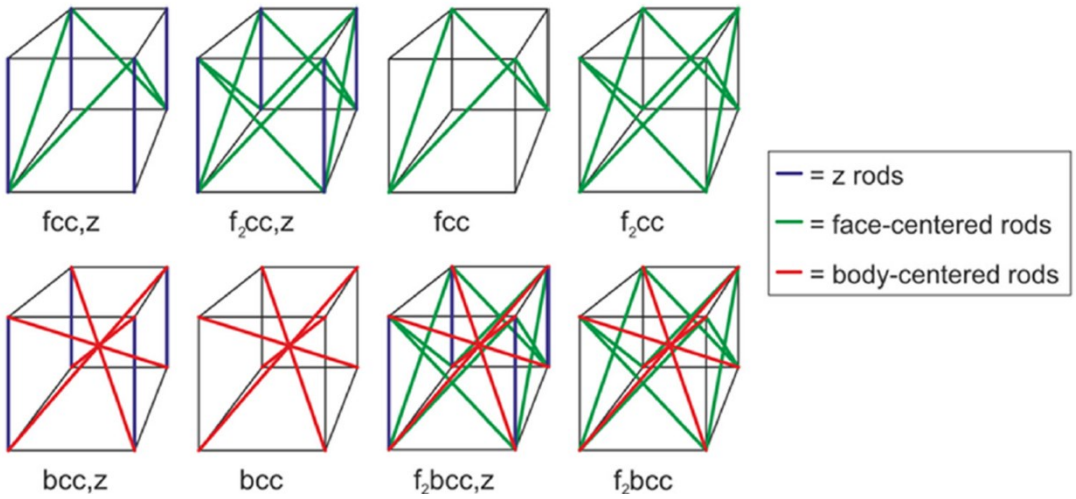


Figure 2.17 – Cubic crystal system structures. Many porous AM materials are built with these types of repeating unit cells. Reproduced under Creative Commons Attribution License (CC BY). [63]

Stochastic materials, tend to typically be weaker than non-stochastic structures for a given relative density in a given loading direction, as there are often redundant struts or the structure is states of self-stress; whilst non-stochastic structures can be engineered to only include the optimum or relevant struts to withstand a certain loading scenario. However, the benefit of stochastic materials are that they tend to be isotropic whilst unit cells such as cubic crystal structures are inherently anisotropic. They also offer far more flexibility and freedom in design of gradients and specific structural anisotropy as well as avoiding row-by-row failure planes (i.e. they tend to behave as continuums) [51, 90, 91].

Typically mechanical testing of porous structures utilises compression testing. The behaviour of porous structures have been described by models by Gibson and Ashby [90-92]. They indicate two classifications of compressive behaviour (Figure 2.18). Struts, in the porous structure, can be *bending dominant* and fail by either plastic bending, elastic buckling or brittle fracture. Alternatively, struts can be *stretch dominant*. In *stretch dominant* structures all the same failure mechanics are present as in *bending dominant* structures however struts can also carry an axial tensile load.

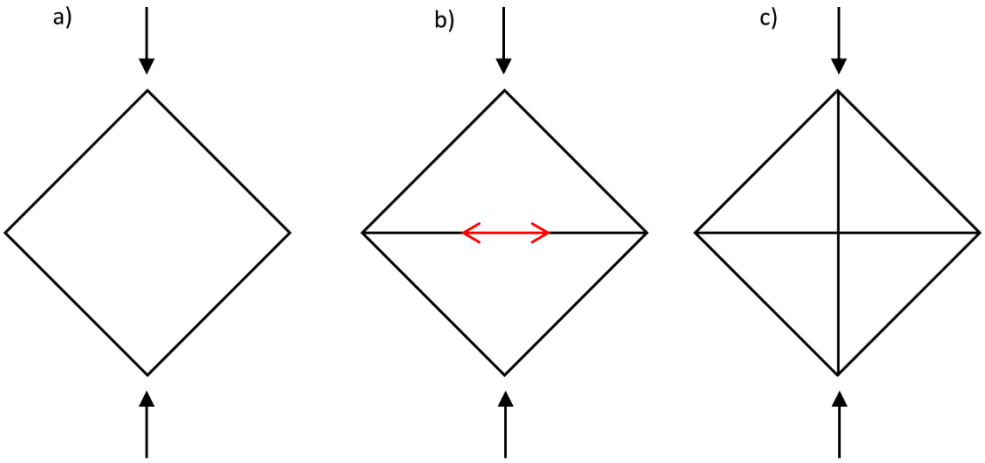


Figure 2.18 – Compressive behaviour of porous structures: a) the struts bend under compression (bending dominant); b) under compression the horizontal strut will carry tension (stretch dominant); c) the structure is over-constrained and possibly in states of self-stress [92]

Under compression, porous structures will exhibit an initial linear portion, which appears to be elastic. This is termed the quasi-elastic gradient [93]. Surface strain measurements have shown that there is localised plasticity in struts and nodes of porous materials at stresses well below the compressive strength of the specimen which reduces the slope of the initial loading curve [90]; therefore hysteresis loops are necessary to obtain better representations of the elastic modulus of porous specimens. In this research, elastic modulus of a porous specimen refers to the effective or apparent modulus of the structure and not the modulus of the base material. As illustrated in Figure 2.19, the elastic region is followed by yielding, with an upper and lower yield sometimes being observed, due to post yield softening or brittle fracture. Following this is a plateau region, during which plastic deformation of the struts occurs with relatively little increase in stress, although this region is not always perfectly horizontal. Eventually the structure collapse and densifies resulting in a sharp increase in stress.

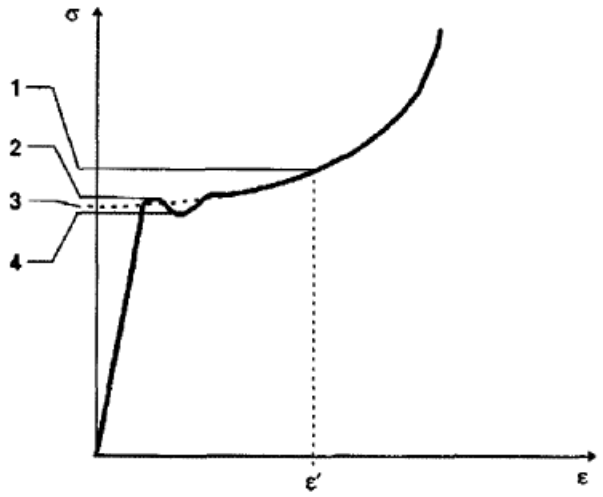


Figure 2.19 – Compressive Stress – Strain curve of a porous metal. Image reproduced with permission of the rights holder, Springer Nature [94].

When the fatigue behaviour of porous AM structures is investigated, compression – compression fatigue testing is usually performed, with structures exhibiting a three – stage fatigue behaviour [77]. As seen in Figure 2.20, in Stage 1 there is a settling in period where specimens accumulate a small amount of plastic strain slowly until Stage 2 where there is a very minimal accumulation of strain with increasing cycles, until finally in Stage 3 the strain increases very rapidly and the specimen fails catastrophically within a limited number of cycles.

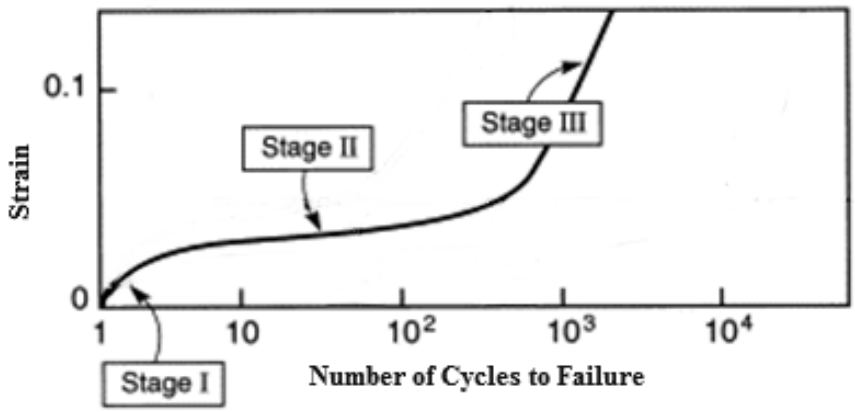


Figure 2.20 – Fatigue failure curve (Strain vs. number of cycles to failure) of a porous metal under compression-compression fatigue. Image modified and reproduced with permission of the rights holder, Elsevier. [95]

Increasingly, researchers have compared different architectures and their static and fatigue properties [80, 83, 96-99] however this has been exclusively on non-stochastic architectures. Most studies have found that maximising the strength of additively manufactured porous metals at low stiffness remains a challenge, particularly in applications under high cyclic loads

[7, 99, 100]. For engineers looking to optimise the yield and fatigue strength for a given stiffness of AM porous structures, there are hurdles still to overcome. Most studies have limited or no samples tested in the higher cycle fatigue region (10^6 or higher cycles) and these studies also tend to present mechanical properties with respect to relative density or cycles-to-failure and not with respect to stiffness. Extracting and comparing stiffness data from these works can prove difficult as often the quasi-elastic gradient and not the elastic modulus of the specimens is reported. There is also often ambiguity regarding how strain has been measured during testing and thus the effect of test machine compliance may be present.

The actual mechanical properties of different unit cells is not particularly relevant to this research. Instead the focus of this work is on how the laser interaction with the powder bed affects mechanical properties. Despite all the research into mechanical properties of porous structures, little attention has been paid to optimising manufacturing parameters (e.g. laser power, scanning speed) and scan strategy for the mechanical performance of these structures. Whilst solid AM research provides some insight, the scales for melting are much different as heat retention and dissipation will be considerably different in large parts than micro-struts.

2.2.4 Parameter Optimisation on AM Material Properties

Parameter optimisation has been performed for solid AM parts focusing on the role of laser parameters on improving material density and strength and achieving a desired microstructure [55, 67, 72, 101, 102]. For porous structures, parameter studies have prioritised geometric accuracy and material density. The few AM porous structure studies that have considered build parameters and mechanical performance, have briefly explored the effect of varying laser parameters on the mechanical properties of the structure. Specifically looking at mechanical properties with respect to relative density (i.e. strength or stiffness-to-weight) [73], whereas, as stated earlier, for bone replacement scaffolds it would be more suitable to optimise parameters to ensure maximum strength of the architectured structure with respect to stiffness. Also, AM porous structure parameter studies have only been performed on a BCC unit cell architecture, and thus have not considered how the variety of build angles, such as are encountered in stochastic architectures, are affected [81, 103].

For research that investigates the effect of laser parameters on AM material properties, such as strut size [73, 81, 103], structure porosity or material density, either a single laser parameter is explored in isolation (Figure 2.21) [103] or an equation for ‘laser energy density’ is used [55, 73, 102].

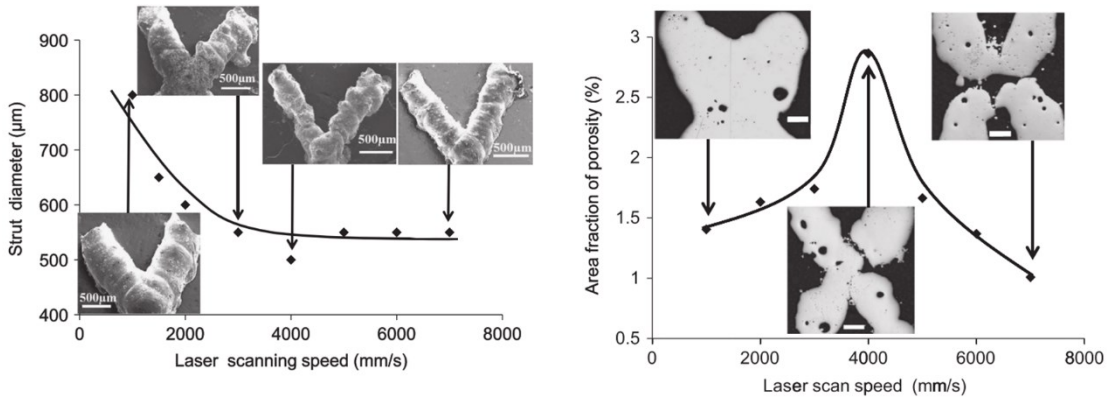


Figure 2.21 – Effect of a single laser parameter (laser scanning speed) on a porous AM material property (left: strut diameter, right: base material porosity). Shown for an aluminium alloy (AlSi10Mg). Reproduced under Creative Commons Attribution License (CC BY). [103]

These equations attempt to relate laser energy density (E_D) delivered to the melt-pool to some combination of laser power (P) and exposure time (t) or to laser scan speed (u), hatch spacing (h) and layer thickness (l). Equation 2.1, shows typical models used.

$$E_D = P \times t \text{ or } E_D = \frac{P}{u \times h \times l} \qquad \text{Equation 2.1}$$

Such models do not include important process variables, and typically generate a process parameter window or a collection of data points with no distinct trend between properties such as strut thickness or porosity against laser energy density [73, 101]. Thus making it difficult to scale or predict values outside the tested experimental range, as depicted in Figure 2.22 [104].

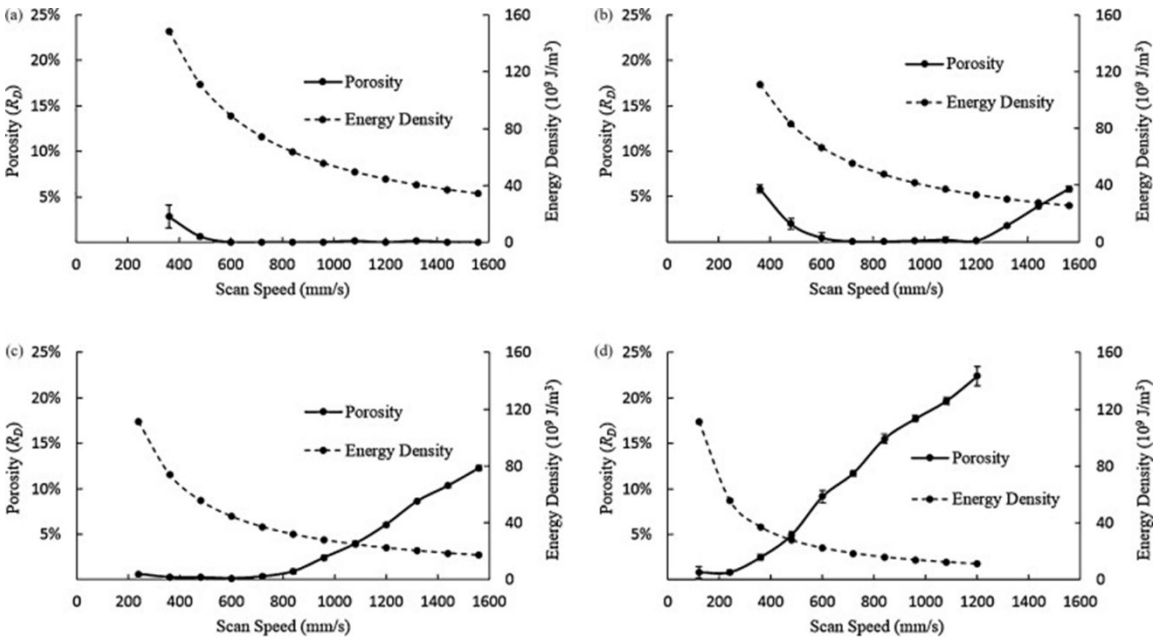


Figure 2.22 – Porosity of titanium grade 5 samples built with varying laser powers (P) and scan speed. (a) P = 160 W. (b) P = 120 W. (c) P = 80 W. (d) P = 40 W. No relationship is

observed between energy density and porosity. Image reproduced with permission of the rights holder, Elsevier. [101].

A more useful term comes from laser welding origins [54, 105], where melt-pool width and depth was found to be related to the absorbed energy density or specific enthalpy (ΔH) delivered by the laser to the powder bed Equation 2.2. Where specific enthalpy is a function of Absorptivity (A), thermal diffusivity (D) and density (ρ_0) of the powder and of the laser parameters, namely, laser power (P), laser scan speed (u) and laser spot diameter ($\emptyset$).

$$\Delta H = \frac{A \cdot P}{\rho_0 \sqrt{\pi \cdot D \cdot u \cdot \emptyset^3}} \qquad \text{Equation 2.2}$$

For a given scan geometry, if strut thickness can be assumed to be proportional to melt-pool width and depth, then a strut thickness versus specific enthalpy plot should produce a scalable model with a distinct and mathematical trend.

Parameter optimisation is further complicated by varying methods of energy delivery. Two approaches have been adopted in literature for porous structures: the traditional contour-hatch [103] scanning strategy or the more novel single-exposure strategy [42, 73, 81, 106]. However a comparison between these scanning strategies is yet to be performed. Another potential scanning strategy to be explored is pulsing which may allow for better control of the melt-pool [107]. Scanning strategies will be described in more detail in Chapter 3.

Finally, current laser parameter optimisation studies only typically report on individual materials and thus do not investigate how optimising laser parameters and scan strategy may change according to the mechanical, material and thermal properties of the powder. Furthermore, the literature has solely reported on static mechanical properties and thus there is a lack of research investigating the effect of laser parameters on fatigue properties of AM materials.

2.3 Biomaterials

The base material of a porous structure naturally plays an important role in governing its behaviour and mechanical properties, such as its strength-to-stiffness ratio. In orthopaedics the trend is towards materials or alloys with low modulus, high strength, high fatigue strength and that are corrosion resistant and biocompatible [108, 109]. The fatigue behaviour of AM porous biomaterials has been reported as both quantitatively and qualitatively different from that of bulk materials and researchers have stated that the relationships normally used for the fatigue design of solid monolithic materials are not applicable when designing AM porous structures. It is suggested that new relationships should be developed for this purpose. It has been broadly observed that, material type and manufacturing imperfections are more important than architecture and structure porosity in the high cycle fatigue behaviour of AM porous structures [97].

2.3.1 Stainless Steel

The first metals successfully used during the 20th century in orthopaedics were stainless steel (SS316) and cobalt–chrome-based alloys. Titanium and its alloys were introduced in the 1940s, but the first successful joint replacement was a total hip prosthesis developed by Charnley in the late 1950s with a cemented stainless steel stem [110]. Currently, stainless steel is mainly used in trauma devices (fracture plates, screws, hip nails etc.) owing to its relatively low cost, corrosion resistance, availability and easy processing. The use of stainless steel in joint replacements is limited due to other materials such as titanium and cobalt–chrome based alloys exhibiting superior mechanical, corrosion and wear properties [110].

Stainless steel has been widely used in LBPF for both solid [111] and porous [81, 86, 112-115] specimens. Due to its low cost, non-reactiveness and ease of melting it is an ideal material [116] for development (of analysis techniques, of understanding of AM phenomena etc.) despite other materials being more suitable for a porous scaffold or as a porous coating on a solid implant. Stainless steel is one of the materials in LBPF where there has been significant success in achieving near full density [111]. The role of laser parameters and scanning strategies on microstructure and mechanical properties has also been studied for solid SS316 [117]. Quantity and constitution of phases has been found to change with process parameters and increase in laser power resulted in crystal growth along the build direction and increase in texture angle and grain shape aspect ratio [118]. One of the few studies that has explored different laser parameters on lattice structures was conducted in stainless steel. Using a single exposure strategy, a variety of individual struts and porous structures with a BCC architecture

were manufactured with different laser parameters. The individual struts were tensile tested whilst the porous structures were compression tested. For SS316L it was claimed lower laser powers resulted in lower strengths for the struts tested in tension. Mechanical properties of the struts was also seen to decrease with build angle. For the porous structures comparisons were made with respect to relative density and structures were grouped with respect to exposure time, whereas laser power has been shown to play a more dominant role in porosity and grain size development [117], The mechanical testing of the porous structures shows for a given relative density mechanical properties will vary depending on the laser parameters used however no takeaways regarding optimum parameters can be extrapolated from the work [81].

2.3.2 Titanium

In the 1950s Branemark discovered the osseointegration phenomenon of titanium, where titanium and its alloys were able to become tightly integrated into bone. Osseointegration can significantly improve the long-term behaviour of implants and decreases the risks of loosening and failure. Due to this property, titanium and its alloys became materials of great interest in orthopaedics. Whilst they can have excellent mechanical properties that include a moderate elastic modulus (~100-110 GPa) high strength, high fatigue strength, good corrosion resistance and low density (~4.4 g/cm^3), surface properties such as wear are relatively poor due to low shear resistance of the material [110].

Pure titanium (CP-Ti) undergoes an allotropic transformation from a closed-packed hexagonal crystal structure (α-phase) to a body-centered cubic crystal structure (β phase) when its temperature is raised above 882 °C. Alloying elements either stabilise the α phase or β phase, increasing or decreasing the β transus temperature respectively or acting as solid solution strengtheners. In addition to the two equilibrium phases, there is also a metastable titanium martensite phase that can form under fast cooling rates (>400°C/s) from the β phase. This martensite phase can exist in two forms, a hexagonal structure (α′) and an orthorhombic crystal structure (α″). In titanium alloys the α phase and β phase are not adjacent as they are in pure titanium but separated by a two-phase α + β region. For Titanium-6Aluminium-4Vanadium (Ti-6Al-4V or Ti64), aluminium is a α stabiliser, whilst vanadium is a β stabiliser and the β transus temperature is 980°C (Figure 2.23), these alloying elements improve the mechanical properties, achieving typically twice the yield and ultimate strength values of CP-Ti.

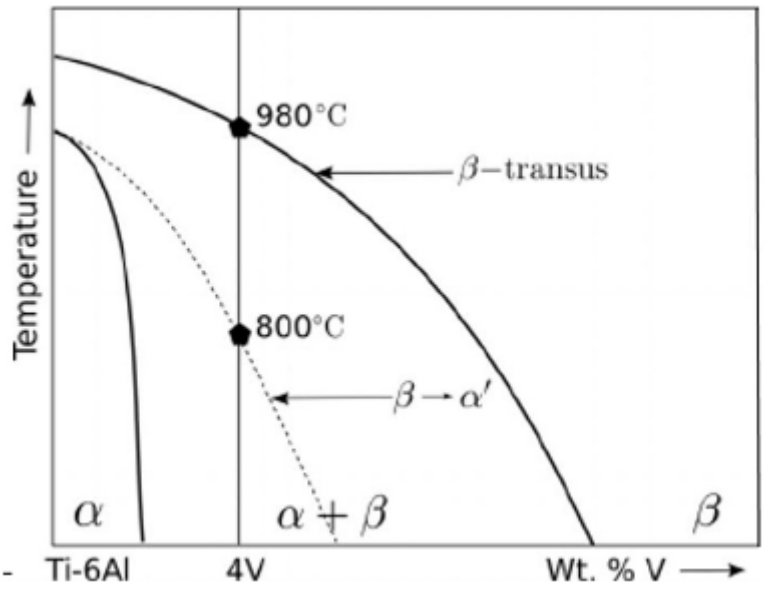


Figure 2.23 – Phase diagram for Ti-6Al-4V. Image reproduced with permission of the rights holder, Elsevier [50].

The high heating and cooling rates (10^3-10^8 K/s) [50] during LBPF of Titanium enable the fabrication of parts with very fine and tailorable microstructure. For CP-Ti, fine microstructures including lath α, acicular α′ and refined zig-zag α′ can be obtained through controlling the process parameters. It has been found that by varying laser power and maintaining energy density, different phase formation, microstructure, texture and mechanical properties can be obtained [67]. If only a single phase is present, the main influence of microstructure on mechanical properties arise from differences in grain size and shape.

In Ti64, as both α and β can be present at room temperature, phase morphology, volume fraction, in addition to grain size and shape can affect mechanical properties. The mechanical properties of LBPF Ti64 depend largely on its constituent phases and their morphology and characteristic length scales as well as the size and orientation (texture) of the prior beta grains. The influence of process parameters on the cooling rate and subsequent microstructure formation and resulting mechanical properties during LPBF processing of Ti alloys has been widely researched and reviewed [50]. Typically the resulting microstructure often features columnar prior β grains, which grow epitaxially through successive layers along the build direction, filled with acicular α' martensite (Figure 2.24) [55, 58].

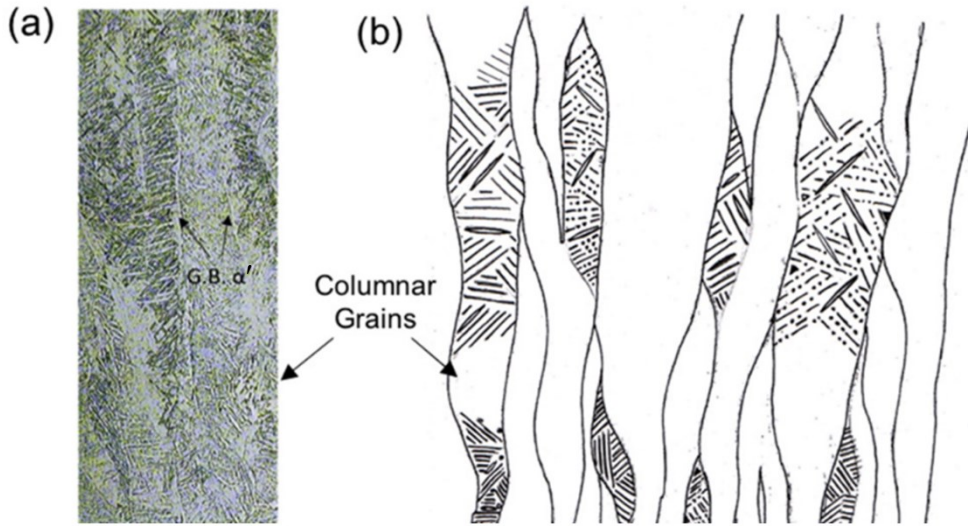


Figure 2.24 – Typical LBPF Ti64 microstructure, columnar prior beta grains are seen filled with acicular α' (Build direction is vertical). Image reproduced with permission of the rights holder, Elsevier [65].

The orientation relationship between α′ and β dictates the α′ preferential growth orientation, and martensitic needles (or laths) are generally observed to be inclined about 40° with respect to the build direction [52]. The elongated prior β grain boundaries in conjunction with the presence of acicular α′ martensite favour intergranular failure. Martensitic microstructures also exhibit poor ductility [50]. Such strongly textured structures lead to significant anisotropic mechanical behaviour. Many consider it necessary to transform the α′ microstructure into an equilibrium α + β to reduce anisotropy and improve fatigue performance. Typically this is done by post-build heat treatments [60-62] but researchers have been able to achieve α + β microstructures via in-situ (in-process) martensite decomposition (Figure 2.25) [102]. Different approaches have been taken but essentially altering process parameters to influence the cooling rate and/or cyclic thermal history allows for very specific microstructures to be obtained, however this area remains in its infancy [50].

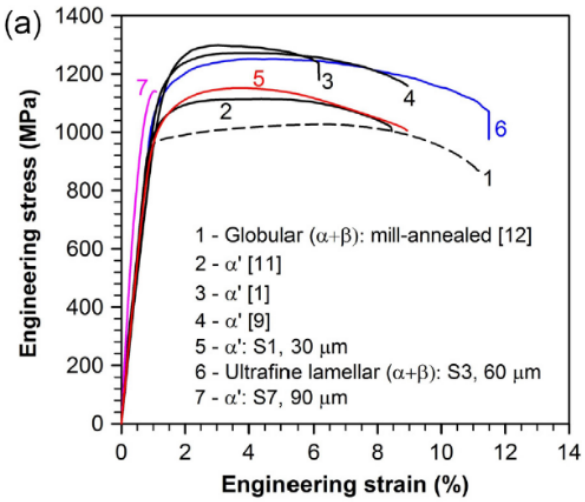


Figure 2.25 - Effect of microstructure on tensile properties of LBPF titanium parts. Image reproduced with permission of the rights holder, Elsevier [102].

The different phases of titanium also have different moduli, with the α″ and β phases considered to have the lowest modulus followed by α′. Young's modulus is an intrinsic property of a material and is determined by the bonding force among atoms. The bonding force is not only related to crystal structure but also to the distances among the atoms. Young's modulus, unlike strength is not sensitive to grain size and morphology of materials [108], but it is clear that by optimising the laser parameters to get a desired thermal history, both the grain size/structure as well as the phases present and their quantities can be altered to maximise strength:stiffness of the part.

With respect to porous structures, as stated earlier practically all research into the area has focused on structural investigations, i.e. changing architecture of the structure. There has been some work [24, 84, 88, 106, 119] into the effect of different laser parameters on microstructure for porous specimens but limited research regarding the effect of different laser parameters on the mechanical performance of titanium porous structures for a given relative density or modulus [106, 119]. There remains no rules or guidelines for optimum laser parameters for porous specimens to maximise static or fatigue mechanical properties with respect to stiffness. Similarly, there has been no work regarding the effect of scanning strategies on the microstructure and mechanical performance of titanium porous structures for a given relative density or modulus.

There has also been some comparative research into the effect of titanium alloy on the properties of porous structures (Figure 2.26). Historically, Ti64 has been used for solid orthopaedic implants due to its high strength and fatigue life. However, some research [24, 41, 120] and current commercial porous implants [42, 73] have supported the use of CP-Ti for

porous features [120]. As a porous structure manufactured via LBPF, CP-Ti has a ductile failure mode as opposed to the brittle failure mode of Ti64. Despite its lower static strength, CP-Ti has been shown to have a higher relative fatigue strength for a given number of cycles-to-failure than Ti64 [24, 120] and better fatigue strength-to-weight (Figure 2.26) [120]. Statically however, both as solid and porous AM parts, CP-Ti appears to have a lower static strength:stiffness ratio than Ti64 [121], however, the limitations and concerns mentioned in 2.2.3 still apply. There remains a need for systematic testing of CP-Ti vs. Ti64 with regards to strength-to-stiffness and fatigue strength-to-stiffness for porous structures.

2.3.3 Tantalum

Tantalum is a hard, ductile, highly chemically resistant material with good apposition to human bone. Tantalum is a period six refractory metal, in the same family as niobium, vanadium, and molybdenum. Tantalum has α-BCC crystal structure and is an isomorphous β–stabiliser in titanium. Isomorphous stabiliser means the lattice structure of the alloying element is the same as the lattice structure of β–phase titanium, i.e. body centred cubic (BCC) [72, 121]. It has been successfully used in clinical applications as a biomaterial since the 1940s, but because it is both expensive and difficult to machine, the use of Ta as a biomaterial has been limited. The biocompatibility and non-toxic behaviour of Ta in general have been reported previously. The attachment, proliferation and differentiation of human osteoblasts on Ta are excellent in comparison to the more commonly used surgical grade Ti64. Despite its promising biological properties, Ta is not considered as an appropriate material for large implants due to its high density, stiffness and price. To avoid stress shielding, Ta is mostly limited to open porous structures in biomedical applications. Knowing that bulk Ta is difficult to process, and therefore commonly produced as a powder, it can also be applied as a coating on both solid, and open porous implant surfaces [41].

Tantalum as a porous structure for orthopaedics is attractive due to its corrosion resistance, biocompatibility, and ductility, however it is prohibitively expensive [41]. As Ta is commonly produced as powder it lends itself to powder-based manufacturing technologies. Recently, both solid and porous Ta parts have been produced by LBPF. AM Ta showed improvements in micro-hardness and tensile strength when compared to cast or powder metallurgy specimens due to fine-grain strengthening. Indeed, like most materials processed by AM porosity, strength, ductility and microstructure were all seen to vary with the laser parameters and scanning strategy, thereby changing the energy supplied to the melt-pool [72]. It was found that epitaxial growth due to partial re-melting of the previous layer, competitive growth

mechanism and a specific global direction of heat flow resulted in the formation of long columnar grains with a specific preferential crystal orientation along the building direction and consequently yield strength anisotropy.

There has been limited research into the manufacturing of porous Ta via LBPF. Preliminary work has also shown that porous AM tantalum, whilst having a similar yield strength to CP-Ti, has a higher relative fatigue strength and better fatigue strength-to-weight than both CPTi and Ti64 (Figure 2.26) [120]. However, only a single type of specimen was tested and it remains unclear, for the reasons specified in Section 2.2.3, whether it has superior strength-to-stiffness and fatigue strength-to-stiffness compared to Ti and its alloys.

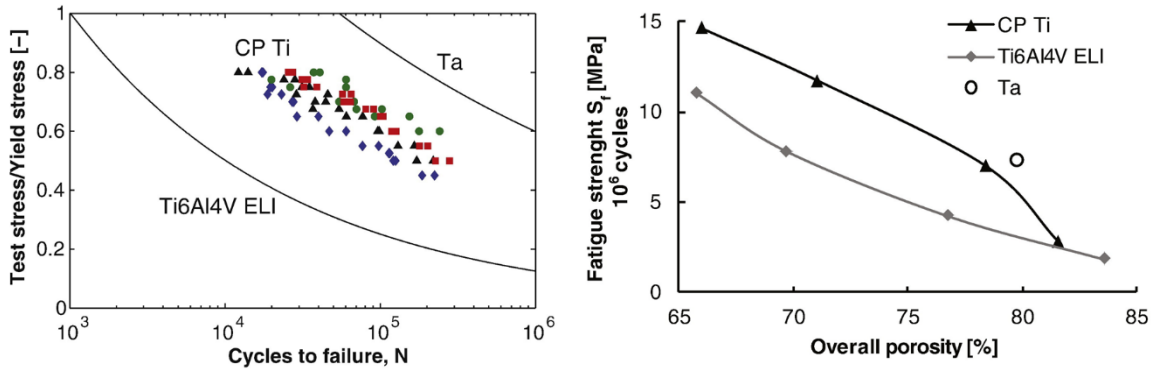


Figure 2.26 – Fatigue strength comparison between porous structures manufactured from titanium alloys and tantalum. Left: Normalised maximum fatigue stress versus number of cycles to failure. Right: Fatigue strength at one million cycles versus overall structure porosity. Image reproduced with permission of the rights holder, Elsevier [120].

2.3.4 Titanium – Tantalum

The risks of Ti-based alloy implants on bone infection or osteomyelitis have been noted and research to overcome their long-term health risks has been conducted. The elements with the highest biocompatibility are Ti, Nb, Mo, Sn, Fe, Zr and Ta (Note: Al and V are not present). As stated earlier the high modulus of Tantalum, makes it only suitable as a porous scaffold but it suffers from poor mechanical properties [108]. Alloying titanium and tantalum together can increase the strength and ductility of the resulting material whilst reducing modulus [7, 108, 109, 121]. Titanium-tantalum alloys are potentially more suitable than pure titanium for biomedical applications because of their lower elastic modulus, higher strength and enhanced corrosion resistance, along with the same excellent compatibility as pure titanium. The effect of tantalum content in a titanium – tantalum alloy has also been investigated via melting in a tri-arc furnace. Microstructure (Table 2.1), modulus, yield and ultimate stress and elongation at failure were all shown to change with Ta content (Figure 2.27). From these studies, it was

seen that a good combination of high strength-to-stiffness ratio, high elongation to failure and low cost was with a 70% titanium – 30% tantalum alloy [122].

Table 2.1 – Constitutional phases and their morphologies of the Ti-Ta alloys [108]

Ta Content (%)	Formed Phase	Morphology
10 – 20	α′	Lamellar
30 – 50	α″	Needle-like
60	β + α″	Equiaxed β + needle-like α″
70 – 80	β	Equiaxed β + unrecrystallised structure

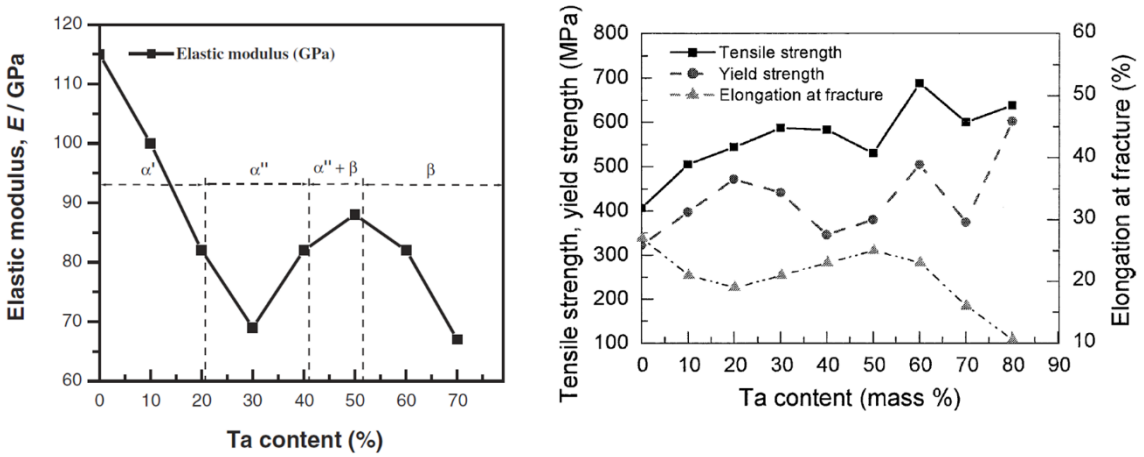


Figure 2.27 – Effect of Ta content on Modulus, Strength and Elongation. Image reproduced with permission of the rights holder, Elsevier. [108, 122]

There has so far only been one study on the LBPF of TiTa alloys, which investigated both solid and porous AM parts, of a 50% titanium – 50% tantalum alloy. Solid parts were shown to have a higher strength:stiffness ratio than CP-Ti and Ti64 specimens and better elongation at failure [121], however the absolute strength of Ti64 was higher than the TiTa alloy which was higher than CP-Ti. The porous TiTa was shown to have an almost equal strength-to-stiffness ratio compared to Ti64 but the TiTa alloy had higher relative density and thus lower modulus. The porous TiTa specimen had a greater strength-to-stiffness ratio compared to CP-Ti and had equal porosity and modulus [123]. There is, however, currently no fatigue data for either solid or porous AM titanium – tantalum materials and there is a need for a more systematic comparison between porous CpTi, Ti64, Ta and TiTa structures with respect to both modulus and density under static and cyclic loading.

2.4 Summary

- Bone is mechano-biological in nature and its remodelling can be accelerated by strain, yet most *in vivo* testing has ignored this property when testing for bone ingrowth. Mechanical environments have not been characterised and thus inconsistencies exist regarding optimal structural characteristics of porous scaffolds.
- Additive manufacturing whilst being an exciting technology is dependent on control of many process variables that are still under characterised, particularly for porous structures.
    - For AM solids, laser parameters and scanning strategies can effect material properties (microstructure, defects etc.) and consequently mechanical strength.
    - There have been no systematic investigation into how the laser parameters and scanning strategies effect build angle and minimum feature size of struts, nor the material and mechanical properties of porous structures.
- Most research into porous structures has been compression testing of different cellular architectures, however there has not been consistency in measurements of modulus vs. quasi-elastic gradients and there is ambiguity in how strain has been measured.
- Fatigue testing of porous structures has again only focused on different cellular architectures and different materials, with the same limitations as above, also there have been sparse number of samples tested in the high-cycle fatigue region.
    - Thus there is ambiguity regarding which material should be used to manufacture low stiffness high strength porous scaffolds that must survive in a high cyclic load environment.
- Most research into porous structures looks to optimise strength with respect to weight or relative density, whereas for bone regeneration scaffolds or features, optimisation with respect to stiffness is more appropriate.
- Alloying titanium and tantalum together can increase the strength and ductility of the resulting material whilst reducing modulus, however no porous specimens have been manufactured in the composition that maximise strength-to-stiffness and there has been no fatigue testing of porous titanium-tantalum.

2.5 References

[1] S. Wu, X. Liu, K.W.K. Yeung, C. Liu, X. Yang, Biomimetic porous scaffolds for bone tissue engineering, Materials Science and Engineering: R: Reports 80 (2014) 1-36.

[2] S. Poelert, E. Valstar, H. Weinans, A.A. Zadpoor, Patient-specific finite element modeling of bones, Proceedings of the Institution of Mechanical Engineers, Part H: Journal of Engineering in Medicine 227(4) (2013) 464-478.

[3] L. Roseti, V. Parisi, M. Petretta, C. Cavallo, G. Desando, I. Bartolotti, B. Grigolo, Scaffolds for Bone Tissue Engineering: State of the art and new perspectives, Materials Science and Engineering: C 78 (2017) 1246-1262.

[4] J. Wieding, T. Lindner, P. Bergschmidt, R. Bader, Biomechanical stability of novel mechanically adapted open-porous titanium scaffolds in metatarsal bone defects of sheep, Biomaterials 46 (2015) 35-47.

[5] D.Y.R. Chong, Biomechanical Analysis of Fixation and Bone Remodelling of Total Knee Replacement, (2009).

[6] K. Myer, BONE MECHANICS, Standard Handbook of Biomedical Engineering & Design, McGraw Hill Professional, Access Engineering, 2003.

[7] X. Wang, S. Xu, S. Zhou, W. Xu, M. Leary, P. Choong, M. Qian, M. Brandt, Y.M. Xie, Topological design and additive manufacturing of porous metals for bone scaffolds and orthopaedic implants: A review, Biomaterials 83 (2016) 127-141.

[8] S.A. Goldstein, D.L. Wilson, D.A. Sonstegard, L.S. Matthews, The mechanical properties of human tibial trabecular bone as a function of metaphyseal location, Journal of Biomechanics 16(12) (1983) 965-969.

[9] K. Alvarez, H. Nakajima, Metallic Scaffolds for Bone Regeneration, Materials 2(3) (2009) 790.

[10] C. Ruff, B. Holt, E. Trinkaus, Who's afraid of the big bad Wolff?: "Wolff's law" and bone functional adaptation, American Journal of Physical Anthropology 129(4) (2006) 484-498.

[11] D.J. Hadjidakis, I.I. Androulakis, Bone Remodeling, Annals of the New York Academy of Sciences 1092(1) (2006) 385-396.

[12] N. Reznikov, R. Shahar, S. Weiner, Bone hierarchical structure in three dimensions, Acta Biomaterialia 10(9) (2014) 3815-3826.

[13] J.M. García-Aznar, M.J. Gómez-Benito, M.Á. Pérez, M. Doblaré, Mechanobiological Models for Bone Tissue. Applications to Implant Design, Biomechanics of Hard Tissues, Wiley-VCH Verlag GmbH & Co. KGaA2010, pp. 123-143.

[14] O.R. Boughton, S. Ma, S. Zhao, M. Arnold, A. Lewis, U. Hansen, J.P. Cobb, F. Giuliani, R.L. Abel, Measuring bone stiffness using spherical indentation, PLOS ONE 13(7) (2018) e0200475.

[15] D.R. Carter, Mechanical loading histories and cortical bone remodeling, Calcified tissue international 36 Suppl 1 (1984) S19-24.

[16] L.F. Bonewald, The amazing osteocyte, Journal of Bone and Mineral Research 26(2) (2011) 229-238.

[17] L. Bonewald, Osteocytes, Muscle and Exercise: Role in Healthy Aging, The FASEB Journal 31(1_supplement) (2017) 7.2-7.2.

[18] D.S. Elliott, K.J.H. Newman, D.P. Forward, D.M. Hahn, B. Ollivere, K. Kojima, R. Handley, N.D. Rossiter, J.J. Wixted, R.M. Smith, C.G. Moran, A unified theory of bone healing and nonunion, The Bone & Joint Journal 98-B(7) (2016) 884-891.

[19] N. Reznikov, C. Phillips, M. Cooke, A. Garbout, F. Ahmed, M.M. Stevens, Functional Adaptation of the Calcaneus in Historical Foot Binding, Journal of Bone and Mineral Research 32(9) (2017) 1915-1925.

[20] J. Henkel, M.A. Woodruff, D.R. Epari, R. Steck, V. Glatt, I.C. Dickinson, P.F.M. Choong, M.A. Schuetz, D.W. Hutmacher, Bone Regeneration Based on Tissue Engineering Conceptions — A 21st Century Perspective, Bone Research 1(3) (2013) 216-248.

[21] S.A. Goldstein, The mechanical properties of trabecular bone: Dependence on anatomic location and function, Journal of Biomechanics 20(11–12) (1987) 1055-1061.

[22] E.F. Morgan, H.H. Bayraktar, T.M. Keaveny, Trabecular bone modulus–density relationships depend on anatomic site, Journal of Biomechanics 36(7) (2003) 897-904.

[23] L.J. Gibson, The mechanical behaviour of cancellous bone, Journal of Biomechanics 18(5) (1985) 317-328.

[24] N.W. Hrabe, Characterization of Cellular Titanium for Biomedical Applications, ProQuest Dissertations And Theses (2010) 262.

[25] J. Parthasarathy, B. Starly, S. Raman, A design for the additive manufacture of functionally graded porous structures with tailored mechanical properties for biomedical applications, Journal of Manufacturing Processes 13(2) (2011) 160-170.

[26] A. Barbas, A.S. Bonnet, P. Lipinski, R. Pesci, G. Dubois, Development and mechanical characterization of porous titanium bone substitutes, Journal of the Mechanical Behavior of Biomedical Materials 9 (2012) 34-44.

[27] M.I.Z. Ridzwan, S. Shuib, A.Y. Hassan, A.A. Shokri, Problem of Stress Shielding and Improvement to the Hip Implant Designs: A Review, Journal of Medical Sciences (2007).

[28] Z. Wang, C. Wang, C. Li, Y. Qin, L. Zhong, B. Chen, Z. Li, H. Liu, F. Chang, J. Wang, Analysis of factors influencing bone ingrowth into three-dimensional printed porous metal scaffolds: A review, Journal of Alloys and Compounds 717 (2017) 271-285.

[29] I. Sanli, J.J.C. Arts, J. Geurts, Clinical and Radiologic Outcomes of a Fully Hydroxyapatite-Coated Femoral Revision Stem: Excessive Stress Shielding Incidence and its Consequences, The Journal of Arthroplasty 31(1) (2016) 209-214.

[30] J.T. Deen, T.B. Clay, D.A. Iams, M. Horodyski, H.K. Parvataneni, Proximal tibial resorption in a modern total knee prosthesis, Arthroplasty Today 4(2) (2018) 244-248.

[31] Z. Zhang, Simulation of the Mechanical and Flow Behaviour of Bone Fixation Implants, (2013).

[32] S. Limmahakhun, A. Oloyede, K. Sitthiseripratip, Y. Xiao, C. Yan, Stiffness and strength tailoring of cobalt chromium graded cellular structures for stress-shielding reduction, Materials & Design 114 (2017) 633-641.

[33] F. Matassi, A. Botti, L. Sirleo, C. Carulli, M. Innocenti, Porous metal for orthopedics implants, Clinical Cases in Mineral and Bone Metabolism 10(2) (2013) 111-115.

[34] H. Kienapfel, C. Sprey, A. Wilke, P. Griss, Implant fixation by bone ingrowth, The Journal of Arthroplasty 14(3) (1999) 355-368.

[35] C.L. Peters, A.G. Rosenberg, Bone ingrowth and total knee replacement, The Knee 1(4) (1994) 189-196.

[36] J.D. Bobyn, G.J. Stackpool, S.A. Hacking, M. Tanzer, J.J. Krygier, Characteristics of bone ingrowth and interface mechanics of a new porous tantalum biomaterial, Journal of Bone & Joint Surgery, British Volume 81-B(5) (1999) 907-914.

[37] A.-M. Pobloth, S. Checa, H. Razi, A. Petersen, J.C. Weaver, K. Schmidt-Bleek, M. Windolf, A.Á. Tatai, C.P. Roth, K.-D. Schaser, G.N. Duda, P. Schwabe, Mechanobiologically optimized 3D titanium-mesh scaffolds enhance bone regeneration in critical segmental defects in sheep, Science Translational Medicine 10(423) (2018).

[38] N. Reznikov, O.R. Boughton, S. Ghouse, A.E. Weston, L. Collinson, G.W. Blunn, J. Jeffers, J.P. Cobb, M.M. Stevens, Individual response variations in scaffold-guided bone regeneration are determined by independent strain- and injury-induced mechanisms, Biomaterials 194 (2019) 183-194.

[39] M. Tuncer, U.N. Hansen, A.A. Amis, Prediction of structural failure of tibial bone models under physiological loads: Effect of CT density–modulus relationships, Medical Engineering & Physics 36(8) (2014) 991-997.

[40] A.I. Itälä, H.O. Ylänen, C. Ekholm, K.H. Karlsson, H.T. Aro, Pore diameter of more than 100 μm is not requisite for bone ingrowth in rabbits, Journal of Biomedical Materials Research 58(6) (2001) 679-683.

[41] R. Wauthle, J. van der Stok, S. Amin Yavari, J. Van Humbeeck, J.-P. Kruth, A.A. Zadpoor, H. Weinans, M. Mulier, J. Schrooten, Additively manufactured porous tantalum implants, Acta Biomaterialia 14 (2015) 217-225.

[42] L. Mullen, R.C. Stamp, P. Fox, E. Jones, C. Ngo, C.J. Sutcliffe, Selective laser melting: A unit cell approach for the manufacture of porous, titanium, bone in-growth constructs, suitable for orthopedic applications. II. Randomized structures, Journal of Biomedical Materials Research Part B: Applied Biomaterials 92B(1) (2010) 178-188.

[43] E. Marin, S. Fusi, M. Pressacco, L. Paussa, L. Fedrizzi, Characterization of cellular solids in Ti6Al4V for orthopaedic implant applications: Trabecular titanium, Journal of the Mechanical Behavior of Biomedical Materials 3(5) (2010) 373-381.

[44] S. Van Bael, Y.C. Chai, S. Truscello, M. Moesen, G. Kerckhofs, H. Van Oosterwyck, J.P. Kruth, J. Schrooten, The effect of pore geometry on the in vitro biological behavior of human periosteum-derived cells seeded on selective laser-melted Ti6Al4V bone scaffolds, Acta Biomaterialia 8(7) (2012) 2824-2834.

[45] S.K. Everton, M. Hirsch, P. Stravroulakis, R.K. Leach, A.T. Clare, Review of in-situ process monitoring and in-situ metrology for metal additive manufacturing, Materials & Design 95 (2016) 431-445.

[46] S.M. Yusuf, N. Gao, Influence of energy density on metallurgy and properties in metal additive manufacturing, Materials Science and Technology (2017) 1-21.

[47] A. Yadollahi, N. Shamsaei, Additive manufacturing of fatigue resistant materials: Challenges and opportunities, International Journal of Fatigue 98 (2017) 14-31.

[48] M.J. Matthews, G. Guss, S.A. Khairallah, A.M. Rubenchik, P.J. Depond, W.E. King, Denudation of metal powder layers in laser powder bed fusion processes, Acta Materialia 114 (2016) 33-42.

[49] A. Bandyopadhyay, K.D. Traxel, Invited review article: Metal-additive manufacturing—Modeling strategies for application-optimized designs, Additive Manufacturing 22 (2018) 758-774.

[50] H. Shipley, D. McDonnell, M. Culleton, R. Coull, R. Lupoi, G. O'Donnell, D. Trimble, Optimisation of process parameters to address fundamental challenges during selective laser melting of Ti-6Al-4V: A review, International Journal of Machine Tools and Manufacture 128 (2018) 1-20.

[51] O. Rehme, Cellular Design for Laser Freeform Fabrication, Cuvillier2010.

[52] S. Gorsse, C. Hutchinson, M. Gouné, R. Banerjee, Additive manufacturing of metals: a brief review of the characteristic microstructures and properties of steels, Ti-6Al-4V and high-entropy alloys, Science and Technology of Advanced Materials 18(1) (2017) 584-610.

[53] C. Song, M. Zhang, Y. Yang, D. Wang, Y. Jia-kuo, Morphology and properties of CoCrMo parts fabricated by selective laser melting, Materials Science and Engineering: A 713 (2018) 206-213.

[54] W.E. King, H.D. Barth, V.M. Castillo, G.F. Gallegos, J.W. Gibbs, D.E. Hahn, C. Kamath, A.M. Rubenchik, Observation of keyhole-mode laser melting in laser powder-bed fusion additive manufacturing, Journal of Materials Processing Technology 214(12) (2014) 2915-2925.

[55] P. Hanzl, M. Zetek, T. Bakša, T. Kroupa, The Influence of Processing Parameters on the Mechanical Properties of SLM Parts, Procedia Engineering 100 (2015) 1405-1413.

[56] R. Li, J. Liu, Y. Shi, L. Wang, W. Jiang, Balling behavior of stainless steel and nickel powder during selective laser melting process, The International Journal of Advanced Manufacturing Technology 59(9) (2012) 1025-1035.

[57] C. Teng, D. Pal, H. Gong, K. Zeng, K. Briggs, N. Patil, B. Stucker, A review of defect modeling in laser material processing, Additive Manufacturing 14 (2017) 137-147.

[58] M. Simonelli, Y.Y. Tse, C. Tuck, Effect of the build orientation on the mechanical properties and fracture modes of SLM Ti–6Al–4V, Materials Science and Engineering: A 616 (2014) 1-11.

[59] J. Robinson, I. Ashton, P. Fox, E. Jones, C. Sutcliffe, Determination of the effect of scan strategy on residual stress in laser powder bed fusion additive manufacturing, Additive Manufacturing 23 (2018) 13-24.

[60] C. Qiu, N.J.E. Adkins, M.M. Attallah, Microstructure and tensile properties of selectively laser-melted and of HIPed laser-melted Ti–6Al–4V, Materials Science and Engineering: A 578 (2013) 230-239.

[61] B. Vrancken, L. Thijs, J.-P. Kruth, J. Van Humbeeck, Heat treatment of Ti6Al4V produced by Selective Laser Melting: Microstructure and mechanical properties, Journal of Alloys and Compounds (2012) 177-185.

[62] M. Thöne, S. Leuders, A. Riemer, T. Tröster, H. Richard, Influence of heat-treatment on Selective Laser Melting products–eg Ti6Al4V, Solid freeform fabrication symposium SFF, Austin Texas, 2012.

[63] S. Merkt, C. Hinke, J. Bültmann, M. Brandt, Y.M. Xie, Mechanical response of TiAl6V4 lattice structures manufactured by selective laser melting in quasistatic and dynamic compression tests, Journal of Laser Applications 27(S1) (2015) S17006.

[64] T.B. Sercombe, X. Xu, V.J. Challis, R. Green, S. Yue, Z. Zhang, P.D. Lee, Failure modes in high strength and stiffness to weight scaffolds produced by Selective Laser Melting, Materials & Design 67 (2015) 501-508.

[65] Y. Kok, X.P. Tan, P. Wang, M.L.S. Nai, N.H. Loh, E. Liu, S.B. Tor, Anisotropy and heterogeneity of microstructure and mechanical properties in metal additive manufacturing: A critical review, Materials & Design 139 (2018) 565-586.

[66] X. Wang, J.A. Muñiz-Lerma, O. Sánchez-Mata, M.A. Shandiz, M. Brochu, Microstructure and mechanical properties of stainless steel 316L vertical struts manufactured by laser powder bed fusion process, Materials Science and Engineering: A (2018).

[67] X.P. Li, J. Van Humbeeck, J.P. Kruth, Selective laser melting of weak-textured commercially pure titanium with high strength and ductility: A study from laser power perspective, Materials & Design 116 (2017) 352-358.

[68] M.H. Farshidianfar, A. Khajepour, A.P. Gerlich, Effect of real-time cooling rate on microstructure in Laser Additive Manufacturing, Journal of Materials Processing Technology 231 (2016) 468-478.

[69] N. Hrabe, T. Quinn, Effects of processing on microstructure and mechanical properties of a titanium alloy (Ti–6Al–4V) fabricated using electron beam melting (EBM), Part 2: Energy input, orientation, and location, Materials Science and Engineering: A 573 (2013) 271-277.

[70] M.H. Farshidianfar, A. Khajepour, A. Gerlich, Real-time control of microstructure in laser additive manufacturing, The International Journal of Advanced Manufacturing Technology 82(5) (2016) 1173-1186.

[71] H. Attar, S. Ehtemam-Haghighi, D. Kent, X. Wu, M.S. Dargusch, Comparative study of commercially pure titanium produced by laser engineered net shaping, selective laser melting and casting processes, Materials Science and Engineering: A 705 (2017) 385-393.

[72] L. Zhou, T. Yuan, R. Li, J. Tang, G. Wang, K. Guo, Selective laser melting of pure tantalum: Densification, microstructure and mechanical behaviors, Materials Science and Engineering: A 707 (2017) 443-451.

[73] L. Mullen, R.C. Stamp, W.K. Brooks, E. Jones, C.J. Sutcliffe, Selective Laser Melting: A regular unit cell approach for the manufacture of porous, titanium, bone in-growth constructs, suitable for orthopedic applications, Journal of Biomedical Materials Research Part B: Applied Biomaterials 89B(2) (2009) 325-334.

[74] S. McKown, Y. Shen, W.K. Brookes, C.J. Sutcliffe, W.J. Cantwell, G.S. Langdon, G.N. Nurick, M.D. Theobald, The quasi-static and blast loading response of lattice structures, International Journal of Impact Engineering 35(8) (2008) 795-810.

[75] V.J. Challis, X. Xu, L.C. Zhang, A.P. Roberts, J.F. Grotowski, T.B. Sercombe, High specific strength and stiffness structures produced using selective laser melting, Materials & Design 63 (2014) 783-788.

[76] P. Heinl, L. Müller, C. Körner, R.F. Singer, F.A. Müller, Cellular Ti–6Al–4V structures with interconnected macro porosity for bone implants fabricated by selective electron beam melting, Acta Biomaterialia 4(5) (2008) 1536-1544.

[77] S. Amin Yavari, R. Wauthle, J. van der Stok, A.C. Riemslag, M. Janssen, M. Mulier, J.P. Kruth, J. Schrooten, H. Weinans, A.A. Zadpoor, Fatigue behavior of porous biomaterials manufactured using selective laser melting, Materials Science and Engineering: C 33(8) (2013) 4849-4858.

[78] J. Van der Stok, O.P. Van der Jagt, S. Amin Yavari, M.F.P. De Haas, J.H. Waarsing, H. Jahr, E.M.M. Van Lieshout, P. Patka, J.A.N. Verhaar, A.A. Zadpoor, H. Weinans, Selective laser melting-produced porous titanium scaffolds regenerate bone in critical size cortical bone defects, Journal of Orthopaedic Research 31(5) (2013) 792-799.

[79] S. Amin Yavari, S.M. Ahmadi, J. van der Stok, R. Wauthle, A.C. Riemslag, M. Janssen, J. Schrooten, H. Weinans, A.A. Zadpoor, Effects of bio-functionalizing surface treatments on the mechanical behavior of open porous titanium biomaterials, Journal of the Mechanical Behavior of Biomedical Materials 36 (2014) 109-119.

[80] O. Rehme, Cellular Design for Laser Freeform Fabrication, Cuvillier Göttingen, 2009.

[81] S. Tsopanos, R.A.W. Mines, S. McKown, Y. Shen, W.J. Cantwell, W. Brooks, C.J. Sutcliffe, The Influence of Processing Parameters on the Mechanical Properties of Selectively

Laser Melted Stainless Steel Microlattice Structures, Journal of Manufacturing Science and Engineering 132(4) (2010) 041011-041011.

[82] S. Arabnejad, R. Burnett Johnston, J.A. Pura, B. Singh, M. Tanzer, D. Pasini, High-strength porous biomaterials for bone replacement: A strategy to assess the interplay between cell morphology, mechanical properties, bone ingrowth and manufacturing constraints, Acta Biomaterialia 30 (2016) 345-356.

[83] S. Ahmadi, S. Yavari, R. Wauthle, B. Pouran, J. Schrooten, H. Weinans, A. Zadpoor, Additively Manufactured Open-Cell Porous Biomaterials Made from Six Different Space-Filling Unit Cells: The Mechanical and Morphological Properties, Materials 8(4) (2015) 1871.

[84] N.W. Hrabe, P. Heinl, B. Flinn, C. Körner, R.K. Bordia, Compression-compression fatigue of selective electron beam melted cellular titanium (Ti-6Al-4V), Journal of Biomedical Materials Research Part B: Applied Biomaterials 99B(2) (2011) 313-320.

[85] P. Heinl, C. Körner, R.F. Singer, Selective Electron Beam Melting of Cellular Titanium: Mechanical Properties, Advanced Engineering Materials 10(9) (2008) 882-888.

[86] C. Yan, L. Hao, A. Hussein, P. Young, D. Raymont, Advanced lightweight 316L stainless steel cellular lattice structures fabricated via selective laser melting, Materials & Design 55 (2014) 533-541.

[87] C. Yan, L. Hao, A. Hussein, P. Young, J. Huang, W. Zhu, Microstructure and mechanical properties of aluminium alloy cellular lattice structures manufactured by direct metal laser sintering, Materials Science and Engineering: A 628 (2015) 238-246.

[88] X.Y. Cheng, S.J. Li, L.E. Murr, Z.B. Zhang, Y.L. Hao, R. Yang, F. Medina, R.B. Wicker, Compression deformation behavior of Ti–6Al–4V alloy with cellular structures fabricated by electron beam melting, Journal of the Mechanical Behavior of Biomedical Materials 16 (2012) 153-162.

[89] E. Hernández-Nava, C.J. Smith, F. Derguti, S. Tammas-Williams, F. Léonard, P.J. Withers, I. Todd, R. Goodall, The effect of density and feature size on mechanical properties of isostructural metallic foams produced by additive manufacturing, Acta Materialia 85 (2015) 387-395.

[90] M.F. Ashby, A.G. Evans, N.A. Fleck, L.J. Gibson, J.W. Hutchinson, H.N.G. Wadley, Metal Foams: A Design Guide, Butterworth-Heinemann, Burlington, 2000.

[91] L.J. Gibson, Cellular solids : structure and properties, 2nd ed., Cambridge University Press, Cambridge, 1999.

[92] M.F. Ashby, The properties of foams and lattices, Philosophical Transactions of the Royal Society A: Mathematical, Physical and Engineering Sciences 364(1838) (2006) 15-30.

[93] ISO13314, Mechanical testing of metals. Ductility testing. Compression test for porous and cellular metals, 2011.

[94] J. Banhart, J. Baumeister, Deformation characteristics of metal foams, Journal of Materials Science 33(6) (1998) 1431-1440.

[95] Y. Sugimura, A. Rabiei, A.G. Evans, A.M. Harte, N.A. Fleck, Compression fatigue of a cellular Al alloy, Materials Science and Engineering: A 269(1) (1999) 38-48.

[96] R. Hedayati, S.M. Ahmadi, K. Lietaert, B. Pouran, Y. Li, H. Weinans, C.D. Rans, A.A. Zadpoor, Isolated and modulated effects of topology and material type on the mechanical properties of additively manufactured porous biomaterials, Journal of the Mechanical Behavior of Biomedical Materials 79 (2018) 254-263.

[97] S.M. Ahmadi, R. Hedayati, Y. Li, K. Lietaert, N. Tümer, A. Fatemi, C.D. Rans, B. Pouran, H. Weinans, A.A. Zadpoor, Fatigue performance of additively manufactured meta-biomaterials: The effects of topology and material type, Acta Biomaterialia 65 (2018) 292-304.

[98] M. Speirs, B. Van Hooreweder, J. Van Humbeeck, J.P. Kruth, Fatigue behaviour of NiTi shape memory alloy scaffolds produced by SLM, a unit cell design comparison, Journal of the Mechanical Behavior of Biomedical Materials 70 (2017) 53-59.

[99] F.S.L. Bobbert, K. Lietaert, A.A. Eftekhari, B. Pouran, S.M. Ahmadi, H. Weinans, A.A. Zadpoor, Additively manufactured metallic porous biomaterials based on minimal surfaces: A unique combination of topological, mechanical, and mass transport properties, Acta Biomaterialia 53 (2017) 572-584.

[100] R. Hedayati, H. Hosseini-Toudeshky, M. Sadighi, M. Mohammadi-Aghdam, A.A. Zadpoor, Computational prediction of the fatigue behavior of additively manufactured porous metallic biomaterials, International Journal of Fatigue 84 (2016) 67-79.

[101] H. Gong, K. Rafi, H. Gu, T. Starr, B. Stucker, Analysis of defect generation in Ti–6Al–4V parts made using powder bed fusion additive manufacturing processes, Additive Manufacturing 1–4 (2014) 87-98.

[102] W. Xu, M. Brandt, S. Sun, J. Elambasseril, Q. Liu, K. Latham, K. Xia, M. Qian, Additive manufacturing of strong and ductile Ti–6Al–4V by selective laser melting via in situ martensite decomposition, Acta Materialia 85 (2015) 74-84.

[103] C. Qiu, S. Yue, N.J.E. Adkins, M. Ward, H. Hassanin, P.D. Lee, P.J. Withers, M.M. Attallah, Influence of processing conditions on strut structure and compressive properties of cellular lattice structures fabricated by selective laser melting, Materials Science and Engineering: A 628 (2015) 188-197.

[104] U. Scipioni Bertoli, A.J. Wolfer, M.J. Matthews, J.-P.R. Delplanque, J.M. Schoenung, On the limitations of Volumetric Energy Density as a design parameter for Selective Laser Melting, Materials & Design 113 (2017) 331-340.

[105] D.B. Hann, J. Iammi, J. Folkes, A simple methodology for predicting laser-weld properties from material and laser parameters, Journal of Physics D: Applied Physics 44(44) (2011) 445401.

[106] S.M. Ahmadi, R. Hedayati, R.K. Ashok Kumar Jain, Y. Li, S. Leeflang, A.A. Zadpoor, Effects of laser processing parameters on the mechanical properties, topology, and microstructure of additively manufactured porous metallic biomaterials: A vector-based approach, Materials & Design 134 (2017) 234-243.

[107] S. Li, H. Xiao, K. Liu, W. Xiao, Y. Li, X. Han, J. Mazumder, L. Song, Melt-pool motion, temperature variation and dendritic morphology of Inconel 718 during pulsed- and continuous-wave laser additive manufacturing: A comparative study, Materials & Design 119 (2017) 351-360.

[108] Y.L. Zhou, M. Niinomi, T. Akahori, Effects of Ta content on Young's modulus and tensile properties of binary Ti–Ta alloys for biomedical applications, Materials Science and Engineering: A 371(1) (2004) 283-290.

[109] L. Yan, Y. Yuan, L. Ouyang, H. Li, A. Mirzasadeghi, L. Li, Improved mechanical properties of the new Ti-15Ta-xZr alloys fabricated by selective laser melting for biomedical application, Journal of Alloys and Compounds 688 (2016) 156-162.

[110] M. Navarro, A. Michiardi, O. Castaño, J.A. Planell, Biomaterials in orthopaedics, Journal of the Royal Society Interface 5(27) (2008) 1137-1158.

[111] C. Kamath, B. El-dasher, G.F. Gallegos, W.E. King, A. Sisto, Density of additively-manufactured, 316L SS parts using laser powder-bed fusion at powers up to 400 W, The International Journal of Advanced Manufacturing Technology 74(1) (2014) 65-78.

[112] R. Gümrük, R.A.W. Mines, Compressive behaviour of stainless steel micro-lattice structures, International Journal of Mechanical Sciences 68 (2013) 125-139.

[113] P. Li, Constitutive and failure behaviour in selective laser melted stainless steel for microlattice structures, Materials Science and Engineering: A 622 (2015) 114-120.

[114] P. Li, Z. Wang, N. Petrinic, C.R. Siviour, Deformation behaviour of stainless steel microlattice structures by selective laser melting, Materials Science and Engineering: A 614 (2014) 116-121.

[115] R. Gümrük, R.A.W. Mines, S. Karadeniz, Static mechanical behaviours of stainless steel micro-lattice structures under different loading conditions, Materials Science and Engineering: A 586 (2013) 392-406.

[116] S.L. Sing, J. An, W.Y. Yeong, F.E. Wiria, Laser and electron-beam powder-bed additive manufacturing of metallic implants: A review on processes, materials and designs, Journal of Orthopaedic Research 34(3) (2016) 369-385.

[117] C. Qiu, M.A. Kindi, A.S. Aladawi, I.A. Hatmi, A comprehensive study on microstructure and tensile behaviour of a selectively laser melted stainless steel, Scientific Reports 8(1) (2018) 7785.

[118] T. Kurzynowski, K. Gruber, W. Stopyra, B. Kuźnicka, E. Chlebus, Correlation between process parameters, microstructure and properties of 316 L stainless steel processed by selective laser melting, Materials Science and Engineering: A 718 (2018) 64-73.

[119] E. Sallica-Leva, A.L. Jardini, J.B. Fogagnolo, Microstructure and mechanical behavior of porous Ti–6Al–4V parts obtained by selective laser melting, Journal of the Mechanical Behavior of Biomedical Materials 26 (2013) 98-108.

[120] R. Wauthle, S.M. Ahmadi, S. Amin Yavari, M. Mulier, A.A. Zadpoor, H. Weinans, J. Van Humbeeck, J.-P. Kruth, J. Schrooten, Revival of pure titanium for dynamically loaded

porous implants using additive manufacturing, Materials Science and Engineering: C 54 (2015) 94-100.

[121] S.L. Sing, W.Y. Yeong, F.E. Wiria, Selective laser melting of titanium alloy with 50 wt% tantalum: Microstructure and mechanical properties, Journal of Alloys and Compounds 660 (2016) 461-470.

[122] Y.-L. Zhou, M. Niinomi, T. Akahori, M. Nakai, H. Fukui, Comparison of Various Properties between Titanium-Tantalum Alloy and Pure Titanium for Biomedical Applications, Materials Transactions 48(3) (2007) 380-384.

[123] S.L. Sing, Selective laser melting of novel titanium-tantalum alloy as orthopaedic biomaterial, 2016.

3 Chapter 3 – Materials and Methods

The following chapter will describe the design and manufacturing for all specimens built and tested throughout this research. All test methodologies will be detailed. Design of experiments and number of specimens tested will be presented in their respective chapters.

3.1 Specimen Design

In order to investigate how the manufacturing parameters in powder bed fusion affect the mechanical and material (microstructure, morphologic and geometric) properties of porous structures as well as what materials these porous structures should be made from for low stiffness – high strength applications (such as for bone ingrowth surfaces) and to test such porous structures *in vivo*, test specimens needed to be designed. All specimens were designed in the CAD software package Rhinoceros 5.0 (Robert McNeel & Associates) as line geometry with slice data (build files) generated through Material Engine 1.0 (Betatype Ltd). Material Engine is a CAD-CAM software platform that creates slice geometry for a variety of scanning strategies directly from line based geometry representation. It is therefore possible to compare different laser parameters, scanning strategies and materials all generated from the same input CAD. The following structures were produced using this methodology:

3.1.1 Characterisation Structure

To evaluate minimum feature size and the effect of laser parameters and scanning strategies on strut size, build angle and surface morphology, a characterisation structure with constant strut length and varying angles was designed (Figure 3.1). The structure features struts of 4 mm length at 90°, 60°, 45°, 30° and 15° with respect to the build plate.

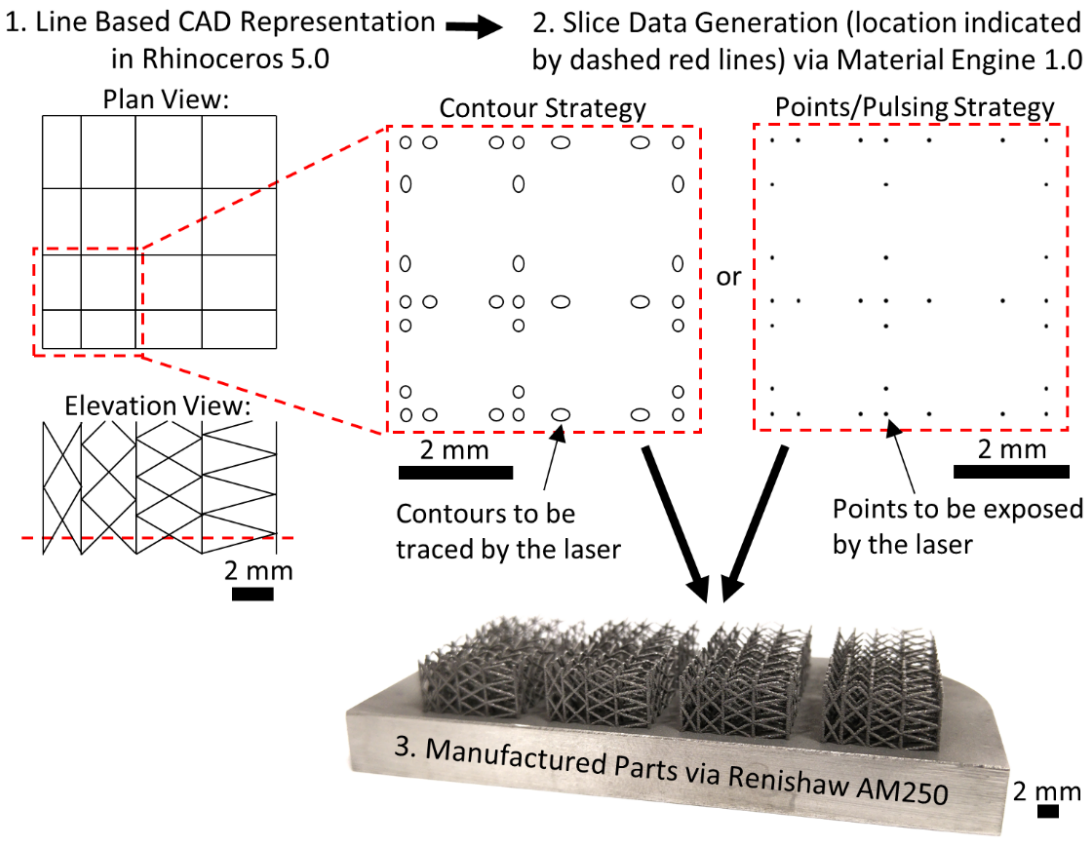


Figure 3.1 – Characterisation Structure Manufacture Workflow

3.1.2 Electron Backscatter Diffraction Specimen

Performing electron backscatter diffraction (EBSD) of a porous structure has many challenges, particularly when trying to compare microstructures of stochastic specimens built by different laser parameters or scanning strategies. When observing sections of a stochastic porous structure it is difficult to attain the exact same section between specimens and as microstructure will likely vary with build angle, build height and nodal connectivity of struts it would prove difficult to make conclusions regarding how build parameters effect microstructure. Alternatively, when observing sections of a non-stochastic structure or a single strut it is difficult to grind and polish to the exact same location (say the middle of a strut). To combat these issues, a single row of struts were designed, 10 mm tall spaced 1 mm apart embedded into a solid base (Figure 3.2). A 1° shim was also manufactured. When the sample is placed on the shim, mounted and ground back, the thickest strut visible should be the strut closest to the central portion.

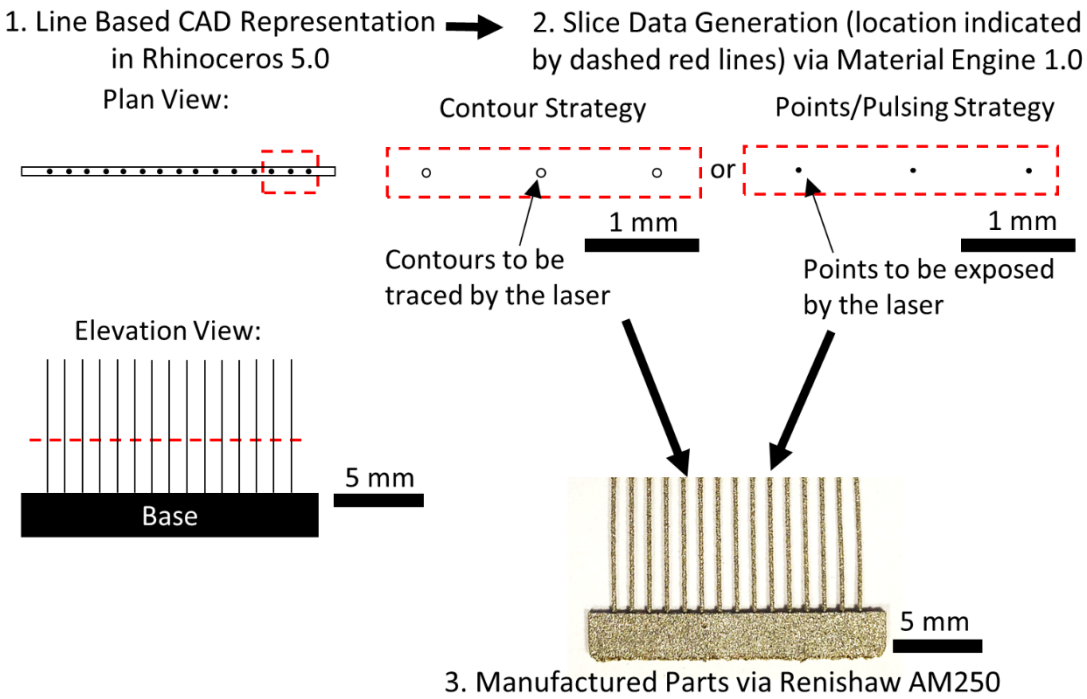


Figure 3.2 – EBSD Structure Manufacture Workflow

3.1.3 Stochastic Architectured Structure

As stated in the literature review, AM stochastic porous structures have received little attention in literature, with the majority of work being on periodic (repeating) uniform unit cell structures. Stochastic porous geometries also more closely resemble the trabecular architecture of bone when compared to periodic structures. Whilst non-stochastic structures, such as a BCC or cubic unit cells, can be optimal for a specific loading case they are inherently anisotropic and often can suffer from row by row failures. Stochastic structures, whilst potentially being weaker in a given direction (for an equivalent weight or stiffness) are inherently more isotropic, due to having material in all directions, and behave more like a continuum. Using a stochastic structure also removes any angular effects that may occur due to the AM process, as struts will be present in a wide range of build angles. But most important, and particularly relevant to the structures in this work, it allows for stiffness/density gradients to be more easily incorporated. This property also allows for a desired anisotropy to be designed as struts can be thickened and thinned where desired and based on build angle.

A stochastic structure was produced for mechanical testing by filling a 3D volume with a random distribution of points using a Poisson Disk algorithm that maintains a specific minimum proximity (0.8mm between points). These points were then connected to each other, as zero thickness lines, to achieve a desired connectivity (average connectivity of ~5) with a strut density of (4 lines/mm^3), as seen in Figure 3.3. Struts below a specified angle (<30°) were

removed to optimise the structure for the AM build process. As only a single laser parameter would be applied to all struts and since low angle struts can only be built with very specific laser parameters, it was necessary to remove the low angled struts. The designed structure was ⌀13 mm x 21 mm to ensure after removal from the build plate it maintains a Height:Diameter ratio of >1.5 and conforms to ISO 13314:2011 – Compression test for porous and cellular metals [1]. The structure served as a test coupon to compare the role of different laser parameters, build strategies and materials on mechanical strength.

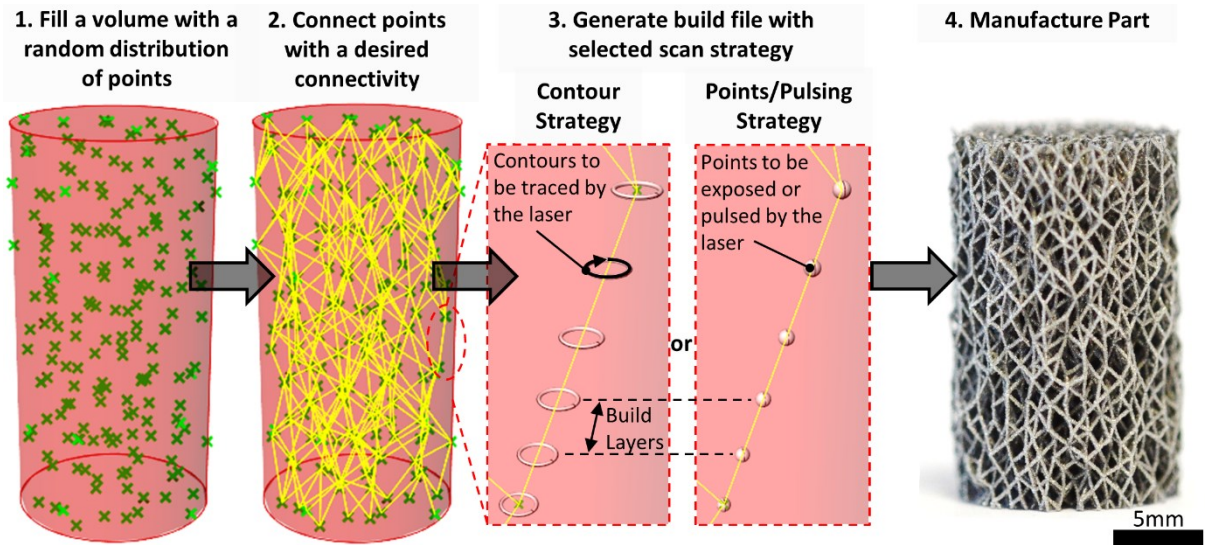


Figure 3.3 – Manufacturing Workflow from Specimen Design to Build File Generation to Manufacture. Note: 1-3 are simplified for clarity and not to scale.

3.1.4 Locally Stiffness Matched Porous Scaffold

Similar to as described above, a stochastic porous scaffold was designed by filling a 3D volume (⌀16 x 15mm) with a random distribution of points using a Poisson disk algorithm and consequently connecting these points to each other as zero-thickness lines at a desired connectivity (average connectivity of ~5). As bone properties vary between species and vary both globally and locally at anatomical sites as well as due to age, sex, nutrition, activity level, bone health and diseases, a methodology was developed to characterise local bone properties in a clinical and pragmatic way. This ultimately can lead to patient specific, cohort specific and site specific implants. In order for the scaffold to locally match the stiffness of bone it would be replacing during *in vivo* testing, it was first discretised into 27 sections (a 3 × 3 × 3 array). The modulus of each section was altered by changing the laser parameters, thereby producing sections with thicker or thinner struts and thus stiffer or less stiff sections respectively (Figure 3.4). Laser parameters were selected so that the modulus of each section would match the

modulus of the bone it would be replacing. This process along with the local quantification of bone properties will be discussed in greater detail in Chapter 6.

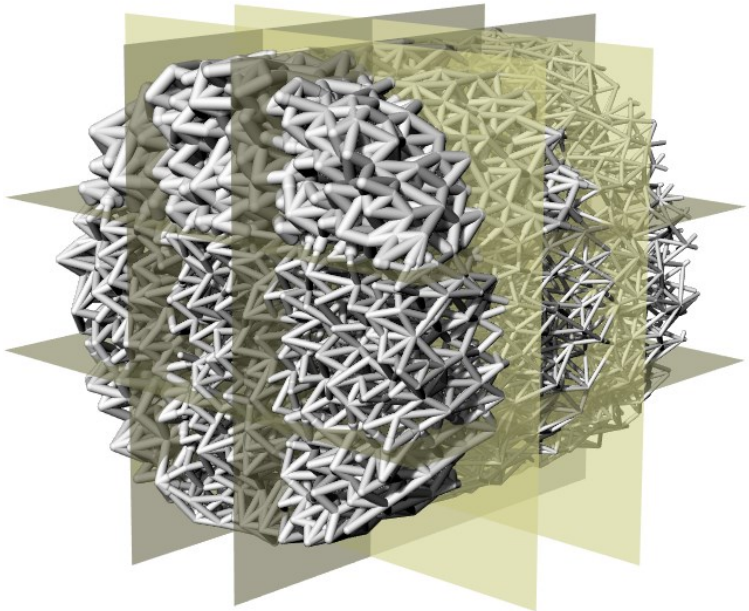


Figure 3.4 – 3D Rendering of Locally Stiffness-Matched Scaffold

3.2 Build File Generation

Material Engine 1.0 (Betatype Ltd.) was used to create the slice data (build files) for all the specimens described in section 3.1. The software can generate different slice data dependent on the chosen scanning strategy all using the same line geometry. Laser parameters (laser power, laser speed, slice thickness etc.) can be assigned on a part-by-part or even line-by-line basis. The three scan strategies that were used to generate slice data are described below for a powder bed fusion system:

3.2.1 Contour Strategy

The most common build strategy in AM is the Contour-Hatch strategy. For a given 2D slice, the original CAD geometry contours are offset (typically by half the melt-pool diameter) and the resulting contour scans are traced by the laser, with the area enclosed by the contours being filled in with 'hatch' scans (Figure 3.5). However, issues arise with this approach at small scale, due to STL geometry and resolution errors resulting in limited laser interaction with the powder-bed, i.e. the slice data's laser scan paths do not accurately reflect the intended geometry. This strategy also causes many scan vectors and jumps between scan vectors, resulting in a high amount of scanner delays and is computationally expensive. For the contour strategy employed in this research the diameter of the contour scan was set equal to the spot

size of the laser (70 µm), this was to ensure there was no need for interpolative calculations to generate additional border or hatch scans, strut thickness was then controlled purely by the laser parameters. The contour strategy used in this research is depicted in Figure 3.1, Figure 3.2, Figure 3.3, and Figure 3.6.

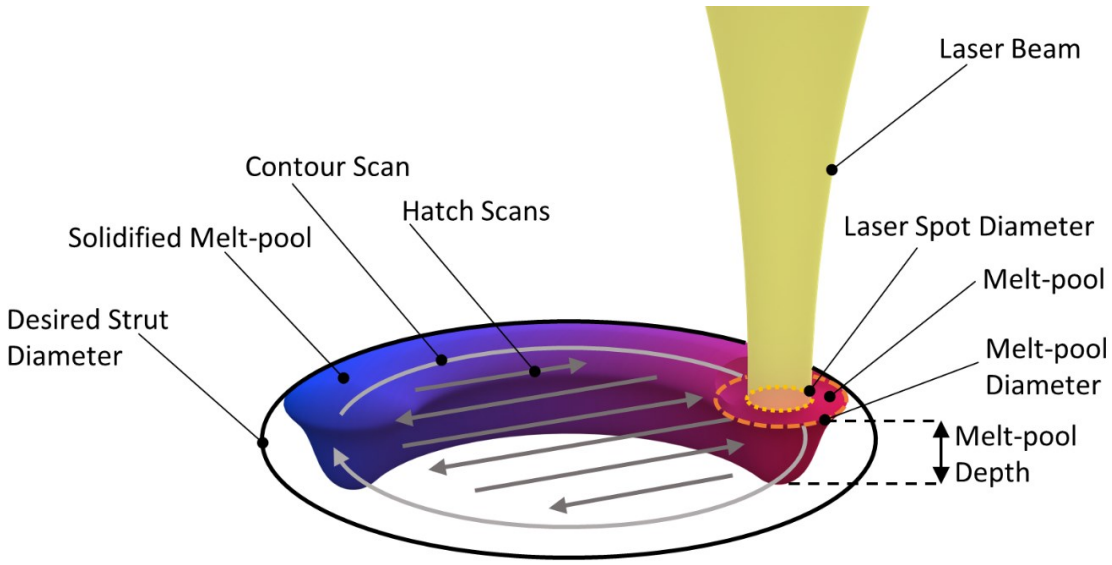


Figure 3.5 – Traditional Contour-Hatch Scanning Strategy

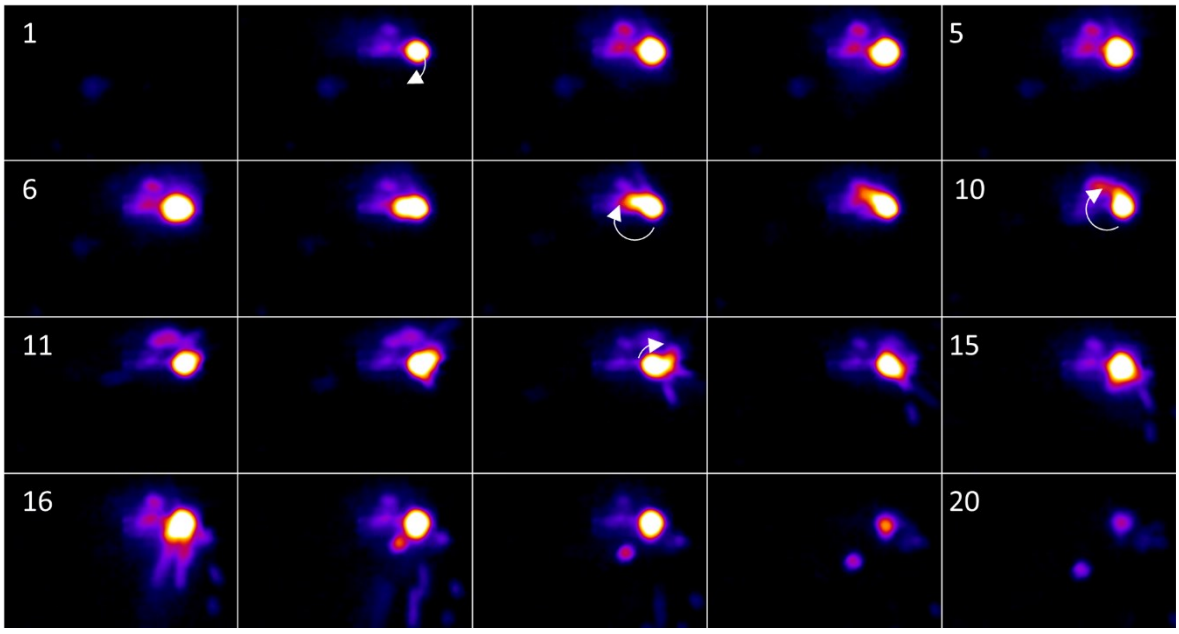


Figure 3.6 – Melt-pool video of a contour scan: Laser scans a specified diameter circle/ellipse (2-19). Upon completion scanners jump to the next location and the following contour scan occurs (not shown).

3.2.2 Points Strategy

Only a few researchers have utilised a single-exposure or point-like-exposure strategy for manufacturing struts or porous structures [2-4]. To create a strut with the single-exposure

approach, instead of the laser scanning a contour and hatching the intersecting geometry on a 2D slice (Figure 3.5), it fires a single exposure at the intersection between build layers and strut locations for a specified period of time with the resulting strut thickness and morphology being equal to the width and shape of the melt-pool (Figure 3.7). The single-exposure approach is only possible when the struts of a porous structure are represented by lines as opposed to solid geometry. Examples of slice data with a points strategy are seen in Figure 3.1, Figure 3.2 and Figure 3.3.

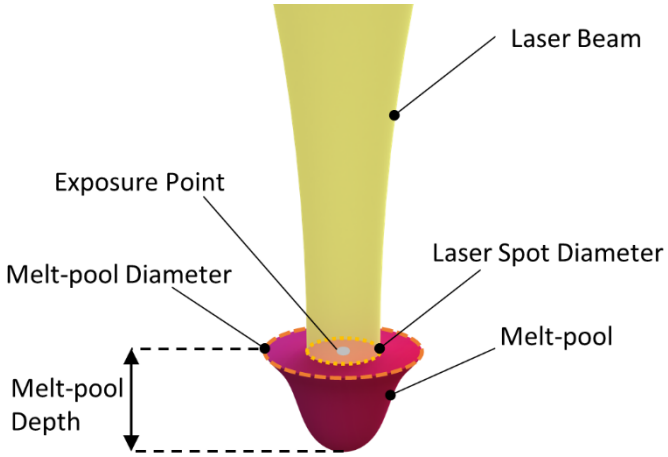


Figure 3.7 – Single Exposure Scanning Strategy

The single-exposure approach is believed to be more suited to building porous structures in terms of both minimum feature size, computational cost and build time due to it reducing the complex geometry of a porous structure to a set of points of exposure where less jumps and scanner delays are caused. The drawbacks lie in the control of strut morphology as well as the manufacturability and mechanical competence of low angled struts. This is because as the build angle of a strut gets closer to the horizontal the overlap between the current layer's melt-pool and the previous layer's melted strut is reduced as has been depicted by several authors [5, 6] and seen in Figure 3.8

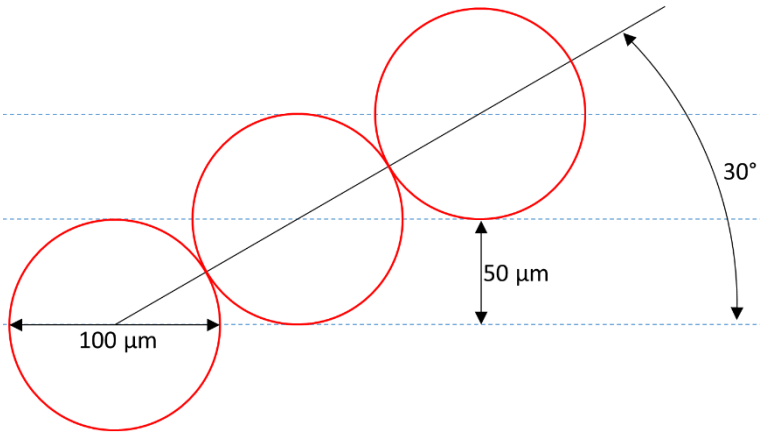


Figure 3.8 – Single Exposure issues for low angled struts: When building a strut at 30° at a 50 µm layer thickness and assuming a melt-pool width and depth of 100 µm, a typical single exposure strategy would likely not build a strut, as there are no overlapping melt-pools (for simplicity melt-pools are shown as spherical).

This research has utilised a novel interpretation of the single-exposure strategy, developed in conjunction with Betatype Ltd. This new interpretation eliminates the problem where melt-pools would not overlap for low angle struts. When building a low angle strut the horizontal component of the strut is projected onto the slice layer (Figure 3.9).

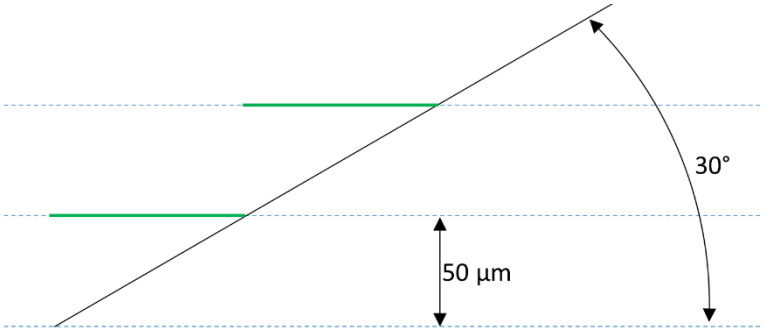


Figure 3.9 – Points Strategy: Projection of horizontal component of strut onto slice layer (green lines)

Exposures are then fired along this contour (Figure 3.10); this type of approach would in theory allow the efficient manufacture of struts at any build angle, even horizontal.

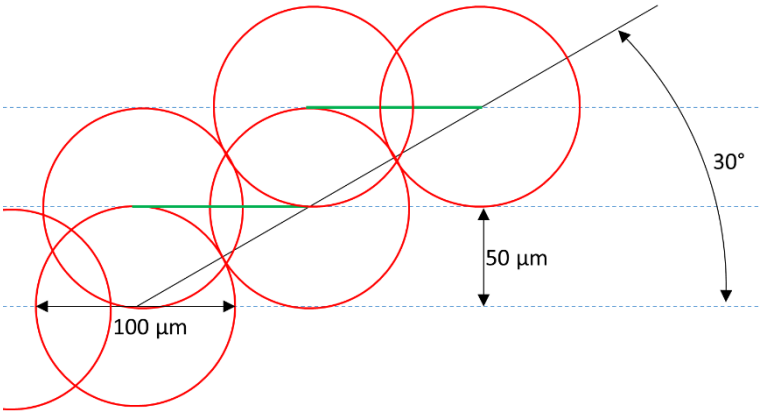


Figure 3.10 – Points Strategy for low angled struts: Exposures are fired along the projected horizontal component of the strut on a layer-by-layer basis

The thickness of struts manufactured by the new Points Strategy was still determined by the melt-pool size and thus ultimately controlled by the laser parameters. Figure 3.11 depicts images from a melt-pool video of the points strategy building a vertical strut.

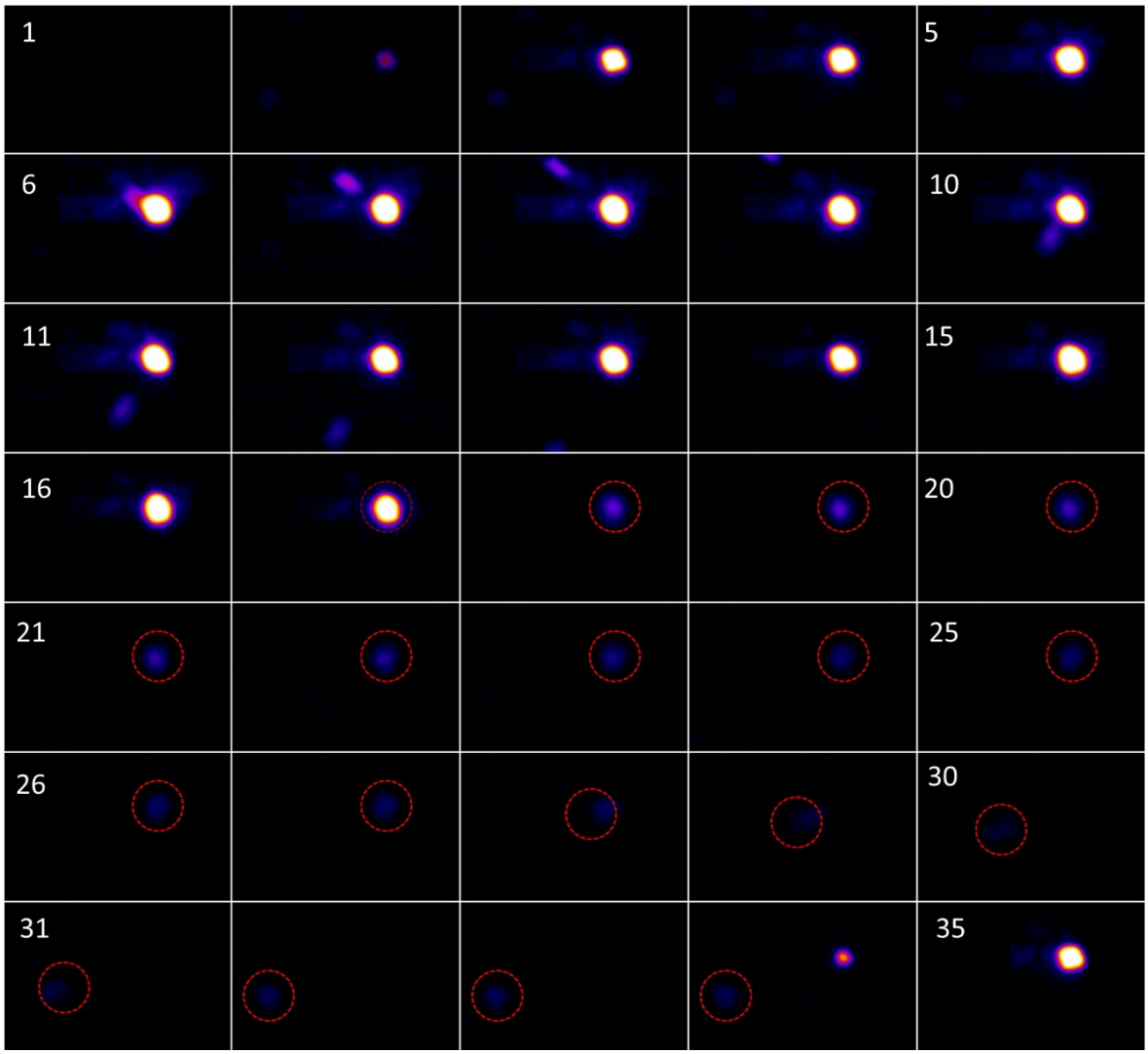


Figure 3.11 – Point Exposure (shown for a vertical strut): The laser is held at a fixed position and exposes (fires) for a specified time (2-17). Upon completion scanners jump to the next exposure point (18-34) and the following exposure occurs (34-35). Previous exposure point is circled during the scanners jump to the next point.

3.2.3 Pulsing Strategy

Pulsing a laser can lead to a smaller melt-pool [7] and consequently may be able to produce finer features. By repeatedly firing the laser at each point in the *Points Strategy* the effect of pulsing can be explored. In addition to the typical laser parameters which control melt-pool size, new variables are available, namely the duty cycle (how long the laser is off between repeated exposures) and the number of repeated exposures per point (Figure 3.12).

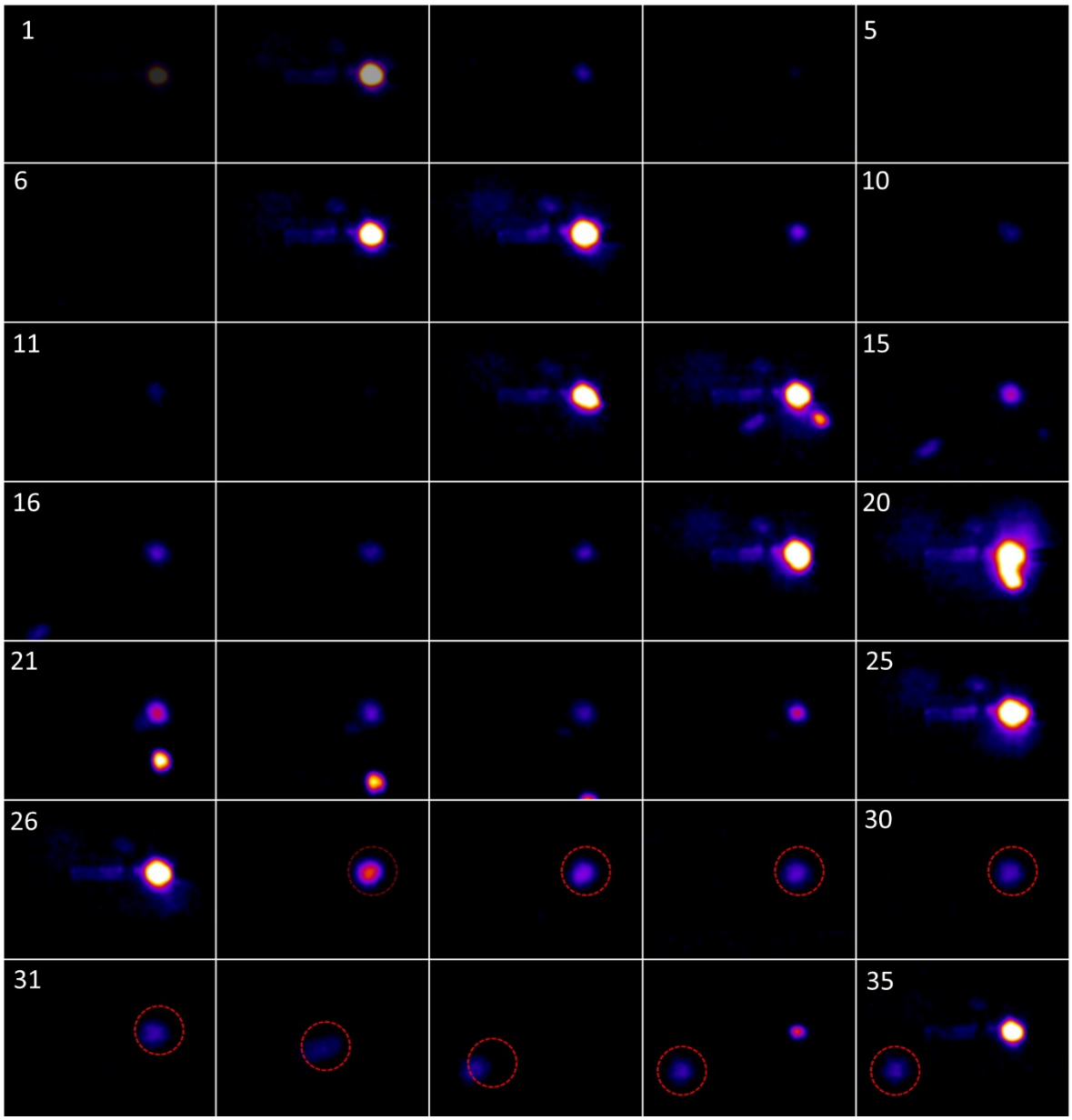


Figure 3.12 – Pulsing Strategy (shown for a vertical strut): The laser is held at fixed position and exposes (fires) for a specified time (e.g. 7-8) then the laser turns off for a specified time (e.g. 9-12); this point gets repeatedly pulsed with exposures (in this example 5x with a 50% duty cycle). Upon completion scanners jump to the next exposure point (27-34) and the following pulsed exposures occur (34-35). Previous exposure point is circled during the scanners jump to the next point.

3.3 Materials and Manufacturing

All specimens in this study were manufactured on a Renishaw AM250, a metal powder bed fusion AM system. In contrast to most powder bed fusion machines (EOS, ConceptLaser, SLM Solutions etc.) which fire continuously when scanning a contour or a hatch, the AM250 is a pseudo-modulated ("move-fire") system, meaning the laser is held at a point and fires for a fixed exposure time then turns off and moves rapidly to the next point by a set point distance and the process repeats along each scan vector. The main laser parameters, in combination with the different scanning strategies, which control the melting process are therefore Laser Power, Exposure Time, Point Distance and Layer Thickness.



Figure 3.13 – Renishaw AM250

The system, equipped with a Gaussian beam CW fibre laser (max. 200 W, 70 µm spot size, wavelength (λ) =1.07 µm), was modified to include process monitoring equipment. The laser optical train was fitted with a beam splitter attached to two high speed cameras enabling imaging of the melt-pool. A photodiode was connected to the optics to monitor the laser input to the powder bed (Figure 3.14).

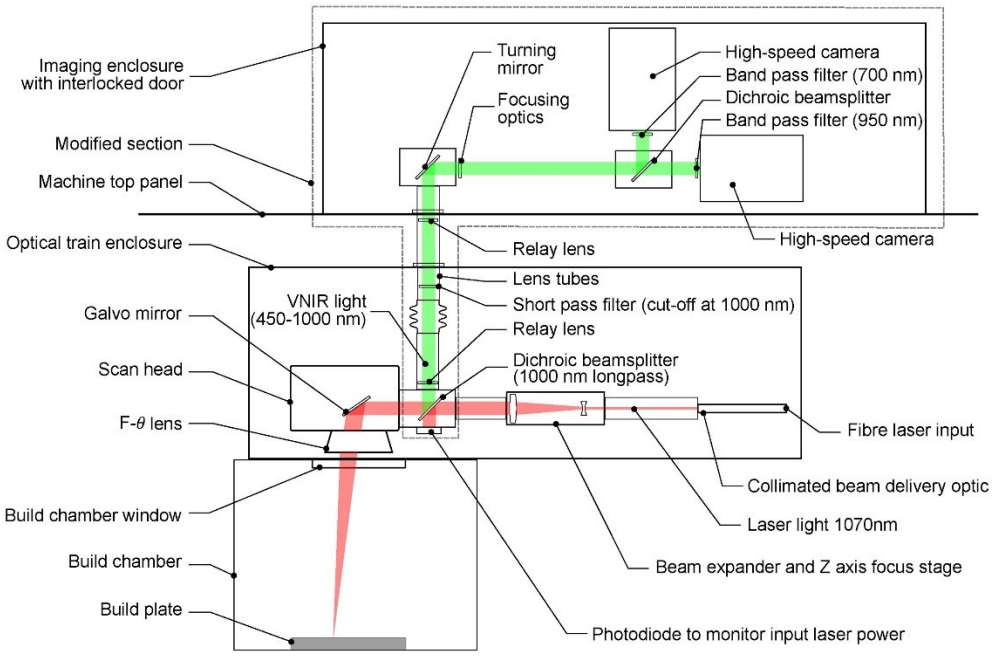


Figure 3.14 – Diagram showing optical layout of the commercial LPBF machine and modification to allow coaxial imaging of the melt pool [8] Reproduced under Creative Commons Attribution License (CC BY).

The following materials were used to manufacture specimens in this research:

- Commercially Pure Titanium Grade 2 (CP-Ti)
- Titanium Grade 23 (Ti6Al4V ELI hereafter referred to as Ti64)
- Tantalum (Ta)
- A 70% Commercially Pure Titanium – 30% Tantalum mix (Ti-30Ta hereafter referred to as TiTa)
- Stainless Steel (SS 316L)

All powders were of spherical shape (Figure 3.15), with the titanium and stainless steel powders having a particle size range of 10-45 µm (D_{50}: 27 µm) whilst the tantalum powder had a particle size range of 5-25 µm (D_{50}: 15 µm). The TiTa powder was a blend of titanium and tantalum powders rather than pre-alloyed powder. All powders were supplied by LPW Technology who also performed the powder blending. Manufacturing occurred in an environment initially vacuumed to -960 mbar and then back filled with 99.995% pure Argon to 10 mbar with an oxygen content of ~0.1%. Stainless steel specimens were built onto steel substrates with all other specimens being built onto titanium substrates. Post build all specimens were cleaned ultrasonically in ethanol. The stochastic architectured porous structures and the locally stiffness-matched scaffold were removed from the substrate by

electro discharge machining (EDM). All specimens for mechanical testing were made parallel by EDM and manual grinding.

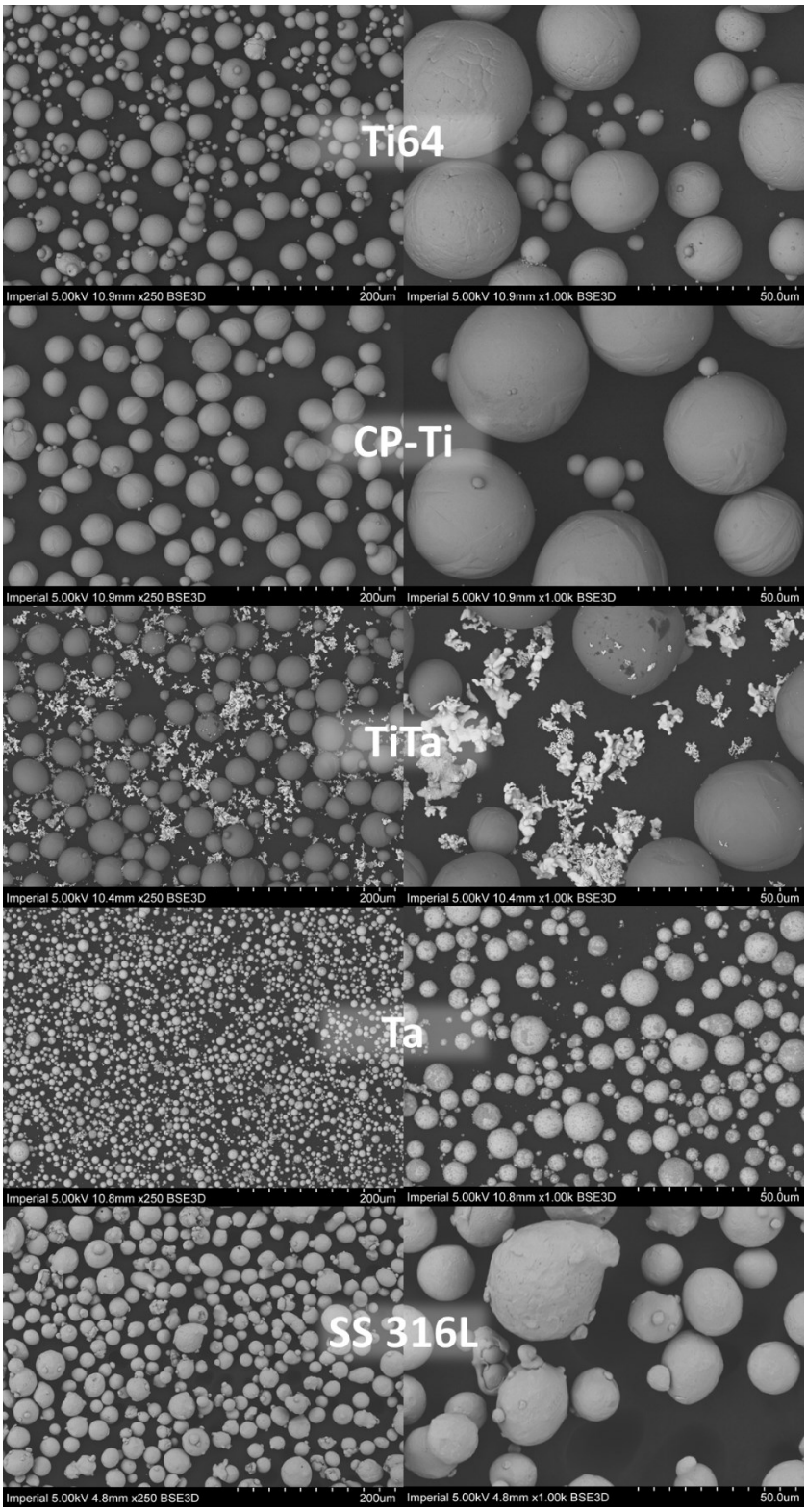


Figure 3.15 – BSEM Images of Powder Feedstock. Note: All powder shown in recycled condition except Ta which is shown in virgin condition. In the TiTa images the large dark spheres are CP-Ti powder whilst the small light particles are Ta powder (agglomerated due to being through the powder bed fusion process numerous times)

3.4 Porous Structure Testing

By varying the laser parameters and scanning strategy, the energy delivered to the melt-pool can be altered, this consequently will have an effect on the morphological and material properties as well as the static and high cycle fatigue strength of porous structures. In addition to this, how the base/parent material effects the mechanical properties of porous structures will be investigated. The following sections describe the test methods used. Note: *a unique specimen* refers to a specimen manufactured by a distinct combination of laser parameters, scan strategy and material and *laser parameters* is defined as a combination of any or all of the following: laser power, exposure time, and where applicable duty cycle and number of repeated exposures per point.

3.4.1 Morphological Analysis

A scanning electron microscope (Hitachi S-3400N) was used for imaging specimens produced in this work. The characterisation structure was built with a large range of laser parameters and scanning strategies and imaged. Strut thickness was then measured utilising ImageJ [9]. For any successfully built specimen/strut, at least 10 measurements were taken from a variety of struts per strut angle from both Plan (Top) and Elevation (Front/Side) views (Figure 3.1). Measurements were then averaged, and this was deemed ‘strut diameter’.

For the stochastic porous structures, overall structure relative density per unique specimen was measured by dry weighing in atmospheric conditions with n=5 (repeated with 5 different specimens). Relative density was calculated by dividing actual weight by the theoretical weight of the macro volume using a density of 4.42 g/cm^3 for Ti6Al4V ELI [10], 4.51 g/cm^3 for CP-Ti [11], 16.6 g/cm^3 for Ta [12], 5.71 g/cm^3 for TiTa [13] and 8.1 g/cm^3 for SS316L [4]. A micro-CT (Bruker Skyscan 1172) was used to validate structure relative density and to measure internal porosity (pores in struts) for select Ti64 and SS316L samples only. Samples were scanned over a height of 5 mm with a 5 µm resolution from approximately the middle of the specimen. CT images were reconstructed and then analysed in CTAn 1.16.4.1 (Bruker N.V.).

To observe the microstructure of the stochastic porous structure specimens, samples were sectioned parallel and perpendicular to the build direction with a diamond blade at low force (Accutom-10, Struers), vacuum mounted, ground with 400, 800, 1200 and 2400 SiC papers and polished with diamond suspensions of 6 and 1 µm and a colloidal silica suspension of 0.04 µm. Grinding and polishing was performed on a Saphir 520. CP-Ti, Ti64 and TiTa

specimens were etched with Kroll's reagent, Ta specimens were etched with etchant 177 as per ASTM E407. Samples were imaged via both optical microscope and SEM; SEM samples were gold sputter coated prior to imaging.

For EBSD, if non-conductive cold mounting resins are used, there may be issues with conductivity and charging. Whilst samples may be gold or carbon sputter coated this may effect EBSD results. Alternatively, using conductive hot mounting resins often destroy porous structures due to the high compressive forces and potentially do not fill all the pore spaces because of the high viscosity of the resin. This dictated the design of the EBSD specimen. The EBSD specimen was consequently hot mounted (Opal 410) on top of a 1° shim/wedge in a conductive epoxy resin (Conducto-Mount 2) and ground with 320 grit SiC papers until multiple struts were visible. The specimens were then ground and polished with 400, 800, 1200 and 2400 grit SiC papers, diamond suspensions of 6 and 1 μm and a colloidal silica suspension of 0.04 μm. The EBSD specimens were not etched as EBSD requires a smooth flat surface. Following preparation samples were placed on a stub with silver cement and a conductive silver track was made from the specimen to the stub. Samples were tilted to 70° inside the SEM and EBSD was performed with a Bruker e-Flash FS EBSD detector. Imaging was done at ~20mm working distance at 456x magnification, 20kV accelerating voltage, with a EBSP map size of 400 x 300 pixels and a pixel resolution of 0.8 – 1 μm.

3.4.2 Quasi – Static Testing

Quasi-Static compression testing was performed to ISO 13314:2011 [1] using a materials testing machine (Instron 8872) equipped with either a 5 kN, 10 kN or 25 kN load-cell depending on the specimen. Specimens were centred between hardened (>62 HRC – Rockwell Hardness) lubricated platens, equipped with a spherical seating, and crushed at a constant strain rate of ~0.1 strain/min. Note: As mentioned earlier, throughout this thesis all measurements of stress, strain, modulus, strength etc. for porous structures refer to the entire structure and are thus effective or apparent measurements, i.e. treating the structure as a uniform material. These are not measurements of local stress or strain in the struts Stress or strain measurements are engineering stress or strain and not true stress or strain.

For each unique specimen, a preliminary sample was compressed to 50% strain to estimate the yield strength. To determine the mechanical properties per unique specimen (n=5), samples were loaded to 50% strain with a hysteresis loop between 70% and 20% of the

estimated yield strength (Figure 3.16) to account for the localised plasticity in porous structures which reduces the slope of the initial loading curve [14].

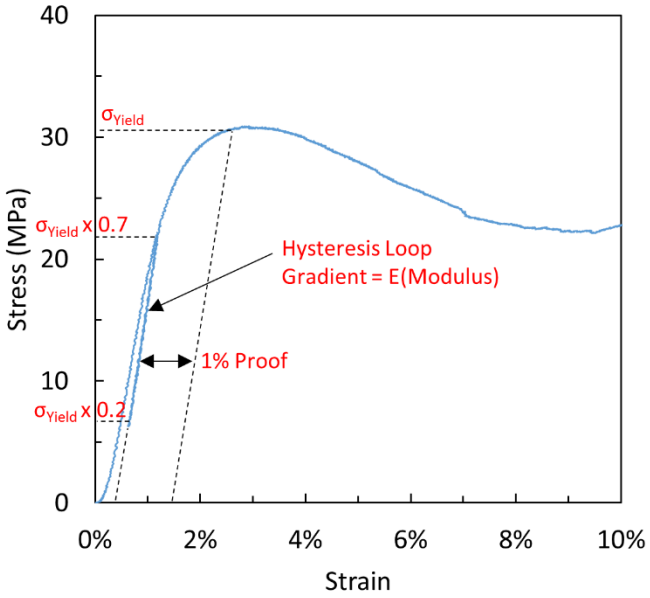


Figure 3.16 – Compression Stress-Strain curve of an AM stochastic porous structure (only shown to 10% Strain)

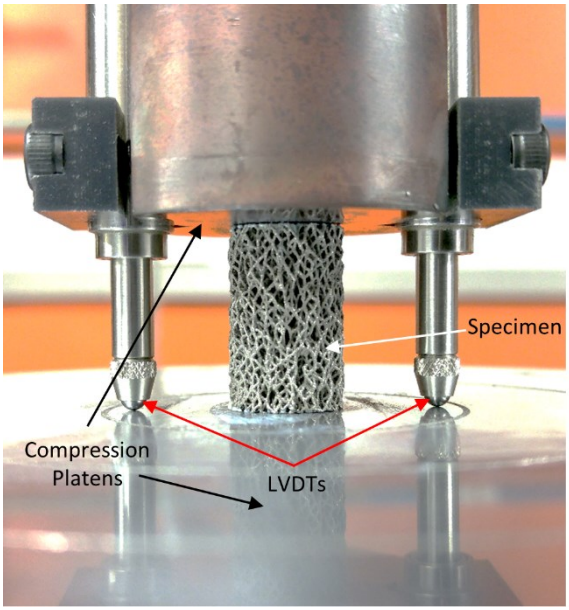


Figure 3.17 – Compression Test Setup

Displacement between the platens was measured at 30 Hz by two LVDTs (RDP D6/05000A) to reduce test-machine compliance errors (Figure 3.17). Strain was the average LVDT displacement (ΔL) divided by the specimen's initial height (L_0). Stress (σ) was the measured load (F) divided by the specimen's initial cross-sectional area (A_0), calculated from the initial diameter of the specimen ($\varnothing_0$).

$$\varepsilon = \frac{\Delta L}{L_0} \qquad \text{(Equation 3.1)}$$

$$\sigma = \frac{F}{A_0} = \frac{F}{\frac{\pi \times \emptyset_0^2}{4}} \qquad \text{(Equation 3.2)}$$

Stress-Strain curves were produced for each test; elastic modulus (E) was the linear regression of the hysteresis loop whilst the yield strength (σ_y) is determined as compressive stress at a plastic compressive strain of 1.0% relative to the elastic modulus (Figure 3.16).

3.4.3 Fatigue Testing

Compression – compression fatigue testing was performed to ISO 1099:2017 [15] using a similar setup as for quasi-static testing except displacement between the platens was measured by a single un-guided LVDT (RDP D6/05000URA) to be suitable for fatigue loading (Figure 3.18).

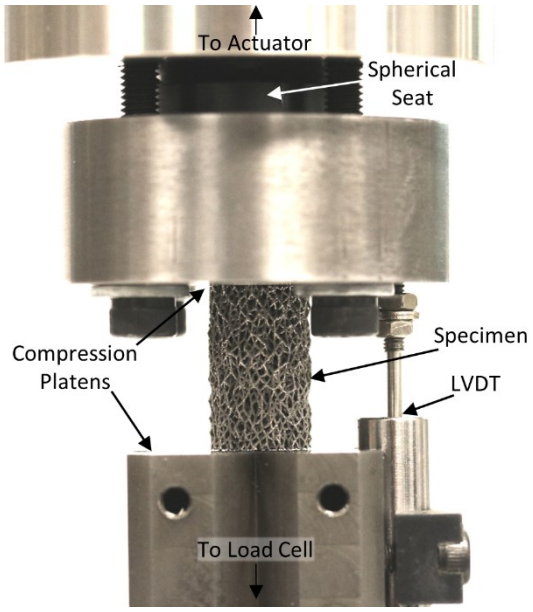


Figure 3.18 – Compression – Compression Fatigue Test Setup

A 250N, 1 kN or 5 kN load-cell was used depending on the specimen. Specimens were tested in load control at a frequency of 15Hz (sinusoidal wave form) with an R=0.1 ratio between the minimum stress and the test (or maximum) stress. Compressive strain as a function of cycles was recorded and tests were ended either at 1 million cycles or final catastrophic failure. Based on previous research, this was estimated as 5% strain (i.e. a 5% compressive shortening from the specimen's original height), in order to ensure specimens were not too

damaged after failure to examine failure planes. The staircase method, as described in ISO 12107:2012 [16], was used to find mean fatigue strength at 10^6 cycles ($\widehat{\sigma}_{FS}$) and the standard deviation ($\widehat{SD_{FS}}$), with fatigue strength being defined as the highest stress the porous structure can withstand for a given number of cycles (10^6 cycles) without failure. In the staircase method, specimens are tested sequentially under increasing or decreasing test stresses based on survival or failure of the sample, respectively. From the beginning, the last non-failure is the first data point included in the analysis (Figure 3.19); following this a further 7 samples were tested, per unique specimen. Thus only 8 data points were used for fatigue strength quantification, limitations to this method will be discussed in Chapters 4 & 5.

Initial test stresses were chosen based on literature [10-12, 17] and for each unique specimen the test stress was increased or decreased by a step size (d) of 1.25% of its yield strength. Following collection of data, the data is rearranged to count the frequencies of failure and non-failure of the specimens tested at different stress levels (Figure 3.19). Analysis is performed for the events "failure" or "non-failure" for the group with the least number of observations. The stress levels are arranged in ascending order by $S_0 \leq S_1 \leq \ldots \leq S_i$, where i is the number of stress levels and the number of events per stress level are tallied (f_i,).

$$\widehat{\sigma_{FS}} = S_0 + d\left(\frac{A}{C} \pm \frac{1}{2}\right) \quad \text{(Equation 3.3)}$$

$$\widehat{SD_{FS}} = 1.62 \times d(D + 0.029) \quad \text{(Equation 3.4)}$$

Where

$$A = \sum_{i=1}^{l} i f_i$$

$$B = \sum_{i=1}^{l} i^2 f_i$$

$$C = \sum_{i=1}^{l} f_i$$

$$D = \frac{BC - A^2}{C^2}$$

In the equation for fatigue strength (Equation 3.3), the value of ±1/2 is positive when the event analysed is non-failure and negative when the event analysed is failure.

Stress S_i MPa	Sequence number of specimen														
	1				5					10					15
540								X							X
520				X				O		X		X			O
500			O		X		O				O		X		O
480		O*				O								O	
460	O*														

X for failure
O for non-failure
* not counted

Stress S_i MPa	Level i	Values f_i	if_i	i^2f_i
540	2	2	4	8
520	1	3	3	3
500	0	2	0	0
Sum	—	7	7	11

Figure 3.19 – A 15 specimen example of the staircase method of fatigue testing and data collection from ISO 12107:2012 [16]

3.4.4 Build Time Measuring

Build time was calculated, via the build file generation software, for each unique stochastic porous specimen and defined as all the scanning time including the laser firing time, scanner and jump delays and processing delays; essentially the total time required to build a single part except for physical powder dosing time (which would be constant between specimens).

3.5 *In Vivo* Testing

In order to investigate the bone in-growth into a locally stiffness matched scaffold, *in vivo* testing was performed in an ovine model. The surgical procedure to implant the scaffolds and the test methods used to analyse the explants are detailed below.

3.5.1 Surgical Procedure

Six skeletally mature (older than 4 years) non-pregnant female sheep were enrolled in the study. Ethical approval for this study was received from the United Kingdom Home Office (Project License Number 70/8247). Study design and ethical approval was performed by Dr Gordon Blunn, Dr Natalie Reznikov and Dr Oliver Boughton. Only one hind leg of each sheep was used for this study, whilst the other hind leg was used for another study investigating different scaffold material, architecture and stiffness as described in [18]. One scaffold (diameter 16 mm, length 15 mm) was inserted into each hind leg, in the distal medial femoral condyle (Figure 3.20). Of the six sheep, 3 right legs and 3 left legs were used for implantation with the respective (left or right version) stiffness-matched scaffold.

Pre-operative antibiotics were given to each sheep and continued for 3 days postoperatively (Cefalexin 1ml/25kg animal once a day). Under a general fentanyl anaesthesia the distal medial femoral condyle was exposed and periosteum removed over the area of implant insertion. A flat bottom ⌀15×15mm cylindrical defect (1mm under-ream) through the medial-lateral femoral axis was created by use of drills and reamers of increasing diameter equipped with a depth gauge (Figure 3.20 and Figure 3.21). Simultaneously with the defect preparation, a scaffold was centrifuged in 30 ml of animal's blood (drawn from the jugular vein) in a sterile test tube at 3000 RPM for 3 minutes to dislodge micrometer-scale air bubbles from the surface of the scaffold. The centrifuged scaffold was press fit into the cavity by hand, followed by gentle application of force from a surgical mallet. The surgery was performed by Dr Gordon Blunn and Dr Oliver Boughton.

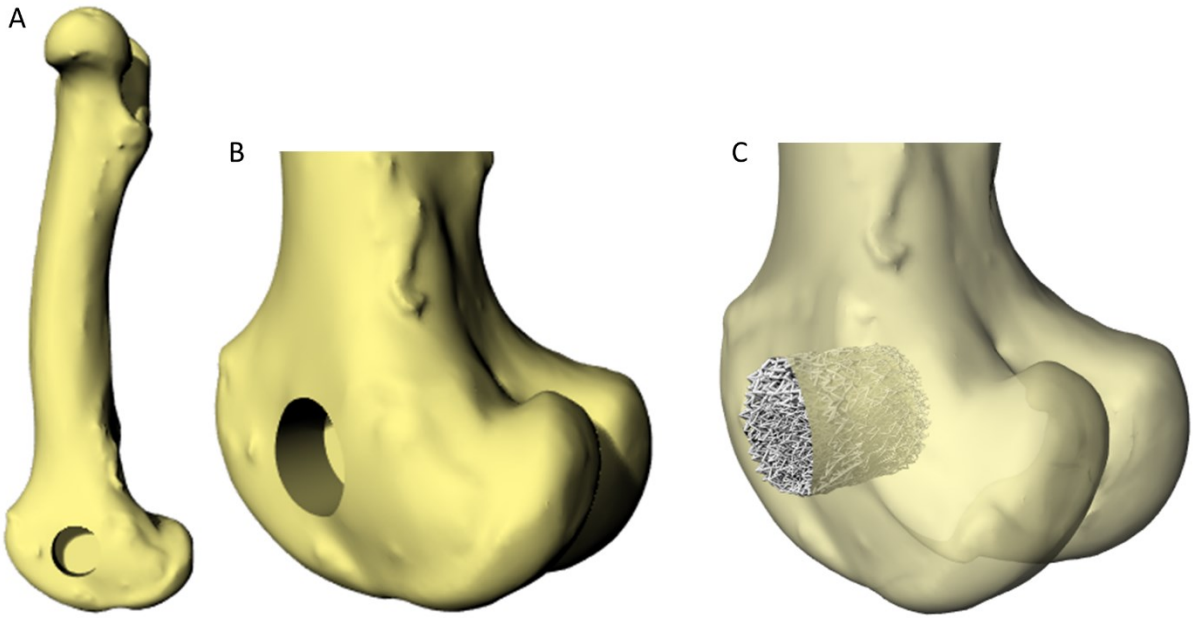


Figure 3.20 – Implant Placement



Figure 3.21 – Implant Placement during Surgery

The wound was closed in 3 layers (fascia, subcutaneous soft tissue and then skin) using resorbable sutures then covered with an aseptic spray (Opsite). Postoperatively, once a swallowing reflex had been established, the animal was transferred back to a single pen with straw bedding. The animals recovered in sternal recumbency and were allowed hay, food concentrate and water as is the normal feeding regime. The sheep received analgesia for 60 hours post-operatively (Fentanyl 75 mcg patches). Oxytetracycline was administered by slow

intravenous injection on day 28 postoperatively at 30mg per kg of body weight in order to tag the site of active osteogenesis with a fluorophore and to quantify the rate of bone accretion over the last two weeks of the in-life phase.

3.5.2 Explant Analysis

All animals were euthanised at six weeks post-operatively, six weeks was chosen in order to make ingrowth comparisons to two studies. The first, an associated study, used uniform modulus scaffolds both significantly stiffer and less stiff than the bone it would be replacing [18] whilst the other was an empty defect study [19]. All studies had identical surgical sites. For explant retrieval, the femur was disarticulated and its distal metaphysis was cut and trimmed to the size of about 5 cm in all dimensions (Figure 3.22a). The samples were stored in formalin at room temperature until analysis.

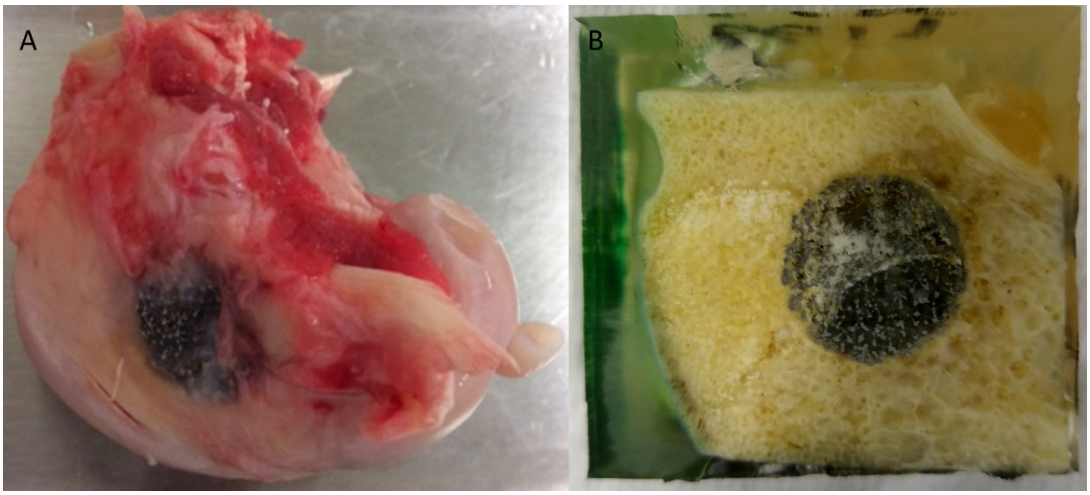


Figure 3.22 – Specimen retrieval: A) Distal Femur removed. B) Specimen trimmed around scaffold and defect, mounted and sectioned.

3.5.2.1 Micro-Computed Tomography (micro-CT)

Tomographic imaging was conducted in an Xradia Versa 510 (Zeiss) at 140 kV, 70 µA at 3201 projections and a pixel size of ~ 25 µm by Dr Natalie Reznikov. The 3D reconstructed tomographic images were segmented and analyzed using CT-analyser v.1.18.4.1 (Bruker N.V.). Segmentation of the sample was performed in three steps. The defect (region of interest) was delineated as a cylindrical volume around the diameter and length of the scaffold and a three level multi-level Otsu segmentation was used to distinguish between the scaffold, bone and other. As the CT scans revealed beam hardening, visible in a tomogram as a structureless halo of higher pixel values around the titanium scaffold elements, a 2 pixel dilation was applied to the scaffold segmentation and subtracted from the images prior to quantifying the new bone ingrowth. This step labelling of bone based on the local grey values was necessary to avoid the

inclusion of bright pixels around the metal elements that were not bone, but the effect of beam hardening.

3.5.2.2 Microscopy

Post μ-CT scanning, samples were dehydrated for embedding by immersing in methylated spirits of increasing concentration (50%, 75%, 85%, 95% and 2x 100%) followed by chloroform immersion for 24 hours, and then methylmetacrylate resin (LR White) for 72 hours. Following resin saturation, the accelerator was added and the blocks were polymerised at low temperature (-20°C). The blocks were trimmed and then sectioned by cutting perpendicular to the defect axis (medial-lateral axis) and therefore, parallel to the scaffold face (Figure 3.22b).

For all the samples two central slices were prepared for microscopy. Slices were mounted, ground and polished with one of the slices being thinned down to a thickness of approximately 50μm. The thinned sections underwent fluorescent microscopy, followed by histological staining. Fluorescent microscopy was performed using a Zeiss Wide-Field light microscope (WF3 Zeiss Axio Observer, Zeiss Germany). After fluorescent microscopy toluidine blue and paragon were used to stain the samples to identify histological features. Histological microscopy was performed identical to the fluorescent microscopy. The non-thinned section was gold sputter coated and was imaged by scanning electron microscopy using a back scatter detector (Hitachi S-3400N).

3.5.2.3 Grading of Scaffolds

For the assessment of peripheral and central osteogenesis in the defect a library was created for independent scoring. It contained 2D images of virtual sections perpendicular to the central axis of the cylindrical scaffold were taken at depth of 2, 5, 8, 11 and 14 mm from the periosteal surface, five such sections from each of the 6 specimens. The peripheral and central osteogenesis were scored on each image using a scale from 0 to 4 by three operators independently, using a shared list of criteria (Table 3.1).

Table 3.1 – Scoring criteria for bone formation at the bone-implant interface (periphery of the defect) and within the interior of the implant and defect.

Score	Bone-implant-interface (periphery of the defect)	Implant interior
0	No observed contact between implant outline and host bone	No bone observed
1	Partial bone contact along approximately one-third of the implant outline	Small specks of high density attributable to bone
2	Partial bone contact along approximately two-thirds of the implant outline	Small fine networks of woven bone or thin deposits on the scaffold struts
3	Complete circular contact between implant outline and host bone	Substantial semilunar deposits of bone within the pores or extensive networks of woven bone
4	Nascent bone engulfs the outer scaffold struts up to fully occupying the outermost tier of scaffold pores	Massive amounts of well-defined bone in all discernible pores of the scaffold

3.6 References

[1] ISO13314, Mechanical testing of metals. Ductility testing. Compression test for porous and cellular metals, 2011.

[2] O. Rehme, Cellular Design for Laser Freeform Fabrication, Cuvillier Göttingen, 2009.

[3] L. Mullen, R.C. Stamp, W.K. Brooks, E. Jones, C.J. Sutcliffe, Selective Laser Melting: A regular unit cell approach for the manufacture of porous, titanium, bone in-growth constructs, suitable for orthopedic applications, Journal of Biomedical Materials Research Part B: Applied Biomaterials 89B(2) (2009) 325-334.

[4] S. Tsopanos, R.A.W. Mines, S. McKown, Y. Shen, W.J. Cantwell, W. Brooks, C.J. Sutcliffe, The Influence of Processing Parameters on the Mechanical Properties of Selectively Laser Melted Stainless Steel Microlattice Structures, Journal of Manufacturing Science and Engineering 132(4) (2010) 041011-041011.

[5] R. Hasan, Progressive Collapse of Titanium Alloy Micro-Lattice Structures Manufactured Using Selective Laser Melting (PhD Thesis), University of Liverpool, 2013.

[6] O. Cansizoglu, O.L.A. Harrysson, H.A. West, D.R. Cormier, T. Mahale, Applications of structural optimization in direct metal fabrication, Rapid Prototyping Journal 14(2) (2008) 114-122.

[7] S. Li, H. Xiao, K. Liu, W. Xiao, Y. Li, X. Han, J. Mazumder, L. Song, Melt-pool motion, temperature variation and dendritic morphology of Inconel 718 during pulsed- and continuous-wave laser additive manufacturing: A comparative study, Materials & Design 119 (2017) 351-360.

[8] P.A. Hooper, Melt pool temperature and cooling rates in laser powder bed fusion, Additive Manufacturing 22 (2018) 548-559.

[9] C.A. Schneider, W.S. Rasband, K.W. Eliceiri, NIH Image to ImageJ: 25 years of image analysis, Nat Meth 9(7) (2012) 671-675.

[10] S. Amin Yavari, R. Wauthle, J. van der Stok, A.C. Riemslag, M. Janssen, M. Mulier, J.P. Kruth, J. Schrooten, H. Weinans, A.A. Zadpoor, Fatigue behavior of porous biomaterials manufactured using selective laser melting, Materials Science and Engineering: C 33(8) (2013) 4849-4858.

[11] R. Wauthle, S.M. Ahmadi, S. Amin Yavari, M. Mulier, A.A. Zadpoor, H. Weinans, J. Van Humbeeck, J.-P. Kruth, J. Schrooten, Revival of pure titanium for dynamically loaded porous implants using additive manufacturing, Materials Science and Engineering: C 54 (2015) 94-100.

[12] R. Wauthle, J. van der Stok, S. Amin Yavari, J. Van Humbeeck, J.-P. Kruth, A.A. Zadpoor, H. Weinans, M. Mulier, J. Schrooten, Additively manufactured porous tantalum implants, Acta Biomaterialia 14 (2015) 217-225.

[13] Y.L. Zhou, M. Niinomi, T. Akahori, Effects of Ta content on Young's modulus and tensile properties of binary Ti–Ta alloys for biomedical applications, Materials Science and Engineering: A 371(1) (2004) 283-290.

[14] M.F. Ashby, A.G. Evans, N.A. Fleck, L.J. Gibson, J.W. Hutchinson, H.N.G. Wadley, Metal Foams: A Design Guide, Butterworth-Heinemann, Burlington, 2000.

[15] ISO1099, Metallic materials -- Fatigue testing -- Axial force-controlled method, 2017.

[16] ISO12107, Metallic materials -- Fatigue testing -- Statistical planning and analysis of data, 2012.

[17] N.W. Hrabe, P. Heinl, B. Flinn, C. Körner, R.K. Bordia, Compression-compression fatigue of selective electron beam melted cellular titanium (Ti-6Al-4V), Journal of Biomedical Materials Research Part B: Applied Biomaterials 99B(2) (2011) 313-320.

[18] N. Reznikov, O.R. Boughton, S. Ghouse, A.E. Weston, L. Collinson, G.W. Blunn, J. Jeffers, J.P. Cobb, M.M. Stevens, Individual response variations in scaffold-guided bone regeneration are determined by independent strain- and injury-induced mechanisms, Biomaterials 194 (2019) 183-194.

[19] A. Malhotra, M.H. Pelletier, Y. Yu, C. Christou, W.R. Walsh, A Sheep Model for Cancellous Bone Healing, Frontiers in Surgery 1(37) (2014).

4 Chapter 4 – Influence of Laser Parameters and Scanning Strategies on the Mechanical and Material Properties of Porous structures

The future of the generation of architectured materials is likely to move from solid CAD modelling, which is computationally expensive, to line based representation. Therefore, the relationship between laser parameters and scan strategy to strut thickness must be understood. As stated earlier, there has been research that investigates the effect of laser parameters on AM material properties, such as strut size [1-3], structure porosity or material density. However, either a single laser parameter is explored in isolation [3] or an equation for 'laser energy density' is used [1, 4, 5]. These models do not include important process variables, and typically generate a process parameter window or a collection of data points with no distinct trend when graphing a property such as strut thickness against the laser energy density [1, 6], thus making it difficult to scale or predict values outside the tested experimental range [7]. They also tend to not look at the role of these process parameters on mechanical properties.

Therefore, this chapter will focus on whether different porous structures, having the same strut thicknesses or same stiffness or relative density but manufactured from different laser parameters or scan strategies, will have the same mechanical properties. This chapter will investigate and quantify how the laser parameters and scan strategies influence strut thickness and the mechanical and material properties of porous structures, specifically looking to maximise the strength and fatigue strength of a structure for a given stiffness and whether any trends found are material specific. Ti64 and SS316 will be used as the materials investigated to see if laser parameter and scanning strategy trends are material specific. Fatigue testing and microstructural characterisation will only be performed on Ti64, as whilst SS316 is a cheap and useful material to explore trends and phenomena in AM its application as a porous bone in-growth scaffold is limited.

4.1 Materials and Methods

4.1.1 Evaluation of Characterisation Structures

By varying the laser parameters and scanning strategy, the energy delivered to the melt-pool can be altered to produce struts of different diameters. For the contour and points strategy, per laser power explored, five values of exposure time were chosen from the given range. For the pulsing strategy, two exposure times were selected at 50 W and 200 W each and five values of repeated exposures per point were chosen from the given range. Thus 20 laser parameters per material per scanning strategy were manufactured and analysed giving 120 unique specimens total (Table 4.1). As detailed in Chapter 3, the structures were imaged using a scanning electron microscope and analysed via ImageJ. Raw data can be found in Appendix A.

Table 4.1 – Evaluation of Characterisation Structures Study Design and Manufacturing Conditions

Test	Evaluation of Characterisation Structure
Materials	Ti64, SS316
Scanning Strategies	Contour, Points, Pulsing
Laser Power (W)	50, 100, 150, 200
Exposure Time (µs)	20 - 2800
Duty Cycle[1]	50%
# of Repeated Exposures[1]	×2 - ×20
Point Distance (µm)	50
Layer Thickness (µm)	50
Laser Parameters[2] per test variable	20
Unique Specimens[3]	120
Repeats per Parameter Set	1
Total # of Specimens Tested	120

[1]Applicable for the Pulsing Strategy only
[2]A combination of any or all of the following: laser power, exposure time, and where applicable duty cycle and # of repeated exposures per point
[3] A specimen manufactured by a distinct combination of laser parameters, scan strategy and material

4.1.2 Evaluation of Stochastic Architectured Porous Structures

4.1.2.1 Effect of Laser Parameters and Scanning Strategies on Quasi-Static Strength and Material Properties

Altering laser powers can cause differences in phenomena such as spatter ejection, volatility of the melt-pool and cooling rates. A coarse optimisation of laser powers was performed based on the maximum and minimum power the AM machine can reliably produce, with the maximum laser power of the machine being 200W and 50W being deemed an acceptable reliable minimum. A minimum of five unique samples were built at both low power (50 W) and high power (200 W) with exposure time and pulsing parameters (for the pulsed

strategy) altered for all three strategies (points, contour and pulsing) for both Ti64 and SS316, thus giving at least 60 unique specimens.

The number of specimens built and tested are listed in Table 4.2. The same input geometry was used to generate all specimens with changes in strut diameter and thus specimen relative density and modulus being solely controlled by the laser parameters and scan strategy. Overall structure relative density was measured by dry weighing, as described in 3.4.1, for all unique specimens with n=5. Internal porosity was measured by µ-CT scanning on 4 unique specimens per laser power per scanning strategy for both materials and a single sample of each type was scanned. Quasi-Static compression testing was performed as described in 3.4.2 with 5 repeats per unique specimen. Laser parameters for every manufactured specimen can be found in Appendix B.

Table 4.2 – Stochastic Porous Structures quasi-static Testing Study Design and Manufacturing Conditions

Test	Quasi-Static & Relative Density Testing	µ-CT Scanning
Materials	Ti64, SS316	
Scanning Strategies	Contour, Points, Pulsing	
Laser Power (W)	50, 200	50, 200
Exposure Time (µs)	20 - 2800	
Duty Cycle[1]	50%	
# of Repeated Exposures[1]	×2 - ×20	
Point Distance	50	
Layer Thickness (µm)	50	
Laser Parameters[2] per test variable	10	4
Unique Specimens[3]	60	24
Repeats per Parameter Set	5	1
Total # of Specimens Tested	300	48

[1]Applicable for the Pulsing Strategy only
[2]A combination of any or all of the following: laser power, exposure time, and where applicable duty cycle and # of repeated exposures per point
[3] A specimen manufactured by a distinct combination of laser parameters, scan strategy and material

4.1.2.2 Effect of Laser Parameters and Scanning Strategies on High Cycle Fatigue Strength and Microstructure

Due to the testing time required to measure fatigue strength to 1 million cycles, the number of variables tested needed to be limited compared to quasi-static testing. Therefore, only Ti64 would be used as the base material and as before, the same input geometry was used to generate all specimens with changes in strut diameter and thus specimen porosity and modulus being solely controlled by altering the energy delivered to the melt-pool via the laser parameters and scan strategy. To investigate the effect of laser parameters on high cycle fatigue

strength, 4 unique samples were built with a single strategy (points) at both low power (50 W) and high power (200 W) with exposure time being altered (Table 4.3) and were fatigue tested. The laser power used to manufacture specimens that produced structures with the greatest fatigue strength for a given stiffness would then be used to manufacture specimens in the remaining strategies (contour and pulsing) to determine the effect of scan strategy on fatigue strength (Table 4.3). Again 4 unique specimens per strategy were built and tested. Microstructure and EBSD was performed on 1 unique specimen for each of the fatigue testing test variables (low power vs. high power and points vs. contour vs. pulsing) as described in 3.4.1. Laser Parameters for every manufactured specimen can be found in Appendix B.

Note: All specimens fatigue tested were of the same laser parameters (i.e. same unique specimen type) that had been μ-CT scanned. Therefore quasi-static properties, relative density and internal porosity for all unique specimens fatigue tested were taken from the results of 4.1.2.1.

Table 4.3 – Stochastic Porous Structures fatigue Testing Study Design and Manufacturing Conditions

Test	**Effect of Laser Power on Fatigue Strength**	**Effect of Scan Strategy on Fatigue Strength**
Materials	Ti64	
Scan Strategy	Points	Contour, Points, Pulsing
Laser Power (W)	50, 200	50
Exposure Time (μs)	20 – 2000	
Duty Cycle[1]	-	50%
# of Repeated Exposures[1]	-	x2 - x20
Point Distance (μm)	50	
Layer Thickness (μm)	50	
Laser Parameters[2] per test variable	4	
Unique Specimens[3]	8	12
Repeats per unique specimen	8	8
Total # of Specimens Tested	64	96

[1]Applicable for the Pulsing Strategy only
[2]A combination of any or all of the following: laser power, exposure time, and where applicable duty cycle and # of repeated exposures per point
[3] A specimen manufactured by a distinct combination of laser parameters and scan strategy

4.2 Results

4.2.1 Evaluation of Characterization Structures

Struts ranging in build angles from 90° to 15° were successfully manufactured in both materials for all 3 scanning strategies. Table 4.4 lists the minimum strut diameter produced successfully for each scanning strategy per material whilst Table 4.5 lists the laser parameters used to produce the minimum strut diameters.

Table 4.4 – Minimum Strut Thickness (Values are average Strut Thickness ± S.D). Superscripts refer to the Laser Parameters used to produce minimum strut thickness as detailed in Table 4.5.

	Strut Thickness (mm)				
Build Angle	**90°**	**60°**	**45°**	**30°**	**15°**
Ti64 – Points	0.142±0.014[1]	0.153±0.014[1]	0.153±0.014[1]	0.174±0.017[2]	0.219±0.026[2]
Ti64 – Pulsing	0.154±0.020[3]	0.161±0.014[3]	0.164±0.020[3]	0.168±0.020[3]	0.224±0.022[3]
Ti64 – Contour	0.151±0.020[4]	0.164±0.020[4]	0.163±0.014[4]	0.178±0.010[4]	0.236±0.029[5]
SS316 – Points	0.133±0.007[6]	0.147±0.020[6]	0.145±0.009[6]	0.168±0.012[6]	0.218±0.039[7]
SS316 – Pulsing	0.130±0.011[8]	0.150±0.012[8]	0.154±0.009[8]	0.174±0.017[8]	0.224±0.024[9]
SS316 – Contour	0.137±0.012[10]	0.164±0.019[10]	0.152±0.009[10]	0.172±0.017[10]	0.238±0.013[10]

Table 4.5 – Laser Parameters used to produce minimum Strut Thickness (minimum specific enthalpy) to build successful structures.

	Laser Power (W)	**Exposure Time (µs)**	**Point Distance (µm)**	**Equivalent Laser Speed (m/s)**	**# of Repeated Exposures**	**Duty Cycle**
1	50	200	50	0.24	N/A	
2	50	400	50	0.12	N/A	
3	50	50	50	0.83	x5	50%
4	50	50	50	0.83	N/A	
5	50	100	50	0.45	N/A	
6	100	100	50	0.45	N/A	
7	50	800	50	0.06	N/A	
8	50	50	50	0.83	x10	50%
9	50	100	50	0.45	x6	50%
10	100	80	50	0.56	N/A	

Increasing specific Enthalpy (Equation 2.2) resulted in an increase in melt-pool size and thus an increase in strut thickness (Figure 4.1 and Figure 4.2). At low specific enthalpies, the melt-pool size is not large enough to consistently melt to the layer below or surrounding features (particularly for low angled struts) and thus the characterisation structure will either be non-existent or will contain broken struts (Figure 4.1). As specific enthalpy increases so does the 'stability' of strut elements as does the weld-neck and the quantity of semi-fused particles (Figure 4.2). Specific enthalpy values for the laser parameters listed can be found in Appendix A.

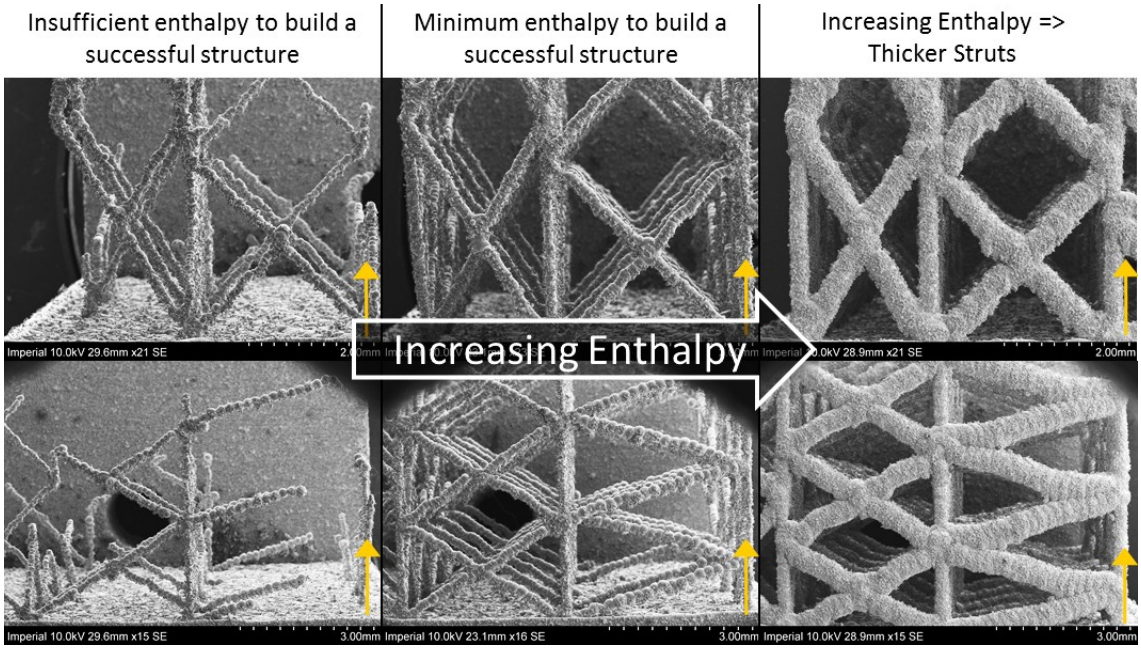


Figure 4.1 – SEM images of characterization structure for increasing enthalpy. Top row: 90°, 60° and 45° struts. Bottom row: 90°, 30° and 15° struts. Orange arrows indicate vertical build direction

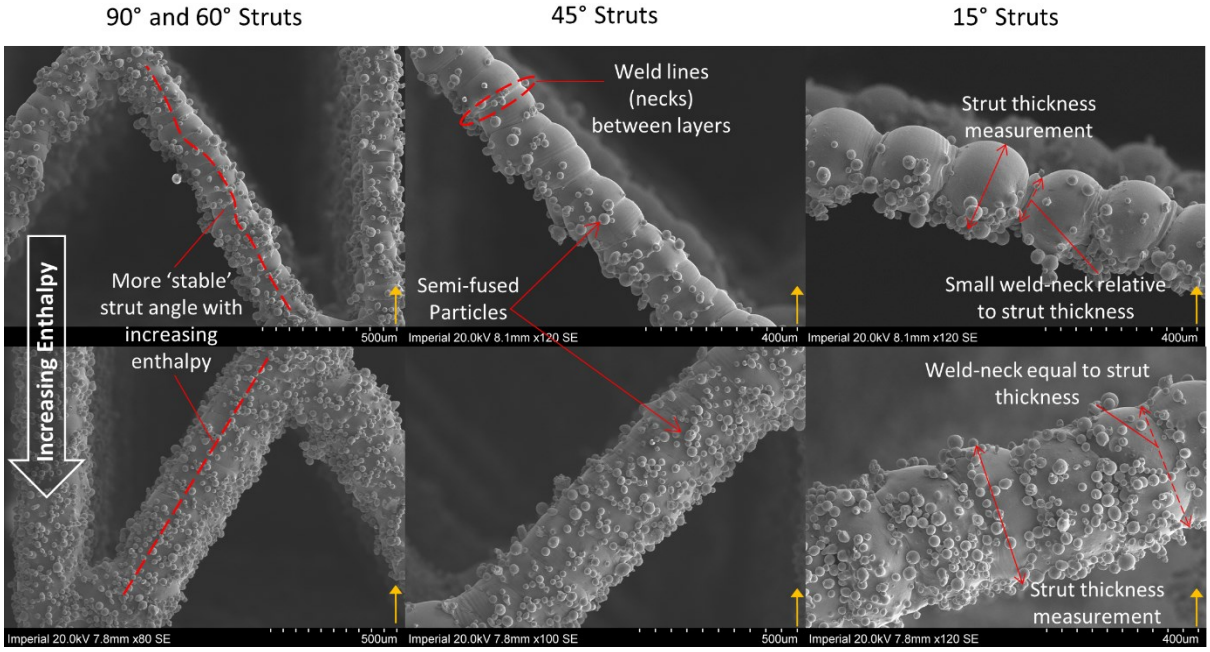


Figure 4.2 – SEM images of Characterization Structure Struts for increasing Enthalpy and different build angles. Orange arrows indicate vertical build direction

The relationship between specific enthalpy and strut thickness was found to be linear for all materials, scanning strategies and build angles (Figure 4.3). The relationship was found to be more accurate when specific enthalpy was calculated with actual laser power and exposure time (not requested power and time) as measured by the process monitoring equipment.

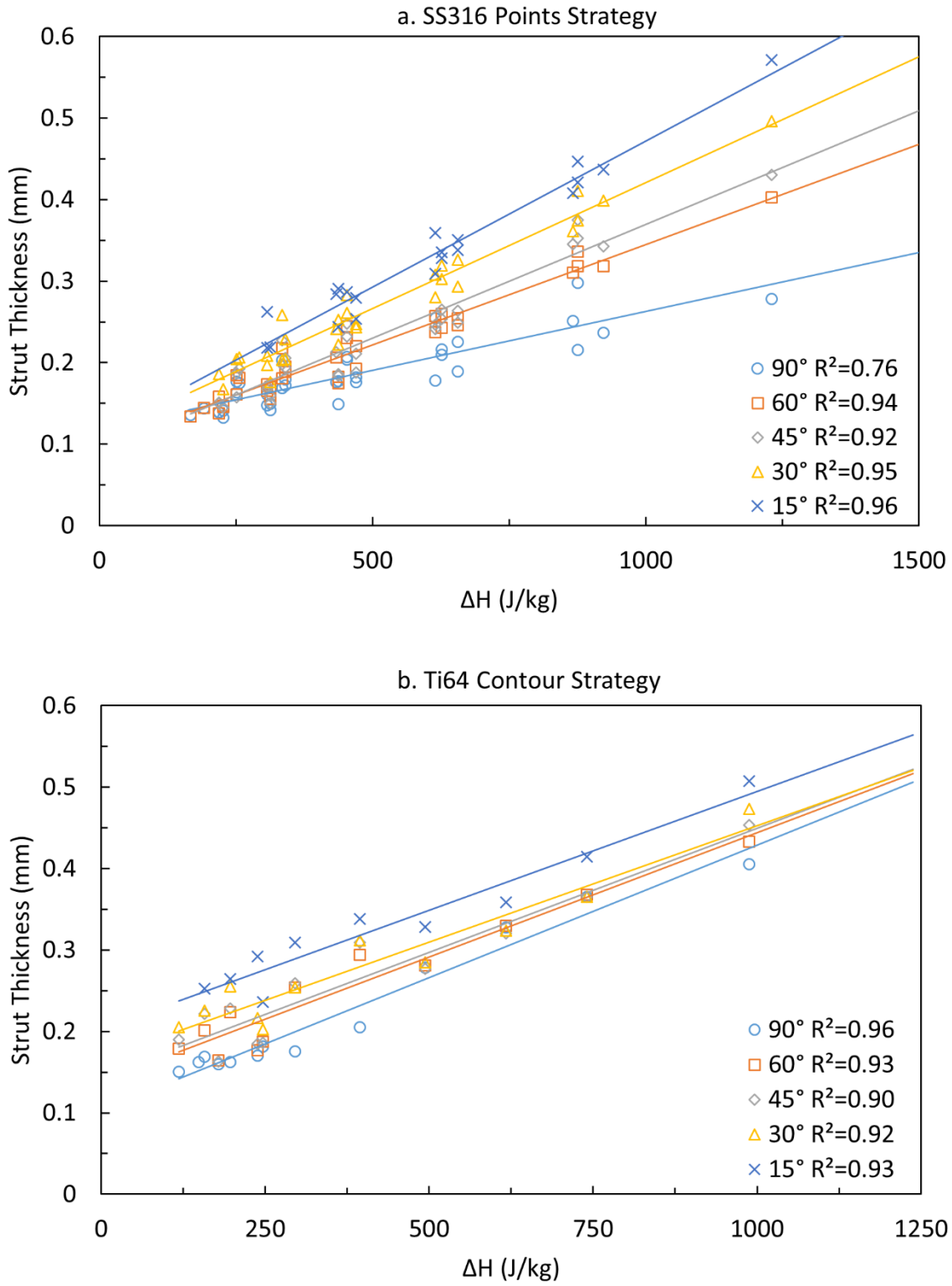


Figure 4.3 – Strut Thickness vs. Specific Enthalpy Plots for a) the Points Strategy in SS316 (also typical for the Pulsing Strategy) and b) the Contour Strategy in Ti64. Plots are typical for both materials. Due to high number of data points and for graphical clarity, error bars not shown. Average S.D. for strut thickness measurements was 0.018mm. The laser parameters associated with these specific enthalpy values can be found in Appendix A.

4.2.2 Mechanical Testing of Stochastic Porous Structures

Manufactured stochastic porous specimens (Figure 4.4) had relative densities ranging from 5 – 25% and moduli of 0.2 – 4.5 GPa for Ti6Al4V ELI and 0.3 – 5 GPa for SS316. All samples had the same structure, with different porosity and modulus a result of varying strut thickness by altering the energy delivered to the melt-pool via the laser parameters and scan strategy.

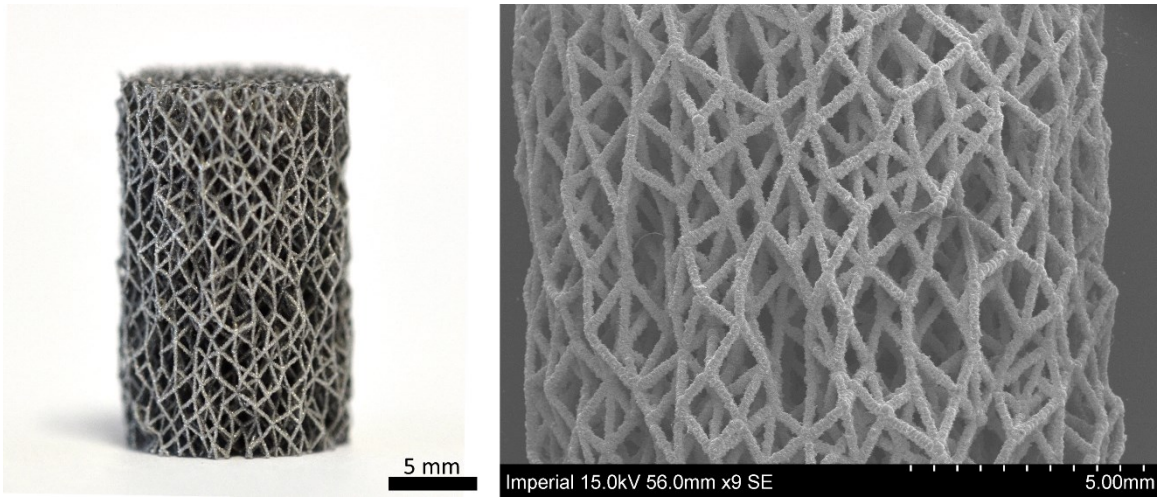


Figure 4.4 – Stochastic Porous Structure

Typical stress-strain plots for both materials are seen in Figure 4.5. Ti64 exhibited a relatively brittle failure mode whilst SS316 exhibited a ductile failure mode. Figure 4.6 depicts the failure mechanisms of the stochastic structures under compressive load. The structures behaved like a continuum and did not fail on a row by row basis which is an advantage of the stochastic structure compared to some repeating unit cell designs.

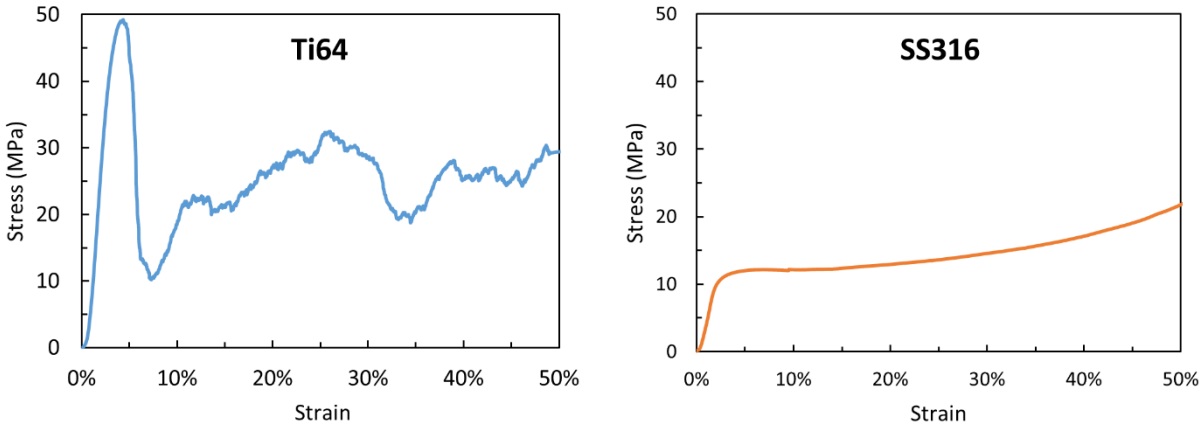


Figure 4.5 – Typical Porous structure Stress-Strain Curves for Ti64 and SS316. Ti64 exhibits relatively brittle failure whilst SS316 exhibits more ductile failure. Curves shown for specimens with a 3.3 and a 3.5 GPa modulus respectively, and without hysteresis loops to 50% strain.

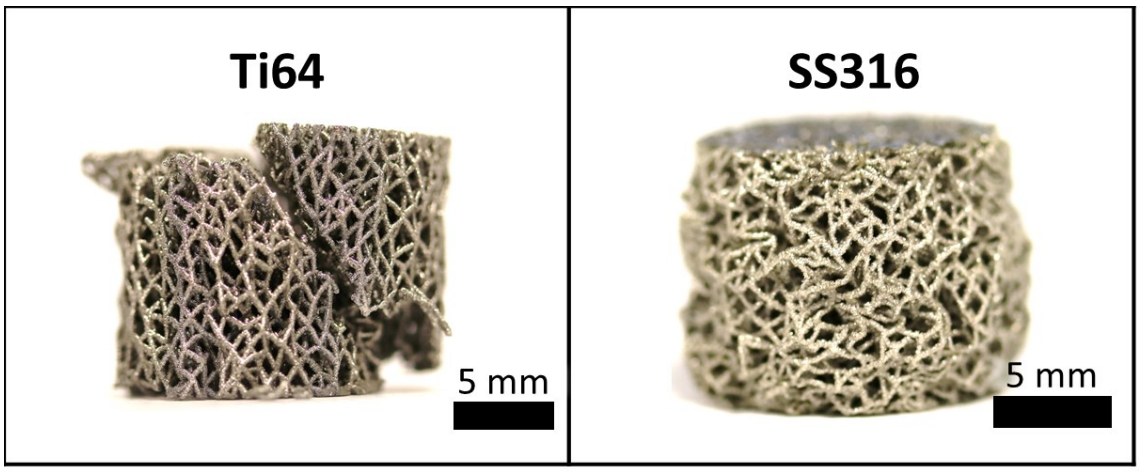


Figure 4.6 – Failed porous structures during quasi-static testing with a ~3.0 GPa modulus

A power-law relationship was modelled between yield strength and modulus (Figure 4.7 and Figure 4.9) as suggested by Gibson and Ashby [8, 9] regardless of material, laser parameter and scanning strategy. This will be discussed in greater detail in Section 4.3.1. R^2 values for all curve fits were 0.99 and error bars on plots (Figure 4.7 and Figure 4.9) are standard deviations. Linear scaled axes are used throughout to better visualise the differences between datasets/trend-lines. Ti64 samples built at 50 W have up to 10% higher strength:modulus (σ_y:E) ratio than those built at 200 W (Figure 4.7a), with the average difference being 7.9±0.2%. The opposite phenomenon is seen for SS316, where samples built at 200 W have up to 10% higher σ_y:E ratio than those built at 50 W (Figure 4.7b), with the average difference being 8.0±0.1%. For both materials, these relationships were consistent for all scan strategies (contour, points, pulsed). Internal porosity (Φ) was found to increase with modulus or relative density and was significantly lower for samples built at 50 W than at 200 W, this was true for both materials and all scan strategies (Figure 4.8). A power-law relationship is observed between yield strength and relative density and between modulus and relative density, as seen in Appendix B.

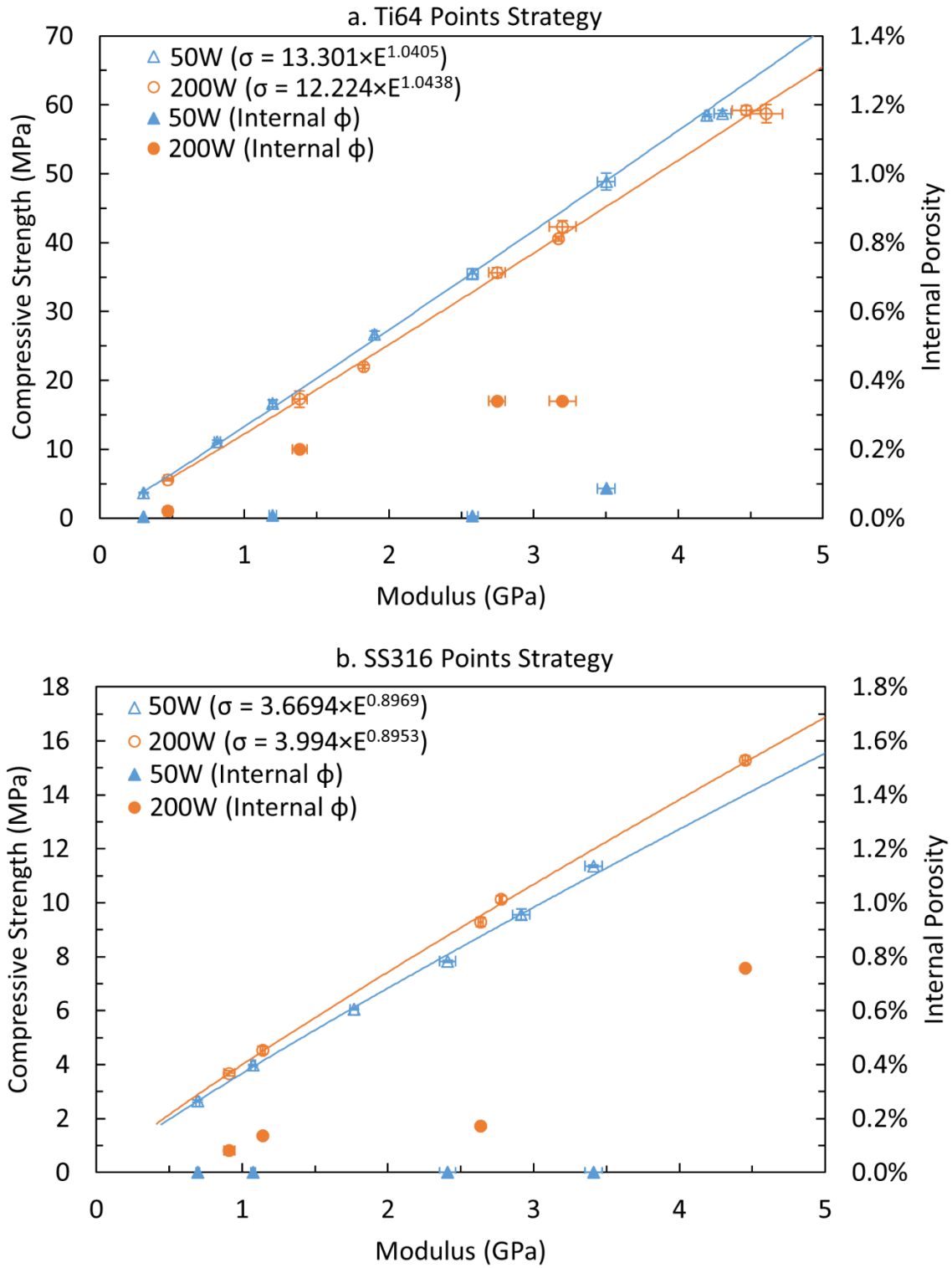


Figure 4.7 – Compressive yield stress & internal porosity (Φ) vs. Modulus Plots for the Points Scan Strategy. For each material, two separate curves/points are seen, one for samples built at 50W and one for samples built at 200W, with increase in strut diameter and thus modulus/density being controlled by an increase in exposure time.

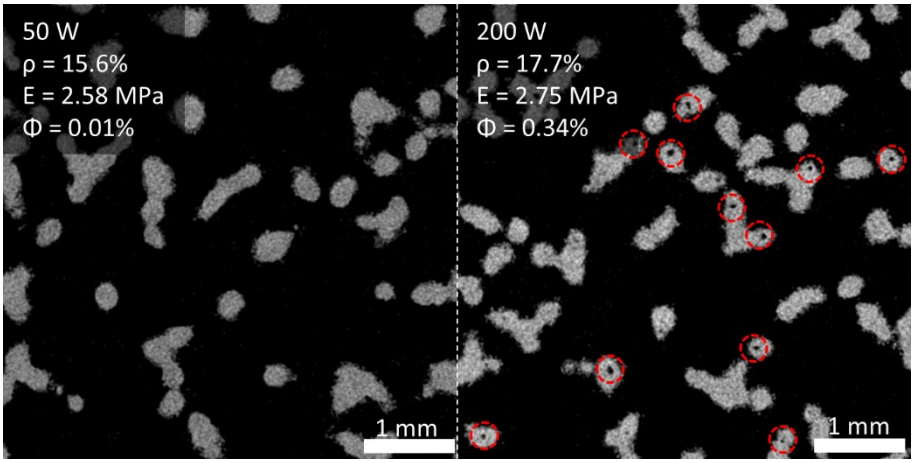


Figure 4.8 – Micro-CT slices of Ti64 stochastic porous structures built via the Points Strategy at Laser Powers of 50 W and 200 W. For a given Modulus (E) and Density (ρ), greater Internal Porosity (Φ) is observed (circled in red) in samples built at 200 W for both Ti64 and SS316.

Selecting the optimum laser power for each strategy in terms of strength (i.e. samples built at 50 W for Ti64 and samples built at 200 W for SS316) and plotting the compressive yield strength vs. modulus; it was found that at low stiffness (<1.5 GPa) the σ_y:E ratio is similar for all three strategies but as stiffness increases the contour strategy produces samples with the highest σ_y:E ratio, then the points strategy then the pulsing strategy(Figure 4.9). For Ti64 the contour strategy produced structures with a greater strength for a given modulus, on average 5.2±1.4% greater than the points strategy and 6.9±1.5% greater than the pulsing strategy. In SS316 the contour strategy produced structures with a greater strength for a given modulus on average 2.9±1.7% greater than the points strategy and 4.8±1.7% greater than the pulsing strategy. For both materials the difference between the contour and other strategies increases with increasing modulus. No discernible variation in internal porosity was observed between samples built via the points and contour strategy for either material, however the pulsing strategy had significantly more porosity than the other scanning strategies in both Ti64 and SS316.

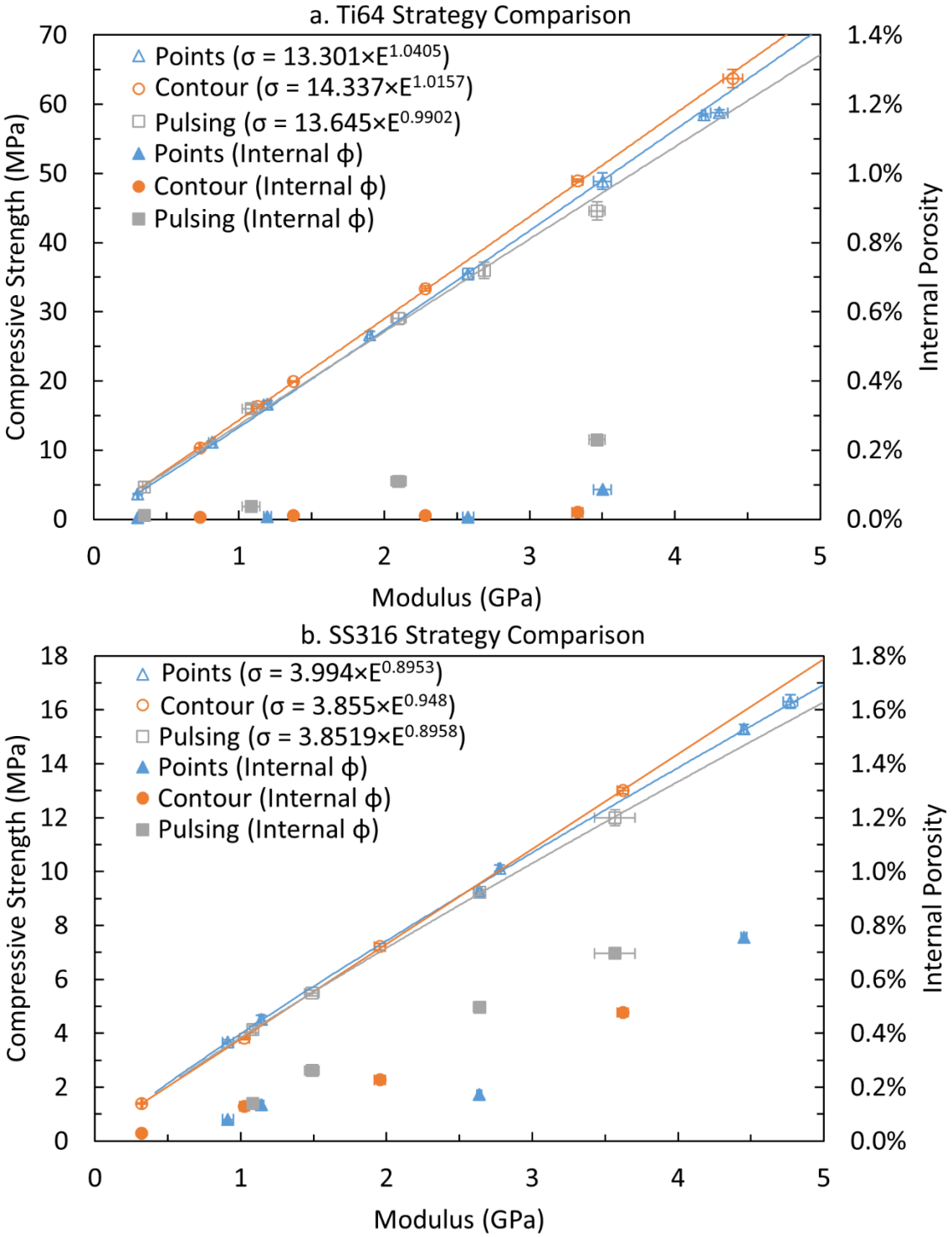


Figure 4.9 – Scan Strategy Comparisons on Compressive Strength & Internal Porosity (Φ) vs Modulus Plots. At low modulus values scan strategy did not affect the σ_y:E ratio, but as modulus increases the contour strategy produced samples with the highest σ_y:E ratio.

Build time was found to vary linearly with relative density and modulus for all scanning strategies. The points strategy offered the fastest build time, double the speed of the Pulsing strategy and 20% faster than the contour strategy.

4.2.3 Effect of Laser Parameters and Scanning Strategies on High Cycle Fatigue Strength

All Ti64 specimens fatigue tested in this work exhibited 3 stage fatigue failure behaviour, regardless of laser parameter or scan strategy used during the manufacturing process (Figure 4.10). For all specimens, angled crush bands (fracture planes), characteristic of porous structures [10, 11], were observed; likely following the weakest planes of the stochastic porous structure. Extensive cracking and fracture was observed at or near nodes and plastic deformation of struts was not evident (Figure 4.11). Regardless of laser parameters or scanning strategies used, no differences were observed in failure modes.

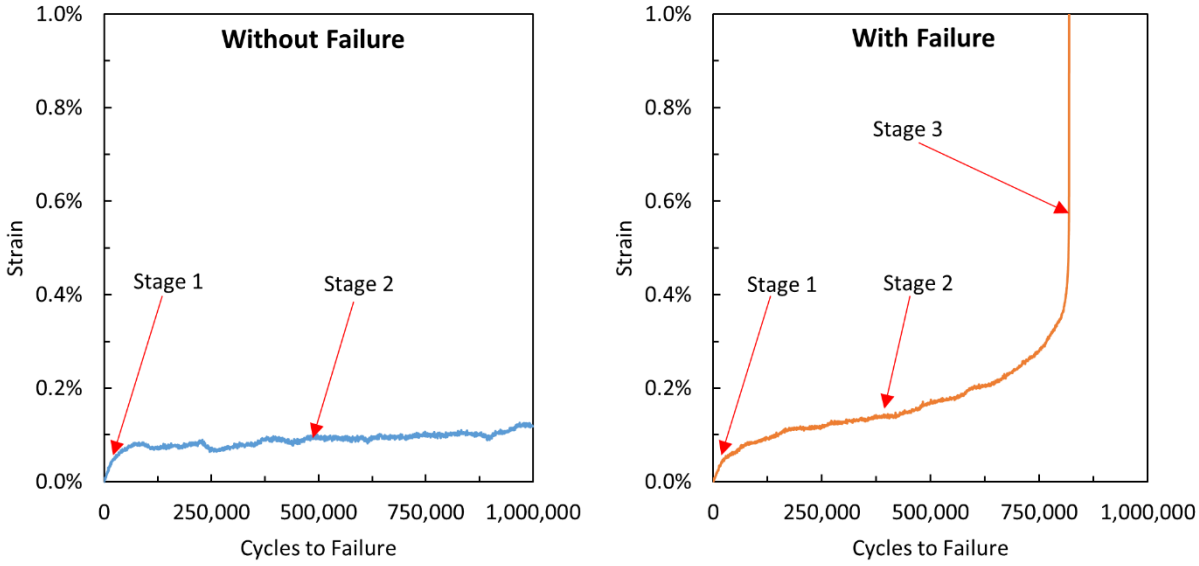


Figure 4.10 – Typical Compressive Strain vs. Cycles-to-Failure Curves for specimens without (left) and with (right) failure.

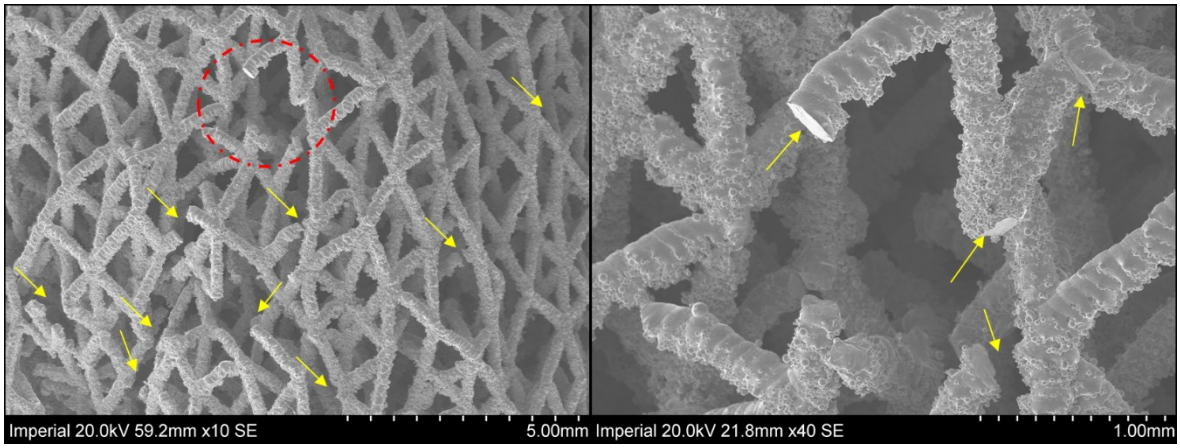


Figure 4.11 – SEM Images of a fatigue failed Ti64 specimen. Extensive cracking and fracture was observed at or near nodes, as indicated by arrows. Plastic deformation of struts is not evident. Higher magnification of the circled area is also seen. Build direction for both images is vertical.

Ti64 samples built at 50W exhibited a higher fatigue strength at 10^6 cycles than those built at 200W by 7.0±0.2% (Figure 4.12 and Table 4.6). As per [11], a power-law trend is modelled between fatigue strength and modulus for both laser powers. This will be discussed in greater detail in Section 5.3.2. To explore the effect of scan strategy on fatigue strength, samples were built in Ti64, all with a 50W laser power, as this produced structures with the greatest fatigue strength (Figure 4.12a). The contour strategy produced specimens with the greatest fatigue strength at 10^6 cycles for a given stiffness, 8.4±2.4% greater than the points or pulsed strategy (Figure 4.12b and Table 4.6). No significant difference was observed between the points and pulsed strategy. A power-law trend is again modelled between fatigue strength at 10^6 cycles and modulus regardless of scan strategy used.

Table 4.6 – Effect of Laser Parameters and Scan Strategy on the Mechanical Properties of a Ti64 Stochastic Structure (Values are mean ± S.D.)

Specimen	Modulus (GPa)	Yield Strength (MPa)	Fatigue Strength (MPa)	Relative Density	Internal Porosity
Points (50W)	0.3±0.0	3.6±0.1	0.5±0.1	9%	0.00%
	1.2±0.0	16.4±0.3	2.5±0.2	12%	0.01%
	2.6±0.0	35.4±0.8	5.3±0.5	18%	0.01%
	3.5±0.1	48.3±1.7	7.2±0.7	21%	0.09%
Points (200W)	0.5±0.0	5.5±0.2	0.8±0.1	10%	0.02%
	1.4±0.1	17.0±1.3	2.5±0.2	15%	0.2%
	2.7±0.1	35.5±0.7	5.3±0.5	18%	0.34%
	3.2±0.1	42.1±0.9	6.3±0.6	20%	0.34%
Contour (50W)	0.7±0.0	10.2±0.1	1.5±0.1	10%	0.01%
	1.4±0.0	19.8±0.1	3.0±0.3	12%	0.01%
	2.3±0.0	32.8±0.3	4.9±0.5	16%	0.01%
	3.3±0.0	48.5±0.3	7.3±0.7	20%	0.02%
Pulsing (50W)	0.3±0.0	4.6±0.1	0.6±0.1	8%	0.01%
	1.1±0.1	15.9±0.6	3.2±0.2	12%	0.01%
	2.1±0.0	28.6±1.0	4.3±0.4	18%	0.11%
	3.5±0.1	41.3±2.6	7.2±0.6	27%	0.23%

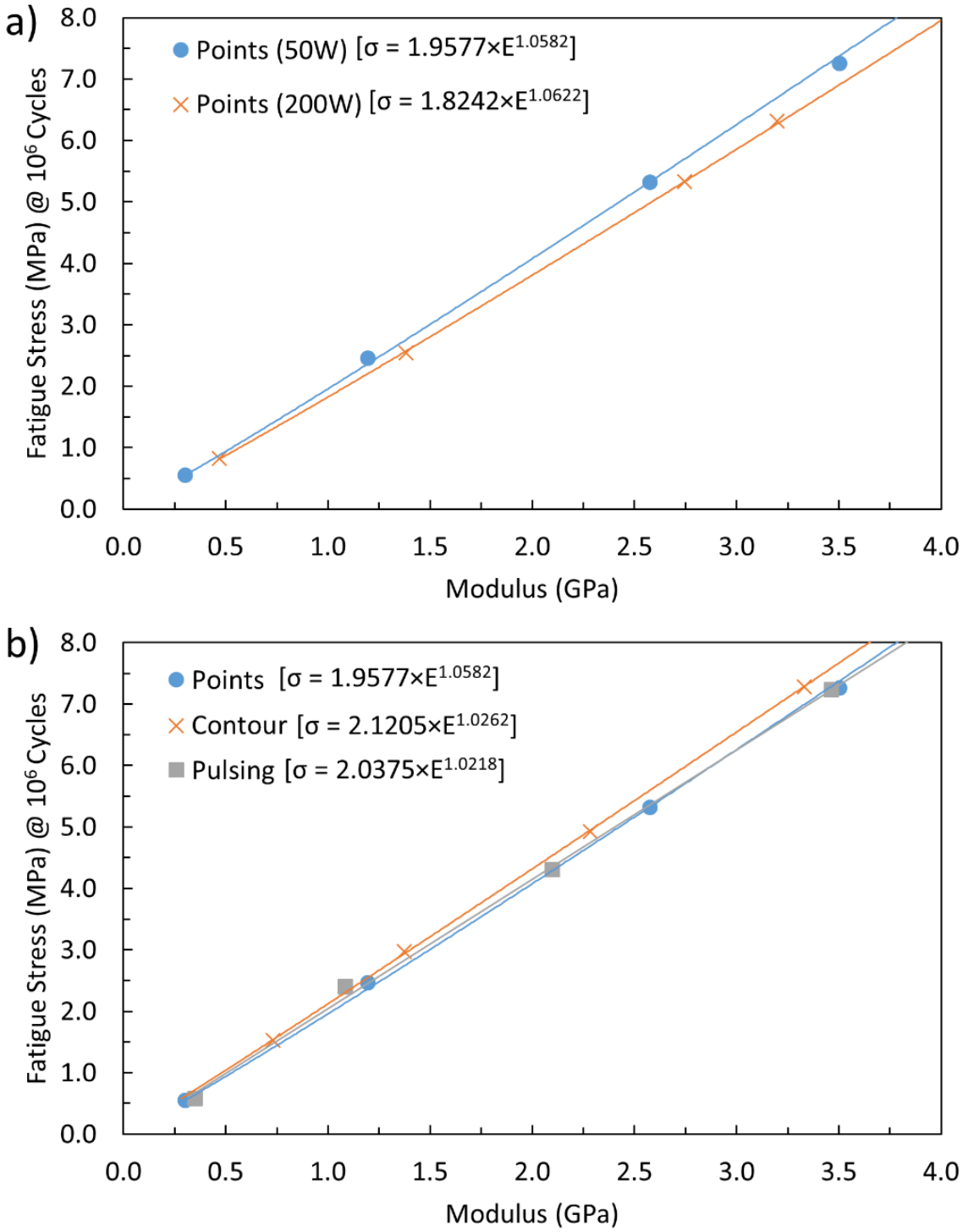


Figure 4.12 – Effect of Laser Parameters (a) and Scanning Strategy (b) on High Cycle Fatigue Strength (10^6 Cycles) for Ti6Al4V ELI. R^2 values for all curve fits were 0.99. For clarity error bars are not shown, however standard deviations for all values are given in Table 4.6.

4.2.4 Effect of Laser Parameters and Scanning Strategies on Microstructure

Differences in mechanical properties, namely strength:stiffness and fatigue strength:stiffness as well as differences in internal porosity have been observed for stochastic porous specimens produced by different laser parameters and scanning strategies. A cause for

strength:stiffness and fatigue strength:stiffness ratios changing between test variables may be due changes in microstructure. Microstructure was observed by optical microscopy and SEM, with all specimens analysed having similar moduli (3.2 - 3.5 GPa) and relative density but built with different laser parameters and scanning strategies (Appendix B). All specimens exhibited semi-sintered particles on strut surfaces, texture lines between build-layers and/or melt-pools and microstructural heterogeneity (Figure 4.13, Figure 4.14 and Figure 4.15). The microstructure of all specimens was also typical of as-built LPBF Ti64. Specimens exhibited acicular (needle like) α' grains in larger prior β grains, with the α' martensitic needles generally observed to be inclined at about 40° with respect to the build direction. For the optical microscopy, the etchant used causes the alpha phase (α') of titanium to appear white, whilst inter-granular beta structure and beta grains will be darkened (Figure 4.13 and Figure 4.14). The microstructure appears to be different with both laser parameter and scanning strategy used, as well as strut angle and nodal connectivity for sections parallel and perpendicular to the build direction. The most evident difference in the microstructure images is differences in texture. Specimens built at low power appear to have a much stronger texture than those built at high power, with the low power specimens exhibiting columnar prior β grains through the build height, which grow epitaxially through successive layers along the build direction (Figure 4.13) whilst high power specimens exhibit more equaixed prior β grains. The grains of the high power structure also appear to be in groups with more randomised orientation. Equiaxed prior β grains are seen in sections parallel to the build plate (Figure 4.14).

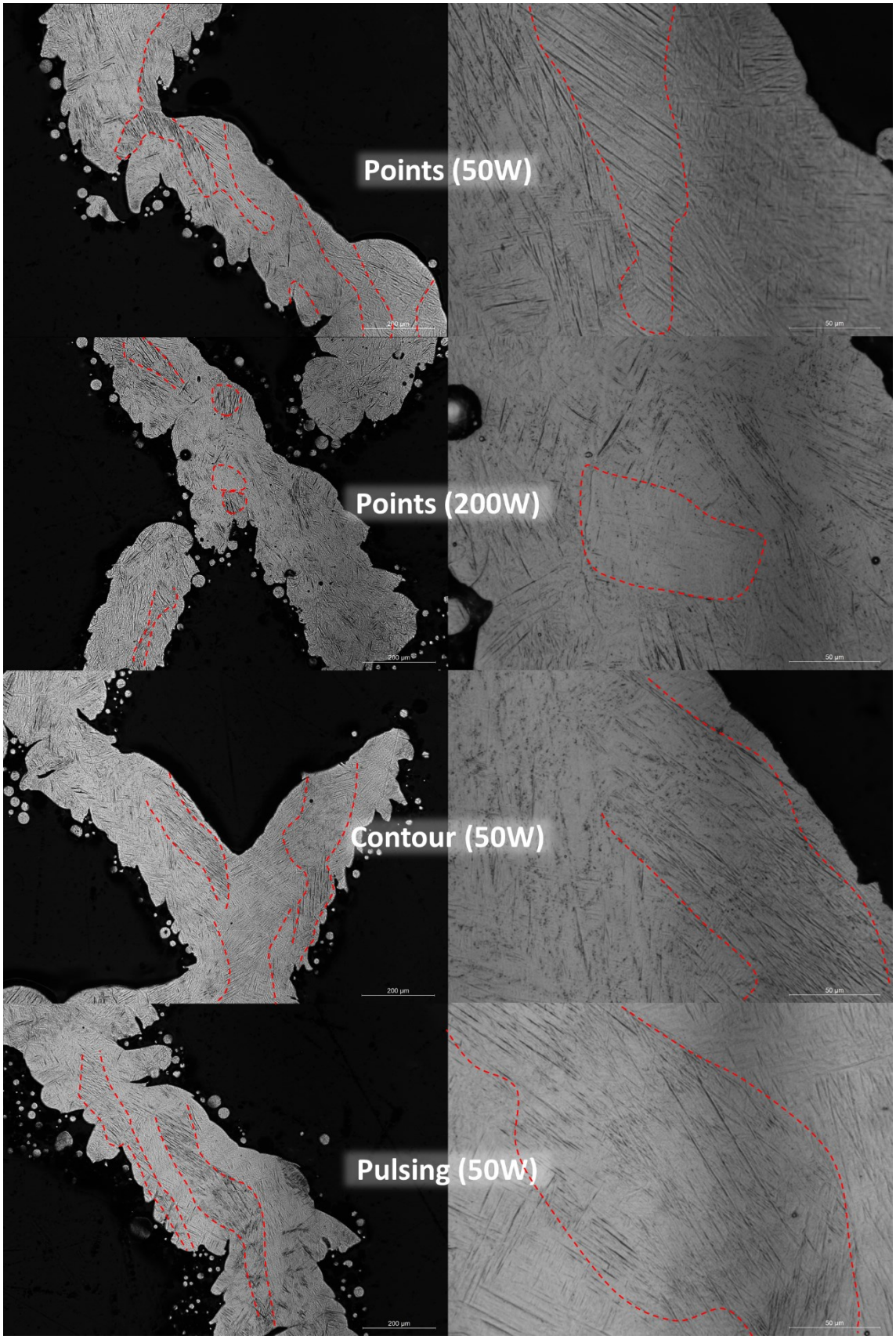


Figure 4.13 – Microstructure of Ti64 specimens at varying laser parameters and scanning strategies parallel to build direction. Typical prior β grains indicated (Build direction is vertical in all images).

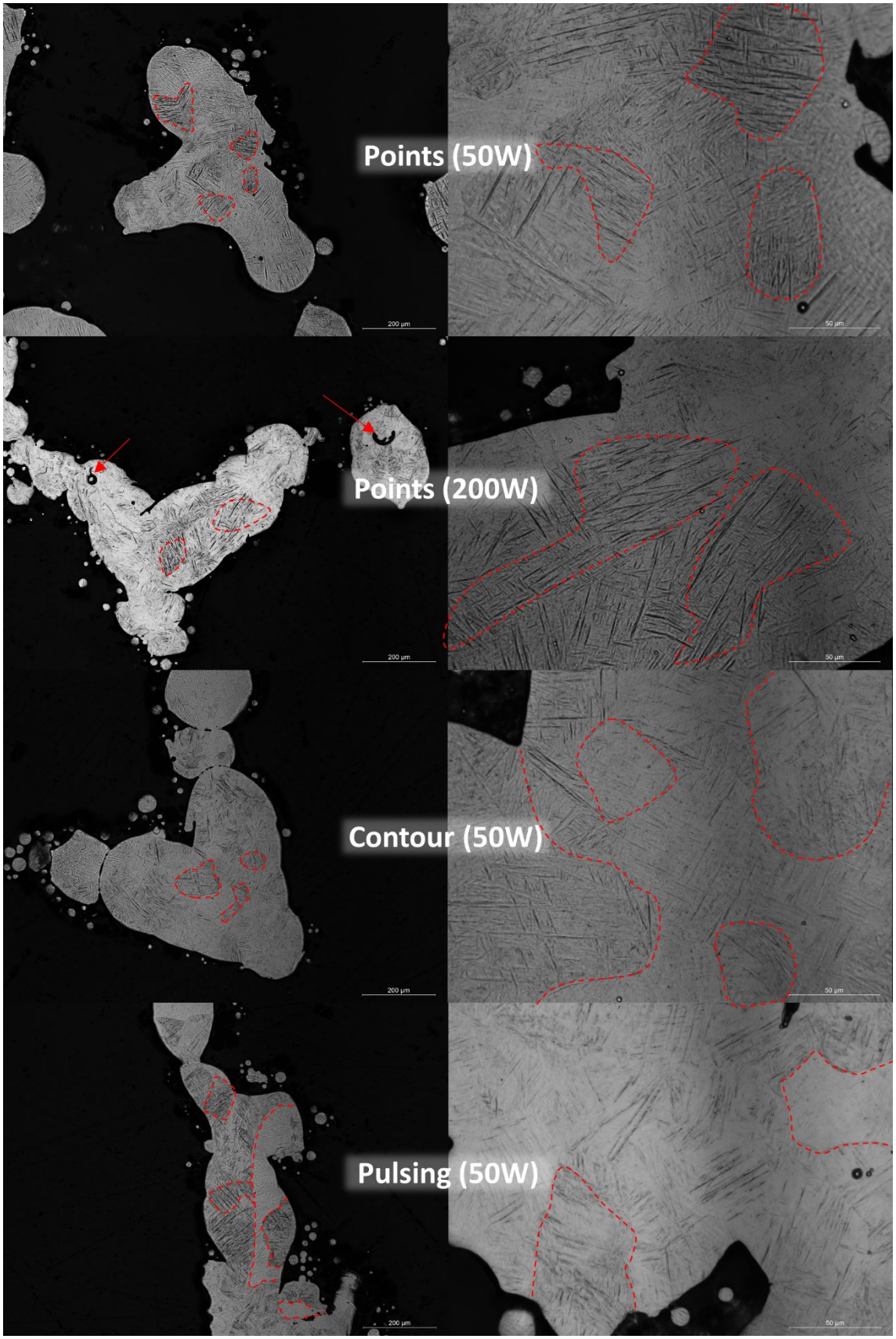


Figure 4.14 – Microstructure of Ti64 specimens at varying laser parameters and scanning strategies perpendicular to build direction. Typical prior β grains indicated, pores arrowed.

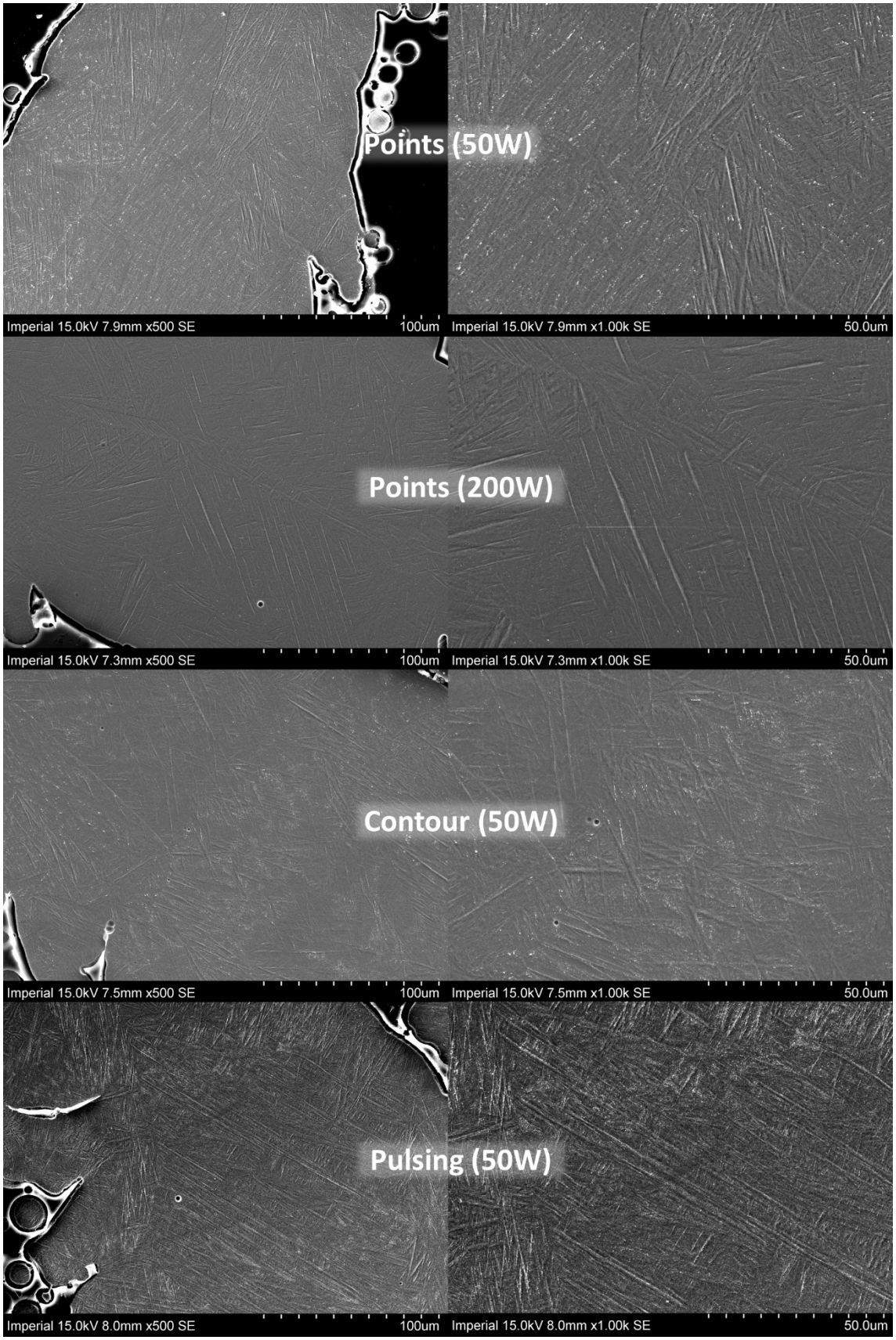


Figure 4.15 – SEM Microstructure of Ti64 specimens at varying laser parameters and scanning strategies parallel to build direction (Build direction is vertical in all images).

The challenge in analysing metallurgical slices of stochastic structures is that often it is difficult to analyse the exact same section of the structure and make conclusions regarding differences in grain size, grain morphology, texture etc. Therefore EBSD was performed on single struts to see whether the microstructural differences observed in the optical and SEM images would also be found by EBSD. The EBSD specimen contained single struts of ~10mm tall spaced 1mm apart. The laser parameters were identical to those used for the microstructure analysis of the stochastic porous structure, i.e. laser parameters and scanning strategies that produced structures with a similar modulus (3.2 - 3.5 GPa) and relative density (Appendix B). Specimens were ground and polished back to the centre of a single strut as described in 3.4.1 and imaged by SEM and EBSD. A portion at the midpoint of the struts height was analysed (Figure 4.16).

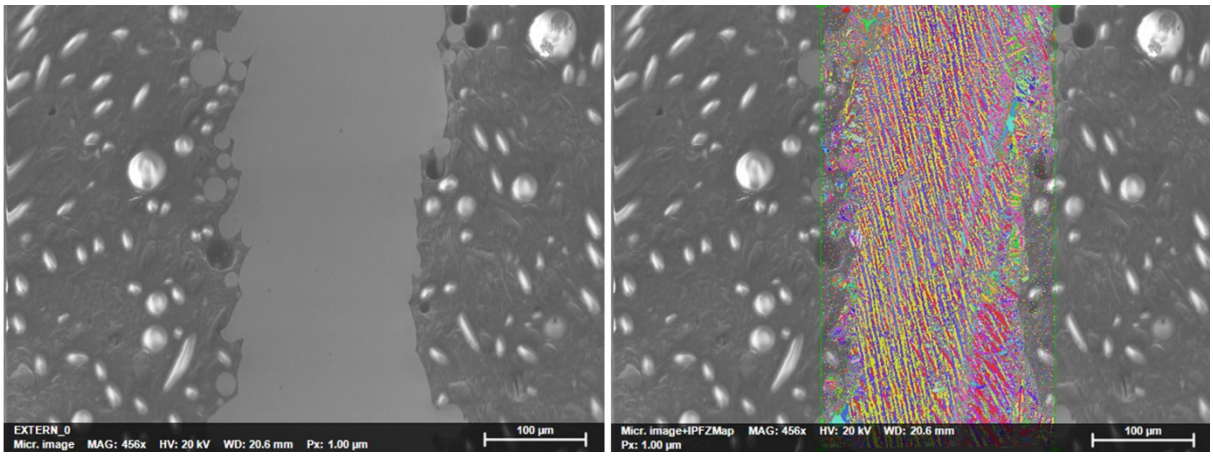


Figure 4.16 – SEM image of a single strut (left) and with an EBSD crystal orientation map overlaid (right)

The EBSD inverse pole figures (Figure 4.17) confirm the findings from the optical imaging. It is shown that there are clear differences in texture depending on the laser parameters and scan strategy used. High laser powers (Points 200 W) result in weak textures whereas the low laser power (Points, Contour and Pulsing 50 W) results in elongated columnar prior β grains and stronger textures. The pulsing scan strategy results in the strongest textured specimen as evidenced by the greater uniformity of colour in the inverse pole figure (Figure 4.17). This is to be expected due to the repeated directional melting and solidification. The contour strategy produced specimens with 2nd strongest texture followed by the points strategy. This is also highlighted by the pole figures (Figure 4.18) where the weaker the texture the more of the pole figure will be coloured in whereas stronger textures are characterised by fewer concentrations of crystal orientations

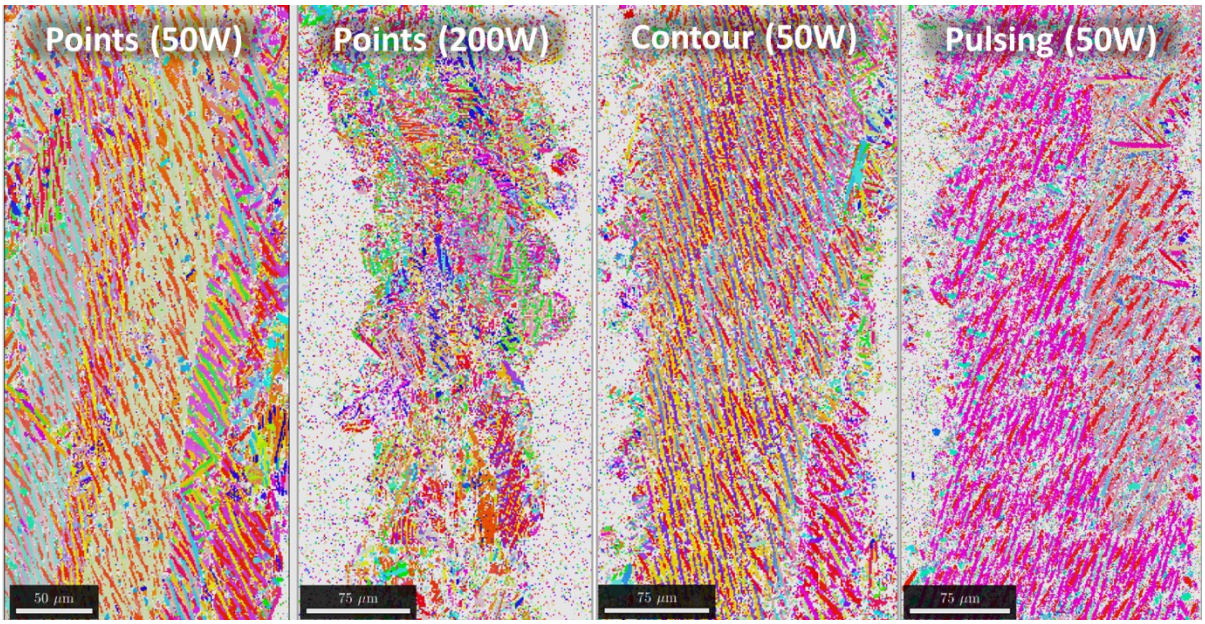


Figure 4.17 – EBSD orientation maps (inverse pole figures) of Ti64 specimens at varying laser parameters and scanning strategies parallel to build direction. (Build Direction is vertical in all images). Columnar grains are seen for all 50 W specimens. Greater uniformity of colors reflects stronger texture whereas the 200 W sample is characterised by a greater variety of colour and grains in many orientations. Refer to Figure 4.19 for crystal orientation colour reference

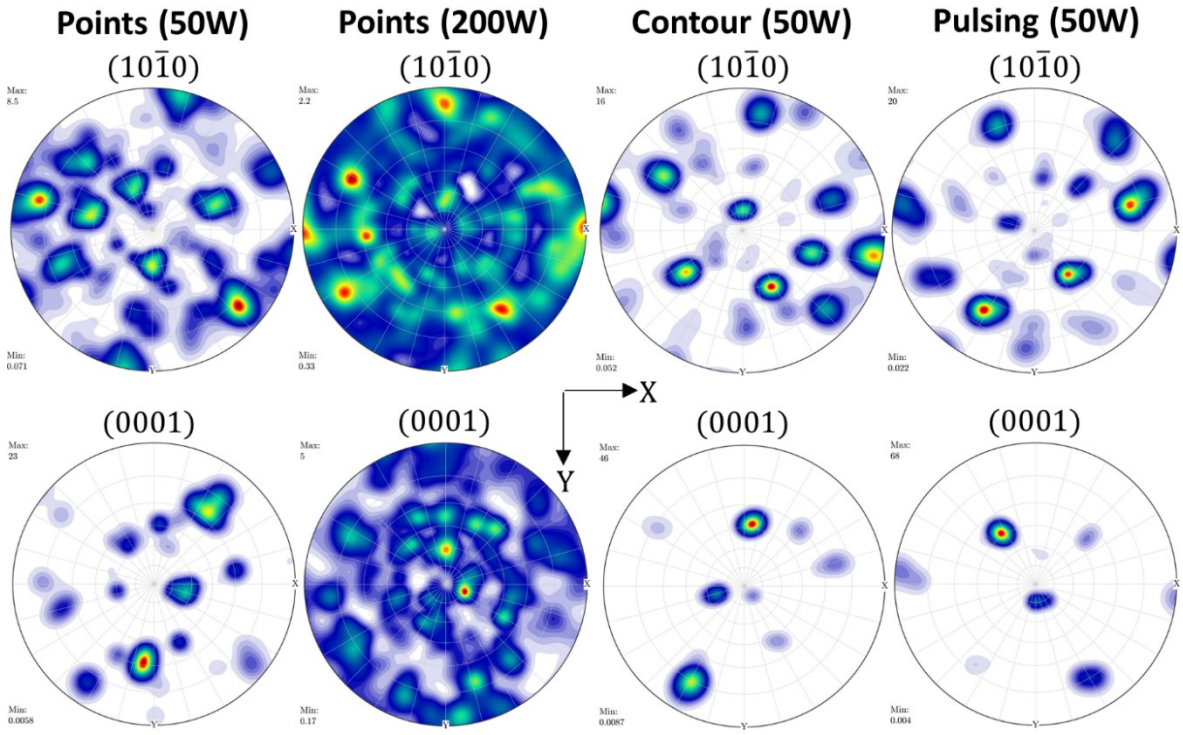


Figure 4.18 – EBSD Pole figures for Ti64 specimens at varying laser parameters and scanning strategies parallel to build direction.

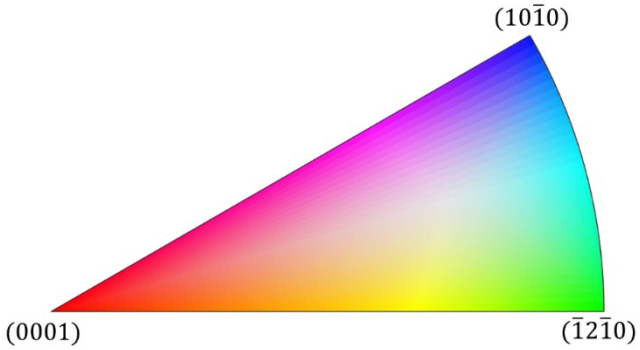


Figure 4.19 – Colour Code representing the crystal orientation for titanium

Grain size, grain morphology (aspect ratio and shape factor), grain angle and quantity of phases present varied depending on laser power or scan strategy used. Indicating that for a given strut thickness, or structure modulus/relative density altering the thermal history of the melt pool or part results in changes in microstructure for porous structures. However, as the EBSD imaging had a relatively low hit rate (on average ~80%), phase maps, grain images, grain size, grain angle and gain aspect ratio measurements are only presented in Appendix C due to lack of confidence. Furthermore both a larger area would have to be analysed as well as validating EBSD pixel size to be confident grain size measurements are accurate and statistically reflected the entire sample. Further development of sample preparation, polishing and EBSD analysis is therefore required for porous specimens to get more complete microstructure data.

4.3 Discussion

4.3.1 Optimisation of the mechanical properties of architectured structures

This study demonstrates how build strategy and laser parameters affect mechanical properties of an AM architectured structure for a given stiffness or relative density. The optimum rate of energy delivered to the melt-pool for maximising strength for a given stiffness was found to be material dependent. Structures built in Titanium (Ti6Al4V ELI), were 10% stronger when built at low power (50W) than at high power (200W); the opposite trend was seen for structures built in Stainless Steel (SS316L). This was found for all scan strategies. When the optimum rate of energy delivery was selected for each scan strategy, it was found that as stiffness increased the Contour Strategy produced samples with the highest σ_y:E ratio, then the Points Strategy then Pulsing.

The mechanical properties and behaviour of the stochastic material was as expected. Strength (σ) increased with relative density (ρ) by a power law, as described by Gibson and Ashby (Equation 4.1) [8, 9]. This relationship has been found to be true for AM structures by a number of authors [12, 13].

$$\frac{\sigma}{\sigma_0} = C_1 \left(\frac{\rho}{\rho_0}\right)^n \qquad \text{Equation 4.1}$$

They also found modulus (E) to increase with relative density by a power law (Equation 4.2)

$$\frac{E}{E_0} = C_2 \left(\frac{\rho}{\rho_0}\right)^m \qquad \text{Equation 4.2}$$

Where σ_0, ρ_0 *and* E_0 are the properties of the base material (i.e. solid titanium or stainless steel) and C, m and n are constants found experimentally. It is important to note these equations are only accurate to a relative density of 0.3 [9]. The power-laws described by Equation 4.1 and Equation 4.2 were also found to accurately model the relationship between strength and relative density and between modulus and relative density for the stochastic porous structures produced in this research as seen in Appendix B. Interestingly the values of m and n were seen to be very close to each other and consequently when Equation 4.2 is substituted into Equation 4.1 for relative density, a relationship between strength and stiffness is obtained, as seen in Equation 4.3. This is the same relationship as the trend lines seen in Figure 4.7 and Figure 4.9. As the values for n and m are very close, the exponent of n/m is very near to 1 which is why the trend lines seen in Figure 4.7 and Figure 4.9 appear linear.

$$\frac{\sigma}{\sigma_0} = C_1\left(\frac{E}{C_2 E_0}\right)^{\frac{n}{m}} = C_3\left(\frac{E}{E_0}\right)^{\frac{n}{m}} \qquad \text{Equation 4.3}$$

Brittle failure was seen for structures built in Ti64, whilst a ductile failure mechanism was observed for the Stainless Steel specimens tested in this study (Figure 4.5 and Figure 4.6). The titanium structures had far superior strength for a given stiffness (approx. 2x) compared to the stainless steel structures. The Ti64 structures are also in the range of strength of cancellous bone for the same stiffness [14] which is highly encouraging for their adoption in new orthopaedic devices.

4.3.2 Effect of laser parameters and scanning strategies on material properties

This study highlights that the strength of AM architectured materials is a factor of many variables, including, structure relative density , internal porosity, microstructure, quality of the strut junctions, strut thickness, weld-neck thickness and surface finish [2, 9]. Figure 4.7 and Figure 4.9 illustrates that as structure modulus and relative density increases, due to an increase in specific enthalpy (struts getting thicker), so does the internal porosity. This is corroborated in literature, as researchers have shown that for changing a single laser parameter (i.e. power, scanning speed etc.) whilst keeping all others constant results in a curve for internal porosity with three distinct regions: a decreasing negative gradient region, a minimum (zero gradient) region and an increasing positive gradient region. At low enthalpies (negative gradient region) there is insufficient energy/heat to cause full melting of the powder particles and there is a lack of melt-pool overlap resulting in porosity. As enthalpy or laser energy increases (going from the minimum region to positive gradient region) eventually excessive heat and energy will cause increasing porosity due to excess evaporation and ablation of powder, denudation zones, keyhole porosity and a volatile turbulent melt-pool which results in splashing of molten material [3, 6, 15]. Only the minimum region and positive gradient region of the internal porosity curves were observed in Figure 4.7 and Figure 4.9. This was because unlike for AM solids, if there was not enough energy to cause full melting of the powder particles, a porous AM structure would not successfully build for the scanning strategies, laser parameters and strut thicknesses explored in this research (Figure 4.1).

For a given structural modulus, differences were observed in internal porosity depending on the laser power and scan strategy used. Maintaining a constant enthalpy whilst changing the laser parameters or scan strategy does not result in a constant internal porosity (Figure 4.8). This was also found to be true for solid Ti64 [6] and SS316 [16] parts, where researchers varied the laser power and scanning speeds whilst maintaining a constant enthalpy; which resulted in

variations in internal porosity. This is likely due to melt-pool turbulence and volatility not being constant with the quantity of energy delivered but varying with the rate and manner with which energy is delivered by the laser to the melt-pool. [3, 17]

Figure 4.7 and Figure 4.9 also highlight that in quasi-static compression testing of porous architectured materials, internal porosity in struts was not solely responsible for variations in strength between samples built at different powers or with different strategies. Changes in the laser parameters and scan strategy used during manufacture affects the thermal history of the melt-pool and therefore the microstructure of the material [17]. This was initially thought to be seen in the microstructure images (Figure 4.13, Figure 4.14 and Figure 4.15) and consequently confirmed by EBSD (Figure 4.17), where distinct differences in texture and likely grain characteristics (size/morphology/angle) and quantity of phases present were seen depending on laser parameter and scanning strategy used. Thermal strain hardening may also be present, particularly for SS316. The same is seen in literature for both solid [5, 18, 19] and porous [3] AM materials, where changing the laser parameters and scanning strategies resulted in changes in microstructure and consequently changes in strength. Farshidianfar et al. [20] built SS316 samples with constant energy density (Equation 2.1) but different laser parameters via blown-powder laser AM. Between samples, they observed variations in peak and average melt-pool temperatures, time spent at peak temperature and cooling rates during solidification and subsequently different microstructures were seen in each sample. Li et al [19] compared pulsed versus continuous build strategies and found that the pulsed-wave strategy had double the cooling rate which resulted in finer columnar microstructure when compared to the continuous-wave strategy. Furthermore, there is a breadth of AM research establishing the effect of the microstructure obtained after processing on the mechanical properties of AM parts [17].

In this study, structures with a given modulus but built by different laser parameters or scanning strategies had differences in strength caused by a combination of variations in internal porosity and microstructure. Brittle materials (Ti64) were likely more sensitive to internal porosity than ductile materials (SS316). The grain size, grain morphology, quantity of phases and texture will all contribute to a materials strength as they will affect how cracks propagate and thus alteration to the microstructural characteristics will result in changes in strength. For both materials at a given modulus or enthalpy, samples built at 50 W, had lower internal porosity, due to less melt-pool turbulence and volatility, than those built at 200 W [3, 17]. Whilst this translated to samples built at 50 W having greater strength in Ti64, it was not the case in SS316. The greater strength of specimens built at 200 W versus 50 W in SS316 would

therefore be driven by differences in microstructure rather than by internal porosity. The opposing trends observed for Ti64 and SS316 (Figure 4.7) with respect to optimum laser power, can also be attributed to differences in the absorbtivity, melting point, boiling point, thermal conductivity and density of the materials with respect to melt-pool thermal history and grain and phase structure development. Particularly Ti64's lower density, lower thermal conductivity and higher absorptivity means titanium absorbs more laser energy in a given time whilst the melt-pool heat conducts away slower when compared to stainless steel.

There was no discernible variation in internal porosity between samples built via the Points and Contour strategy for either material, however the Pulsing strategy had significantly more porosity than the other scanning strategies. SEM and micro-CT imaging did not reveal any large differences in surface finish or quality of strut junctions between strategies. Therefore, the greater strength of specimens built by the Contour strategy at higher stiffness or relative density can be attributed to variations in microstructure (texture, grain size, grain morphology, grain angle, quantity of phases present etc.). It has also been seen for solid AM parts that scanning strategy affects the thermal history of the melt-pool which consequently alters microstructure and strength [17-19].

As stated earlier, at low stiffness or minimum to very thin strut thicknesses, no variation was observed between the strength of the porous structures manufactured by the 3 scan strategies. This can be attributed to a change in failure mechanics and low effective or specific metal strength of the structure [2, 3]. This is because at very thin strut thicknesses there exists very small weld-necks between melt-pools (Figure 4.2) and poor quality strut junctions and there is premature failure due to these defects and therefore the differences in strength due to microstructure or porosity are not as visible.

4.3.3 Effect of Laser Parameters and Scanning Strategies on High Cycle Fatigue Strength

The mechanisms of how laser parameters and scanning strategies affect the microstructure and internal porosity of AM materials are becoming more established. Changing cooling rates of the melt-pool depending on laser interaction as well as the cyclic thermal history will affect microstructure. Insufficient energy or volatility and turbulence due to excessive energy in the melt-pool is one of the main drivers of internal porosity [20-26]. The effect of microstructure, internal porosity and surface finish (i.e. crack initiation sites) on fatigue is also well understood [27-30].

Statically it was seen that that for Ti64, specimens built at a low power (50W) exhibited higher strength than those built at a high power (200W) for a given stiffness by approximately 10% [26]. This difference was attributed to reduced internal porosity for the 50W samples and differences in microstructure. This has also been seen in other studies, where solid samples were built at low and high laser powers which resulted in changes in average grain size, grain size distribution and microstructural texture and consequently differences in static mechanical properties were observed [21]. This study demonstrates that the laser parameters also affect the high cycle fatigue strength of AM porous structures. The Ti64 samples built at 50W exhibited a higher fatigue strength at 10^6 cycles than those built at 200W by 7% (Figure 4.12). This can be attributed to a reduction in internal porosity for the 50W specimens [29] and differences in microstructure (Figure 4.17 and Figure 4.18) [30]. It was initially hypothesised that the static strength differences between the low and high power samples would be exacerbated in fatigue [26], however this was not the case. As no observable differences were seen between the surface finish of specimens built with a low or high power specimens, and they were both characterised by an abundance of semi-sintered particles and texture lines between build-layers (Figure 4.2), it is likely that porous AM Ti64's high sensitivity to defects and brittle nature [10, 31] makes it more sensitive to surface crack initiation than internal porosity [27, 29].

When investigating the effect of scan strategy on a porous structure's static strength-to-stiffness ratio, it was seen that building with a contour strategy produced structures with the greatest strength for a given stiffness (Figure 4.12), when compared to the points and pulsing strategies [26], and this remains true during high cycle fatigue testing. As with the laser power investigation, these differences can be attributed to reduced internal porosity for the contour strategy and microstructural differences [29]. There was possibly also some minor structural differences between structures built via different scan strategies, such as quality of strut junctions, weld-neck thickness and surface finish/roughness however they were not discernible. It has been seen that the method and rate of energy delivery when building AM parts affects microstructure and consequently mechanical properties [3, 5, 26], however this work has been exclusively done on solid parts and specimens were only tested statically. This work represents the start of research on the effect of different as-built microstructures caused by altering the laser parameters on fatigue strength for AM specimens.

4.3.4 Validity of the Specific Enthalpy Model

This study has also shown that strut thickness in a porous structure can be driven by laser energy alone, and the specific enthalpy model provides a good relationship for strut thickness.

This means that a single line-based geometrical definition of a part can be assigned different thickness, stiffness, strength or density by building it with the appropriate laser parameters. Indeed, this approach allows for gradients of properties throughout the same single line-based part simply by changing the laser parameters throughout the part. This is important as the future of architectured material generation is likely to move from solid CAD modelling to line based representations. It is particularly relevant in the orthopaedic field where stiffness gradients are common throughout the human skeleton.

Increasing specific enthalpy resulted in increases in strut thickness. It was seen that strut thickness varies linearly with specific enthalpy regardless of material, scanning strategy and build angle and that the model is accurate to ±50μm over a large range of strut thicknesses. These findings are consistent with what other researchers have found for single track experiments [32, 33] and thus provides more evidence to the validity of using the enthalpy model for predicting melt-pool or strut size. It was seen that as enthalpy increases, struts became more 'stable,' the weld-neck between melt-pools increased, the strut thickness and the strut angle became more consistent and the number of semi-fused particles on the strut increased as well (Figure 4.1 and Figure 4.2). For a given enthalpy the lower the angle of the strut, the thicker it was (Figure 4.3). This was caused by changing conductivity conditions, for vertical struts every layer is built upon solid material and so much of the heat in the melt-pool gets conducted away, whilst for low angle struts which are built partially on solid material and partially on powder the heat gets conducted away far slower as the powder has a lower conductivity than the solid material, consequently this greater heat in the melt-pool results in thicker struts.

For a given enthalpy, the contour strategy produced struts with a more consistent thickness along the strut as well as a more consistent thickness across all build angles when compared to the points and pulsing strategies. It was expected that the points/pulsing strategy would be able to produce thinner struts than the contour strategy due to their ability to deliver energy to the melt-pool in a smaller area, however no difference was seen. Despite the contour strategy delivering energy over a larger area than the points/pulsing strategy, residual heat in the melt-pool may mean less energy needs to be delivered by the laser to create the same size melt-pool as from the points/pulsing strategy. The other reason why no major difference was seen may be because the melt-pool depth needs to be significantly larger than the slice thickness (50 μm) to successfully build a competent strut and all three strategies were able to deliver the

minimum energy required. If a smaller laser spot, thinner slice thickness and smaller powder size were used an observable difference may have been detected between strategies.

4.3.5 Limitations

It should be noted that the specific enthalpy model is intended to be a simple model to better predict and model the effect of laser parameters on strut thickness or historically melt-pool width. However it has limitations and may not reflect the accuracy of complex FE/CFD models. The model assumes a constant value for absorptivity and thermal diffusivity of the metal, however in reality both these values change with temperature, with applied laser power and with the packing of the powder [34]. Most reported values have been for solid metals and not for powders. Inaccuracies also develop when the melting mode changes from conduction to keyhole [32]. Finally the model doesn't take into account residual heat in the melt-pool i.e. during a small contour scan or during pulsing and thus specific enthalpy values do not translate between scanning strategies.

Whilst specific enthalpy may be accurate for predicting strut thickness or melt-pool track width it may not be the best indicator for internal porosity or microstructure. Varying the laser parameters and scanning strategies whilst maintaining a constant specific enthalpy does not guarantee constant internal porosity or a consistent microstructure. Another limitation of the study was that depending on build angle for a given enthalpy, the points/pulsing strut thicknesses vary by a greater amount than those manufactured by the contour strategy (Figure 4.3). This means the structure will have had slightly different strut thicknesses at different angles for a given stiffness or density depending on what strategy it was built with.

A further limitation was due to a deviation from ISO 13314 [35]. The hysteresis loop which was used to calculate the elastic modulus, was based on a percentage of the estimated yield strength of a preliminary sample rather than the plateau stress. This was due to the brittle nature of the titanium alloy used, meaning titanium samples had a far lower and more varied plateau stress than the stainless steel samples. The resulting hysteresis loop was therefore very early on in the elastic portion of the stress-strain curve and gave a low modulus (modulus varies with the location of the hysteresis loop on the elastic/linear portion of the stress-strain curve). By using the yield strength to calculate the percentages for the hysteresis loop the results between the two materials tested were far more consistent and comparable. The low standard deviations of the results and compliance to theoretical models suggests this was appropriate.

4.4 Summary

- As the future of architectured material generation is likely to move from solid CAD modelling, which is computationally expensive, to line based representation it is imperative to know how laser parameters and scan strategy relate to strut thickness.
- This study showed that using the specific enthalpy equations instead of traditional energy density equations can produce an accurate and scalable model relating strut thickness to the laser parameters.
- This study demonstrated that the mechanical properties of a porous structure produced by powder bed fusion are not only affected by its geometric properties (strut thickness, density, internal porosity etc.) but also by its method of manufacture.
- The method and rate of energy delivery and laser scan strategy had a significant effect on the strength of a stochastic porous structure for a given stiffness or density.
- When optimising laser parameters and scan strategy for a porous structure it was found that the optimum method of energy delivery is material dependent and optimisation of the laser power could improve strength:stiffness by ~8% on average.
- Optimising scan strategy was not material dependent and the contour strategy produced structures with a greater strength:stiffness than the points or pulsing strategy.
- The effect of laser parameters and scan strategy on high cycle fatigue strength of AM porous structures was also explored and quantified.
- Optimisation of the laser parameters was found to increase the fatigue strength for a given stiffness of porous AM structure by 7%.
- Building with a contour strategy produced structures with a greater fatigue strength for a given stiffness by 8%, when compared to the points and pulsing strategies.
- Power-law relationships were observed between yield strength, fatigue strength, relative density and modulus regardless of the laser power or scanning strategy used to manufacture the porous specimens.
- Varying the laser parameters and scanning strategies will result in a change in the microstructure of the material. This was clearly seen as changes in texture, as well as it appearing that grain size, grain morphology, constitution and quantity of phases change as well with laser parameters and scan strategies.

4.5 References

[1] L. Mullen, R.C. Stamp, W.K. Brooks, E. Jones, C.J. Sutcliffe, Selective Laser Melting: A regular unit cell approach for the manufacture of porous, titanium, bone in-growth constructs, suitable for orthopedic applications, Journal of Biomedical Materials Research Part B: Applied Biomaterials 89B(2) (2009) 325-334.

[2] S. Tsopanos, R.A.W. Mines, S. McKown, Y. Shen, W.J. Cantwell, W. Brooks, C.J. Sutcliffe, The Influence of Processing Parameters on the Mechanical Properties of Selectively Laser Melted Stainless Steel Microlattice Structures, Journal of Manufacturing Science and Engineering 132(4) (2010) 041011-041011.

[3] C. Qiu, S. Yue, N.J.E. Adkins, M. Ward, H. Hassanin, P.D. Lee, P.J. Withers, M.M. Attallah, Influence of processing conditions on strut structure and compressive properties of cellular lattice structures fabricated by selective laser melting, Materials Science and Engineering: A 628 (2015) 188-197.

[4] P. Hanzl, M. Zetek, T. Bakša, T. Kroupa, The Influence of Processing Parameters on the Mechanical Properties of SLM Parts, Procedia Engineering 100 (2015) 1405-1413.

[5] W. Xu, M. Brandt, S. Sun, J. Elambasseril, Q. Liu, K. Latham, K. Xia, M. Qian, Additive manufacturing of strong and ductile Ti–6Al–4V by selective laser melting via in situ martensite decomposition, Acta Materialia 85 (2015) 74-84.

[6] H. Gong, K. Rafi, H. Gu, T. Starr, B. Stucker, Analysis of defect generation in Ti–6Al–4V parts made using powder bed fusion additive manufacturing processes, Additive Manufacturing 1–4 (2014) 87-98.

[7] U. Scipioni Bertoli, A.J. Wolfer, M.J. Matthews, J.-P.R. Delplanque, J.M. Schoenung, On the limitations of Volumetric Energy Density as a design parameter for Selective Laser Melting, Materials & Design 113 (2017) 331-340.

[8] M.F. Ashby, The properties of foams and lattices, Philosophical Transactions of the Royal Society A: Mathematical, Physical and Engineering Sciences 364(1838) (2006) 15-30.

[9] L.J. Gibson, Cellular solids : structure and properties, 2nd ed., Cambridge University Press, Cambridge, 1999.

[10] N.W. Hrabe, P. Heinl, B. Flinn, C. Körner, R.K. Bordia, Compression-compression fatigue of selective electron beam melted cellular titanium (Ti-6Al-4V), Journal of Biomedical Materials Research Part B: Applied Biomaterials 99B(2) (2011) 313-320.

[11] McCullough, Fleck, The stress–life fatigue behaviour of aluminium alloy foams, Fatigue & Fracture of Engineering Materials & Structures 23(3) (2000) 199-208.

[12] C. Yan, L. Hao, A. Hussein, P. Young, D. Raymont, Advanced lightweight 316L stainless steel cellular lattice structures fabricated via selective laser melting, Materials & Design 55 (2014) 533-541.

[13] C. Yan, L. Hao, A. Hussein, S.L. Bubb, P. Young, D. Raymont, Evaluation of light-weight AlSi10Mg periodic cellular lattice structures fabricated via direct metal laser sintering, Journal of Materials Processing Technology 214(4) (2014) 856-864.

[14] S.A. Goldstein, The mechanical properties of trabecular bone: Dependence on anatomic location and function, Journal of Biomechanics 20(11–12) (1987) 1055-1061.

[15] H. Gong, K. Rafi, T. Starr, B. Stucker, The Effects of Processing Parameters on Defect Regularity in Ti-6Al-4V Parts Fabricated By Selective Laser Melting and Electron Beam Melting.

[16] C. Kamath, B. El-dasher, G.F. Gallegos, W.E. King, A. Sisto, Density of additively-manufactured, 316L SS parts using laser powder-bed fusion at powers up to 400 W, The International Journal of Advanced Manufacturing Technology 74(1) (2014) 65-78.

[17] S.M. Yusuf, N. Gao, Influence of energy density on metallurgy and properties in metal additive manufacturing, Materials Science and Technology (2017) 1-21.

[18] K.G. Prashanth, S. Scudino, J. Eckert, Defining the tensile properties of Al-12Si parts produced by selective laser melting, Acta Materialia 126 (2017) 25-35.

[19] S. Li, H. Xiao, K. Liu, W. Xiao, Y. Li, X. Han, J. Mazumder, L. Song, Melt-pool motion, temperature variation and dendritic morphology of Inconel 718 during pulsed- and continuous-wave laser additive manufacturing: A comparative study, Materials & Design 119 (2017) 351-360.

[20] M.H. Farshidianfar, A. Khajepour, A.P. Gerlich, Effect of real-time cooling rate on microstructure in Laser Additive Manufacturing, Journal of Materials Processing Technology 231 (2016) 468-478.

[21] X.P. Li, J. Van Humbeeck, J.P. Kruth, Selective laser melting of weak-textured commercially pure titanium with high strength and ductility: A study from laser power perspective, Materials & Design 116 (2017) 352-358.

[22] M.H. Farshidianfar, A. Khajepour, A. Gerlich, Real-time control of microstructure in laser additive manufacturing, The International Journal of Advanced Manufacturing Technology 82(5) (2016) 1173-1186.

[23] N. Hrabe, T. Quinn, Effects of processing on microstructure and mechanical properties of a titanium alloy (Ti–6Al–4V) fabricated using electron beam melting (EBM), Part 2: Energy input, orientation, and location, Materials Science and Engineering: A 573 (2013) 271-277.

[24] H. Attar, S. Ehtemam-Haghighi, D. Kent, X. Wu, M.S. Dargusch, Comparative study of commercially pure titanium produced by laser engineered net shaping, selective laser melting and casting processes, Materials Science and Engineering: A 705 (2017) 385-393.

[25] L. Zhou, T. Yuan, R. Li, J. Tang, G. Wang, K. Guo, Selective laser melting of pure tantalum: Densification, microstructure and mechanical behaviors, Materials Science and Engineering: A 707 (2017) 443-451.

[26] S. Ghouse, S. Babu, R.J. Van Arkel, K. Nai, P.A. Hooper, J.R.T. Jeffers, The Influence of Laser Parameters and Scanning Strategies on the Mechanical Properties of a Stochastic Porous Material, Materials & Design 131 (2017) 498-508.

[27] B. Van Hooreweder, J.-P. Kruth, Advanced fatigue analysis of metal lattice structures produced by Selective Laser Melting, CIRP Annals 66(1) (2017) 221-224.

[28] B. Van Hooreweder, Y. Apers, K. Lietaert, J.-P. Kruth, Improving the fatigue performance of porous metallic biomaterials produced by Selective Laser Melting, Acta Biomaterialia 47 (2017) 193-202.

[29] A. Yadollahi, N. Shamsaei, Additive manufacturing of fatigue resistant materials: Challenges and opportunities, International Journal of Fatigue 98 (2017) 14-31.

[30] M. Niinomi, Fatigue characteristics of metallic biomaterials, International Journal of Fatigue 29(6) (2007) 992-1000.

[31] S.M. Ahmadi, R. Hedayati, Y. Li, K. Lietaert, N. Tümer, A. Fatemi, C.D. Rans, B. Pouran, H. Weinans, A.A. Zadpoor, Fatigue performance of additively manufactured meta-biomaterials: The effects of topology and material type, Acta Biomaterialia 65 (2018) 292-304.

[32] W.E. King, H.D. Barth, V.M. Castillo, G.F. Gallegos, J.W. Gibbs, D.E. Hahn, C. Kamath, A.M. Rubenchik, Observation of keyhole-mode laser melting in laser powder-bed fusion additive manufacturing, Journal of Materials Processing Technology 214(12) (2014) 2915-2925.

[33] D.B. Hann, J. Iammi, J. Folkes, A simple methodology for predicting laser-weld properties from material and laser parameters, Journal of Physics D: Applied Physics 44(44) (2011) 445401.

[34] J. Trapp, A.M. Rubenchik, G. Guss, M.J. Matthews, In situ absorptivity measurements of metallic powders during laser powder-bed fusion additive manufacturing, Applied Materials Today 9 (2017) 341-349.

[35] ISO13314, Mechanical testing of metals. Ductility testing. Compression test for porous and cellular metals, 2011.

5 Chapter 5 – Influence of Material on the Static and High Cycle Fatigue Strength of a Stochastic Porous Structure

Maximising strength of additively manufactured (AM) porous metals at low stiffness remains a challenge for engineers, particularly in applications under high cyclic loads [1-3]. As stated earlier, in orthopaedics bone repair and regeneration can be driven by strain response with respect to load [4-6]. Therefore, to accelerate bone regeneration, a porous scaffold or porous coating on an implant should have a stiffness similar to or less than the bone that is being replaced. The porous structure must then not only have maximum strength, but more importantly, maximum fatigue strength as it is constantly under varying loads. Selection of different base materials provides an opportunity to maximise the static and fatigue strength of AM porous structures.

It has been stated that the fatigue behaviour of AM porous biomaterials is both quantitatively and qualitatively different from that of bulk materials. It has been proposed that the relationships normally used for the fatigue design of continuous monolithic materials are not applicable when designing AM porous structures and that new relationships should be developed for this purpose. It has been observed that, in general, material type and manufacturing imperfections are more important than structure architecture and porosity in the high cycle fatigue behaviour of AM porous structures [7]. Therefore, the aim of this work is to investigate the static and dynamic mechanical properties of a stochastic porous structure built from different base materials. A specific focus is to maximise the strength and fatigue strength with respect to stiffness. Structures will be built from common orthopaedic biomaterials (Commercially-Pure Titanium, Titanium Grade 23, Tantalum) and a novel AM titanium-tantalum alloy to determine which material bone scaffolds or bone ingrowth features should be manufactured from, from a mechanical properties perspective.

5.1 Material and Methods

5.1.1 The Effect of Laser Parameters and Material on Strut Thickness

As shown in Chapter 4, by varying the laser parameters and scanning strategy, the energy delivered to the melt-pool can be altered to produce struts of different diameters, with strut thickness being linearly related to the specific enthalpy of the melt-pool. Characterisation structures were built in CP-Ti, Ta and TiTa to establish relationships between strut thickness and specific enthalpy for these materials. The contour strategy would be used to manufacture all specimens as it gave the best strength-to-stiffness and fatigue strength-to-stiffness results. Two laser powers were selected (50 and 200 W) with 10 values of exposure time each, giving a total of 20 distinct laser parameters and thus 20 unique specimens per material (Table 5.1). As detailed in Chapter 3, the structures were imaged using a scanning electron microscope and analysed via ImageJ. Raw data can be found in Appendix A.

Table 5.1 – Effect of laser parameters and material on strut thickness study design and manufacturing conditions

Test	Evaluation of Characterisation Structure
Materials	CP-Ti, Ta, TiTa
Scanning Strategies	Contour
Laser Power (W)	50, 200
Exposure Time (µs)	20 - 1400
Point Distance (µm)	50
Layer Thickness (µm)	50
Laser Parameters[1] per material	20
Unique Specimens[2]	60
Repeats per Parameter Set	1
Total # of Specimens Tested	60

[1]A combination of the laser power and exposure time
[2] A specimen manufactured by a distinct combination of laser parameters and material

5.1.2 The Effect of Material on Static and Fatigue Strength

The laser parameters and scanning strategy used in LBPF also effect the optimisation of mechanical and material properties of specimens. Optimising laser power to give maximum strength-to-stiffness was seen to be material dependent whereas optimising scanning strategy was not material specific. The trends observed statically and for internal porosity seem to be good indicators of laser parameters and scanning strategies that will perform well in fatigue for a given material, as the fatigue strength-to-stiffness results for Ti64 followed similar trends as the static strength-to-stiffness results.

As the optimum laser parameters for Ti64 had already been found in Chapter 4, preliminary samples for the remaining 3 materials, CP-Ti, Ta and TiTa, were built at low (50W)

and high power (200W), with exposure time being altered to generate specimens of varying relative densities and moduli, and tested quasi statically as described in Section 3.4.2. The preliminary quasi-static results dictated the laser power that would be used to manufacture specimens for the suite of mechanical and material testing. Optimum laser power was chosen based on maximising static strength for a given stiffness per material. The contour strategy would be used to manufacture all specimens as it gave the best strength-to-stiffness and fatigue strength-to-stiffness results. Quasi Static testing, high cycle fatigue testing and morphological analysis was then performed on the final specimens for the remaining materials as per Section 3.4 to explore the effect of the parent material on static strength, fatigue strength and microstructure. Note: Quasi-Static and Fatigue strength results for Ti64 taken from Chapter 4, for samples built at low power (50 W) with a contour strategy. The number of specimens manufactured and tested is summarised in Table 5.2, laser parameter values and ranges are also listed. Laser Parameters for every manufactured specimen can be found in Appendix B.

Table 5.2 – Effect of material on static and fatigue strength study design and manufacturing conditions

Test	**Effect of Material on Static Strength**	**Effect of Material on Fatigue Strength**
Section	5.2.2.2	5.2.2.3
Materials	CP-Ti, Ti64 ELI, Ta, TiTa	
Scan Strategy	Contour	
Laser Power (W)	50W (CP-Ti, Ti64 ELI, TiTa), 200W (Ta)	
Exposure Time (µs)	40 – 950	
Point Distance (µm)	50	
Layer Thickness (µm)	50	
Thermal Condition	As-Built	
Laser Parameters[1] per test variable	4	
Unique Specimens[2]	16	
Repeats per unique specimen	5	8
Total # of Specimens Tested	80	128

[1]A combination of laser power and exposure time

[2] A specimen manufactured by a distinct combination of laser parameters, scan strategy and material

5.2 Results

5.2.1 Evaluation of Characterisation Structures

Characterisation structures were built in the remaining three materials, CP-Ti, Ta and TiTa, all in a contour strategy to establish relationships between laser parameters and strut thickness (Figure 5.1).

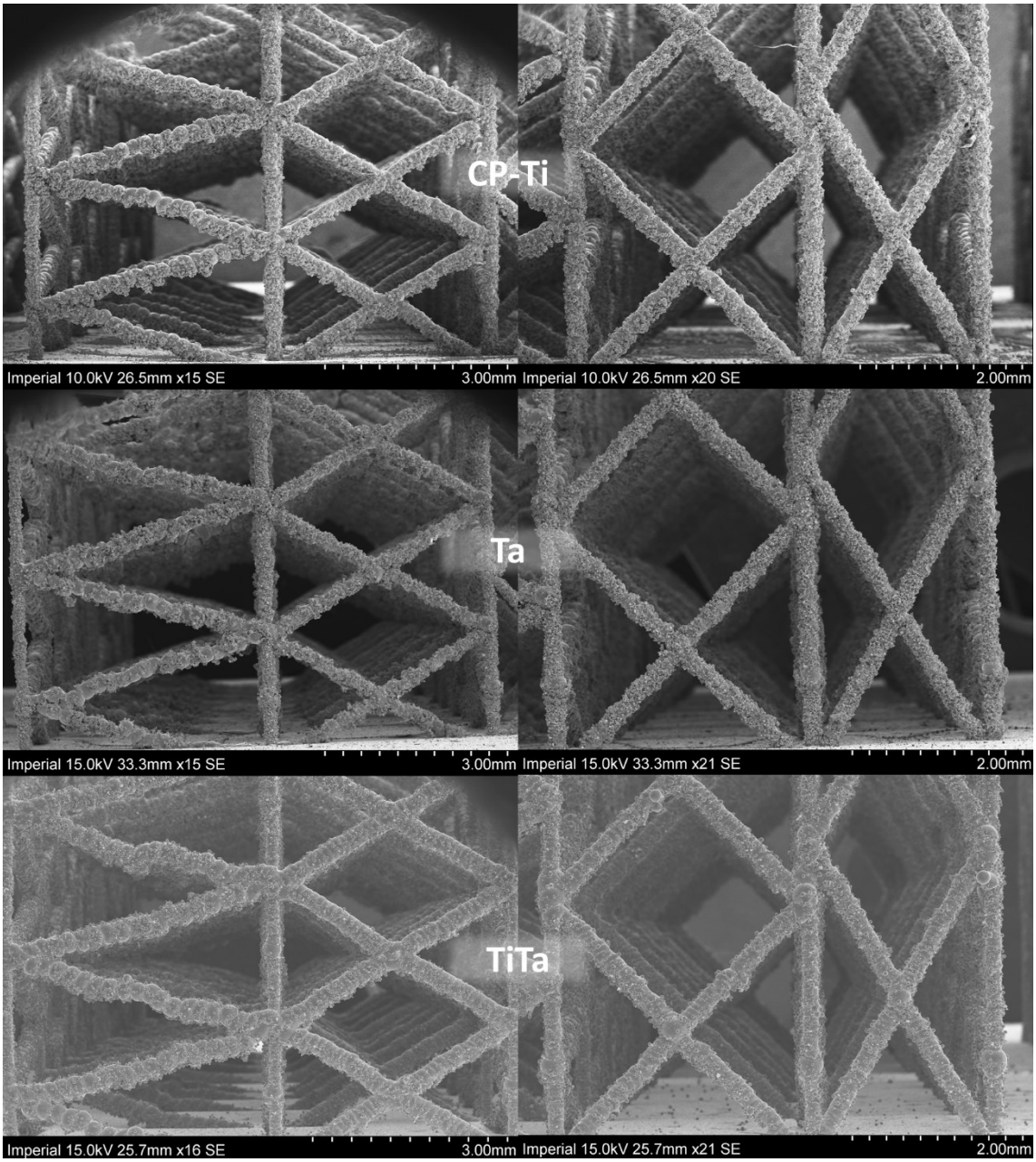


Figure 5.1 - Characterisation Structures in CP-Ti, Ta and TiTa

As seen for the characterisation structures built in Ti64 and SS316 in Chapter 4, increasing enthalpy resulted in an increase in melt-pool size and thus an increase in strut thickness. The relationship between specific enthalpy and strut thickness was found to be linear for all materials and build angles (Figure 5.2, Figure 5.3 and Figure 5.4). As before, the relationship

was found to be more accurate when specific enthalpy was calculated with actual laser power and exposure time delivered as measured by the process monitoring equipment. Due to the small size of the tantalum powder particles, especially relative to the build layer thickness excessive semi-fused particles were abundant all over the strut surface making it difficult to accurately measure the true strut thickness (Figure 5.1). For this reason the tantalum strut thickness data is less clean than for the other materials tested.

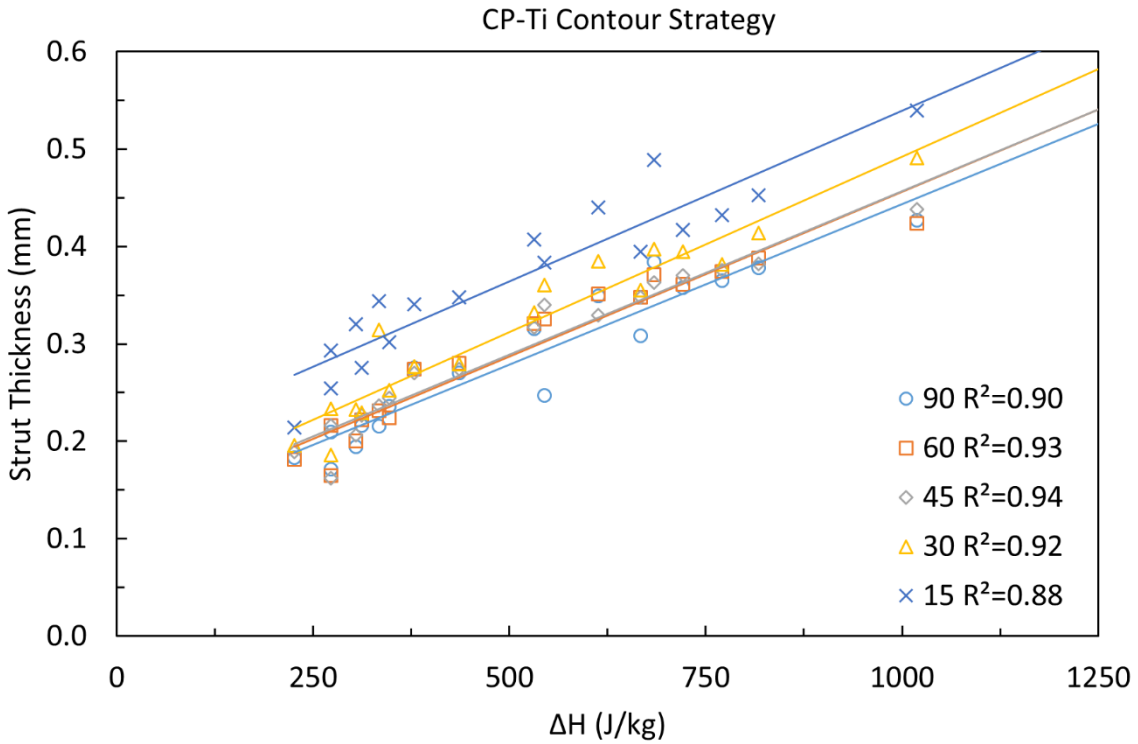


Figure 5.2 - Strut Thickness model for CP-Ti. Average S.D. for strut thickness measurements was 0.019 mm

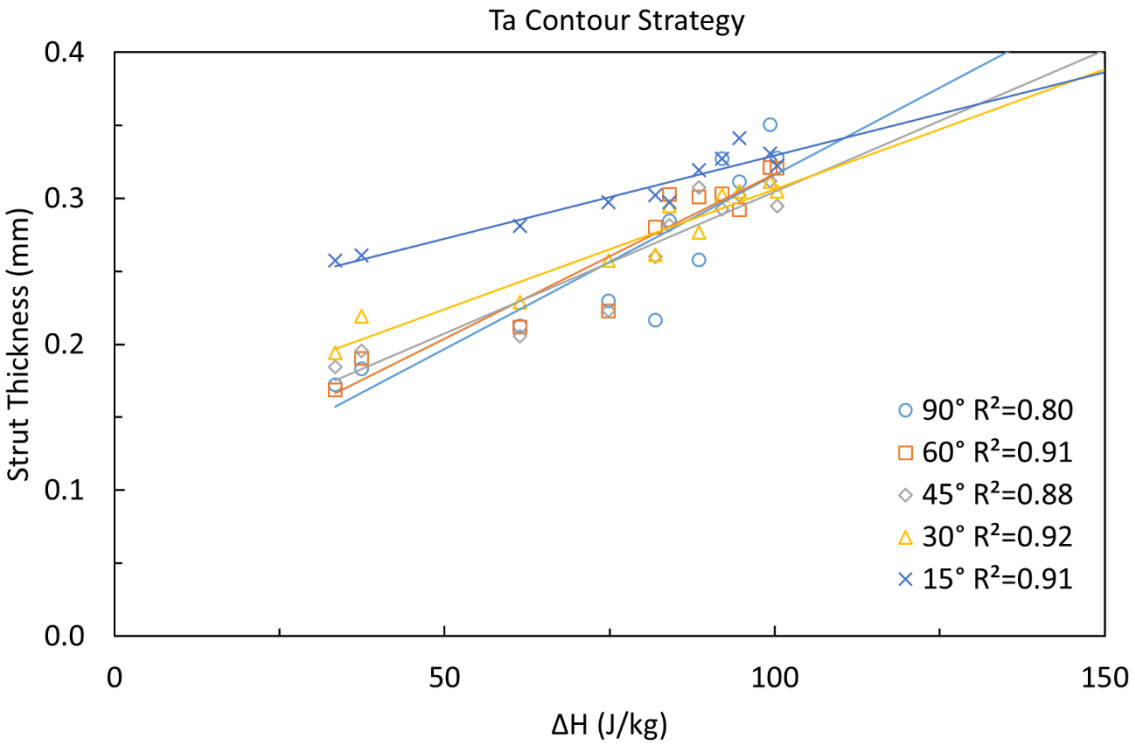


Figure 5.3 - Strut Thickness model for Ta. Average S.D. for strut thickness measurements was 0.019 mm

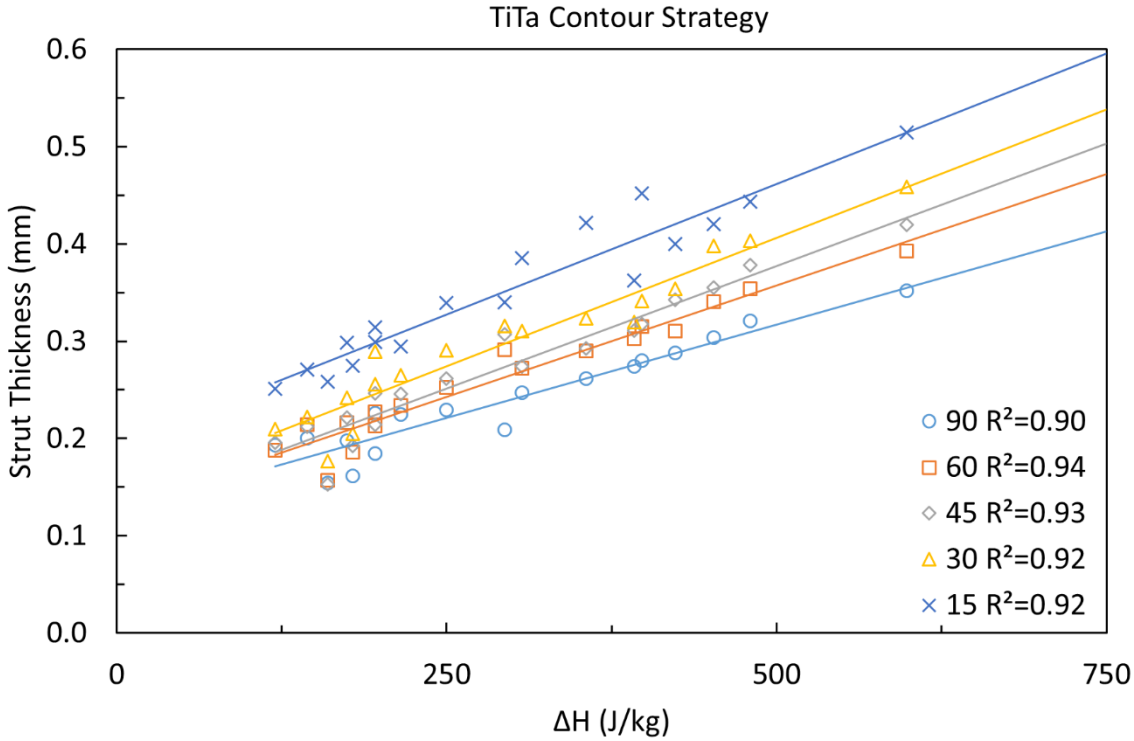


Figure 5.4 - Strut Thickness Model for TiTa. Average S.D. for strut thickness measurements was 0.017 mm

As a consequence of building the stochastic porous structures, the laser parameters required to give a desired relative density can be estimated beforehand based on knowing the strut

thickness, thus reducing iterations of manufacturing and testing specimens with different laser parameters.

5.2.2 Evaluation of Stochastic Porous Structures

Stochastic porous structures were produced in all 4 materials in a range of relative densities and therefore moduli by altering the laser parameters (Figure 5.5).

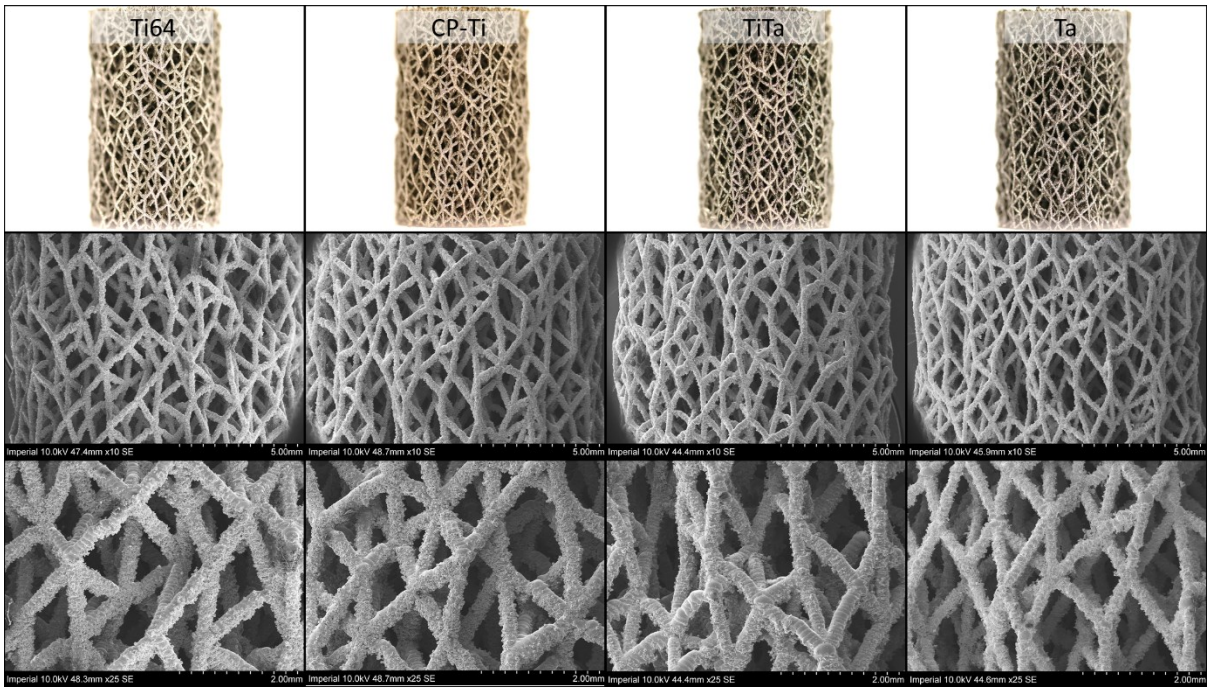


Figure 5.5 – Stochastic Porous Structures

5.2.2.1 Preliminary Laser Power Optimisation for CP-Ti, TiTa and Ta

Since the optimum laser power for manufacturing specimens with the greatest yield strength:stiffness was previously seen to be material specific (Chapter 4), preliminary samples were built at low (50W) and high power (200W) for CP-Ti, Ta and TiTa and tested quasi-statically. As described earlier, altering laser powers can cause differences in phenomena such as spatter ejection, volatility of the melt-pool and cooling rates leading to differences in mechanical strength, microstructure and internal base material porosity. A coarse optimisation of laser powers was performed based on the maximum and minimum power the AM machine can reliably produce. Figure 5.6 shows the preliminary compressive yield stress vs. modulus plots for the three materials. Two separate curves/points are seen, one for samples built at 50W and one for samples built at 200W, with increase in strut diameter and thus modulus/density being controlled by an increase in exposure time.

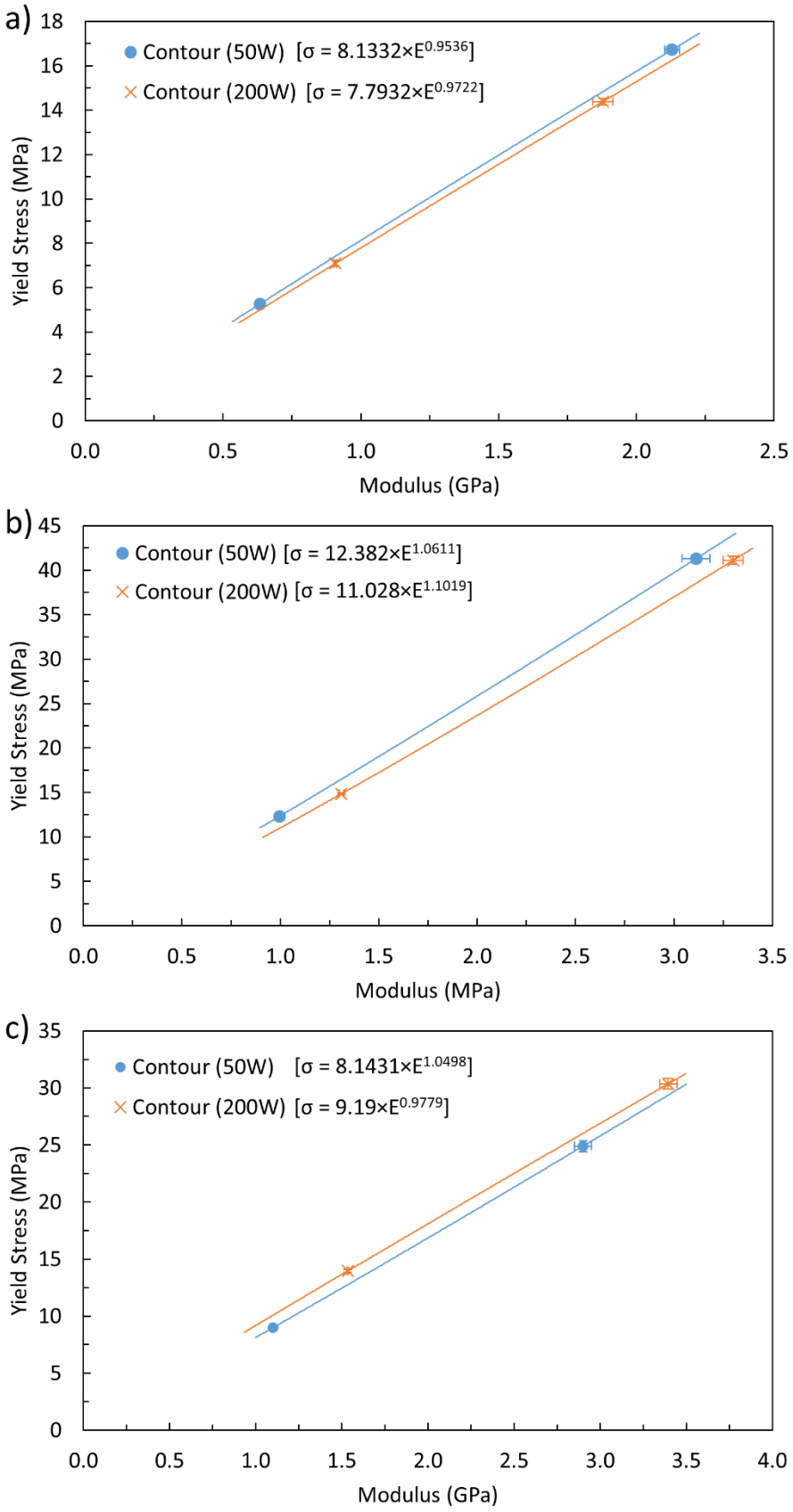


Figure 5.6 – Compressive Yield Stress vs. Modulus Plots for (a) CP-Ti, (b) TiTa, and (c) Ta. 50W is seen to produce specimens with a greater strength:stiffness ratio for CP-Ti and TiTa, whilst 200W produces specimens with a greater strength:stiffness ratio for Ta. Error bars are standard deviations.

Laser powers of 50W for CP-Ti and TiTa and 200W for Ta produced structures with the greatest yield strength for a given stiffness. These laser powers would be used to build the final specimens for static and fatigue testing for the remaining materials (Table 5.1).

5.2.2.2 Effect of Material on Static Strength

Typical quasi-static stress-strain curves and failed specimen images for all materials are seen in Figure 5.7 and Figure 5.8. All stochastic structures display a local maximum; Ti64 has a brittle failure following the maximum and is brittle throughout the plateau region whereas CP-Ti, Ta and TiTa all display a ductile failure mode and plateau region.

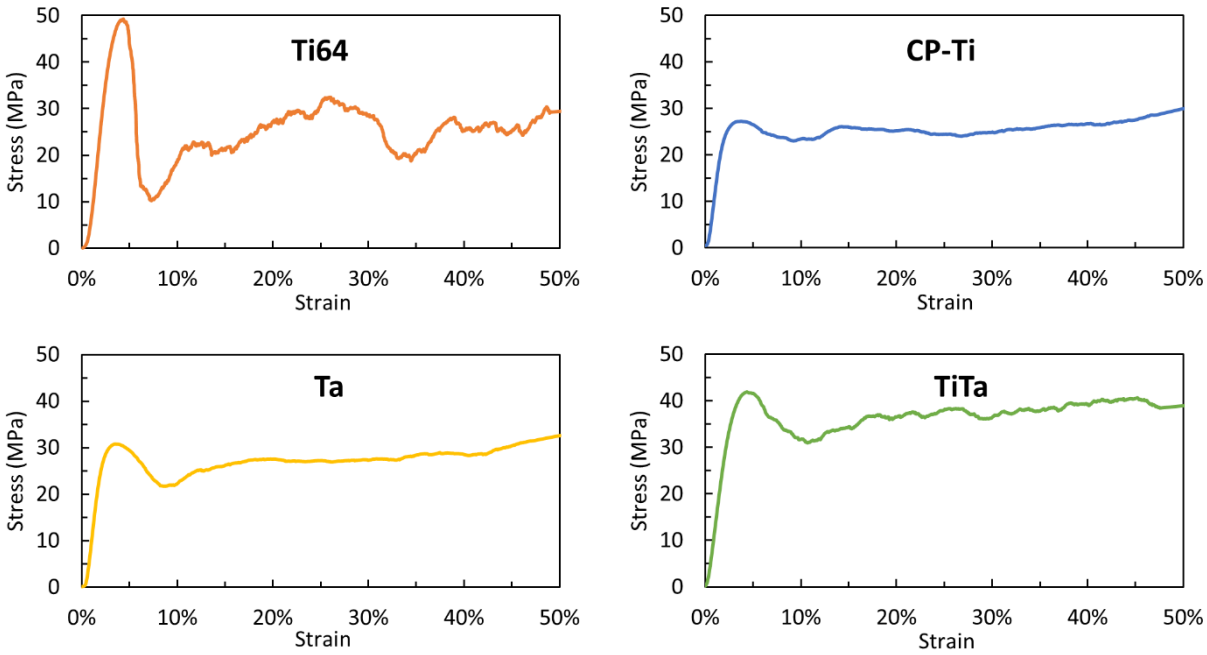


Figure 5.7 – Typical Porous structure Stress-Strain Curves. Curves shown for specimens with a ~3.1 – 3.4 GPa modulus and without hysteresis loops to 50% strain

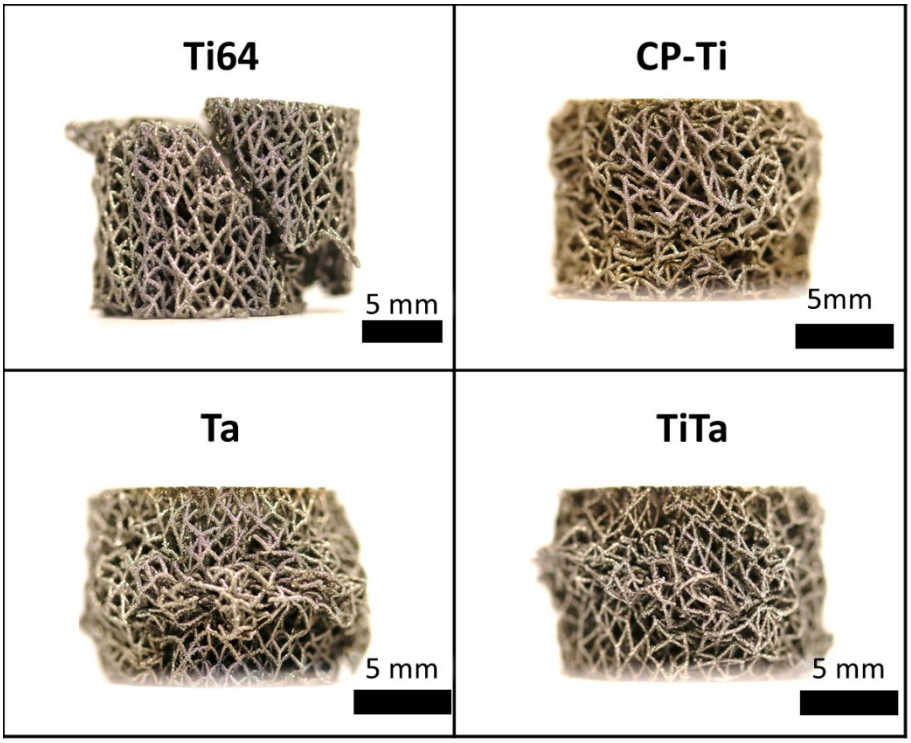


Figure 5.8 – Failed porous structures during quasi-static testing with a ~3.1 – 3.4 GPa modulus crushed to ~50% strain

The effect of material on compressive strength is seen in Figure 5.9 and Table 5.3. For AM porous structures, Ti64 has the greatest strength for a given stiffness followed by TiTa then Ta then CP-Ti. Ti64 has a greater σ_y:E than TiTa by 9%, 38% greater than Ta and 45% greater than CP-Ti. As per Gibson and Ashby [8, 9], a power-law relationship is modelled between yield strength and modulus (discussed in Section 4.3.1). Appendix B presents the relationships between yield strength and relative density and between modulus and relative density for stochastic porous structures built from the materials explored and power-law relationships are clearly seen.

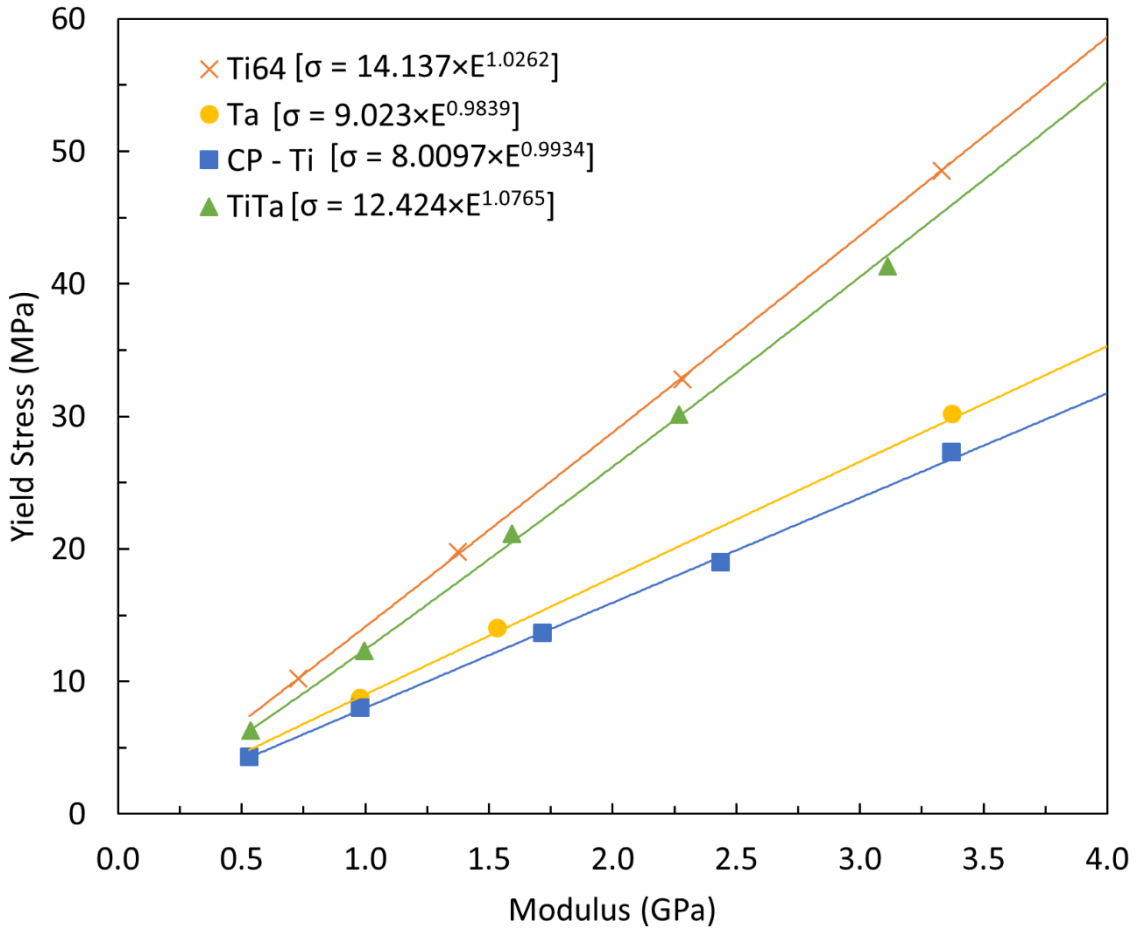


Figure 5.9 – Effect of Material on Static Compressive Properties. R^2 values for all curve fits were 0.99. Error bars are not shown, however standard deviations for all values are given in Table 5.3.

5.2.2.3 Effect of Material on Fatigue Strength

All specimens fatigue tested exhibited 3 stage fatigue failure behaviour, regardless of laser parameter, scan strategy or material used during the manufacturing process (Figure 5.10)

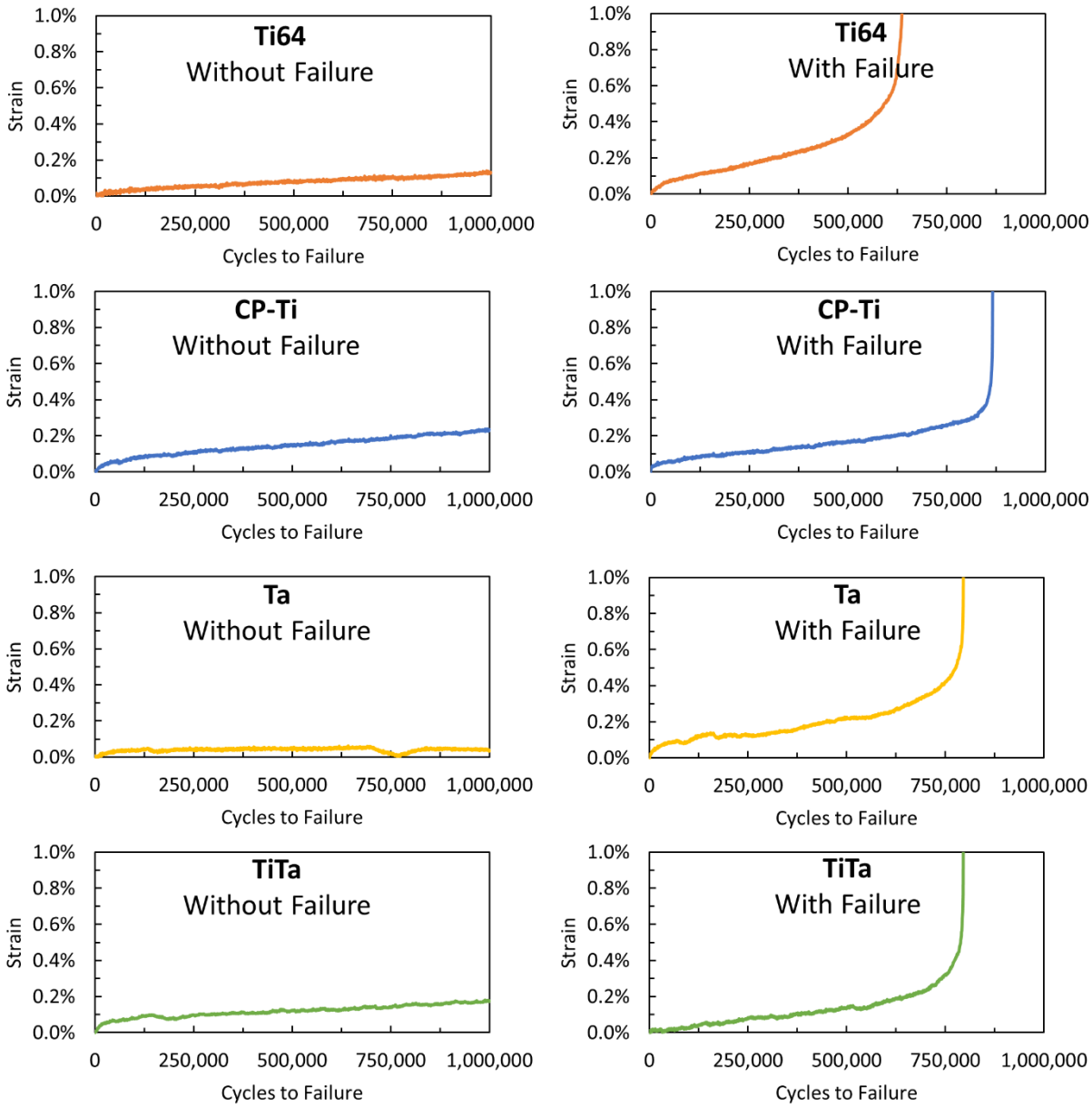


Figure 5.10 – Typical Compressive Strain vs. Cycles-to-Failure Curves per material for specimens without (left) and with (right) failure.

For all specimens, angled crush bands (fracture planes), characteristic of porous structures [10, 11], were observed (Figure 5.11); likely following the weakest planes of the stochastic porous structure. Extensive cracking and fracture was observed at or near nodes (Figure 5.12). For all materials tested there were no differences observed in the fatigue failure mode.

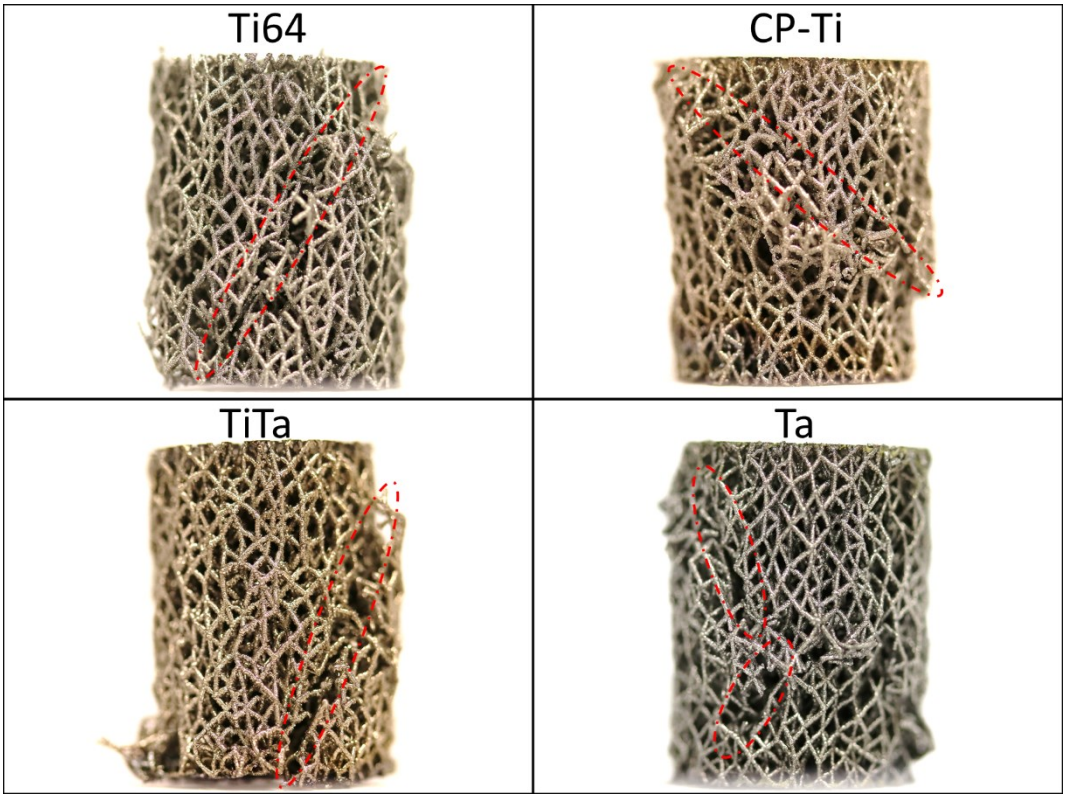


Figure 5.11 – Compression – compression fatigue failed Ti64, CP-Ti, TiTa and Ta specimens. Angled fatigue failure fracture planes (crush bands) are indicated, likely following the weakest planes of the stochastic porous structure.

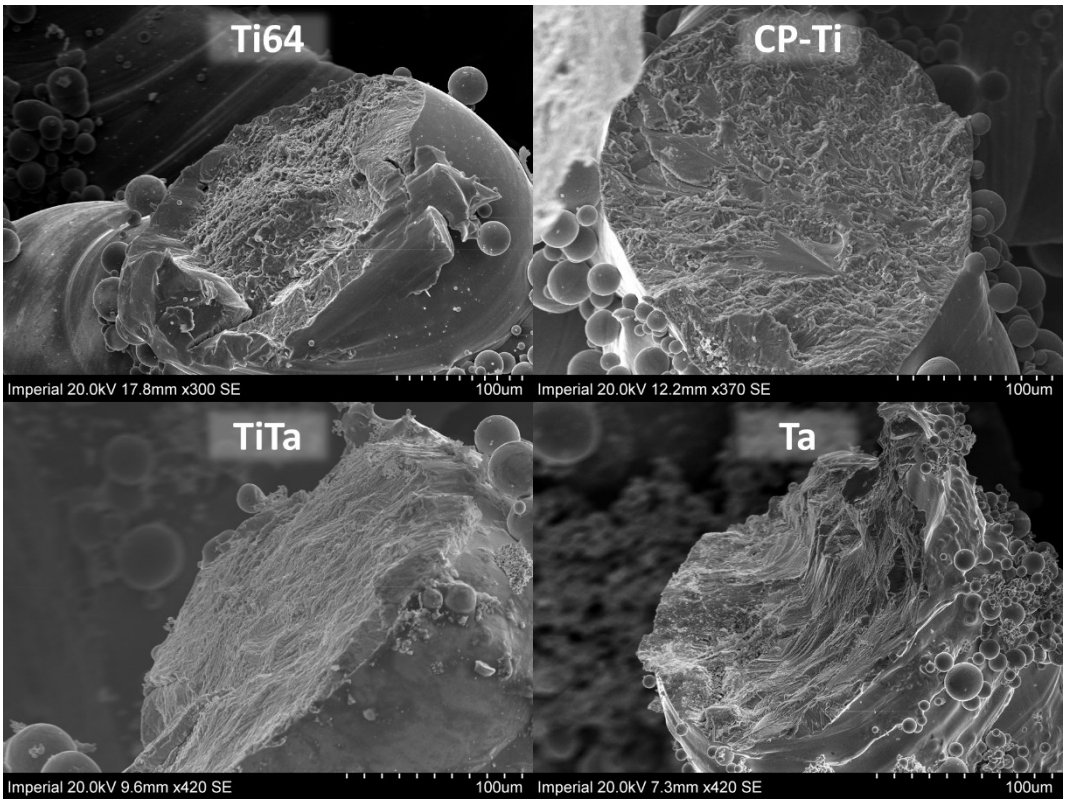


Figure 5.12 – SEM Images of a fatigue fracture surfaces

The effect of material on high cycle fatigue strength is seen in Figure 5.13 and Table 5.3. The trends seen during static testing are not observed during fatigue testing. Ti64, which had the highest σ_y:E statically and the greatest fatigue strength as a solid metal, has the lowest fatigue strength-to-stiffness ratio as a porous structure. Tantalum and the titanium-tantalum alloy had the greatest fatigue strength for a given stiffness, 8% greater than CP-Ti and 19% greater than Ti64. A power-law trend is again modelled between fatigue strength and modulus regardless of material, this will be discussed in greater detail in Section 5.3.2.

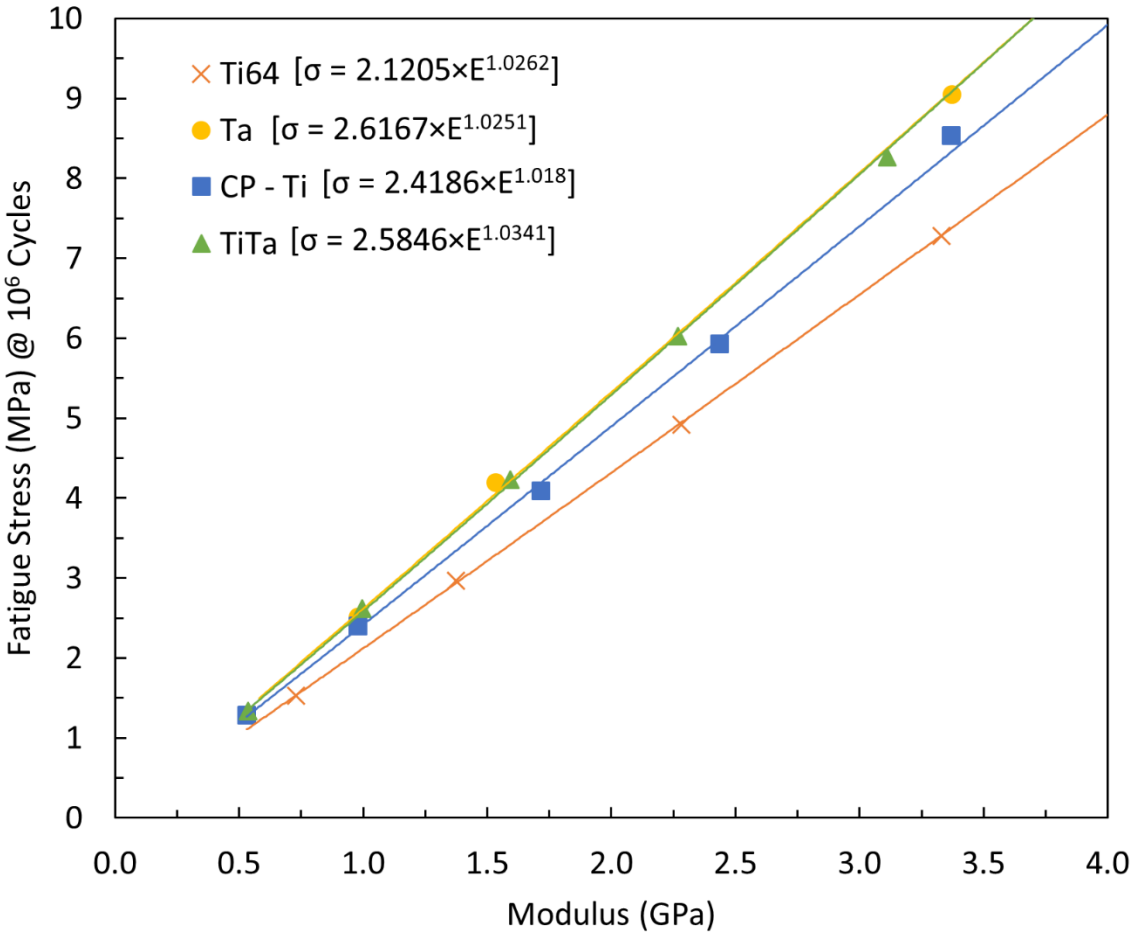


Figure 5.13 – Effect of Material on Fatigue Strength at 10^6 Cycles. R^2 values for all curve fits were 0.99. Error bars are not shown, however standard deviations for all values are given in Table 5.3.

Table 5.3 – Effect of Material on the Mechanical Properties of a Stochastic Structure (Values are mean ± S.D.). Italicised values are mechanical properties for the solid material, these values are only given as a reference as mechanical properties are heavily dependent on the manufacturing method and thermal history of the material.

Material	Modulus (GPa)	Yield Strength (MPa)	Fatigue Strength (MPa)	Yield Strength:Modulus	Fatigue Strength: Modulus	Relative Density
Ti64	0.7±0.0	10.2±0.1	1.5±0.1	13.96	2.1	10%
	1.4±0.0	19.8±0.1	3.0±0.3	14.4	2.2	12%
	2.3±0.0	32.8±0.3	4.9±0.5	14.4	2.1	16%
	3.3±0.0	48.5±0.3	7.3±0.7	14.6	2.2	20%
	114 [12]	*800-1000 [12, 13]*	*600-800 [14]*	*7.0-8.7*	*5.5*	*100%*
CP-Ti	0.5±0.0	4.3±0.0	1.3±0.1	8.0	2.4	8%
	1.0±0.0	8.0±0.0	2.4±0.1	8.1	2.4	10%
	1.7±0.0	13.6±0.2	4.1±0.2	7.9	2.4	13%
	2.4±0.0	19.0±0.0	5.9±0.3	7.8	2.4	15%
	3.4±0.0	27.3±0.4	8.5±0.4	8.1	2.5	18%
	103[12]	*300-700 [12, 13]*	*200-400 [14]*	*2.9-6.8*	*1.9-3.8*	*100%*
Ta	1.0±0.0	8.7±0.2	2.5±0.1	8.9	2.5	8%
	1.5±0.0	14.0±0.1	4.2±0.2	9.1	2.7	9%
	3.4±0.0	30.1±0.5	9.0±0.4	8.9	2.7	14%
	5.1±0.1	44.2±0.7	13.8±0.6	8.7	2.7	16%
	185[12]	*200-600 [12, 15]*	*200-400 [14]*	*1.1-3.2*	*1.1-2.2*	*100%*
TiTa	0.5±0.0	6.3±0.0	1.3±0.1	11.7	2.4	8%
	1.0±0.0	12.3±0.1	2.6±0.2	12.4	2.6	11%
	1.6±0.0	21.1±0.1	4.2±0.3	13.3	2.6	14%
	2.3±0.0	30.1±0.1	6.0±0.4	13.3	2.6	17%
	3.1±0.1	41.3±0.4	8.3±0.6	13.3	2.7	21%
	69 [16]	*587 [16]*	-	*8.5*	-	*100%*

5.2.2.4 Morphology and Microstructure Observations

All specimens exhibited semi-sintered particles on strut surfaces, texture lines between build-layers and/or melt-pools (Figure 5.14b) and microstructural heterogeneity (Figure 5.14e). All metallographic and microstructure images shown in Figure 5.14 are parallel to the build direction. Potential surface crack initiation sites were more pronounced on Ti64 and CP-Ti specimens, whilst TiTa and Ta specimens exhibited a more consistent surface finish (Figure 5.14c). The microstructure of Ti64 specimens exhibit acicular (needle like) α' grains in larger prior β grains [7, 10] whilst the CP-Ti specimens display lath-like grains of α phase [17]. The TiTa specimens consist of a solid solution matrix with un-melted tantalum particles (circled in Figure 5.14), the matrix microstructures contains martensite α'' grains [16] with a needle-like

structure inside columnar prior β grains. Meltpool and build-layer texture lines are also evident in the microstructure of the TiTa specimens. The etchant used for CP-Ti, Ti64 and TiTa, (Figure 5.14e) causes the alpha phases (α, α', α'') of titanium to appear white, whilst inter-granular beta structure and beta grains will be darkened, it has no effect on the un-melted Ta particles in the TiTa alloy. Tantalum, which has a α-BCC crystal structure [18], shows equiaxed grains with substructure, elongated along the strut and build direction (Figure 5.14e). Internal porosity was also evident in the tantalum specimens (Figure 5.15).

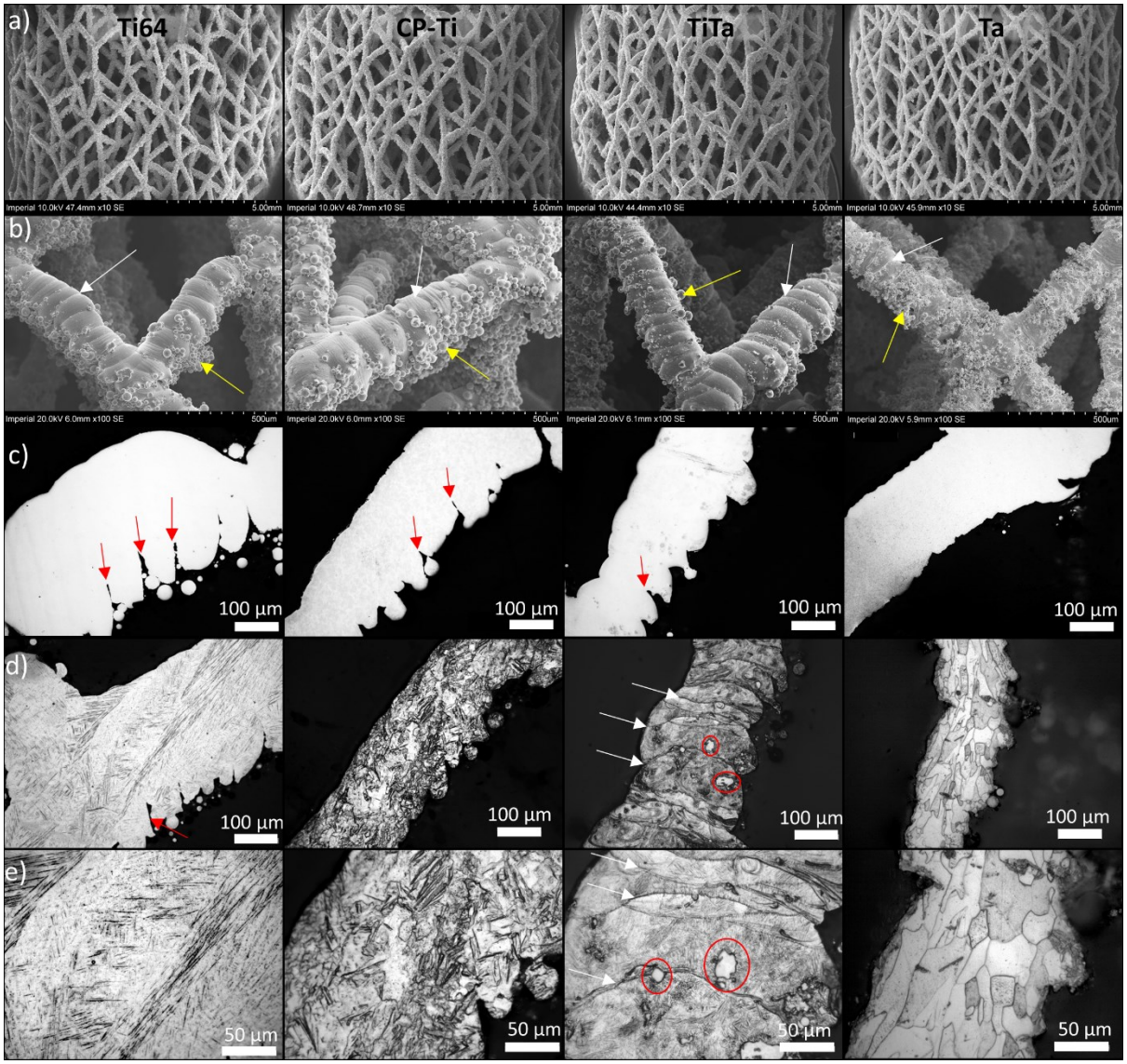


Figure 5.14 – SEM and Microscopy Images. Build direction in all images is vertical. Row a & b: SEM Images; build layer and/or melt-pool texture lines (white arrows) and semi sintered particles (yellow arrows) are evident. Row c: Microscopy Images where crack initiation sites (red arrows) are evident particularly on the Ti64 specimen. Row d & e: Microstructure Images. Manufacturing Parameters are listed in Appendix B.

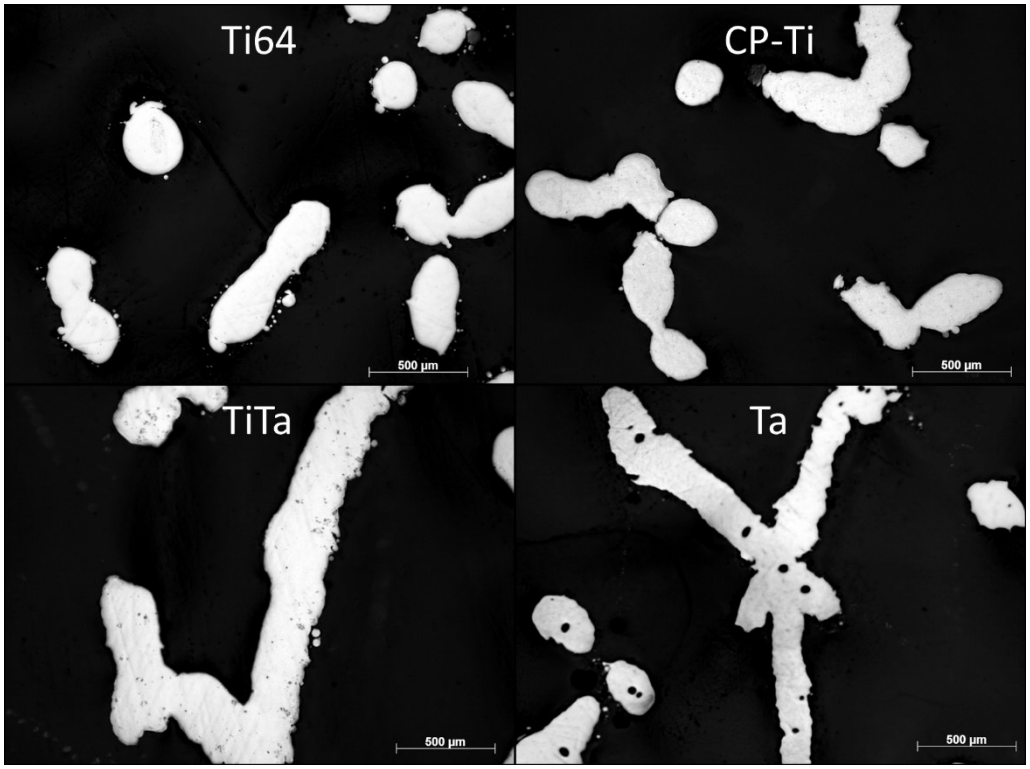


Figure 5.15 – Polished microscopy Images for Ti64, CP-Ti, TiTa and Ta specimens. Build direction in all images is vertical.

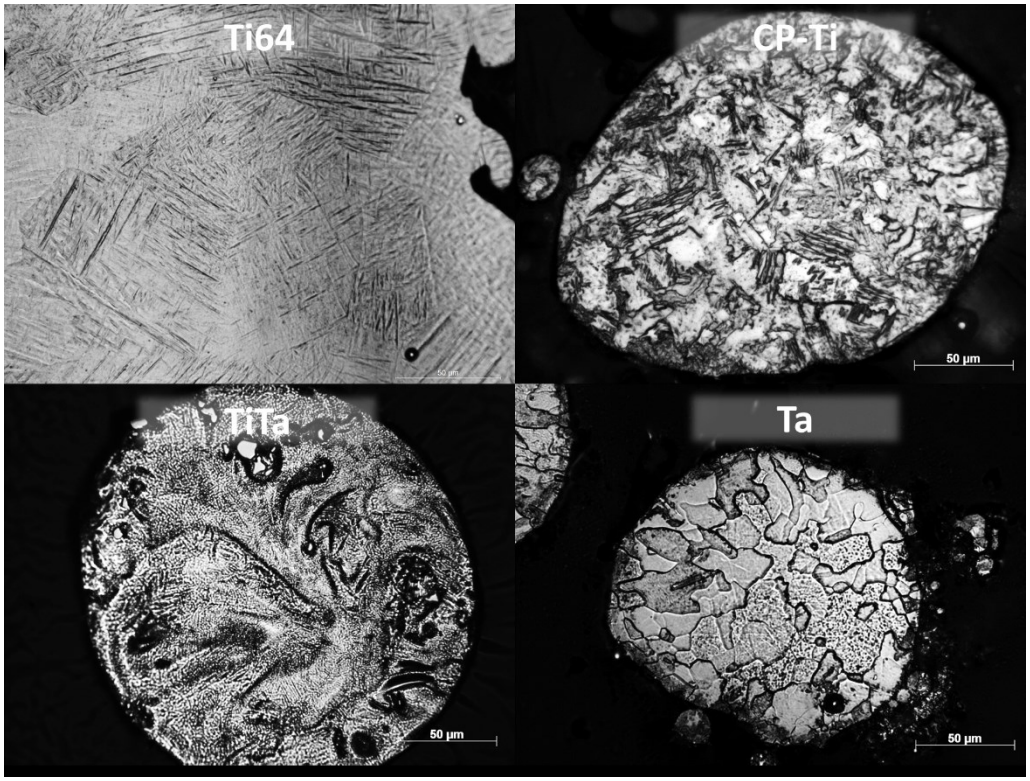


Figure 5.16 – Microstructure parallel to build plate. Build direction in all images is into the image.

5.3 Discussion

The most important finding of this chapter was that the trends observed during fatigue testing for monolithic metals and statically for solid and porous AM structures are not always indicative of the high cycle fatigue behaviour of porous AM structures. Ti64, in solid form, which is widely used in a number of industries for its high fatigue strength, was outperformed as a porous structure by CP-Ti, Ta and TiTa in fatigue strength for a given stiffness and thus may not be the most suitable choice as a low stiffness porous structure. The titanium – tantalum alloy produced (Ti-30Ta) shows promise as a porous structure, specifically for low stiffness – high static and cyclic load applications, such as porous scaffolds for bone regeneration. This is due to its high strength:stiffness and fatigue-strength:stiffness ratios all at a much lower cost to pure tantalum.

5.3.1 Material Optimisation of Porous Structures

Statically it was seen that Ti64 had the greatest strength for a given stiffness, Ti64 had a greater σ_y:E than TiTa by 9%, 38% greater than Ta and 45% greater than CP-Ti. The strength:stiffness trends seen statically for porous structures match those that have been reported for the solid monolithic materials used for manufacturing specimens in this study [12, 13, 19]. During quasi-static testing, brittle failure was seen for structures built in Ti64 whilst a ductile failure mechanism was observed for the CP-Ti, Ta and TiTa structures. The trends observed during quasi-static testing were not seen during fatigue testing, where it was observed that tantalum and the titanium-tantalum alloy had the greatest high cycle fatigue strength for a given stiffness, 8% greater than CP-Ti and 19% greater than Ti64. During high cycle fatigue testing all materials exhibited similar catastrophic failure behaviour. The fatigue failure of these materials were typical of AM porous structures previously reported and exhibited similar the failure modes and fracture characteristics to those that have been detailed by other researchers [2, 7, 10, 11].

The stochastic structures produced in this study all exhibit semi-sintered particles on strut surfaces, texture lines between build-layers and microstructural heterogeneity, all characteristics of the AM process (Figure 5.14) [10, 20]. These lead to stress concentrations, potential crack initiation sites and decreases crack propagation resistance. As high cycle fatigue is governed by the number of cycles for crack initiation, these features reduce the fatigue life of these porous structures, when compared to their solid conventionally manufactured counterparts [10, 21]. Sensitivity to defects and ductility are therefore vital in maximising fatigue strength of a porous structure as they reduce sensitivity to notches, cracks and internal

porosity whilst lowering crack initiation and propagation by softening the material when loaded [12]. This begins to explain why the fatigue-strength:stiffness trends observed for porous AM structures do not match expectations based on the mechanical properties of the solid materials, as solid metal specimens for fatigue testing tend to have smooth polished outer surfaces, no internal porosity and a homogenous microstructure. As a solid material Ti64 has the highest fatigue-strength:stiffness ratio [14], however as a porous structure it performed the worst (Table 5.3).

Ti64's poor notch sensitivity and brittle nature contribute to its poor high cycle fatigue behaviour as a porous structure [7, 10]. This has been found to be true by multiple researchers who have reported CP-Ti having a higher normalised high cycle fatigue strength than Ti64 as a porous AM structure [12, 22] despite CP-Ti having lower static and fatigue strength as a solid material (Table 5.3). AM Ti64 also typically results in Widmanstätten microstructures which is linked to poor high cycle fatigue resistance [22]. Ta, CP-Ti and TiTa all appear to have better ductility [14] and notch sensitivity contributing to their higher fatigue strength. The microstructure of the TiTa alloy consists of α'' phase inside columnar prior β grains [16], which have been reported to have the lowest moduli of Ti phases, whilst its high quasi-static strength can be attributed to the solid solution strengthening that occurs when alloying with Ta, which is a β stabiliser for titanium [13, 16, 18, 19]. It has also been found that the two phase α''+ β microstructure of Ti-Ta alloys shows improved fatigue resistance and decreased notch sensitivity compared to titanium [18]. Tantalum, as a solid material, despite having a yield strength and fatigue strength-to-modulus ratio lower than all other materials discussed (Table 5.3), had greater fatigue strength for a given stiffness as an AM porous structure, this is attributed primarily to its microstructure, ductility and sensitivity to defects [14].

Internal porosity also can affect fatigue performance as it decreases strut material cross-sectional area and acts as stress concentration sites thus reducing fatigue strength [20]. The high atomic weight of tantalum made μ-CT scanning for internal porosity quantification prohibitively difficult [23], therefore observations regarding internal porosity could only be made through microscopy on the metallographic samples. Similar levels of extremely low internal porosity were observed on the micrographs for Ti64, CP-Ti and TiTa specimens, whilst significant internal porosity was observed on the Ta specimens (Figure 5.15). This corroborates that the Ta specimens produced had a low sensitivity to defects.

5.3.2 Modelling the Mechanical Behaviour of Stochastic Porous structures

The relationship between strength, modulus and relative density of porous structures has been described by models developed by Gibson and Ashby [8, 9] (Equation. 4.1 and 4.2) explained previously in Chapter 4. Relative stress/strength increases with relative density by a power law ($\frac{\sigma}{\sigma_0} \propto \left(\frac{\rho}{\rho_0}\right)^n$) as does modulus ($\frac{E}{E_0} \propto \left(\frac{\rho}{\rho_0}\right)^m$). As stated earlier, this relationship was found to be true for AM structures by a number of authors [24] and can be seen in the results of Table 5.3 and Appendix B. Substituting Equation 4.2 into Equation. 4.1 gives Eq. 4.3 and it shows that the relative strength of a porous structure increases with relative stiffness by a power law ($\frac{\sigma}{\sigma_0} \propto \left(\frac{E}{E_0}\right)^{\frac{n}{m}}$). This is the same relationship as the trend lines seen in Figure 5.9.

A simple model for predicting the fatigue life of foams under compression-compression loading had previously been developed by modifying the creep model of Gibson and Ashby [11]. They however had insufficient data to support or refute their model. Equation 5.1 shows the developed relationship between cycles-to-failure (N_f), relative density, test stress ($|\sigma|_{max}$) and load ratio (R).

$$\frac{1}{N_f} = \frac{C(1-R)^P}{\varepsilon_y} \frac{0.6}{n+2} \left[\frac{1.7(2n+1)}{\sigma_0} \frac{|\sigma|_{max}}{\sigma_0}\right]^n \left(\frac{\rho}{\rho_0}\right)^{\frac{(3n+1)}{2}} \qquad \text{Equation 5.1}$$

If cycles-to-failure is set to 10^6 cycles, and the load ratio to R=0.1, then a power-law relationship between test stress (i.e. fatigue strength), relative density and the strain at the compressive yield stress of the porous structure (ε_y) is obtained. This was found to accurately (R^2=0.99) model the effect of relative density on fatigue strength at 10^6 cycles for the results presented in Table 5.3 and Appendix B. As before, substituting Equation 4.2 into Equation 5.1 for relative density, then yields a power relationship between test stress (fatigue strength), modulus and yield strain (ε_y). Figure 5.13 display this power-law trend between modulus and fatigue strength. However, over the range of moduli tested, it was found that both linear and power trends accurately (R^2=0.99) describe the relationship between fatigue strength at 10^6 cycles and modulus. Typically, fatigue testing of AM porous structures generates S-N curves, where a power-law models the relationship between fatigue stress or relative fatigue stress and cycles-to-failure [7, 10, 12, 25, 26]. There remains a lack of research investigating the relationship between modulus and high cycle fatigue strength for porous structures and consequently comparisons to other literature can't be made.

5.3.3 Limitations

The primary limitation of this study was that all specimens were in the as-built condition. Residual stress, microstructure and surface finish/roughness all have a negative effect on fatigue strength, and certain materials (e.g. Ti64) are more sensitive to these issues. Ideally, all specimens would have smooth struts to delay crack initiation, would be stress relieved to resist fatigue cracks and have a microstructure suitable or optimised for fatigue loading. Limitations were also present in mechanical testing. As described in Chapter 4, during quasi-static testing the hysteresis loop which was used to calculate the elastic modulus, was based on a percentage of the estimated yield strength of a preliminary sample rather than the plateau stress as described in ISO 13314. By using the yield strength to calculate the percentages for the hysteresis loop, the results between the brittle and ductile materials are far more consistent and comparable. This has been deemed acceptable in other research and the low standard deviations of the results and compliance to theoretical models suggests this was appropriate in this work as well [12].

For fatigue strength testing, ISO 12107:2012 recommends n=15 for exploratory testing and n=30 for reliability testing when the standard deviation is unknown and n=6 for when the standard deviation is known. However, due to the number of variables explored and availability of samples only n=8 was possible. Despite this, the results still satisfied all criteria for the validity of calculating mean fatigue strength and standard deviation. Improvements to this study and future work will be discussed in Chapter 7.

5.4 Summary

- This work has demonstrated that the trends observed during fatigue testing for monolithic metals and statically for solid and porous structures are not always indicative of the high cycle fatigue behaviour of porous additively manufactured materials.
- The static strength and fatigue strength to stiffness ratio of common orthopaedic biomaterials (CP-Ti, Ti64 and Ta) and a TiTa alloy were reported.
- Statically it was seen that Ti64 had the greatest strength for a given stiffness, Ti64 had a greater σ_y:E than TiTa by 9%, 38% greater than Ta and 45% greater than CP-Ti.
- The strength:stiffness trends seen statically for the porous structures match those that have been reported for their solid counterparts.
- Unlike their solid counterparts, porous Ta and TiTa had the greatest fatigue strength for a given stiffness, 8% greater than CP-Ti and 19% greater than Ti64.
- Therefore, not only do the mechanical properties of the base material need to be considered when choosing a material to maximise the high cycle fatigue behaviour of porous AM structures. It is vital to also consider notch sensitivity, ductility, internal porosity and microstructure of the material.
- Power-law relationships were observed between yield strength, fatigue strength, relative density and modulus regardless of the base material of the porous structure.
- The TiTa alloy produced shows great promise as a bone scaffold porous structure. This is due to its high strength:stiffness (2nd highest of the materials tested) and high fatigue-strength:stiffness (joint highest of the materials tested) ratios all at a much reduced cost to pure tantalum.

5.5 References

[1] X. Wang, S. Xu, S. Zhou, W. Xu, M. Leary, P. Choong, M. Qian, M. Brandt, Y.M. Xie, Topological design and additive manufacturing of porous metals for bone scaffolds and orthopaedic implants: A review, Biomaterials 83 (2016) 127-141.

[2] F.S.L. Bobbert, K. Lietaert, A.A. Eftekhari, B. Pouran, S.M. Ahmadi, H. Weinans, A.A. Zadpoor, Additively manufactured metallic porous biomaterials based on minimal surfaces: A unique combination of topological, mechanical, and mass transport properties, Acta Biomaterialia 53 (2017) 572-584.

[3] R. Hedayati, H. Hosseini-Toudeshky, M. Sadighi, M. Mohammadi-Aghdam, A.A. Zadpoor, Computational prediction of the fatigue behavior of additively manufactured porous metallic biomaterials, International Journal of Fatigue 84 (2016) 67-79.

[4] D.R. Carter, Mechanical loading histories and cortical bone remodeling, Calcified tissue international 36 Suppl 1 (1984) S19-24.

[5] A.-M. Pobloth, S. Checa, H. Razi, A. Petersen, J.C. Weaver, K. Schmidt-Bleek, M. Windolf, A.Á. Tatai, C.P. Roth, K.-D. Schaser, G.N. Duda, P. Schwabe, Mechanobiologically optimized 3D titanium-mesh scaffolds enhance bone regeneration in critical segmental defects in sheep, Science Translational Medicine 10(423) (2018).

[6] J. Van der Stok, O.P. Van der Jagt, S. Amin Yavari, M.F.P. De Haas, J.H. Waarsing, H. Jahr, E.M.M. Van Lieshout, P. Patka, J.A.N. Verhaar, A.A. Zadpoor, H. Weinans, Selective laser melting-produced porous titanium scaffolds regenerate bone in critical size cortical bone defects, Journal of Orthopaedic Research 31(5) (2013) 792-799.

[7] S.M. Ahmadi, R. Hedayati, Y. Li, K. Lietaert, N. Tümer, A. Fatemi, C.D. Rans, B. Pouran, H. Weinans, A.A. Zadpoor, Fatigue performance of additively manufactured meta-biomaterials: The effects of topology and material type, Acta Biomaterialia 65 (2018) 292-304.

[8] L.J. Gibson, Cellular solids : structure and properties, 2nd ed., Cambridge University Press, Cambridge, 1999.

[9] M.F. Ashby, The properties of foams and lattices, Philosophical Transactions of the Royal Society A: Mathematical, Physical and Engineering Sciences 364(1838) (2006) 15-30.

[10] N.W. Hrabe, P. Heinl, B. Flinn, C. Körner, R.K. Bordia, Compression-compression fatigue of selective electron beam melted cellular titanium (Ti-6Al-4V), Journal of Biomedical Materials Research Part B: Applied Biomaterials 99B(2) (2011) 313-320.

[11] McCullough, Fleck, The stress–life fatigue behaviour of aluminium alloy foams, Fatigue & Fracture of Engineering Materials & Structures 23(3) (2000) 199-208.

[12] R. Wauthle, S.M. Ahmadi, S. Amin Yavari, M. Mulier, A.A. Zadpoor, H. Weinans, J. Van Humbeeck, J.-P. Kruth, J. Schrooten, Revival of pure titanium for dynamically loaded porous implants using additive manufacturing, Materials Science and Engineering: C 54 (2015) 94-100.

[13] S.L. Sing, W.Y. Yeong, F.E. Wiria, Selective laser melting of titanium alloy with 50 wt% tantalum: Microstructure and mechanical properties, Journal of Alloys and Compounds 660 (2016) 461-470.

[14] M. Niinomi, Fatigue characteristics of metallic biomaterials, International Journal of Fatigue 29(6) (2007) 992-1000.

[15] L. Zhou, T. Yuan, R. Li, J. Tang, G. Wang, K. Guo, Selective laser melting of pure tantalum: Densification, microstructure and mechanical behaviors, Materials Science and Engineering: A 707 (2017) 443-451.

[16] Y.L. Zhou, M. Niinomi, T. Akahori, Effects of Ta content on Young's modulus and tensile properties of binary Ti–Ta alloys for biomedical applications, Materials Science and Engineering: A 371(1) (2004) 283-290.

[17] X.P. Li, J. Van Humbeeck, J.P. Kruth, Selective laser melting of weak-textured commercially pure titanium with high strength and ductility: A study from laser power perspective, Materials & Design 116 (2017) 352-358.

[18] J. Fuerst, D. Medlin, M. Carter, J. Sears, G. Vander Voort, LASER Additive Manufacturing of Titanium-Tantalum Alloy Structured Interfaces for Modular Orthopedic Devices, JOM 67(4) (2015) 775-780.

[19] Y.-L. Zhou, M. Niinomi, T. Akahori, M. Nakai, H. Fukui, Comparison of Various Properties between Titanium-Tantalum Alloy and Pure Titanium for Biomedical Applications, Materials Transactions 48(3) (2007) 380-384.

[20] A. Yadollahi, N. Shamsaei, Additive manufacturing of fatigue resistant materials: Challenges and opportunities, International Journal of Fatigue 98 (2017) 14-31.

[21] B. Van Hooreweder, J.-P. Kruth, Advanced fatigue analysis of metal lattice structures produced by Selective Laser Melting, CIRP Annals 66(1) (2017) 221-224.

[22] N.W. Hrabe, Characterization of Cellular Titanium for Biomedical Applications, ProQuest Dissertations And Theses (2010) 262.

[23] R. Wauthle, J. van der Stok, S. Amin Yavari, J. Van Humbeeck, J.-P. Kruth, A.A. Zadpoor, H. Weinans, M. Mulier, J. Schrooten, Additively manufactured porous tantalum implants, Acta Biomaterialia 14 (2015) 217-225.

[24] C. Yan, L. Hao, A. Hussein, P. Young, D. Raymont, Advanced lightweight 316L stainless steel cellular lattice structures fabricated via selective laser melting, Materials & Design 55 (2014) 533-541.

[25] S. Amin Yavari, R. Wauthle, J. van der Stok, A.C. Riemslag, M. Janssen, M. Mulier, J.P. Kruth, J. Schrooten, H. Weinans, A.A. Zadpoor, Fatigue behavior of porous biomaterials manufactured using selective laser melting, Materials Science and Engineering: C 33(8) (2013) 4849-4858.

[26] B. Van Hooreweder, Y. Apers, K. Lietaert, J.-P. Kruth, Improving the fatigue performance of porous metallic biomaterials produced by Selective Laser Melting, Acta Biomaterialia 47 (2017) 193-202.

6 Chapter 6 – The Design and *In Vivo* Testing of a Locally Stiffness Matched Porous Scaffold

Historically it has been reported that one of the requirements for bone ingrowth into a porous scaffold or into a porous coating of an orthopaedic implant is that it should match the mechanical properties of the surrounding bone tissue [1-3]. However, an increasing volume of work supports taking advantage of the mechanobiology of bone and that the lower the stiffness of a porous scaffold is, relative to the bone it is replacing, the more bone ingrowth occurs [4, 5]. The challenges are then to ensure porous materials retain sufficient mechanical competence at low stiffness and to know the properties of the bone being replaced. However, not only are the mechanical properties of bone difficult to measure, resulting in variations in reported properties in literature [1, 6], but bone properties also vary between species and anatomical site and due to age, sex, nutrition, activity level, bone health and diseases [1, 7, 8]. Typically, when porous materials are tested *in vivo* or implanted during surgery the mechanical properties of the animal's or patient's bone being replaced are unknown and not quantified. It is therefore difficult to compare ingrowth results between studies and to translate *in vivo* animal testing to human subjects.

Most commercial or research-grade porous scaffolds have a homogenous structure and are consistent regardless of skeletal location or animal used despite bone varying locally at joints, globally through-out the skeleton and between species. As an increasing volume of work indicates mechanobiology is an important factor in how bone responds to a scaffold or implant [4], there is a need for scaffolds and porous implants with stiffness gradients tailored to invoke the desired mechanobiological response from bone, specific to the site being investigated. More so, there is a need for a method to create such structures in a pragmatic way that can be deployed clinically in humans. This chapter will present the design and development of a locally stiffness-matched scaffold. The mechanical properties of trabecular bone in the medial condyle of the femur of skeletally mature ewes will be characterised; consequently a scaffold will be produced with local variations in stiffness equivalent to the bone it will be replacing (i.e. maintaining mechanical homeostasis) and its performance will be discussed *in vivo* in an ovine model. The goal of this study is not to maximise bone ingrowth into a porous scaffold but rather to produce a scaffold that mimics the local mechanical properties (specifically modulus) of bone and to develop a methodology that takes into consideration the mechanobiology of bone, which will hopefully lead to better and more clinically translatable porous implants.

6.1 Material and Methods

As bone properties vary between species and vary both globally and locally at anatomical sites as well as due to age, sex, nutrition, activity level, bone health and diseases a methodology was developed to characterise local bone properties in a clinical and pragmatic way. This ultimately can lead to patient specific and site specific implants. The following section describes the design of a heterogeneous porous scaffold, stiffness matched to the bone it would be replacing.

6.1.1 Specimen Design

6.1.1.1 Coarse Resolution Bone Property Quantification

In order to produce a locally stiffness-matched bone scaffold, the properties of the bone that is to be replaced need to be quantified. Eight ovine femora were CT scanned (SOMATOM Definition AS; SIEMENS AG) using a clinical protocol (512×512 resolution, 140 kVp, 0.6 mm slice thickness, and ~0.5 mm pixel spacing). A five-material calibration phantom (Model 3; Mindways Software Inc) was placed under the specimens for bone mineral densitometry and was visible on each CT slice (Figure 6.1.1). A 10mm thick slice approximately perpendicular from the mechanical axis of the femur and 10mm from the femoral condyle joint line was cut from each specimen. Four bone cores of ⌀5mm were extracted from the medial condyle of each of these slices (Figure 6.2). Each bone core was mechanically tested as per section 3.4.2 to determine elastic modulus (Figure 6.1.2a), with some minor adjustments. Bone cores were still crushed at a constant strain rate of ~0.1 strain/minute but for each specimen, every 100 N a hysteresis loop was present reversing at 20% of the load to account for the localised plasticity in the porous material and broken cell effects both of which reduces the slope of the initial loading curve. For each unique porous metal specimen it was possible to perform preliminary tests to estimate the yield strength to find the hysteresis loop values that would be used in consequent tests as batches of unique specimen types were identical. However as the bone core properties would vary by location and between animals and it was unsure when each specimen would yield it was then necessary to perform hysteresis loops at regular intervals.

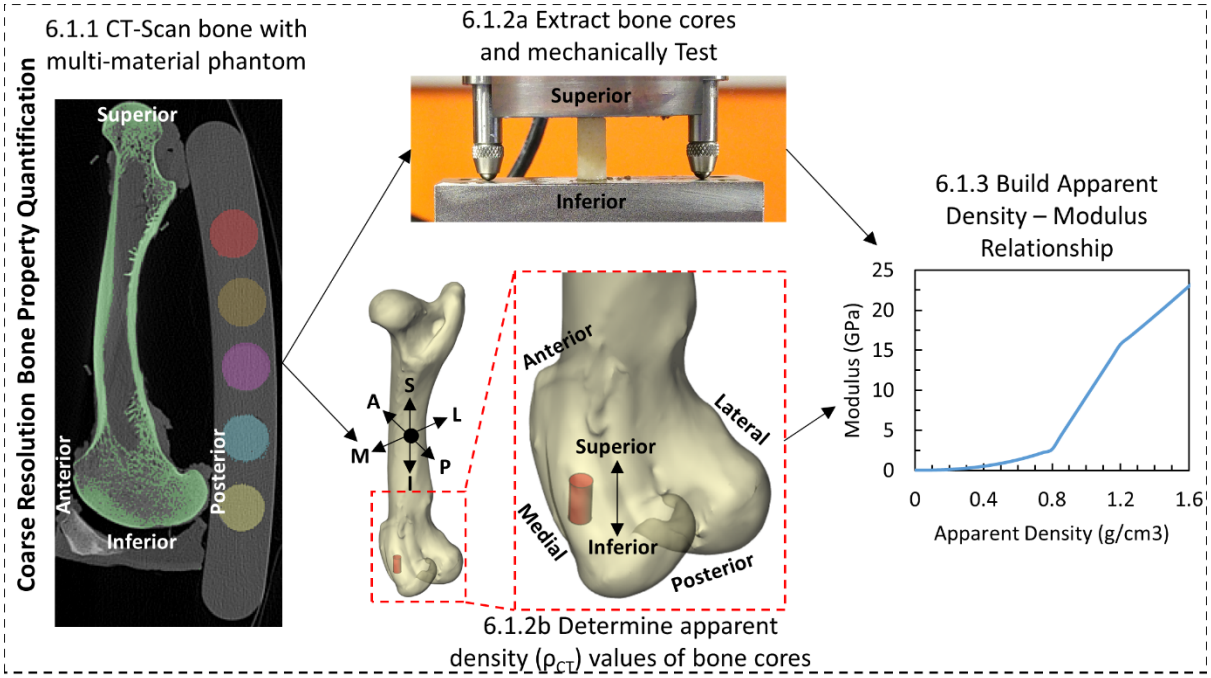


Figure 6.1 - Coarse Local Bone Property Quantification. Notation: Anterior (A), Posterior (P), Medial (M), Lateral (L), Inferior (I) and Superior (S).

As the CT scans of the ovine femur were performed with a calibrated phantom, the material properties of the tested trabecular bone cores could be determined. However, in order to do this the location of each bone core needed to be known. Therefore, after removal of the bone cores from each of the 10mm thick slices, the slices were CT scanned as per the protocol described earlier. The CT scans of the bone slices were registered to their parent bone in order to accurately determine the location of the bone cores being tested (Figure 6.2). Solid ⌀5×10 mm cylinders were then computationally modelled and meshed in a finite element simulations program (ANSYS 13). These cylinders were then imported into bone density mapping software (Bonemat v3.2) at the locations of the removed bone cores to determine apparent density (Figure 6.1.2b, Figure 6.2 and Appendix D).

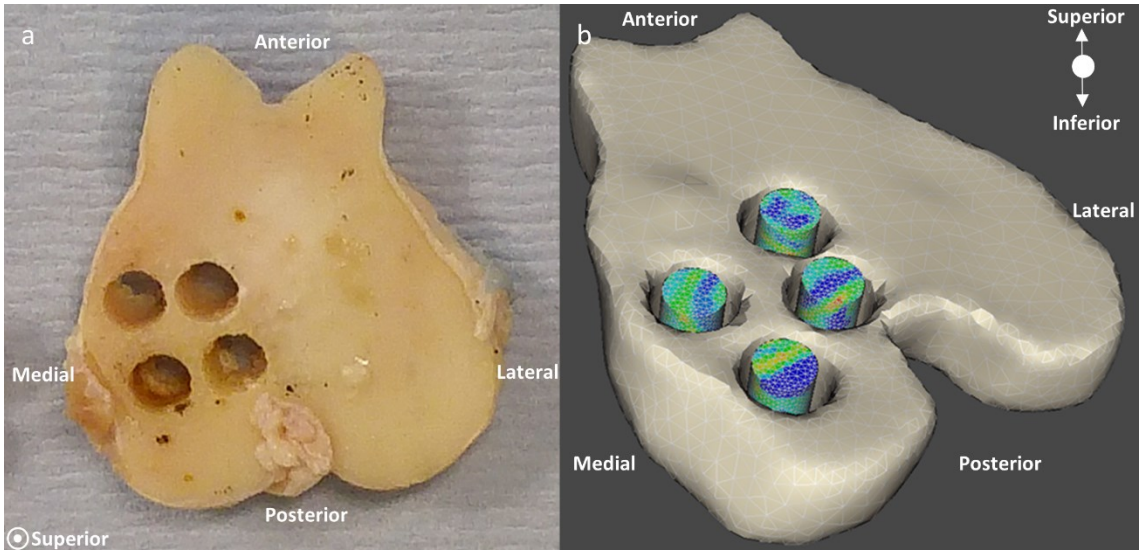


Figure 6.2 – 10mm Thick bone slice. a) Four bone cores drilled out. b) CT reconstruction of slice and meshed cylinders registered for bone mineral densitometry.

Consequently a relationship between apparent density and modulus could be produced for trabecular bone. This relationship was combined with one for ovine cortical bone [9] with a linear interpolation between the trabecular and cortical bone relationships in a similar manner as described in [6] in order to have a continuous apparent density – modulus relationship covering the entire density range of ovine femoral bone (Figure 6.1.3).

6.1.1.2 Fine Resolution Bone Property Quantification

The porous scaffold used in the *in vivo* trial had global dimensions of ⌀16 x 15mm and was implanted in the medial femoral condyle 20 mm from the joint line along the medial-lateral axis (Figure 6.3.1). As a continuous relationship has been established between apparent density and modulus for ovine bone, the local mechanical properties of the bone to be replaced by the scaffold could be determined at the desired resolution. The scaffold was first modelled as a solid object, discretised into 3 equally sized sections in all 3 axes (medial-laterial, anterior-posterior, distal-proximal), i.e. a 3×3×3 array (27 sections) and placed at the surgical site in the bone density mapping software (Figure 6.3.1). Each section extracted the average bone density (ρ_{CT}) based on the densitometry calibration and consequently the modulus was determined using the apparent density - modulus relationship derived (Figure 6.3.1 and Appendix D).

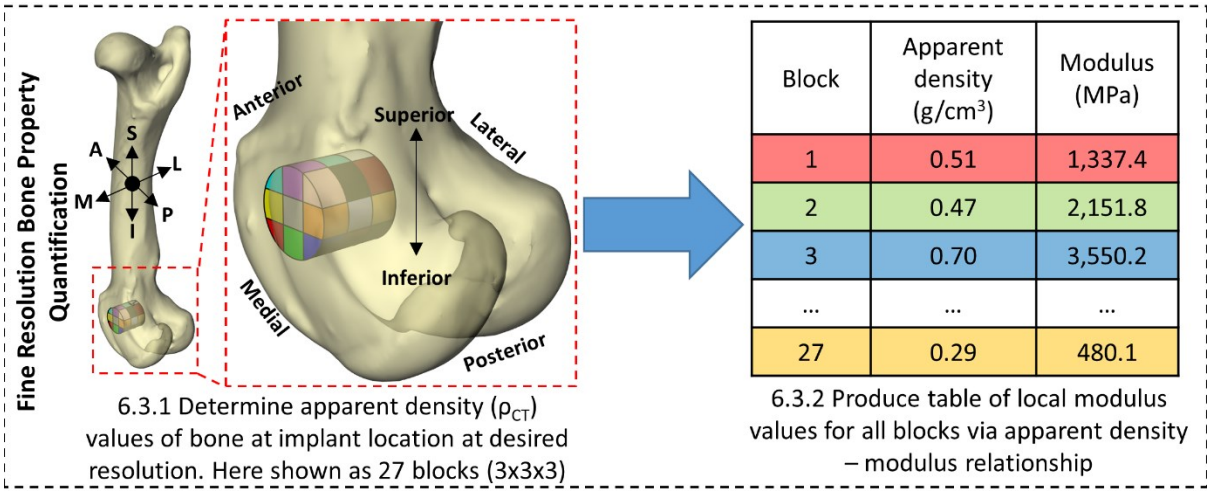
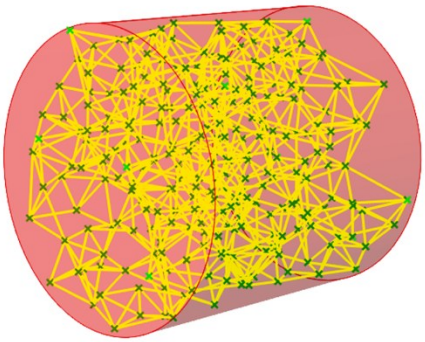


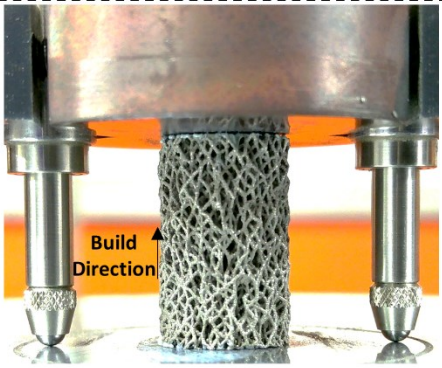
Figure 6.3 - Fine Local Bone Property Quantification. Notation: Anterior (A), Posterior (P), Medial (M), Lateral (L), Inferior (I) and Superior (S).

6.1.1.3 Design of a Locally Stiffness Matched Porous Bone Scaffold

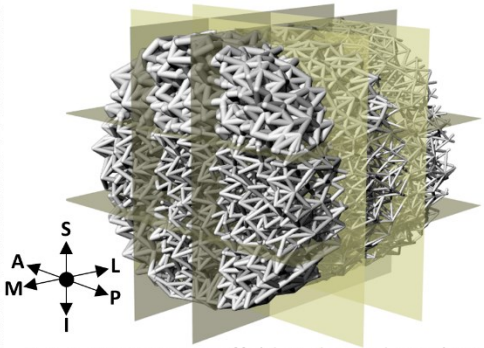
A stochastic porous scaffold was designed by filling a ⌀16 x 15mm 3D volume with a random distribution of ~5000 points using a Poisson disk algorithm and consequently connecting these points to each other as zero-thickness lines (Figure 6.4.1) at an average connectivity of ~5. Previously in Chapters 4 and 5 stochastic porous materials were manufactured in a range of relative densities and moduli by altering the laser parameters used. For these specimens, a single laser parameter was used per porous structure thus giving a structure with a uniform apparent relative density and apparent modulus (Figure 6.4.2). In order for the scaffold in this *in vivo* study to locally match the modulus of the bone it would be replacing, it was discretised into 3×3×3 sections, as described earlier (Figure 6.4.3). In each of these 27 sections modulus was controlled by changing the laser parameters based on the CP-Ti specimens manufactured in Chapter 5. Right and left leg versions of the scaffold were created which were mirrored versions of each other. The scaffold also contained a geometric feature to ensure correct orientation upon implantation and to distinguish between left and right versions.



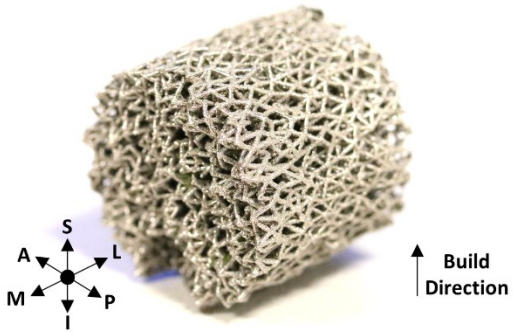
6.4.1 Design of a stochastic porous scaffold: fill a volume with a random distribution of points. Connect points with a desired connectivity



6.4.2 Manufacture scaffolds of varying modulus. Establish a relationship between laser parameters and/or strut thickness and the modulus of the scaffold



6.4.3 Discretize scaffold at desired resolution (shown here as a 3 x 3 x 3 array) with each section having a strut thickness (or laper parameter) which produces a desired modulus equal to the bone it will be replacing



6.4.4 Manufacture locally stiffness-matched porous scaffold

Figure 6.4 – Design of a locally bone-stiffness matched porous scaffold. Notation: Anterior (A), Posterior (P), Medial (M), Lateral (L), Inferior (I) and Superior (S).

6.1.2 Specimen Manufacture

The scaffolds were manufactured with a contour strategy and in CP-Ti in the same method as described in Section 3.2 and 3.3. As per Chapters 4 & 5 the specimens were manufactured at low power (50 W) and with a contour strategy to maximise both the strength-to-stiffness and fatigue strength-to-stiffness ratios of the structure. Despite other investigated materials displaying superior mechanical properties for a given stiffness, the high atomic weight of tantalum makes μ-CT scanning for bone ingrowth quantification prohibitively difficult. After production, items were removed from the substrate by EDM and shot-blast. Specimens were rinsed and cleaned ultrasonically in a cleaning solution (0.2 μm filtered water and Decon Neutracon) followed by sterile isopropanol to remove all contaminants (Hunt Developments UK Ltd). Following filtered drying, specimens were vacuum packed/sealed in pouches and sterilised via Gamma Irradiation (25-35 kGy).

The surgical procedure and explant analysis methodology was detailed in Chapter 3, section 3.5.

6.2 Results

6.2.1 Bone Core Testing

Stress-Strain curves of the trabecular bone cores and commercially pure titanium specimens of uniform modulus (manufactured and tested in Chapter 5) indicate similar behaviour under compression as seen in Figure 6.5. Two distinct regions are seen, an initial linear portion and following a local maximum, a plateau of almost constant stress; if tested to higher levels of strain a third region of densification and rapidly increasing stress would be seen [10]. The hysteresis loop for both bone and the CP-Ti specimens indicate that there is localised plasticity in the specimen at stresses well below the compressive strength of the specimen as well as settling due to broken structural walls/edges. This is evident as the hysteresis loop has a steeper gradient than the initial loading portion. The plateau region of the trabecular bone indicates slightly more brittle failure of the trabecular structure compared to the more ductile collapse of the porous CP-Ti specimens.

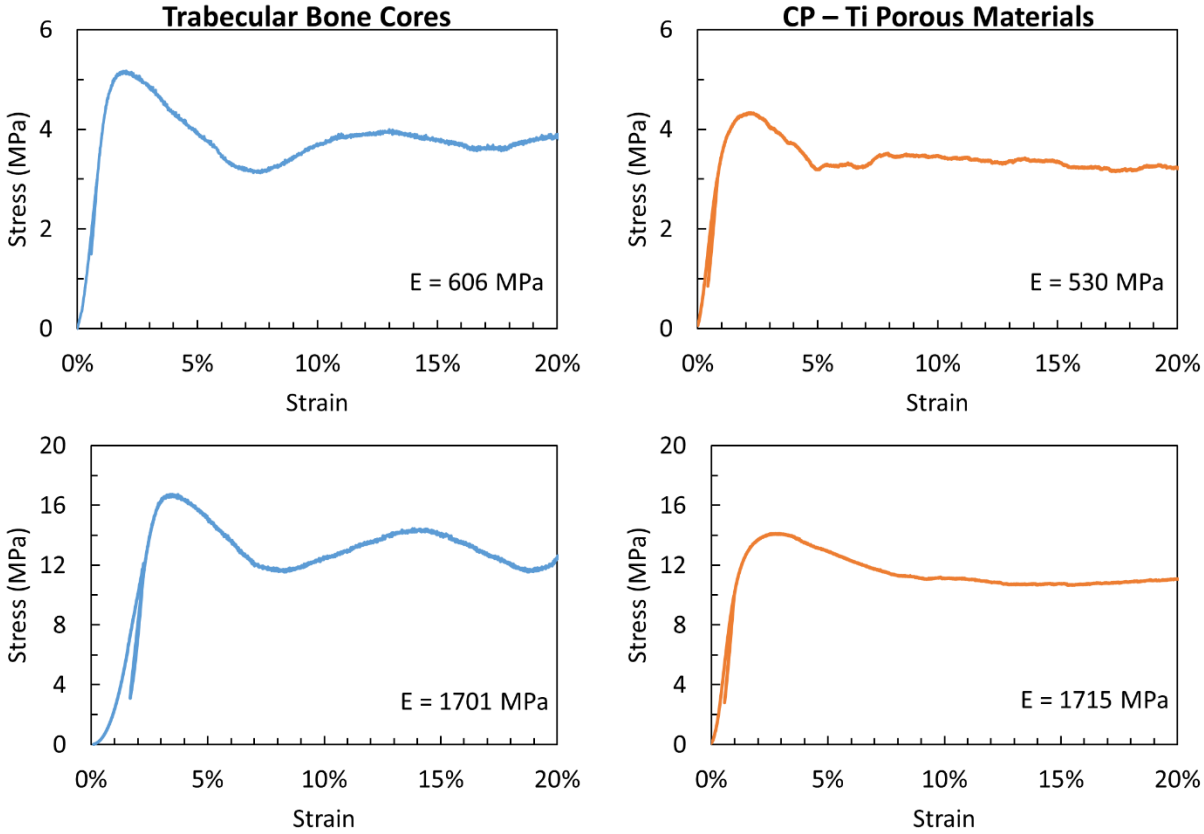


Figure 6.5 – Compression Stress – Strain Curves for Trabecular Bone Cores and uniform stiffness CP – Ti porous materials of ~500-600 MPa modulus and ~1700 MPa modulus. CP – Ti specimens tested in Chapter 5

Apparent density of the bone core specimens, obtained from CT-scans, ranged between 0.2 and 0.8 g/cm^3 whilst modulus, obtained from the mechanical testing, ranged between 56.5 and

2,737.7 MPa. A power-law relationship was observed between apparent density and modulus of the specimens as described by Gibson and Ashby [10, 11] and seen in Figure 6.6.

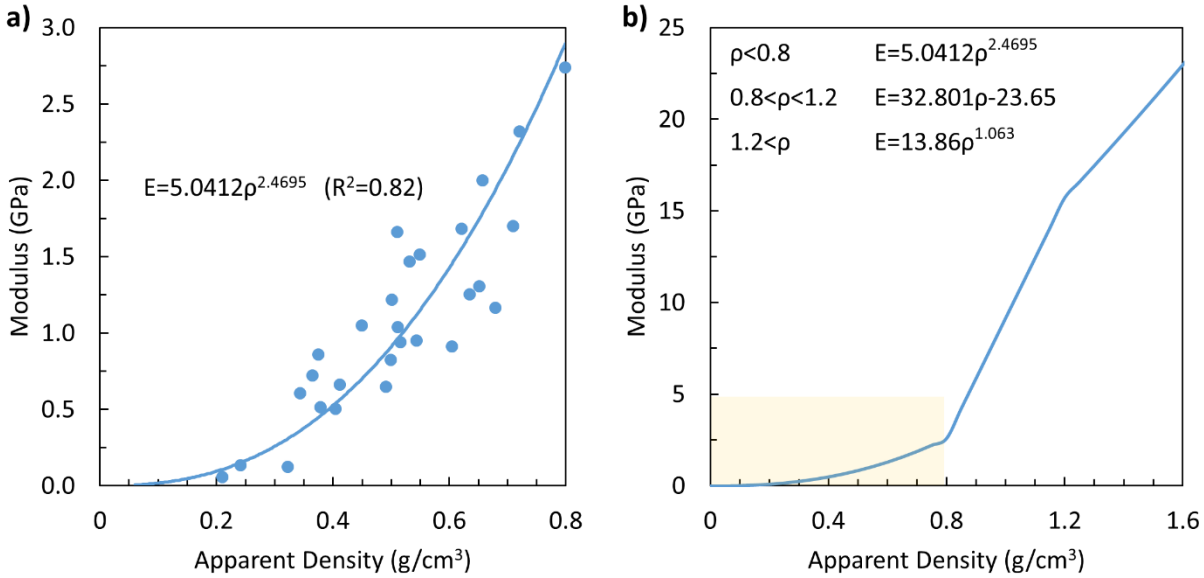


Figure 6.6 – Apparent Density vs. Modulus; a) tested points and trend line for trabecular bone in the medial femoral condyle, b)trend line over entire bone range (trabecular + cortical)

If the apparent density-modulus trend, as seen in Figure 6.6a, is extrapolated further it would underestimate modulus values for cortical bone. Therefore in a similar manner as was presented in [6], the cancellous bone data for the ovine medial femoral condyle was combined with ovine femoral cortical bone data also obtained by mechanical testing, reported in [9] with a linear interpolation between the two datasets (Figure 6.6b). This produces a continuous relationship covering the entire apparent density range of ovine bone. Both a power-law relationship, as per Gibson and Ashby [10, 11] and a linear relationship, accurately model the relationship between yield strength and modulus for the trabecular bone cores, Figure 6.7, as discussed in Section 4.3.1. Compared to the uniform moduli porous CP-Ti scaffolds produced in Chapter 5, over the modulus range tested, ovine trabecular bone displays greater strength for a given modulus, on average 24% ± 2% S.D. difference greater.

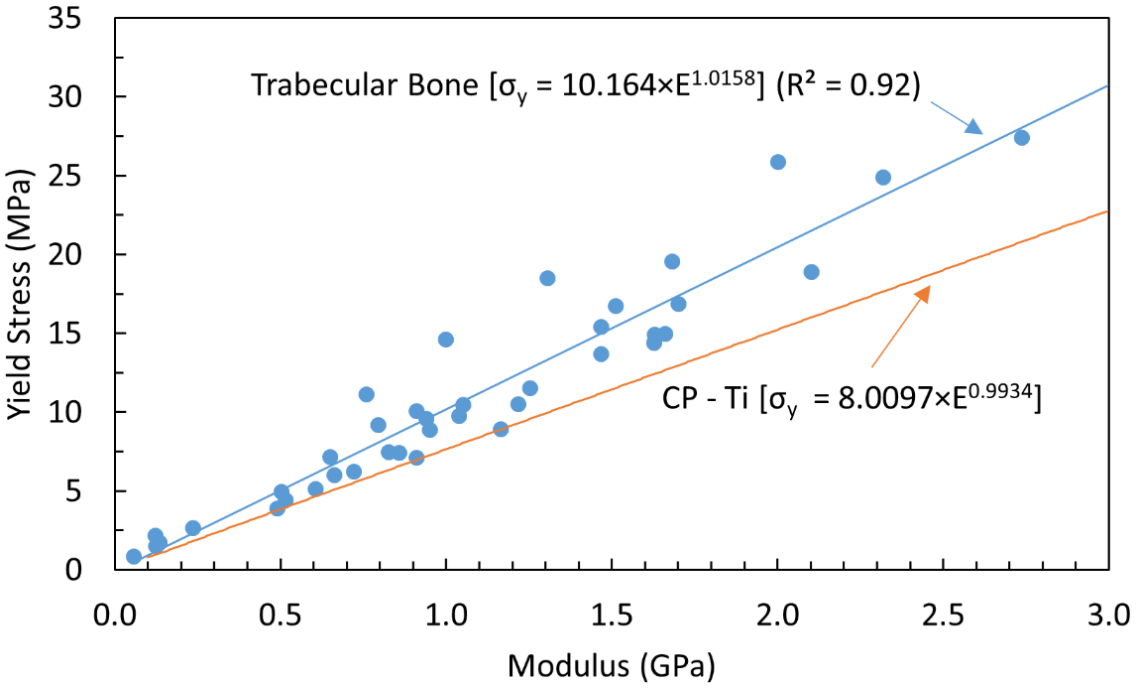


Figure 6.7 – Yield Stress vs. Modulus for the trabecular bone cores

6.2.2 Locally Stiffness-Matched Scaffold

Apparent density for the surgical site ranged on average from 0.27 to 0.76 g/cm^3 with a modulus varying between 262.2 and 3,644.2 MPa respectively with an average modulus over the 27 sections of 1383.5 MPa. The local apparent density and modulus variations for the surgical site, discretised into 27 sections, are presented in Table 6.1, as are the designed moduli of each of the 27 sections of the scaffold, where the laser parameters and consequent modulus values chosen were based on the testing and relationships established in Chapter 5. The produced scaffold (Figure 6.4.4 and Figure 6.9) had a modulus ranging from 566.0 to 3584.4 MPa with an average modulus over the 27 sections of 1435.2 MPa.

Table 6.1 – Localised Density and Modulus Variations of Bone at implant Site and Modulus variations of scaffold. Location notation: XYZ, X: Posterior-Anterior, Y: Medial-Lateral, Z: Inferior-Superior; all going 1-3 respectively.

Location	Apparent Density of bone (g/cm^3)	Modulus of Bone (MPa)	Modulus of Scaffold (MPa)	Difference (MPa)
111	0.56±0.15	1337.4±678.4	1320.6	-16.8
112	0.65±0.16	2151.8±1389.0	2263.9	+112.0
113	0.76±0.16	3550.2±1822.9	3584.4	+34.2
121	0.51±0.10	998.4±397.0	943.3	-55.1
122	0.61±0.13	1595.6±700.2	1697.9	+102.3
123	0.72±0.21	3644.2±4969.3	3584.4	-59.8
131	0.47±0.12	890±510.5	943.3	+53.3
132	0.49±0.09	900.1±406.7	943.3	+43.2
133	0.6±0.15	1873.2±1800.6	1886.6	+13.3
211	0.51±0.15	1095.7±641.9	1132.0	+36.3
212	0.62±0.21	2365.8±2801.5	2452.5	+86.7
213	0.71±0.15	2757.6±1645.7	2792.1	+34.5
221	0.42±0.13	691.6±390.6	754.7	+63.0
222	0.52±0.15	1143.5±620.3	1132.0	-11.5
223	0.6±0.14	1618.5±1015.7	1697.9	+79.4
231	0.32±0.09	334.8±195.9	566.0	+231.2
232	0.38±0.10	506.4±294.3	566.0	+59.6
233	0.43±0.15	753.6±753.3	754.7	+1.0
311	0.51±0.10	1011.3±507.0	943.3	-68.0
312	0.56±0.11	1272.5±616.6	1320.6	+48.1
313	0.7±0.12	2679.2±1722.3	2678.9	-0.3
321	0.42±0.11	656.7±304.4	641.5	-15.3
322	0.46±0.08	787.5±274.4	754.7	-32.8
323	0.58±0.14	1648.5±1374.8	1697.9	+49.4
331	0.27±0.12	262.2±191.5	566.0	+303.8
332	0.32±0.08	344.2±196.5	566.0	+221.8
333	0.36±0.12	480.1±384.0	566.0	+85.9
Average ± S.D.	**0.52±0.13**	**1383.5±923.7**	**1435.2±897.2**	**+51.8**

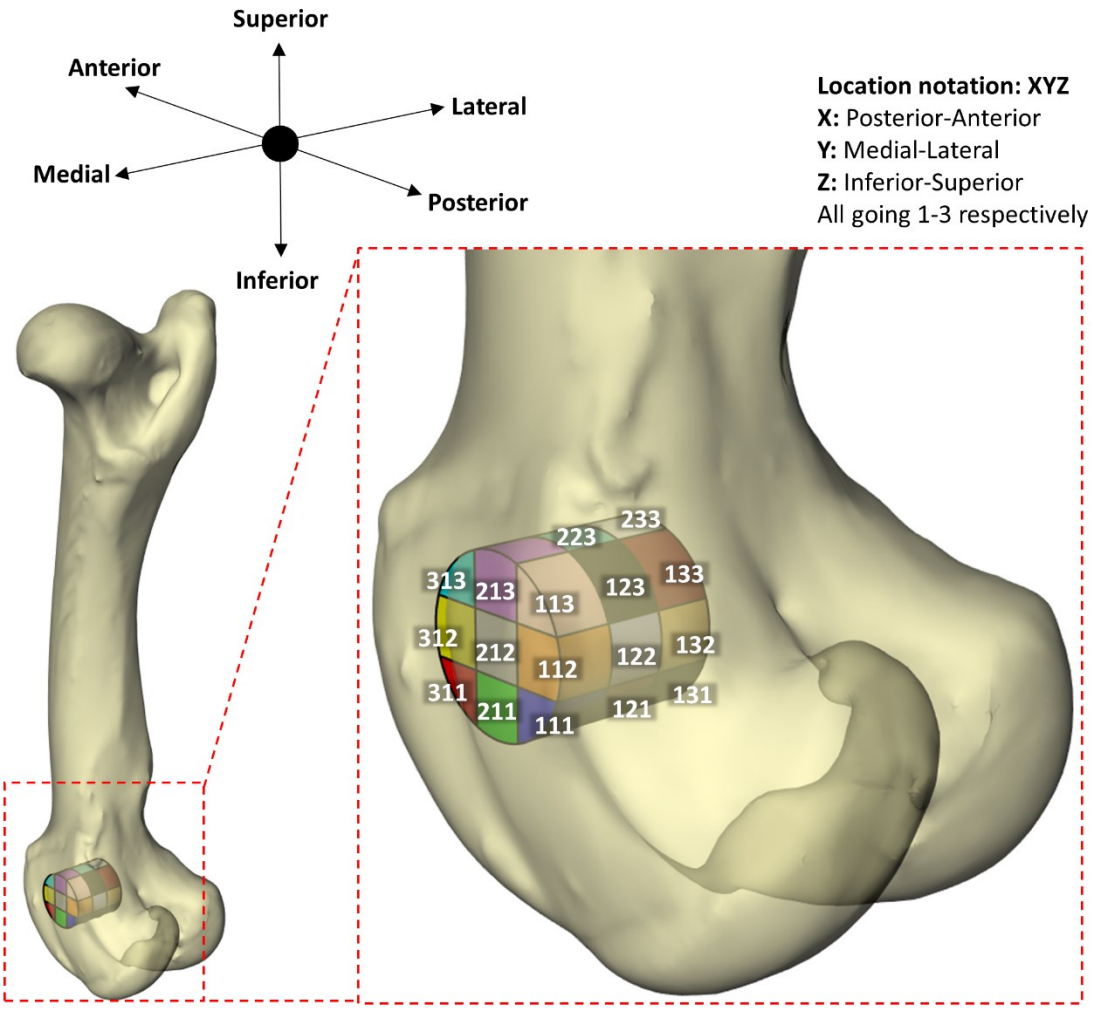


Figure 6.8 – Scaffold Location Notation (shown for a right leg)

As determined from the µ-CT scans, the scaffold had an average relative density of 12.7 % (i.e. 87.3% porous) with strut size ranging from ~80 – 400 µm (D_{50} = 210 µm) and pore size ranging from ~80 – 1300 µm (D_{50} = 830 µm). The strut size and pore size distribution can be seen in Figure 6.10. The µ-CT scans also revealed that no loose powder was present in the scaffold or visible in the surrounding bone and therefore the scaffolds had been properly cleaned. SEM images of the scaffold can be seen in Figure 6.9.

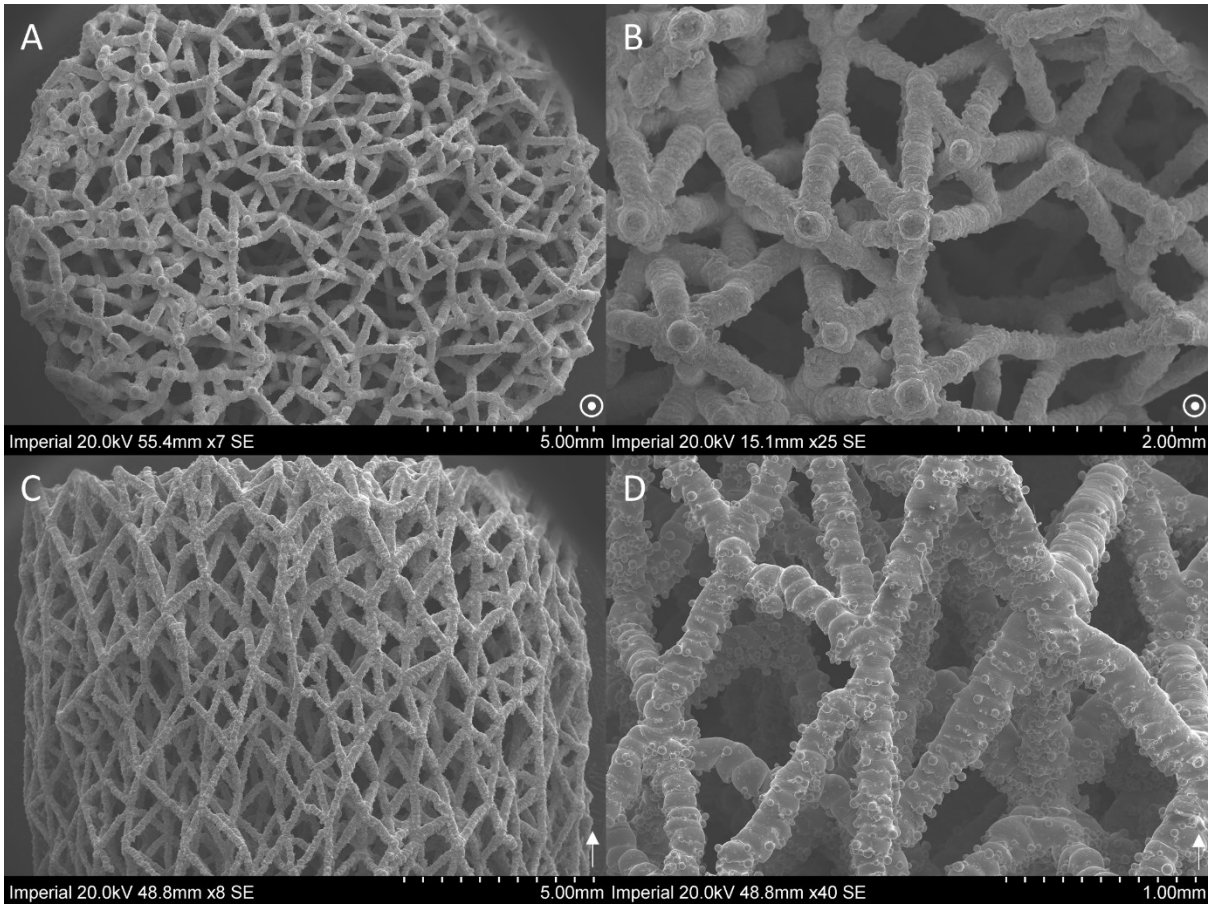


Figure 6.9 – Scaffold SEM Images (Build Direction indicated). A) Medial End of Scaffold, B) Higher magnification of medial end, C) Scaffold Periphery, D) Higher magnification of scaffold periphery

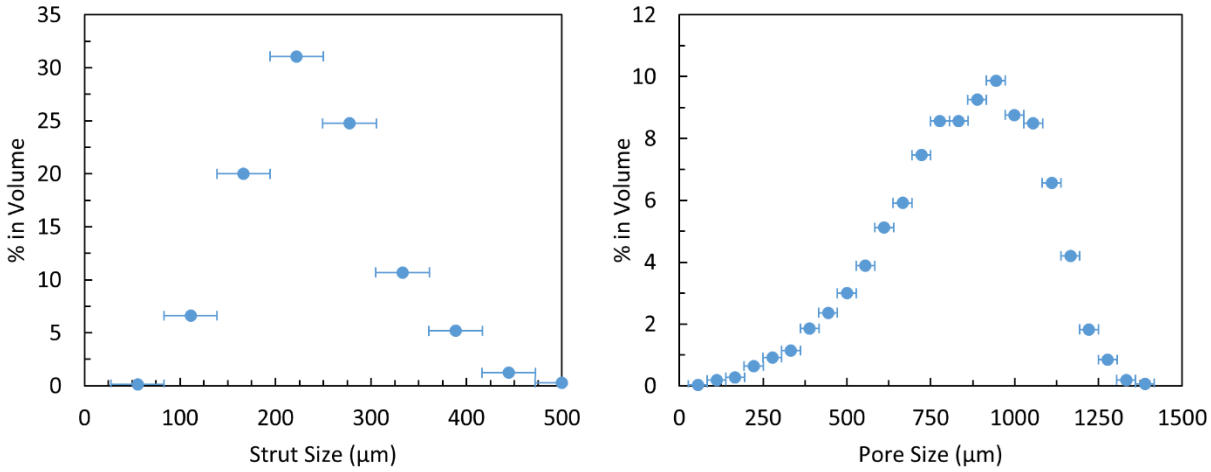


Figure 6.10 – Scaffold Strut and Pore Size Distribution

6.2.3 *In Vivo* Results

All sheep were euthanized after 6 weeks following implantation of the stiffness-matched scaffold. The volume of bone ingrowth into the scaffolds (BV) was quantified through µ-CT scans, and was divided by the total defect volume (TV) minus the scaffold volume (SV), both

also quantified through the µ-CT scans per animal and implant, to determine the percentage of new bone-ingrowth. Bone ingrowth ranged from 7.69% – 16.38% with an average of 10.73% ± 2.97% S.D. (Table 6.2).

Table 6.2 – Bone ingrowth results

Animal	Leg	New Bone Surface Area (mm^2)	New Bone Volume (mm^3)	BV/TV	BV/(TV-SV)
1 (Pilot)	Right	3218.5	106.6	6.76%	7.69%
2	Left	4362.4	165.3	8.02%	9.11%
3	Left	8271.1	238.9	11.07%	12.61%
4	Left	8206.5	286.9	14.51%	16.38%
5	Right	3926.5	132.6	7.35%	8.47%
6	Right	6606.9	207.9	8.91%	10.11%
Average ± S.D.	**-**	**5765.3±2032.3**	**189.7±61.9**	**9.44±2.65%**	**10.73±2.97%**

A typical 3D reconstruction of new bone ingrowth into the scaffolds is seen in Figure 6.11. For most specimens intimate contact was present between bone and the scaffold over the entire diameter along the entire scaffold length.



Figure 6.11 – µ-CT Renderings of bone ingrowth into a locally stiffness matched porous scaffold (not shown)

However, for two specimens (Animal 1 and 5) this was not the case. Animal 1 was the pilot and used a conical end (jobber) drill of ⌀15.5mm and consequently gaps were observed between the defect diameter and the scaffold. Following the pilot, the drill was changed to a flat bottom ⌀15mm drill. Defect creation and consequently implant placement on animal 5 was slightly too distal and not the entirety of the defect was surrounded by bone (Figure 6.12).

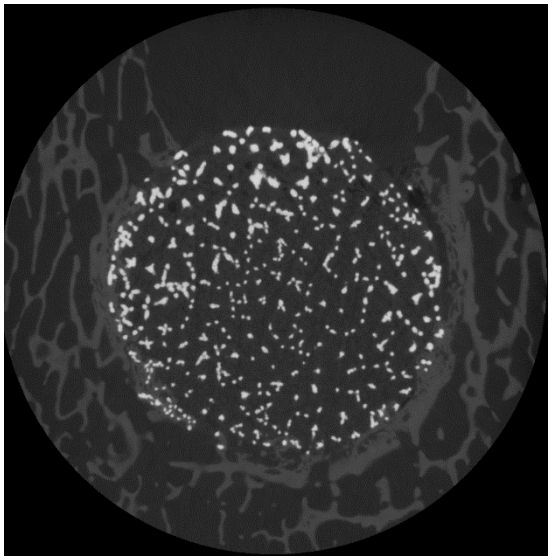


Figure 6.12 – Distal Placement of Scaffold in Animal 5. 9.5 mm from the medial end of the scaffold.

These issues likely contributed to lower bone ingrowth in these two animals. The μ-CT scans also revealed a gap between the lateral end of the scaffold and the end of the defect tunnel ranging between 3-5mm between the animals. However, for animals 2, 3, 4 and 6 bone had almost bridged the ⌀15 defect and there was evidence of growth into the lateral end of the implant and not just radially around the diameter (Figure 6.13).

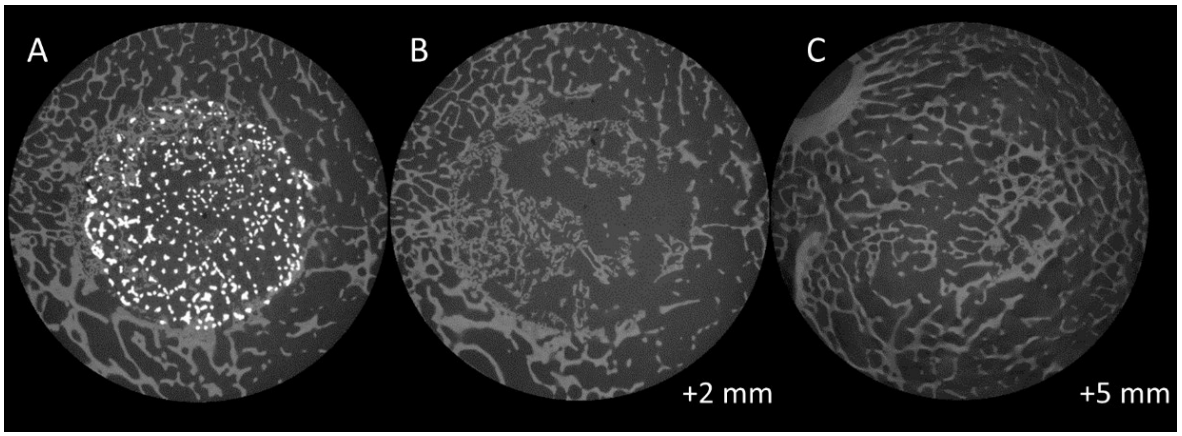


Figure 6.13 – Bone bridging gap. From left to right: A) Bone ingrowth into the lateral end of the scaffold, B) bone almost bridging the entire defect diameter 2mm from the lateral end of the scaffold and the defect tunnel, c) end of the cylindrical defect tunnel, 5mm from the lateral end of the scaffold.

Quantitative evaluation of osteogenic activity at the bone-implant interface and from the interior is shown in Figure 6.14. Five μCT slices per animal were analysed at consecutive defect depths, from the periosteal surface towards the bottom of the defect, perpendicular to the implant axis (slice 1, periosteal face of the implant; slice 5, marrow face of the implant; slices

1-5 were evenly spaced by 3 mm). Grading criteria is seen in Section 3.5.2.3. At the scaffold-bone interface the average formation score was 3.35±0.7 whilst in the interior it was 1.31±1.01.

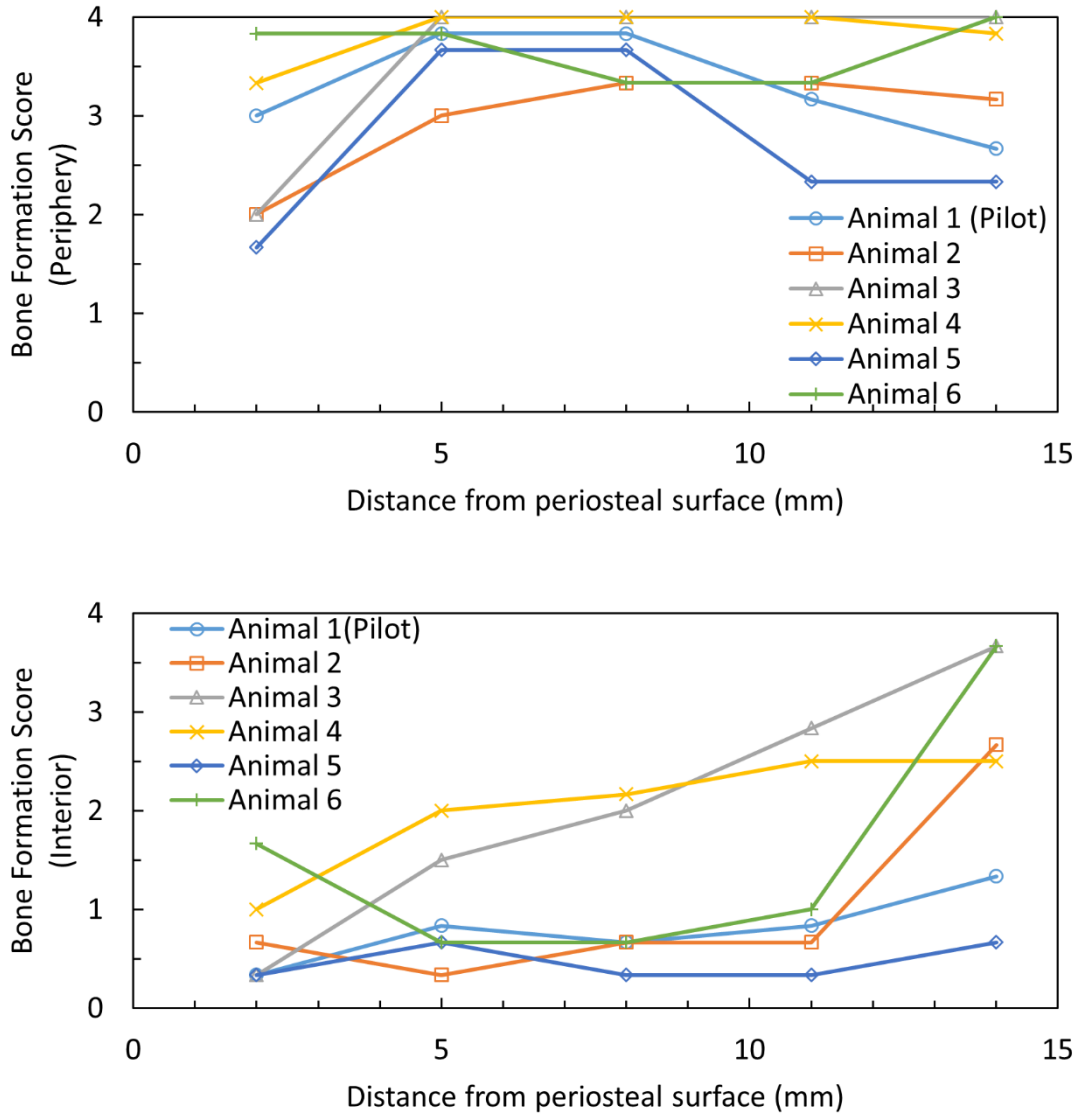


Figure 6.14 – Osteogenic activity at the bone-implant interface (top) and implant interior (bottom).

Around the scaffold periphery bone ingrowth depth was consistently 1-2mm and would encompass the outer strut elements (Figure 6.15, Figure 6.16 and Figure 6.17). In animals 3, 4 and 6 where a greater amount of bone ingrowth was found, thin branches or islets of bone were also observed deep within the scaffold interior. These are seen in the fluorescent microscopy image, which highlights mineralization of nascent bone during the last 2 weeks of the study, as high intensity specks in the scaffold interior (Figure 6.15) and in the histology images (Figure 6.16) as thin branches between the struts.

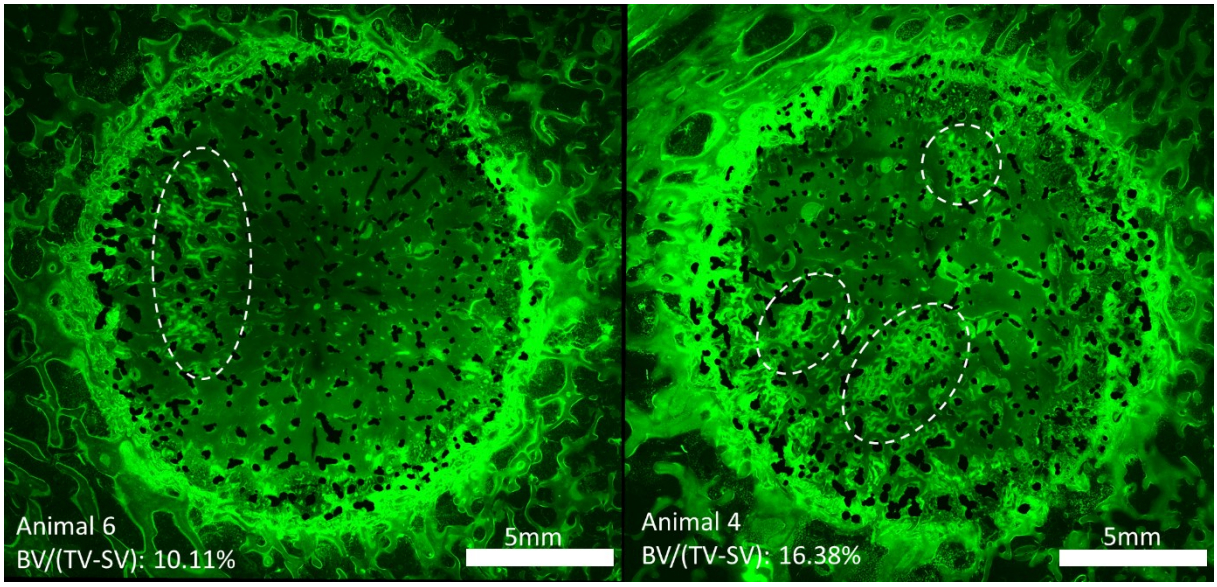


Figure 6.15 – Fluorescent Microscopy Images for animals 4 and 6. Islets of bone deep within the scaffold interior circled

The histology images provide additional information about the pathways of bone formation within the scaffold. The sections taken, through the middle of the scaffolds (7-8 mm deep from the periosteal surface), show the nascent bone ingrowth as woven bone tissue. The structure of which is a very fine, densely branching struts, forming a delicate mesh resembling embryonic bone. At the periphery of the defect (around the scaffold diameter) at the bone-implant interface is where the most intense formation of fine woven bone is observed overlaid with lamellar bone. Embryonic-looking woven bone (Figure 6.16b) is seen in the interior of select scaffolds (animals 3, 4 and 6), however the networks of woven bone and titanium struts were intercalated without intimate contact. Osteoblasts line the outer surfaces of all the very newly formed bone in the scaffold interior (Figure 6.16b), reduced number of osteoblasts are observed around the more developed bone at the scaffold periphery (Figure 6.16a).

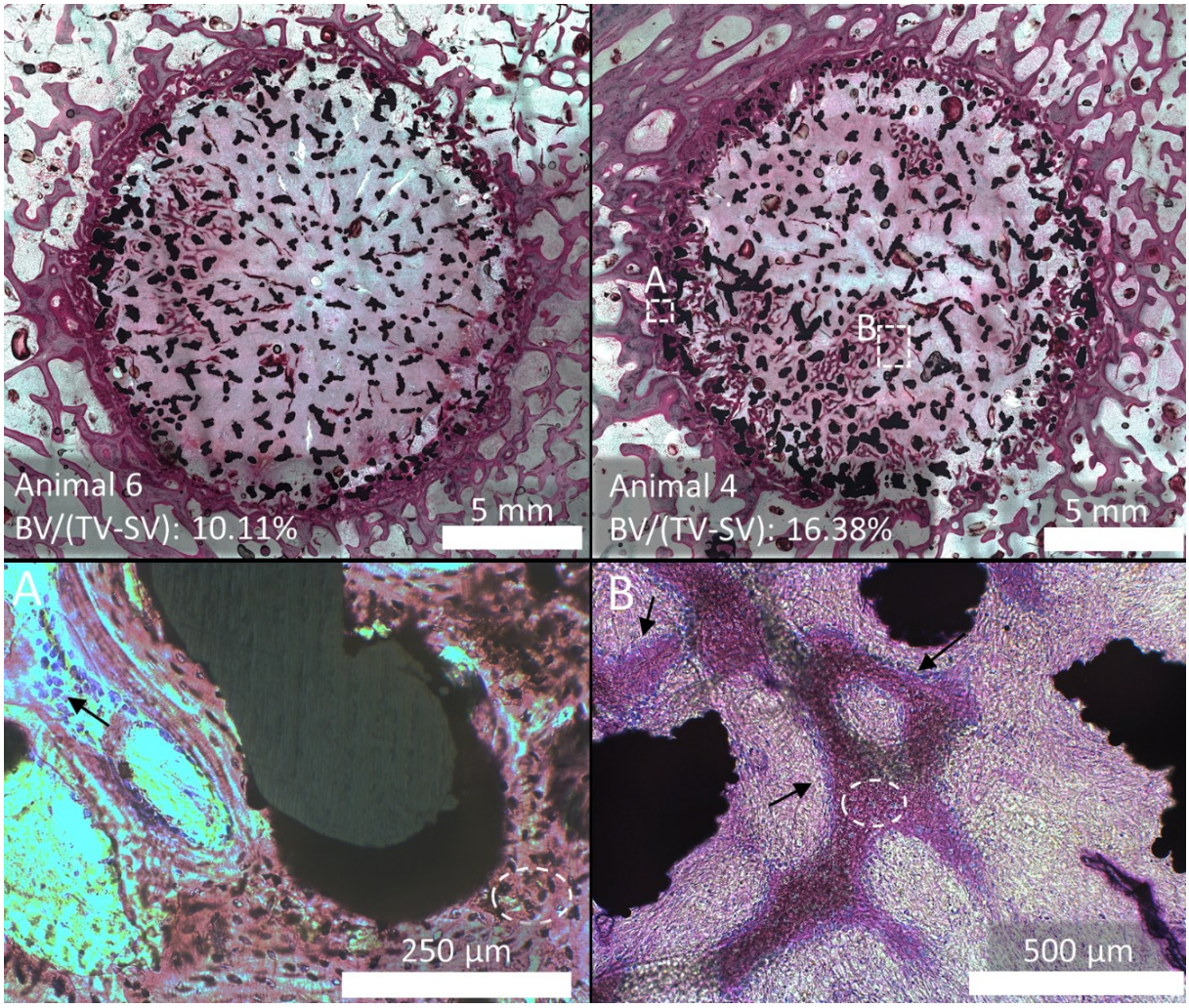


Figure 6.16 – Histology Images for animals 4 and 6. A and B are magnified sections of the scaffold periphery and interior respectively. Osteoblasts are indicated by arrows, osteocytes are circled.

Scanning electron microscopy images obtained with a back-scattered detector confirmed the histological findings. Figure 6.17 illustrates fine branching networks of woven bone within the titanium scaffolds. These bone formations contained irregularly shaped osteocytes, characteristic of woven bone (Figure 6.17b). The variability between contact between the scaffold and bone is also clearly seen, sometimes bone will engulf the scaffold elements without intimate contact (Figure 6.17a), whilst there is also evidence of bone on-growth onto some scaffold elements (Figure 6.17c) and furthermore in areas where newly formed bone is present, the bone has no to little association with the scaffold (Figure 6.17b). The SEM back-scatter detector also highlights mineral density, thus the areas of newly formed bone have a less dense organization and a lower degree of mineralization leading to a darker appearance. On the scaffold periphery at the scaffold-bone interface, where more developed and mature woven bone is present, a denser woven – lamellar bone structure is seen. The mature

woven bone is characterised by a higher degree of mineralization and appears brighter (Figure 6.17a and Figure 6.17b).

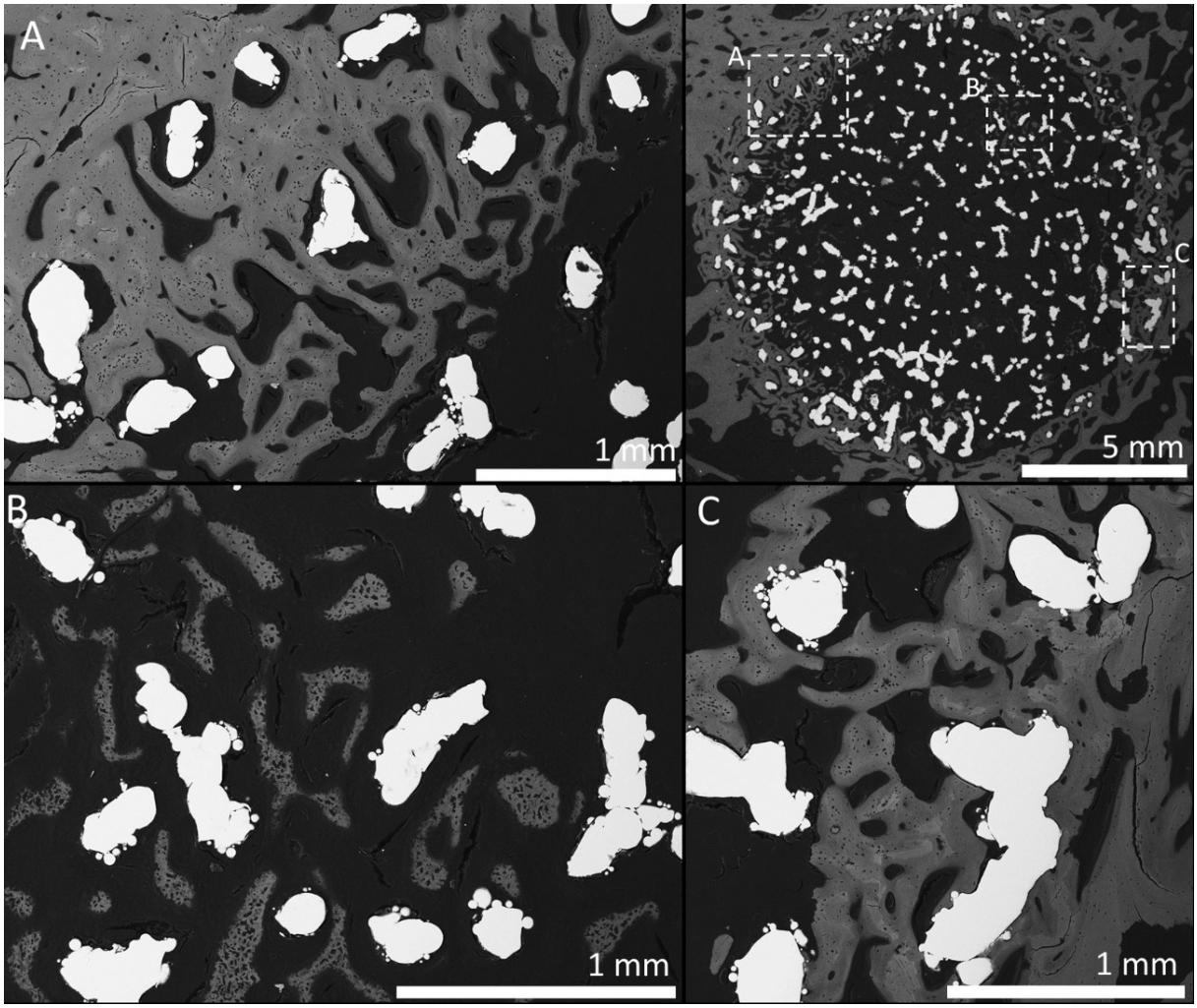


Figure 6.17 – BSEM Images of Animal 4. A and C) Scaffold periphery: older (brighter) woven bone is seen overlaid by lamellar bone. Both complete engulfing of strut elements and intimate contact between strut and bone are observed. B) Scaffold interior: new embryonic-looking woven bone is seen with a lower degree of mineralization thus a darker appearance

6.3 Discussion

This study has presented a method to create implantable devices with a tailored stiffness gradient that controls the local strain environment to invoke and test a desired mechanobiological response from bone. The modulus and strength of trabecular bone from the medial condyle of skeletally mature ewes was characterised and by utilising a clinical CT protocol with a calibrated multi-material phantom a continuous relationship was established between apparent density and modulus. Consequently, a porous scaffold was produced to maintain the mechanical environment of homeostasis at the surgical site, i.e. a 0% strain difference between scaffold and bone it would be replacing. The short term *in vivo* performance of the scaffold in a load bearing environment was seen. The average bone ingrowth into the scaffolds pores was 10.73±2.97% after 6 weeks. To be able to translate *in vivo* testing in animals to humans and to compare results between studies related to bone healing and bone ingrowth, the mechanical environment should be considered and should replicate conditions close to clinical practise. The goal of this study was not to maximise bone ingrowth into a porous scaffold but rather to provide a methodology to better test the mechanobiology of bone. For this reason no bioactive additives, coatings and fillers, or cells and cell derived factors were used. Yet, this study has demonstrated that an additively manufactured porous titanium scaffold that is stiffness-matched to the bone it is replacing is a suitable solution for repairing large bone defects; and by further tailoring the stiffness of the scaffold a desired strain in the bone can be produced to maximise the speed and quantity of bone repair [2, 4, 5]. The type of approach presented, could lead to patient specific or cohort specific implants, for example implants that either, take advantage of the higher healing capacity of younger active patients and provide very low stiffness porous implants that accelerate bone regeneration or consider the poorer bone quality of older patients and provide more load bearing and durable implants. As well as moving towards porous structures mechanically tuned to specific anatomical locations to either reduce stress-shielding or to improve bone repair.

6.3.1 Mechanical Response of Trabecular Bone and AM Porous Materials

The behaviour of the trabecular bone tested and of the porous CP-Ti specimens were typical of open-cell stochastic materials [11]. The use of a hysteresis loop or preconditioning remains contentious in bone testing [12]. For porous metal specimens, a hysteresis loop is necessary as surface strain measurements have indicated that there is localised plasticity in the specimen at stresses well below the compressive strength of the foam, reducing the slope of the initial loading curve [13]. From the stress-strain plots in Figure 6.5 it is clear that stiffness measured

from the initial loading curve vs. the hysteresis loop will give different results, however to reduce structural edge effects and since bone is a material that is constantly under cyclic loading it seems appropriate to obtain stiffness from a hysteresis loop.

As bone is responsive to the loading environment, it has been found that the structure and density of trabecular bone will vary with anatomical site [7, 10, 14]. Regardless of the structure, the relationship between strength, modulus and relative density of bone or any porous structures has been described by models developed by Gibson and Ashby and detailed earlier. With relative stress/strength and relative modulus both being proportional to relative density to a power exponent $\frac{\sigma}{\sigma_0} \propto \left(\frac{\rho}{\rho_0}\right)^n$ and $\frac{E}{E_0} \propto \left(\frac{\rho}{\rho_0}\right)^m$ respectively and relative strength being proportional to relative modulus to a power exponent ($\frac{\sigma}{\sigma_0} \propto \left(\frac{E}{E_0}\right)^{\frac{n}{m}}$). These relationships have been found to be true for the porous metal structures tested in this research (Chapters 4, 5 and Appendix B) as well as by other authors in literature [15, 16]. These relationships also accurately describe the trends seen in Figure 6.6a and Figure 6.7 for trabecular bone. It is important to note that the bone relationships are not only animal specific but potentially site-specific and for on-axis loading only. It has been found that there is no single, universal modulus-density relationship across anatomic sites for on-axis loading, as predicted values of modulus at a given apparent density can differ between sites by 49% [14].

The mechanical testing results also highlight one of the key aspects of trabecular bone as a material; and that is its high strength to stiffness ratio. At high porosity (low relative density) and thus low stiffness, the strength-to-stiffness ratio of bone was on average 24% ± 2% S.D. difference greater than the porous CP-Ti specimens. Previously in Chapter 5 it was shown that statically Ti64 has a 45% difference greater strength-to-stiffness than CP-Ti however in high cycle fatigue however CP-Ti was seen to have a 19% difference greater fatigue strength-to-stiffness and thus was the preferred alloy for this study, in addition to lower infection risks. Materials such as tantalum or titanium-tantalum alloys may be even better suited for low stiffness porous scaffolds that require high cyclic fatigue strength [17, 18] as seen in Chapter 5, however, CP-Ti was chosen as the implant material due to the requirements of quantifying bone ingrowth via tomographic imaging and in order to make comparisons to an associated study [5].

6.3.2 *In Vivo* Performance of Stiffness-matched Scaffolds

There is difficulty in comparing *in vivo* studies as different animal models, study lengths and implantation sites and sizes are used; combined with varying mechanical properties of scaffolds there will be different biomechanical environments. A similar defect location and size was also used in an ovine model, however bone ingrowth was only studied in an empty defect [19]. This model naturally has a far higher modulus difference between the original bone and the empty defect when compared to the original bone and the stiffness-matched porous scaffold. Consequently, they found greater bone ingrowth, BV/TV of 17.7% than this study. However, the bone was given a radiographic score of 1 (no visible bone formation within the defect, radiographic density considerably less than adjacent bone), all the new bone was centred around the periphery of the defect, whilst the centre was filled with fibrous tissue. In a related study to this work, different scaffold materials, porous architectures and moduli were investigated in an identical ovine model. The study reported two mechanisms of osteogenesis; that regardless of scaffold stiffness bone regeneration around the periphery of the bone-implant interface was consistent however bone ingrowth deep into the scaffold interior was inversely correlated to scaffold stiffness with the lower the stiffness of the scaffold the greater the bone ingrowth [5]. The low stiffness (~200 MPa) scaffolds from the related study were significantly less stiff than the bone they were replacing (Table 6.1) and lamellar bone was seen both on the periphery and deep within the scaffold.

The short 6 week study length allowed for a snapshot of bone regeneration to be observed. Embryonic-looking woven bone in the interior of scaffolds to more developed and mature structure of woven bone overlaid with lamellar bone at the periphery of the bone-implant interface were present (Figure 6.17). The structure and function of woven bone differs from lamellar bone, woven bone is a trait of the initial, transient stage of osteogenesis and can be initiated by events such as an injury response or in foetal development. Thus, it normally precedes lamellar bone, in order to provide anchorage and be a suitable substrate for deposition of lamellar bone [20]. Whilst its mechanical properties are inferior to lamellar bone, woven bones provides a biological scaffold whose properties can be adapted by deposition of lamellar bone. “True osteoinduction” is the term used to describe the formation of woven bone within a fracture callus not associated with existing trabeculae. This also accurately describes the networks of woven bone within select scaffold interiors that were dissociated from the struts of the porous scaffold. Conversely, lamellar bone occurs as an adaptive response [21] and is typically deposited in response to bone strain exceeding about 0.1% [22]. This is consistent

with the findings of the study, the stiffness-matched scaffold which was designed to maintain homeostasis saw little amounts of lamellar bone formation, whilst for scaffolds significantly less stiff than the bone it was replacing, such as in [5] vast amounts of lamellar bone were present due to the mechanical demands.

A similar pathway of bone regeneration was also found for porous titanium additively manufactured scaffolds implanted in the cortical bone of a critical segmental sized defect mid-tibia in an ovine model [4]. The study recapitulated the postulated "two waves theory" of cortical bone growth in an unimpaired defect healing situation [20, 23]. Bone regeneration was found to begin with woven bone, which also showed a less organised and less mineralised structure, whereas the older bone at the interface between adjacent tibia and scaffold had already been augmented and overlaid with lamellar bone. Thus, the initially highly porous primary bone structure served as an endogenous scaffold to direct the formation of lamellar bone with improved mechanical properties. The results of the study also supported the consideration of mechanobiology and found the lower the stiffness of the implant the greater the bone ingrowth. [4]

6.3.3 Limitations

There are a number of improvements that could be made to this study. Firstly, the locally stiffness-matched scaffold was designed based on an *ex-vivo* cohort and not tailored on a sheep by sheep basis. Variability in bone ingrowth can be explained by a number of factors including the capacity for mechanosensation of the host, age and physical activity of the animal, although in this study neither the individual nor group levels of mobility of the sheep were monitored [24, 25]. It has been reported that in sheep there is high variations in load at the knee, and that the inter-subject variation, which was also representative of human subjects, was attributed to individual gait patterns [26]. In this study, the apparent density, modulus and strength results (Figure 6.6 and Figure 6.7) for the ovine bone mechanically tested showed a wide spread of data despite the trends for apparent density vs. modulus and modulus vs. strength having high correlation coefficients. Therefore to better ensure a 0% strain difference between the scaffold and bone and that the local biomechanical demands for each individual subject were taken into account, each sheep could have been CT-scanned prior to surgery and based on those apparent density values a custom (patient-specific) scaffold could have been manufactured utilising the apparent-density modulus relationship derived earlier.

A limitation to the bone property quantification portion of this study is the large specimen size required for mechanical testing (⌀5×10 mm), particularly relative to the fine CT-Scan resolution (0.5 mm voxels). The specimen size is necessary for accurate mechanical testing, as in order for a cellular structure to behave as a continuum and not be effected by individual trabeculae or edge effects of the structure it must be of sufficient size [12]. However, since trabecular bone varies locally, as is evident when looking at the apparent density, the results of the mechanical testing will reflect the least stiff and weakest portion of the bone core and not necessarily the average of the entire bone core.

Another limitation was that bone and the porous scaffold were only stiffness-matched in 1 direction, for bone that was along the mechanical axis of the femur and for the porous scaffolds it was along the build direction. The isotropy or anisotropy of both the porous scaffolds and the bone in the medial femoral condyle needs to be characterised in order to truly ensure a 0% (or whatever the strain gradient being tested) strain difference in all directions. Also no mechanical validation was performed of the stiffness matched lattice to measure whether the desired moduli were achieved in each respective section. There are many challenges to test a functionally graded or variable stiffness structure and thus new test methodologies or validation methods would need to be developed.

Finally during surgery, patient specific drill guides could have been used to better standardise defect locations and sheep weights and activity could be better monitored. The last consideration regarding this study is how much the modulus of the base material of the porous scaffold and the resulting stiffness mismatch between the individual titanium struts and bone trabeculae affects bone ingrowth. It is likely reducing this mismatch would improve osseointegration into the scaffold and on-growth onto the strut elements.

6.4 Summary

- This chapter has demonstrated a workflow to not only more accurately test the mechanobiology of bone in response to an implanted porous scaffold, but to test any variable of a porous scaffold whilst maintaining consideration of the mechanical environment.
- The apparent density and modulus of trabecular bone in the medial femoral condyle of skeletally mature ewes was characterised by utilising a clinical CT protocol with a calibrated multi-material phantom and mechanical testing. Apparent density ranged from 0.2 to 0.8 g/cm^3 whilst modulus ranged between 56.5 and 2,737.7 MPa
- A power law relationship was observed between apparent density and modulus of the trabecular bone cores as well as between yield strength and modulus.
- The cancellous bone data for the ovine medial femoral condyle was combined with ovine femoral cortical bone data (reported in [9]) with a linear interpolation between the two datasets to produce a continuous relationship covering the entire apparent density range of ovine bone.
- The bone cores displayed greater strength-to-stiffness than the uniform moduli porous CP-Ti scaffolds (Chapter 5) by 24%.
- The variation in stiffness was mapped at a fine resolution locally in the medial condyle of sheep at the surgical site, discretised into 27 sections, based on the previously established apparent-density modulus relationship.
    - Apparent density for the surgical site ranged on average from 0.27 to 0.76 g/cm^3 with a modulus varying between 198.2 and 2,588.0 MPa respectively. Average modulus was 1383.5 MPa across the 27 sections.
- A stochastic porous scaffold intended to maintain mechanical homeostasis was designed and manufactured. The scaffold had equivalent stiffness and stiffness variation as the bone it would be replacing.
    - The produced scaffold had a modulus ranging from 566.0 to 3584.4 MPa with an average modulus over the 27 sections of 1435.2 MPa.
- Scaffolds were implanted into the medial femoral condyle of 6 ewes.
- The average bone ingrowth into the scaffolds pores was 10.73±2.97% after 6 weeks and displayed various stages of bone development from fine embryonic-looking woven bone in the interior of the scaffold to more developed and mature bone structure of

intense formations of fine woven bone overlaid with lamellar bone at the implant-bone interface.

- The clinically applicable and pragmatic workflow presented will allow future *in vivo* testing to test specific bone strains on bone ingrowth in response to a scaffold and allow for better translation from *in vivo* testing to commercial implants.

6.5 References

[1] X. Wang, S. Xu, S. Zhou, W. Xu, M. Leary, P. Choong, M. Qian, M. Brandt, Y.M. Xie, Topological design and additive manufacturing of porous metals for bone scaffolds and orthopaedic implants: A review, Biomaterials 83 (2016) 127-141.

[2] J. Wieding, T. Lindner, P. Bergschmidt, R. Bader, Biomechanical stability of novel mechanically adapted open-porous titanium scaffolds in metatarsal bone defects of sheep, Biomaterials 46 (2015) 35-47.

[3] S. Wu, X. Liu, K.W.K. Yeung, C. Liu, X. Yang, Biomimetic porous scaffolds for bone tissue engineering, Materials Science and Engineering: R: Reports 80 (2014) 1-36.

[4] A.-M. Pobloth, S. Checa, H. Razi, A. Petersen, J.C. Weaver, K. Schmidt-Bleek, M. Windolf, A.Á. Tatai, C.P. Roth, K.-D. Schaser, G.N. Duda, P. Schwabe, Mechanobiologically optimized 3D titanium-mesh scaffolds enhance bone regeneration in critical segmental defects in sheep, Science Translational Medicine 10(423) (2018).

[5] N. Reznikov, O.R. Boughton, S. Ghouse, A.E. Weston, L. Collinson, G.W. Blunn, J. Jeffers, J.P. Cobb, M.M. Stevens, Individual response variations in scaffold-guided bone regeneration are determined by independent strain- and injury-induced mechanisms, Biomaterials 194 (2019) 183-194.

[6] M. Tuncer, U.N. Hansen, A.A. Amis, Prediction of structural failure of tibial bone models under physiological loads: Effect of CT density–modulus relationships, Medical Engineering & Physics 36(8) (2014) 991-997.

[7] S.A. Goldstein, The mechanical properties of trabecular bone: Dependence on anatomic location and function, Journal of Biomechanics 20(11–12) (1987) 1055-1061.

[8] K. Alvarez, H. Nakajima, Metallic Scaffolds for Bone Regeneration, Materials 2(3) (2009) 790.

[9] C.A. Grant, L.J. Wilson, C. Langton, D. Epari, Comparison of mechanical and ultrasound elastic modulus of ovine tibial cortical bone, Medical Engineering & Physics 36(7) (2014) 869-874.

[10] L.J. Gibson, The mechanical behaviour of cancellous bone, Journal of Biomechanics 18(5) (1985) 317-328.

[11] L.J. Gibson, Cellular solids : structure and properties, 2nd ed., Cambridge University Press, Cambridge, 1999.

[12] R.M. Aspden, Mechanical Testing of Bone Ex Vivo, in: M.H. Helfrich, S.H. Ralston (Eds.), Bone Research Protocols, Humana Press, Totowa, NJ, 2003, pp. 369-379.

[13] M.F. Ashby, A.G. Evans, N.A. Fleck, L.J. Gibson, J.W. Hutchinson, H.N.G. Wadley, Metal Foams: A Design Guide, Butterworth-Heinemann, Burlington, 2000.

[14] E.F. Morgan, H.H. Bayraktar, T.M. Keaveny, Trabecular bone modulus–density relationships depend on anatomic site, Journal of Biomechanics 36(7) (2003) 897-904.

[15] C. Yan, L. Hao, A. Hussein, P. Young, D. Raymont, Advanced lightweight 316L stainless steel cellular lattice structures fabricated via selective laser melting, Materials & Design 55 (2014) 533-541.

[16] C. Yan, L. Hao, A. Hussein, S.L. Bubb, P. Young, D. Raymont, Evaluation of light-weight AlSi10Mg periodic cellular lattice structures fabricated via direct metal laser sintering, Journal of Materials Processing Technology 214(4) (2014) 856-864.

[17] Y.-L. Zhou, M. Niinomi, T. Akahori, M. Nakai, H. Fukui, Comparison of Various Properties between Titanium-Tantalum Alloy and Pure Titanium for Biomedical Applications, Materials Transactions 48(3) (2007) 380-384.

[18] S.L. Sing, W.Y. Yeong, F.E. Wiria, Selective laser melting of titanium alloy with 50 wt% tantalum: Microstructure and mechanical properties, Journal of Alloys and Compounds 660 (2016) 461-470.

[19] A. Malhotra, M.H. Pelletier, Y. Yu, C. Christou, W.R. Walsh, A Sheep Model for Cancellous Bone Healing, Frontiers in Surgery 1(37) (2014).

[20] M. Kerschnitzki, W. Wagermaier, Y. Liu, P. Roschger, G.N. Duda, P. Fratzl, Poorly Ordered Bone as an Endogenous Scaffold for the Deposition of Highly Oriented Lamellar Tissue in Rapidly Growing Ovine Bone, Cells Tissues Organs 194(2-4) (2011) 119-123.

[21] S.H. McBride, M.J. Silva, Adaptive and injury response of bone to mechanical loading, BoneKEy Reports 1 (2012) 192.

[22] C.H. Turner, M.R. Forwood, J.-Y. Rho, T. Yoshikawa, Mechanical loading thresholds for lamellar and woven bone formation, Journal of Bone and Mineral Research 9(1) (1994) 87-97.

[23] Y. Liu, I. Manjubala, H. Schell, D.R. Epari, P. Roschger, G.N. Duda, P. Fratzl, Size and habit of mineral particles in bone and mineralized callus during bone healing in sheep, Journal of Bone and Mineral Research 25(9) (2010) 2029-2038.

[24] L. Bonewald, Osteocytes, Muscle and Exercise: Role in Healthy Aging, The FASEB Journal 31(1_supplement) (2017) 7.2-7.2.

[25] Y. Kitase, J.A. Vallejo, W. Gutheil, H. Vemula, K. Jähn, J. Yi, J. Zhou, M. Brotto, L.F. Bonewald, β-aminoisobutyric Acid, L-BAIBA, Is a Muscle-Derived Osteocyte Survival Factor, Cell reports 22(6) (2018) 1531-1544.

[26] J.M. Rosvold, M. Atarod, B.J. Heard, E.J. O'Brien, C.B. Frank, N.G. Shrive, Ligament and meniscus loading in the ovine stifle joint during normal gait, The Knee 23(1) (2016) 70-77.

7 Chapter 7 – Conclusion and Future Work

The overall aims of this research were to maximise the mechanical performance, both quasi-statically and in high-cycle fatigue, of architectured porous structures produced by powder bed fusion for application as a bone in-growth implant and to present a clinically applicable and pragmatic approach to the design, development and *in vivo* testing of the mechanobiology of bone in response to a porous scaffold. The research completed throughout this thesis has included a number of novel studies and investigations. The impact of which will further the development, adoption and improvement of additively manufactured porous structures where mechanical strength is paramount. This chapter will summarise the work produced in this thesis, make concluding statements and discuss future avenues for research.

7.1 Conclusions

As the future of architectured material generation is likely to move from solid CAD modelling, which is computationally expensive, to line based representation it is imperative to know how laser parameters and scan strategy relate to strut thickness and consequently if any process parameters rules can be utilised to maximise strength. The initial finding of this thesis showed that using specific enthalpy equations instead of traditional energy density equations can produce a far more accurate and scalable model relating strut thickness to the laser parameters. Whilst the model has limitations and will not be as accurate as a FEA/CFD model it allows engineers a quick tool to more accurately know what the effect on strut size will be with respect to a change in laser parameters without building a large array of specimens.

It was also shown that the mechanical properties of a porous structure produced by powder bed fusion are not only affected by its geometric properties (strut thickness, density, internal porosity etc.) but also by its method of manufacture. The method and rate of energy delivery and laser scan strategy had a significant effect on the strength of a stochastic porous structure for a given stiffness or density. When optimising laser parameters and scan strategy for a porous structure it was found that the optimum method of energy delivery is material dependent. Therefore it is vital to understand the effect of laser parameters (and consequently on cooling) on microstructure and texture and that must be done on a material by material basis. The effect of laser parameters and scan strategy on high cycle fatigue strength of AM porous structures was also explored and quantified. Optimisation of the laser parameters was found to increase the fatigue strength for a given stiffness of porous AM structures by 7% whilst it was

seen that building with a contour strategy produced structures with a greater fatigue strength for a given stiffness by 8%, compared to the points and pulsing strategies.

This work has demonstrated that the trends observed during fatigue testing for monolithic metals and statically for solid and porous structures are not always indicative of the high cycle fatigue behaviour of porous additively manufactured materials. The static strength and fatigue strength to stiffness ratio of common orthopaedic biomaterials (CP-Ti, Ti64 and Ta) and a TiTa alloy were reported. Statically it was seen that Ti64 had the greatest strength for a given stiffness, Ti64 had a greater σ_y:E than TiTa by 9%, 38% greater than Ta and 45% greater than CP-Ti. The strength:stiffness trends seen statically for the porous structures match those that have been reported for their solid counterparts. However, unlike their solid counterparts, porous Ta and TiTa had the greatest fatigue strength for a given stiffness, 8% greater than CP-Ti and 19% greater than Ti64. Therefore, not only do the mechanical properties of the parent material need to be considered when choosing a material to maximise the high cycle fatigue behaviour of porous AM structures. It is also vital to consider notch sensitivity, ductility, internal porosity and microstructure of the material.

Finally, this work has presented a workflow to more accurately test the mechanobiology of bone in response to an implanted porous scaffold. The work has also highlighted the importance of knowing the properties of the bone being replaced in order to drive the design of the mechanical properties of a porous scaffold. By characterising the local variation of trabecular bone properties in the medial femoral condyle of skeletally mature ewes a scaffold was created that matched the variations in moduli. The difficulty in material selection for porous scaffolds was also evident as the trabecular bone tested displayed higher strength at a given stiffness compared to commercially pure titanium porous scaffolds. The short term *in vivo* performance of the locally stiffness matched scaffold (i.e. to maintain mechanical homeostasis) in a load bearing environment was seen. The average bone in-growth into the scaffolds pores was 10.73±2.97% after 6 weeks and displayed various stages of bone development from fine embryonic-looking woven bone in the interior of the scaffold to more developed and older bone structure of intense formations of fine woven bone overlaid with lamellar bone at the implant-bone interface. The clinically applicable and pragmatic workflow presented in this study will allow future *in vivo* testing to test specific local strain/modulus differences between a porous scaffold and bone. This is in contrast as opposed to the global differences that have been tested historically and should allow for better translation from *in-vivo* testing to commercial implants.

Ultimately potentially leading to porous structures mechanically tuned to specific anatomical locations to either reduce stress-shielding or to improve bone repair. And porous implants tuned to patients or cohort groups; in order to, for example, take advantage of the higher healing capacity of younger active patients and provide very low stiffness porous implants that accelerate bone regeneration or consider the poorer bone quality of older patients and provide more load bearing and durable implants.

7.2 Future Work

The work carried out during this thesis and the conclusions found lead to many future avenues for research, which are detailed below.

7.2.1 Microstructure and Cooling Rates

The focus of this thesis was on mechanical performance of stochastic additively manufactured structures. One of the root causes behind strength differences for a given stiffness between samples built via different laser powers or scanning strategies was deemed to be microstructure. The initial microstructural analysis and EBSD suggest varying the laser parameters and scanning strategies lead to differences in texture and probably grain sizes/morphology, likely caused by changes in cooling rates. Therefore, a more detailed study of microstructure due to different laser parameters and scanning strategies is required. Specifically looking at grain size, grain size distribution, quantity and constitution of phases present and texture. This analysis can be extended by looking at how microstructure and texture change with angle of strut and nodal junctions.

Utilising the two camera setup as described in Chapter 3, allows the temperature of the melt-pool to be measured and consequently cooling rates can be measured as well. Mechanical strength is affected by changes in microstructure which in LBPF is heavily influenced by the cooling rates from melting back to solid. An experiment building and tensile testing single struts manufactured via the points, contour and pulsing strategies and at high and low powers, should be able to tie together how different cooling rates produce specific microstructures and change grain size, grain morphology etc. and ultimately alter the tensile strength of the struts as well. Possibly some minor differences in Young's modulus may be observed as well due to quantity of phases present.

7.2.2 Thermal Post-Processing

All specimens built in this study were in the as-built condition and likely suffer from some residual stress, although it is unlikely that a great deal of thermal stresses are built up in

small porous parts. Also, the amount of residual stress built up in components will be material specific, and so comparison between materials in Chapter 5 may not have been made between materials in the exact same condition. In addition, standards for titanium's use as a medical implants, states that the microstructure must not contain α' acicular microstructure. As well, studies have shown improvements in fatigue life due to thermal treatments. Therefore, future work needs to examine thermal post-processing on both microstructure and mechanical performance. However, optimisation of thermal post-processes to attain a certain microstructure to improve fatigue strength will be material specific. Generally, any thermal post-processing will reduce static strength but will likely increase elongation whilst having negligible effects on modulus. Improvements on fatigue strength-to-modulus will need to be characterised based on different thermal heat treatments. Finally, a comparison should be made between hot isostatic pressing, which can reduce porosity, and a similar thermal heat treatment to understand the role of defect/crack reductions vs. microstructural changes on static and fatigue strength.

7.2.3 Mechanical Post-Processing

As stated in Chapters 4 and 5, fatigue crack initiation sites tend to be on the surface for additively manufactured specimens, thus future work should examine the role of improving surface finish on greater fatigue strength. Initial studies have examined acid etching and electropolishing and have found improvements in specific fatigue strength. However, the effect of mechanical post-processing on long term fatigue strength is still under-reported especially with respect to both relative density and stiffness. Novel methods to either remove semi-fused surface particles or increase the sinter-neck of semi-fused particles should also be explored.

7.2.4 Structural Optimization

A single stochastic specimen was generated for all mechanical testing with changes in relative density and modulus arising from changing the strut thickness via altering the laser parameters and scanning strategies or changing the base material. Initial investigations have suggested that altering the connectivity of the stochastic structure changes the strength-to-stiffness and strength-to-weight, with the lower the connectivity the better the strength-to-stiffness. Future work needs to investigate why this is the case and what the role of connectivity is on fatigue strength with respect to both stiffness and weight. In addition to this, for a given unique specimen, a single laser parameter was applied to all struts regardless of strut angle. Chapters 4 and 5, indicates that for a given laser parameters the lower the angle of the strut the greater the thickness, therefore investigating the effect of varying the laser parameters on

different strut angles on mechanical optimisation and isotropy/anisotropy should be considered. E.g. Increasing the thickness of vertical struts relative to lower angle struts will likely increase stiffness and anisotropy, however it remains unclear what the effect on fatigue strength and strength-to-stiffness would be.

7.2.5 Titanium – Tantalum Alloys

There is also greater scope for more investigation into AM titanium-tantalum alloys. The titanium-tantalum structures produced in this work were made from blended titanium and tantalum powders in a ratio chosen based on maximising strength-to-stiffness, with high elongation and low cost. The first improvement to this should be manufacturing samples from pre-alloyed powder, which would likely produce better and more consistent mechanical properties and microstructure. Also, the effect of tantalum ratio in titanium on high cycle fatigue strength with respect to stiffness should be investigated; as historic testing has typically only performed tensile testing and microstructure analysis when investigating the effect of tantalum ratio in a titanium alloy.

7.2.6 Fatigue Strength

The fatigue strength testing performed in this work was limited by the number of variables that were tested and was used primarily for comparative purposes. To better characterise the long-term behaviour of these structures and better understand their probability of failure in orthopaedic applications, more samples (~n=30) per unique specimen should be tested and at even longer cycles to failure (10 million).

7.2.7 *In Vivo* Testing

As stated in the limitations in Chapter 6, the locally stiffness-matched scaffolds were designed based on an *ex-vivo* population. To better maintain mechanical homeostasis or to better test the mechanobiology of bone, patient specific stiffness matched implants should be produced. Other improvements to the locally stiffness-matched scaffold can include matching the properties of bone in more than one direction (i.e. matching the anisotropy), and developing better methods to locally quantify bone properties (i.e. digital image or volume correlation, ultrasound testing) as the resolution (size of the bone cores) for mechanical testing is relatively coarse when compared to the CT-scanning resolution.

Future work should also look at testing for specific bone strains (modulus differences) as opposed to for mechanical homeostasis. Future *in vivo* studies should also try to characterise and monitor activity level as well as the weight of the sheep in order to try and normalise any

variation in ingrowth results based on load passing through the defect which will vary by sheep. Also, the short-term vs. long term differences in scaffolds which produce different bone strains can also be looked into. In order to better understand the requirement for fatigue strength of porous scaffolds the local mechanical environment should be better characterised, i.e. the local stress due to daily activities such as walking, running etc. Finally, the workflow developed and consideration of mechanobiology now allows for better testing of variables such as pore size, porosity, strut size, pore shape, porous architecture, surface modifications and different alloys; all whilst trying to maintain equivalent mechanical properties between scaffolds and thus these geometric and structural scaffold properties should be investigated again under these considerations.

7.3 List of Publications

Throughout the course of this research a number of publications were produced and conference presentations were given. The following is the list of international peer reviewed journal papers accepted and under review and conference presentations given.

1st Author:

S. Ghouse, S. Babu, R.J. Van Arkel, K. Nai, P.A. Hooper, J.R.T. Jeffers, The Influence of Laser Parameters and Scanning Strategies on the Mechanical Properties of a Stochastic Porous structure, Materials & Design 131 (2017) 498-508.

S. Ghouse, S. Babu, K. Nai, P.A. Hooper, J.R.T. Jeffers, The influence of laser parameters, scanning strategies and material on the fatigue strength of a stochastic porous structure, Additive Manufacturing 22 (2018) 290-301.

S. Ghouse, N. Reznikov, O.R. Boughton, S. Babu, K.C.G. Ng, G. Blunn, J.P. Cobb, M.M. Stevens, J.R.T. Jeffers, The Design and *in vivo* testing of a locally stiffness-matched porous scaffold, Applied Materials Today (2019)

Co-Author:

R.J. van Arkel, **S. Ghouse,** P.E. Milner, and J.R.T. Jeffers, Additive manufactured push-fit implant fixation with screw-strength pull out. J. Orthopaedic Research 36 (2018) 1508-1518

N. Reznikov, O.R. Boughton, **S. Ghouse**, A. Weston, L. Collinson, G. Blunn, J.R.T. Jeffers, J.P. Cobb, M.M. Stevens, Individual response variations in scaffold-guided bone regeneration are determined by independent strain- and injury-induced mechanisms, Biomaterials 194 (2019) 183-194

Conference Presentations:

S. Ghouse, S. Babu, R.J. Van Arkel, K. Nai, P.A. Hooper, J.R.T. Jeffers, The Influence of SLM Laser Parameters on the Mechanical Properties of Porous Structures, Imperial Lattice Symposium 2016

S. Ghouse, R.V. Arkel, S. Babu, K. Nai, P. Hooper, J. Jeffers, Can Additive Manufactured Structures Replace Trabecular Bone in Load Bearing Situations?, International Society for Technology in Arthroplasty 2016

S. Ghouse, N. Reznikov, O.R. Boughton, G. Blunn, J.P. Cobb, M.M. Stevens, J.R.T. Jeffers , Osseointegration of Load Bearing Additive Manufactured Scaffolds in an ovine femoral condyle defect model, Orthopaedic Research Society 2018

S. Ghouse, N. Reznikov, O.R. Boughton, S. Babu, K.C.G. Ng, G. Blunn, J.P. Cobb, M.M. Stevens, J.R.T. Jeffers , The Design and *in vivo* Testing of a Locally Stiffness Matched Porous Scaffold, International Society for Technology in Arthroplasty 2018

8 Appendix A – Specific Enthalpy Models Raw Data

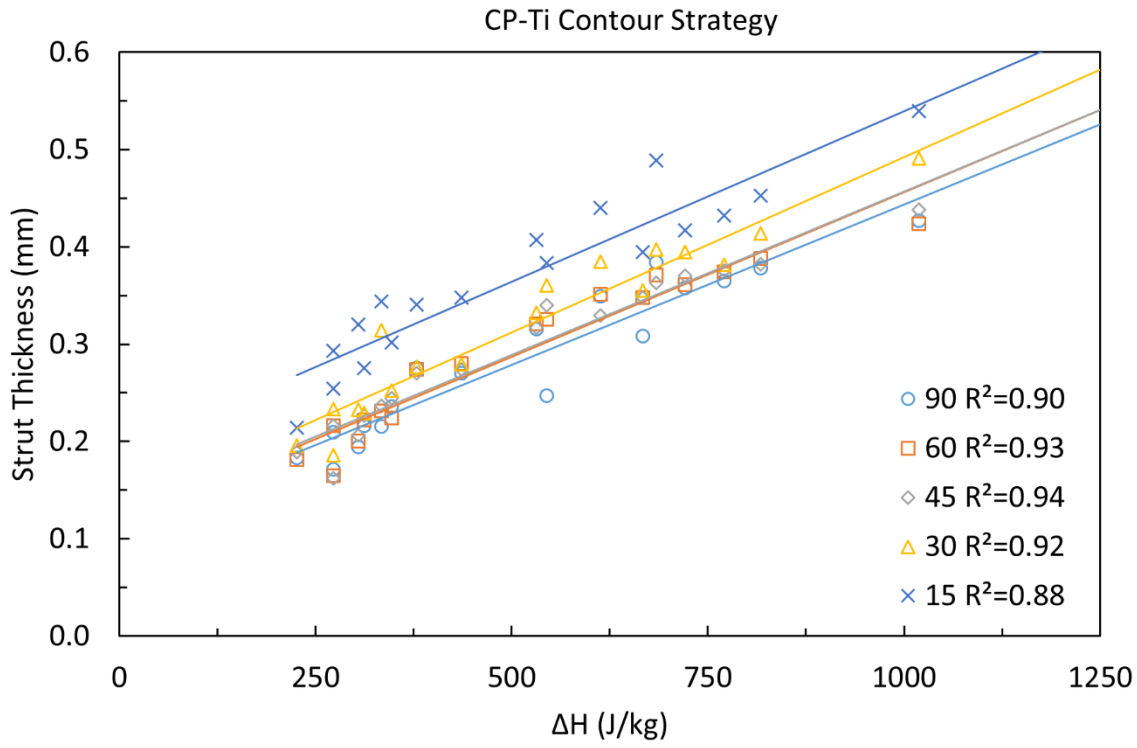
The values used to calculate specific enthalpy for the various materials are seen below, where specific enthalpy (ΔH):

$$\Delta H = \frac{A \cdot P}{\rho_0 \sqrt{\pi \cdot D \cdot u \cdot \emptyset^3}}$$

Material	A	P (kg/m^3)	D (m^2/s)
CP-Ti	0.55 [1]	4510 [2]	8.23x10^{-6} [3]
Ti64	0.45 [1]	4420 [4]	4.8x10^{-6} [3]
Ta	0.42 [1]	16600 [5]	2.35x10^{-5} [3]
TiTa	0.51 [1]	5710 [6]	1.28 x10^{-5} [3]
SS316	0.4 [7]	8100 [8]	5.38x10^{-6} [7]

The following are the strut thickness – specific enthalpy plots for all materials and strategies investigated as well the raw data used to construct the plots.

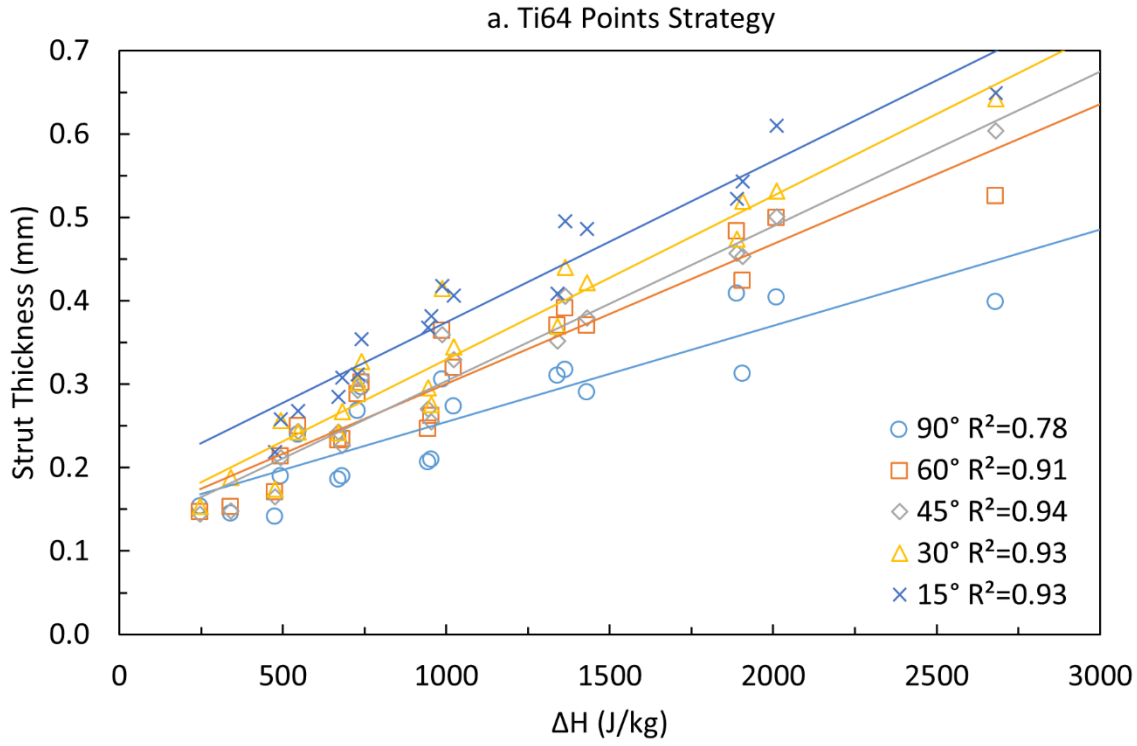
Commercially Pure – Titanium

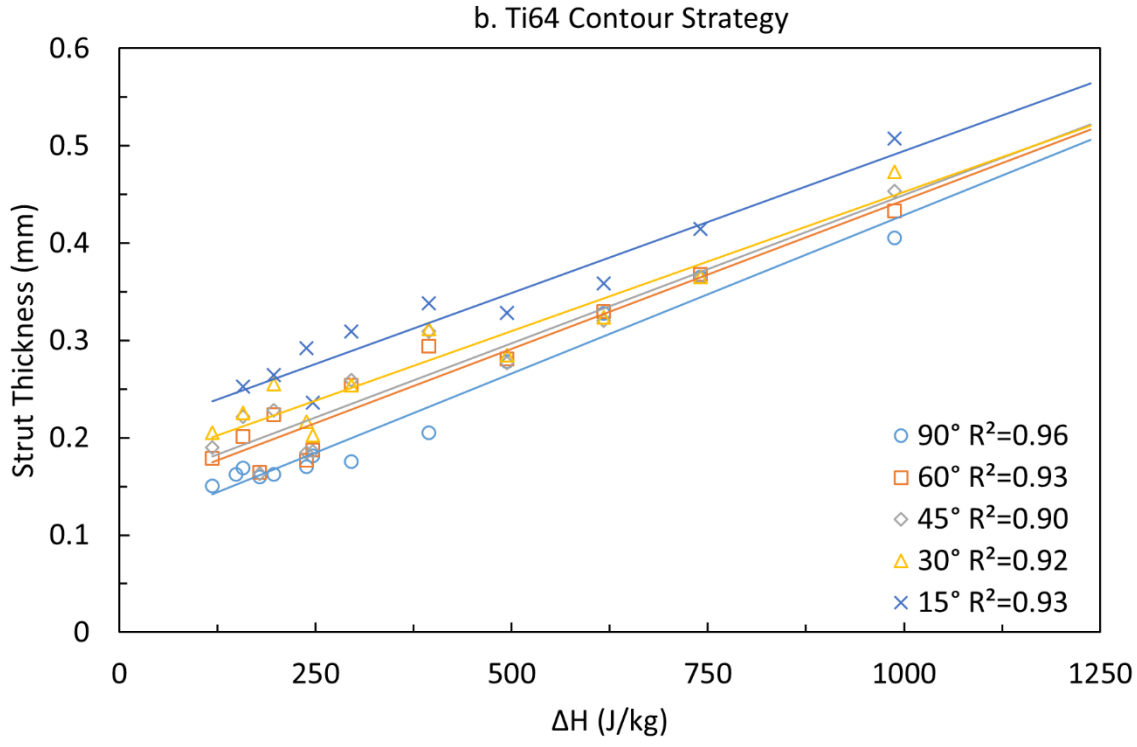


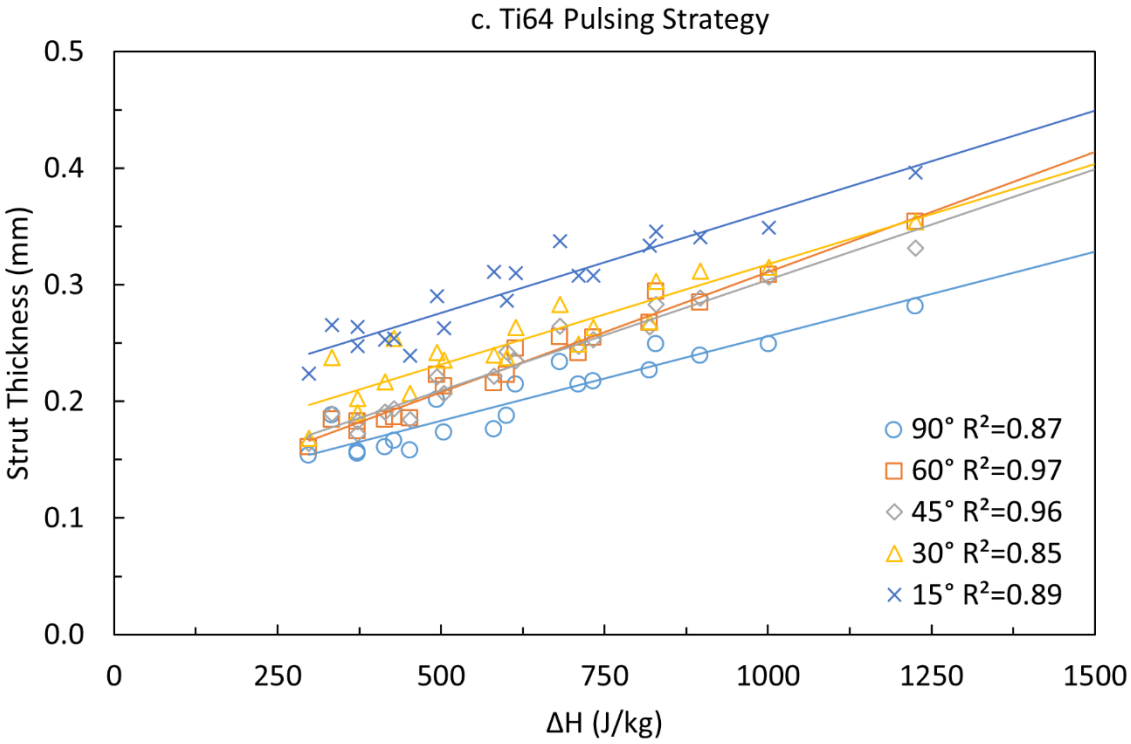
Power	Exposure Time	Point Distance	Pulsing	U	ΔH	90° Strut		60° Strut		45° Strut		30° Strut		15° Strut	
(W)	(us)	um		(m/s)		Width (mm)	S.D. (mm)	Width (mm)	S.D. (mm)	Width (mm)	S.D. (mm)	Width (mm)	S.D. (mm)	Width (mm)	S.D. (mm)
50	50	50		0.833	166.831										
50	100	50		0.455	225.890	0.183	0.014	0.181	0.014	0.189	0.016	0.196	0.019	0.214	0.018
50	150	50		0.313	272.433	0.209	0.017	0.216	0.018	0.216	0.021	0.233	0.014	0.254	0.020
50	200	50		0.238	312.112	0.216	0.014	0.222	0.017	0.227	0.011	0.229	0.022	0.275	0.025
50	250	50		0.192	347.286	0.236	0.017	0.224	0.016	0.245	0.019	0.252	0.026	0.302	0.019
50	300	50		0.161	379.211	0.276	0.022	0.274	0.028	0.270	0.013	0.277	0.024	0.340	0.021
50	400	50		0.122	436.106	0.270	0.019	0.280	0.023	0.274	0.019	0.279	0.031	0.348	0.021
50	600	50		0.082	531.943	0.316	0.014	0.321	0.030	0.317	0.030	0.332	0.023	0.407	0.020
50	800	50		0.062	612.975	0.349	0.015	0.351	0.023	0.329	0.027	0.385	0.024	0.440	0.034
50	1000	50		0.050	684.481	0.384	0.007	0.371	0.028	0.363	0.027	0.397	0.030	0.489	0.029
200	20	50		1.667	471.869										
100	30	50		1.250	272.433	0.171	0.019	0.165	0.014	0.162	0.016	0.186	0.012	0.293	0.009
100	40	50		1.000	304.590	0.194	0.019	0.200	0.014	0.206	0.010	0.233	0.019	0.320	0.018
100	50	50		0.833	333.661	0.216	0.013	0.231	0.017	0.237	0.014	0.314	0.020	0.344	0.030
200	30	50		1.250	544.867	0.247	0.019	0.326	0.026	0.340	0.020	0.360	0.029	0.383	0.025
200	50	50		0.833	667.323	0.308	0.025	0.348	0.026	0.348	0.019	0.355	0.018	0.395	0.020
200	60	50		0.714	720.791	0.358	0.011	0.361	0.019	0.370	0.020	0.395	0.020	0.417	0.015
200	70	50		0.625	770.558	0.365	0.011	0.374	0.016	0.375	0.009	0.382	0.022	0.432	0.019
200	80	50		0.556	817.300	0.378	0.013	0.388	0.004	0.382	0.005	0.414	0.025	0.453	0.016
200	130	50		0.357	1019.353	0.427	0.013	0.423	0.022	0.438	0.016	0.491	0.020	0.539	0.025

CP-Ti Contour Strategy Raw Data

Titanium – 6 Aluminium – 4 Vanadium ELI






c. Ti64 Pulsing Strategy
Strut Thickness (mm)
0.5
0.4
0.3
0.2
0.1
0.0
0
250
500
750
1000
1250
1500
ΔH (J/kg)
90° R²=0.87
60° R²=0.97
45° R²=0.96
30° R²=0.85
15° R²=0.89

Power	Exposure Time	Point Distance	Pulsing	U	ΔH	90° Strut		60° Strut		45° Strut		30° Strut		15° Strut	
(W)	(us)	um		(m/s)		Width (mm)	S.D. (mm)	Width (mm)	S.D. (mm)	Width (mm)	S.D. (mm)	Width (mm)	S.D. (mm)	Width (mm)	S.D. (mm)
50	100	50		0.455	246.934	0.154	0.015	0.148	0.019	0.144	0.022				
50	200	50		0.238	341.188	0.146	0.025	0.153	0.014	0.148	0.016	0.188	0.012		
50	400	50		0.122	476.734	0.142	0.013	0.171	0.023	0.165	0.019	0.174	0.017	0.219	0.028
50	800	50		0.062	670.080	0.186	0.016	0.233	0.014	0.243	0.011	0.242	0.028	0.285	0.027
50	1600	50		0.031	944.706	0.207	0.008	0.247	0.018	0.270	0.021	0.295	0.026	0.368	0.024
100	100	50		0.455	493.867	0.190	0.016	0.214	0.016	0.212	0.026	0.257	0.018	0.258	0.027
100	200	50		0.238	682.376	0.190	0.025	0.235	0.015	0.226	0.021	0.267	0.031	0.308	0.047
100	400	50		0.122	953.467	0.210	0.018	0.263	0.013	0.255	0.015	0.275	0.019	0.382	0.035
100	800	50		0.062	1340.159	0.311	0.017	0.371	0.018	0.351	0.017	0.370	0.035	0.409	0.048
100	1600	50		0.031	1889.412	0.409	0.033	0.484	0.023	0.457	0.022	0.474	0.028	0.522	0.038
150	50	50		0.833	547.118	0.241	0.013	0.250	0.015	0.243	0.012	0.243	0.019	0.268	0.053
150	100	50		0.455	740.801	0.297	0.018	0.303	0.020	0.308	0.012	0.327	0.014	0.354	0.044
150	200	50		0.238	1023.563	0.274	0.025	0.320	0.017	0.330	0.019	0.345	0.016	0.406	0.041
150	400	50		0.122	1430.201	0.291	0.015	0.371	0.015	0.379	0.024	0.422	0.020	0.486	0.047
150	800	50		0.062	2010.239	0.405	0.013	0.500	0.022	0.500	0.018	0.531	0.032	0.610	0.043
200	50	50		0.833	729.490	0.269	0.012	0.289	0.021	0.292	0.010	0.302	0.024	0.311	0.020
200	100	50		0.455	987.734	0.306	0.013	0.365	0.033	0.360	0.019	0.415	0.022	0.418	0.041
200	200	50		0.238	1364.751	0.318	0.014	0.392	0.034	0.406	0.030	0.440	0.035	0.495	0.050
200	400	50		0.122	1906.934	0.313	0.017	0.425	0.030	0.453	0.037	0.519	0.037	0.543	0.054
200	800	50		0.062	2680.318	0.399	0.016	0.526	0.026	0.604	0.027	0.642	0.044	0.649	0.035

Ti64 Points Strategy Raw Data

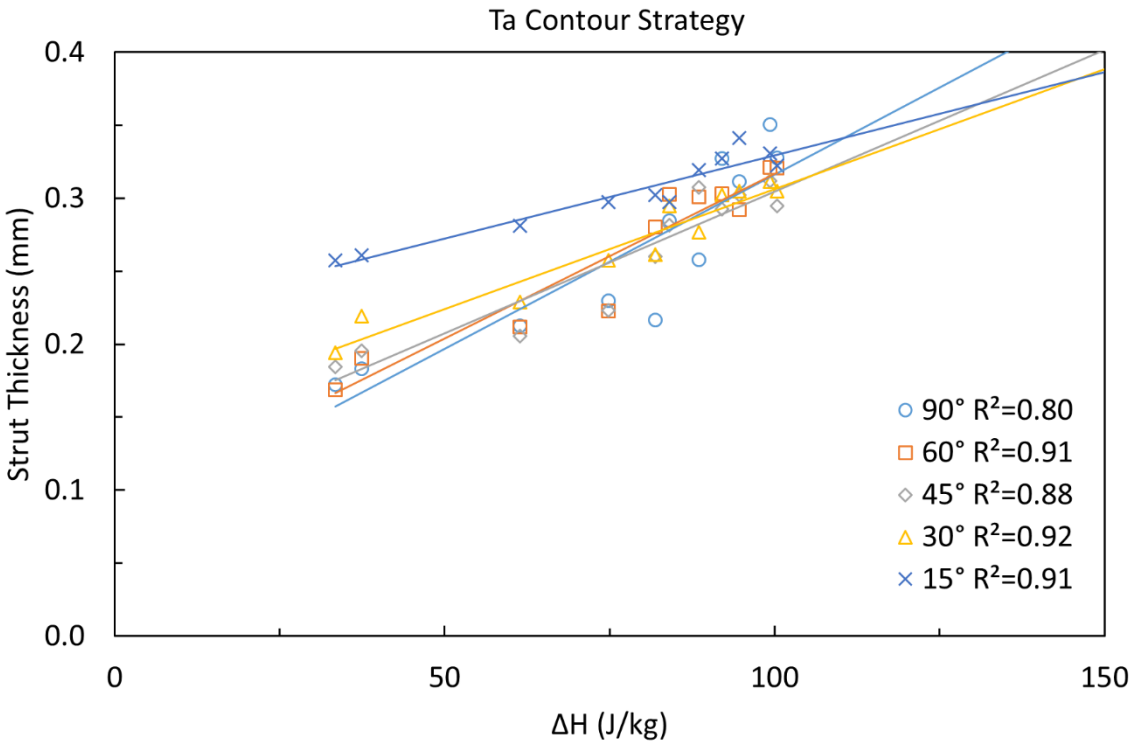
Power	Exposure Time	Point Distance	Pulsing	U	ΔH	90° Strut		60° Strut		45° Strut		30° Strut		15° Strut	
(W)	(us)	um		(m/s)		Width (mm)	S.D. (mm)	Width (mm)	S.D. (mm)	Width (mm)	S.D. (mm)	Width (mm)	S.D. (mm)	Width (mm)	S.D. (mm)
30	30	25		0.714	118.191	0.151	0.020	0.179	0.012	0.190	0.013	0.205	0.023		
40	30	25		0.714	157.588	0.169	0.027	0.201	0.014	0.222	0.012	0.226	0.011	0.252	0.045
50	30	25		0.714	196.985	0.162	0.017	0.224	0.011	0.228	0.012	0.255	0.016	0.264	0.022
75	30	25		0.714	295.477	0.175	0.014	0.254	0.006	0.259	0.013	0.254	0.022	0.309	0.017
100	30	25		0.714	393.970	0.205	0.014	0.294	0.016	0.309	0.012	0.312	0.015	0.338	0.029
50	30	50		1.250	148.907	0.162	0.021								
60	30	50		1.250	178.688	0.160	0.020	0.164	0.020	0.163	0.014				
80	30	50		1.250	238.251	0.170	0.014	0.177	0.011	0.185	0.016	0.216	0.021	0.292	0.020
50	100	50		0.455	246.934	0.181	0.010	0.187	0.011	0.186	0.015	0.202	0.018	0.236	0.029
100	100	50		0.455	493.867	0.278	0.007	0.281	0.014	0.277	0.022	0.285	0.021	0.328	0.024
125	100	50		0.455	617.334	0.328	0.016	0.330	0.017	0.320	0.019	0.324	0.018	0.359	0.032
150	100	50		0.455	740.801	0.365	0.015	0.368	0.026	0.365	0.015	0.365	0.024	0.414	0.029
200	100	50		0.455	987.734	0.406	0.009	0.433	0.017	0.454	0.027	0.473	0.028	0.508	0.033
50	200	100		0.455	246.934	0.193	0.015	0.179	0.013	0.193	0.014	0.211	0.011	0.236	0.018
50	400	100		0.238	341.188	0.225	0.009	0.230	0.015	0.228	0.013	0.237	0.019	0.299	0.027
100	200	100		0.455	493.867	0.278	0.013	0.264	0.011	0.259	0.024	0.294	0.030	0.332	0.020
200	50	100		1.429	557.157	0.180	0.015	0.185	0.011	0.189	0.017	0.221	0.023	0.323	0.030
200	100	100		0.833	729.490	0.268	0.015	0.272	0.013	0.285	0.021	0.391	0.020	0.418	0.030

Ti64 Contour Strategy Raw Data

Power	Exposure Time	Point Distance	Pulsing	U	ΔH	90° Strut		60° Strut		45° Strut		30° Strut		15° Strut	
(W)	(us)	um		(m/s)		Width (mm)	S.D. (mm)	Width (mm)	S.D. (mm)	Width (mm)	S.D. (mm)	Width (mm)	S.D. (mm)	Width (mm)	S.D. (mm)
50	30	50	5	0.313	297.813	0.154	0.020	0.161	0.017	0.164	0.019	0.168	0.019	0.224	0.022
50	30	50	8	0.200	372.266	0.156	0.019	0.183	0.012	0.183	0.021	0.202	0.017	0.264	0.032
50	30	50	10	0.161	414.538	0.161	0.018	0.185	0.014	0.191	0.014	0.217	0.015	0.253	0.023
50	30	50	15	0.109	504.967	0.174	0.003	0.213	0.020	0.207	0.018	0.236	0.015	0.263	0.035
50	30	50	20	0.082	581.499	0.177	0.008	0.216	0.016	0.222	0.013	0.240	0.014	0.311	0.020
50	80	50	3	0.200	372.266	0.158	0.016	0.175	0.015	0.172	0.010	0.190	0.009	0.247	0.020
50	80	50	4	0.152	427.702	0.167	0.017	0.187	0.008	0.194	0.014	0.254	0.025	0.254	0.038
50	80	50	8	0.077	600.262	0.188	0.007	0.223	0.015	0.243	0.014	0.238	0.018	0.286	0.021
50	80	50	12	0.052	733.280	0.218	0.011	0.255	0.018	0.253	0.022	0.263	0.021	0.308	0.028
50	80	50	15	0.041	818.986	0.227	0.010	0.268	0.021	0.264	0.018	0.268	0.025	0.333	0.023
50	180	50	2	0.135	452.882	0.158	0.016	0.186	0.019	0.184	0.016	0.207	0.018	0.239	0.021
50	180	50	5	0.055	710.239	0.215	0.009	0.242	0.009	0.247	0.016	0.249	0.015	0.308	0.021
50	180	50	8	0.034	896.536	0.240	0.015	0.285	0.011	0.289	0.013	0.312	0.016	0.341	0.036
50	180	50	10	0.028	1001.666	0.250	0.010	0.309	0.015	0.307	0.021	0.315	0.020	0.349	0.045
50	180	50	15	0.018	1225.656	0.282	0.011	0.354	0.013	0.331	0.014	0.354	0.017	0.396	0.052
100	20	50	2	1.000	332.965	0.188	0.026	0.185	0.021	0.189	0.008	0.237	0.025	0.265	0.057
100	20	50	5	0.455	493.867	0.202	0.018	0.223	0.018	0.221	0.011	0.242	0.016	0.290	0.023
100	20	50	8	0.294	613.957	0.215	0.019	0.246	0.019	0.235	0.013	0.263	0.015	0.310	0.034
100	20	50	10	0.238	682.376	0.234	0.020	0.256	0.010	0.265	0.011	0.283	0.016	0.337	0.033
100	20	50	15	0.161	829.077	0.249	0.011	0.294	0.017	0.283	0.019	0.303	0.021	0.345	0.039

Ti64 Pulsing Strategy Raw Data

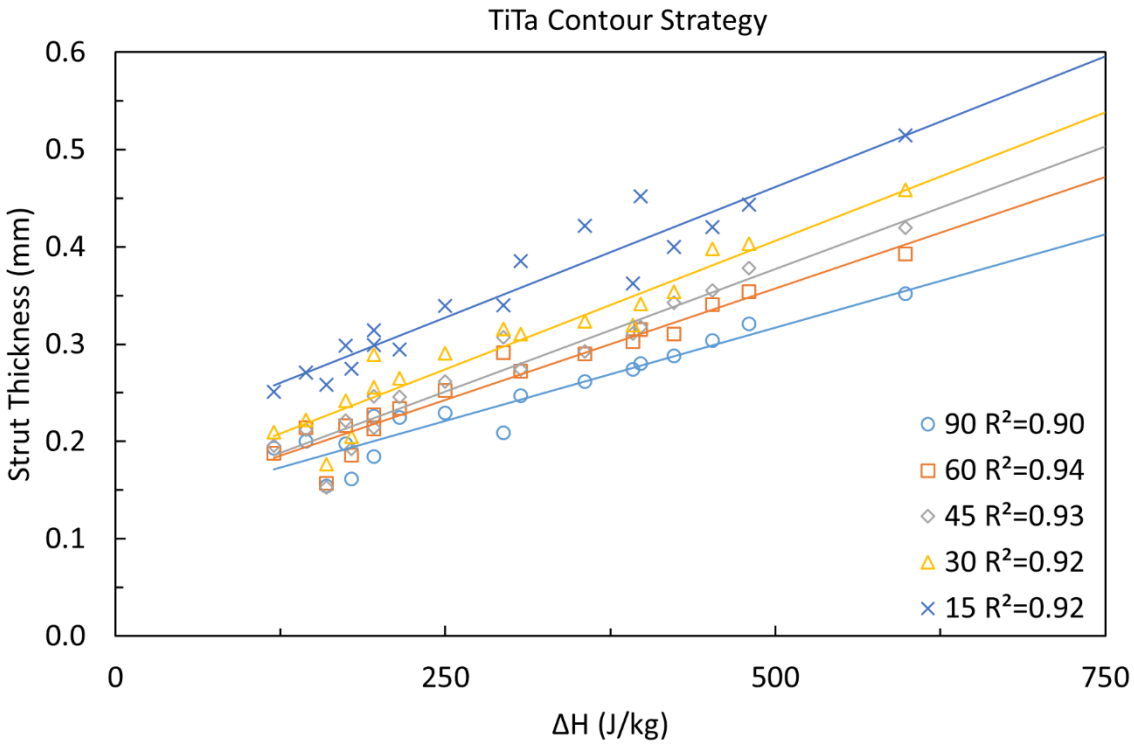
Tantalum


Ta Contour Strategy
Strut Thickness (mm)
0.4
0.3
0.2
0.1
0.0
0
50
100
150
ΔH (J/kg)
90° R²=0.80
60° R²=0.91
45° R²=0.88
30° R²=0.92
15° R²=0.91

Power	Exposure Time	Point Distance	Pulsing	U	ΔH	90° Strut		60° Strut		45° Strut		30° Strut		15° Strut	
(W)	(us)	um		(m/s)		Width (mm)	S.D. (mm)	Width (mm)	S.D. (mm)	Width (mm)	S.D. (mm)	Width (mm)	S.D. (mm)	Width (mm)	S.D. (mm)
50	100	50		0.455	27.734	0.253	0.022	0.223	0.015	0.213	0.015	0.204	0.038	0.262	0.025
50	200	50		0.238	38.320			0.249	0.018	0.231	0.019	0.152	0.018	0.239	0.023
50	400	50		0.122	53.544			0.268	0.018	0.253	0.018	0.169	0.015	0.237	0.018
50	600	50		0.082	65.311			0.271	0.018	0.273	0.016	0.188	0.020	0.262	0.021
50	800	50		0.062	75.260	0.273	0.021	0.263	0.029	0.259	0.016	0.260	0.021	0.267	0.028
50	1000	50		0.050	84.039	0.284	0.024	0.303	0.025	0.282	0.022	0.295	0.023	0.297	0.028
50	1200	50		0.041	91.984	0.327	0.021	0.303	0.024	0.292	0.020	0.302	0.021	0.327	0.018
50	1400	50		0.035	99.296	0.350	0.032	0.321	0.020	0.312	0.014	0.311	0.022	0.331	0.026
100	30	50		1.250	33.449	0.172	0.012	0.169	0.009	0.184	0.017	0.194	0.039	0.257	0.020
100	40	50		1.000	37.397	0.183	0.011	0.190	0.014	0.195	0.021	0.219	0.020	0.261	0.015
150	50	50		0.833	61.450	0.212	0.016	0.212	0.017	0.206	0.024	0.229	0.024	0.281	0.027
200	40	50		1.000	74.794	0.230	0.016	0.223	0.017	0.223	0.012	0.257	0.020	0.297	0.017
200	50	50		0.833	81.933	0.217	0.017	0.280	0.018	0.260	0.012	0.261	0.012	0.302	0.019
200	60	50		0.714	88.497	0.258	0.012	0.301	0.014	0.307	0.017	0.277	0.017	0.319	0.027
200	70	50		0.625	94.608	0.311	0.012	0.292	0.018	0.302	0.020	0.305	0.011	0.341	0.029
200	80	50		0.556	100.347	0.328	0.014	0.320	0.020	0.295	0.013	0.305	0.012	0.322	0.021

Ta Contour Strategy Raw Data

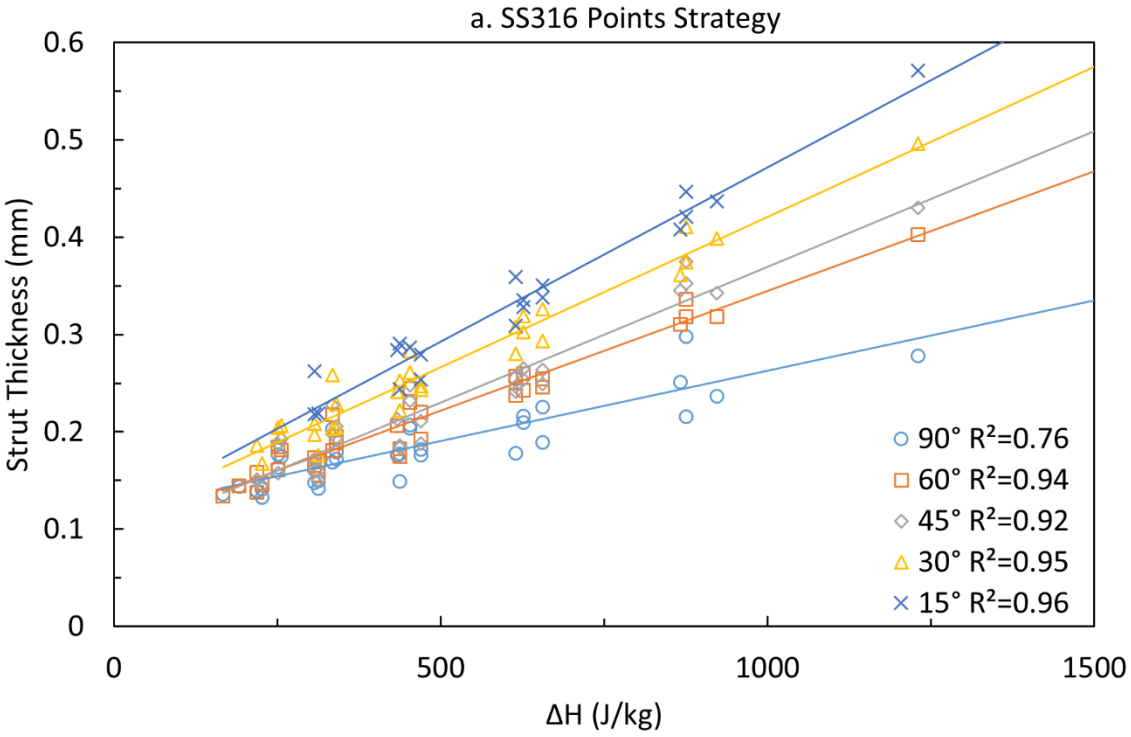
Titanium – 30 Tantalum

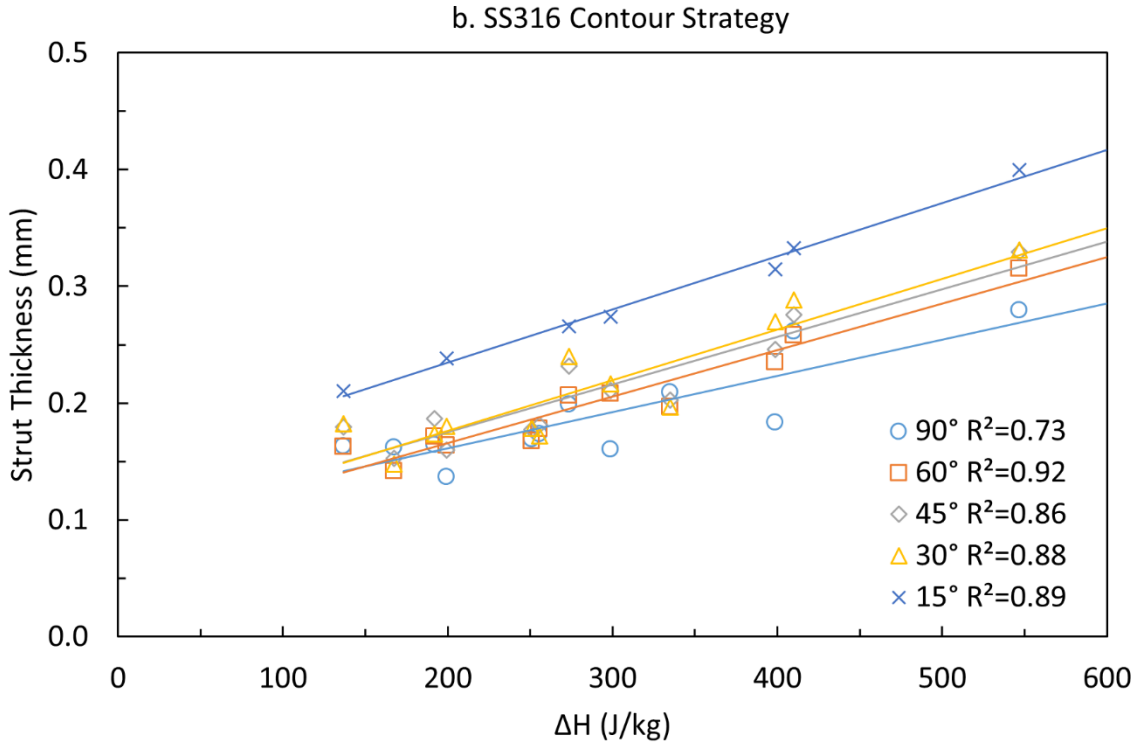


Power	Exposure Time	Point Distance	Pulsing	U	ΔH	90° Strut		60° Strut		45° Strut		30° Strut		15° Strut	
(W)	(us)	um		(m/s)		Width (mm)	S.D. (mm)	Width (mm)	S.D. (mm)	Width (mm)	S.D. (mm)	Width (mm)	S.D. (mm)	Width (mm)	S.D. (mm)
50	80	50		0.556	119.995	0.193	0.017	0.187	0.013	0.196	0.008	0.209	0.025	0.251	0.009
50	120	50		0.385	144.217	0.200	0.013	0.214	0.019	0.212	0.011	0.222	0.022	0.270	0.047
50	180	50		0.263	174.349	0.198	0.006	0.216	0.010	0.222	0.020	0.242	0.012	0.298	0.016
50	230	50		0.208	195.952	0.226	0.012	0.227	0.013	0.246	0.019	0.256	0.023	0.314	0.025
50	280	50		0.172	215.398	0.225	0.011	0.234	0.008	0.246	0.016	0.265	0.030	0.294	0.032
50	380	50		0.128	249.790	0.229	0.011	0.252	0.015	0.262	0.029	0.290	0.025	0.339	0.039
50	580	50		0.085	307.234	0.247	0.013	0.272	0.023	0.274	0.017	0.310	0.018	0.385	0.023
50	780	50		0.063	355.514	0.261	0.008	0.290	0.017	0.293	0.019	0.324	0.023	0.422	0.036
50	980	50		0.051	397.980	0.280	0.012	0.315	0.021	0.317	0.015	0.342	0.020	0.452	0.033
100	30	50		1.250	159.994	0.155	0.011	0.157	0.012	0.153	0.011	0.177	0.015	0.258	0.016
100	40	50		1.000	178.879	0.162	0.007	0.186	0.008	0.192	0.008	0.205	0.015	0.275	0.024
100	50	50		0.833	195.952	0.184	0.007	0.213	0.009	0.214	0.009	0.289	0.014	0.299	0.033
150	50	50		0.833	293.927	0.209	0.004	0.291	0.012	0.307	0.013	0.316	0.014	0.340	0.024
200	50	50		0.833	391.903	0.274	0.005	0.302	0.008	0.311	0.014	0.319	0.018	0.362	0.020
200	60	50		0.714	423.304	0.288	0.012	0.310	0.024	0.343	0.016	0.354	0.012	0.400	0.019
200	70	50		0.625	452.531	0.303	0.022	0.341	0.014	0.355	0.017	0.398	0.014	0.420	0.015
200	80	50		0.556	479.982	0.321	0.012	0.353	0.012	0.378	0.015	0.403	0.012	0.444	0.033
200	130	50		0.357	598.642	0.351	0.017	0.393	0.013	0.419	0.025	0.458	0.013	0.515	0.025

TiTa Contour Strategy Raw Data

Stainless Steel 316





Power	Exposure Time	Point Distance	Pulsing	U	ΔH	90° Strut		60° Strut		45° Strut		30° Strut		15° Strut	
(W)	(us)	um		(m/s)		Width (mm)	S.D. (mm)	Width (mm)	S.D. (mm)	Width (mm)	S.D. (mm)	Width (mm)	S.D. (mm)	Width (mm)	S.D. (mm)
50	100	50		0.454545	113.3452										
50	200	50		0.238095	156.6089										
50	400	50		0.121951	218.8259	0.139	0.016	0.158	0.010	0.151	0.010	0.172	0.015	0.188	0.037
50	800	50		0.061728	307.5738	0.148	0.012	0.166	0.009	0.167	0.012	0.197	0.009	0.218	0.037
50	1600	50		0.031056	433.6304	0.176	0.010	0.206	0.007	0.213	0.015	0.241	0.013	0.284	0.032
100	100	50		0.454545	226.6904	0.133	0.007	0.147	0.020	0.145	0.009	0.168	0.013	0.161	0.039
100	200	50		0.238095	313.2178	0.142	0.011	0.170	0.007	0.160	0.016	0.176	0.014	0.206	0.032
100	400	50		0.121951	437.6518	0.149	0.011	0.175	0.012	0.184	0.013	0.222	0.012	0.244	0.031
100	800	50		0.061728	615.1476	0.178	0.009	0.237	0.008	0.241	0.013	0.280	0.017	0.309	0.021
100	1600	50		0.031056	867.2608	0.251	0.020	0.310	0.021	0.346	0.013	0.361	0.026	0.408	0.038
150	50	50		0.833333	251.1329	0.164	0.024	0.161	0.011	0.158	0.012	0.178	0.020	0.178	0.050
150	100	50		0.454545	340.0356	0.172	0.009	0.195	0.007	0.205	0.010	0.204	0.012	0.214	0.026
150	200	50		0.238095	469.8267	0.176	0.008	0.220	0.012	0.211	0.010	0.247	0.020	0.254	0.028
150	400	50		0.121951	656.4777	0.189	0.032	0.246	0.013	0.249	0.013	0.293	0.019	0.338	0.028
150	800	50		0.061728	922.7213	0.236	0.011	0.318	0.016	0.343	0.016	0.399	0.025	0.437	0.041
200	50	50		0.833333	334.8439	0.169	0.010	0.181	0.017	0.197	0.013	0.203	0.012	0.193	0.017
200	100	50		0.454545	453.3808	0.204	0.013	0.245	0.020	0.248	0.014	0.261	0.023	0.255	0.034
200	200	50		0.238095	626.4356	0.210	0.021	0.259	0.022	0.265	0.016	0.303	0.026	0.335	0.019
200	400	50		0.121951	875.3036	0.216	0.017	0.319	0.022	0.353	0.029	0.374	0.016	0.421	0.020
200	800	50		0.061728	1230.295	0.278	0.010	0.403	0.014	0.430	0.036	0.496	0.015	0.571	0.020
50	100	100		0.833333	83.71098										
50	200	100		0.454545	113.3452										
50	400	100		0.238095	156.6089										
50	800	100		0.121951	218.8259	0.139	0.009	0.138	0.011	0.151	0.018	0.186	0.017	0.206	0.033
50	1600	100		0.061728	307.5738	0.161	0.010	0.174	0.008	0.171	0.007	0.209	0.014	0.263	0.030
100	100	100		0.833333	167.422	0.136	0.010	0.134	0.017	0.146	0.020	0.176	0.019		
100	200	100		0.454545	226.6904	0.141	0.016	0.145	0.010	0.156	0.009	0.172	0.015	0.178	0.030
100	400	100		0.238095	313.2178	0.149	0.026	0.156	0.021	0.150	0.013	0.234	0.031	0.219	0.031
100	800	100		0.121951	437.6518	0.177	0.011	0.183	0.005	0.186	0.012	0.252	0.020	0.290	0.027
100	1600	100		0.061728	615.1476	0.254	0.015	0.257	0.016	0.247	0.012	0.308	0.019	0.359	0.025
150	50	100		1.428571	191.806	0.144	0.010	0.144	0.010	0.150	0.008	0.166	0.017		
150	100	100		0.833333	251.1329	0.177	0.011	0.185	0.012	0.187	0.017	0.204	0.022		
150	200	100		0.454545	340.0356	0.180	0.018	0.189	0.019	0.194	0.014	0.229	0.028	0.246	0.020
150	400	100		0.238095	469.8267	0.182	0.008	0.192	0.016	0.188	0.011	0.243	0.019	0.279	0.017
150	800	100		0.121951	656.4777	0.226	0.015	0.255	0.017	0.264	0.022	0.326	0.014	0.351	0.022
200	50	100		1.428571	255.7413	0.175	0.008	0.181	0.015	0.193	0.012	0.206	0.018		
200	100	100		0.833333	334.8439	0.203	0.008	0.217	0.020	0.227	0.020	0.258	0.016	0.238	0.016
200	200	100		0.454545	453.3808	0.207	0.015	0.230	0.023	0.232	0.018	0.283	0.022	0.287	0.015
200	400	100		0.238095	626.4356	0.216	0.010	0.243	0.020	0.254	0.027	0.319	0.036	0.328	0.017
200	800	100		0.121951	875.3036	0.298	0.016	0.336	0.015	0.375	0.036	0.410	0.017	0.446	0.020

SS316 Points Strategy Raw Data

Power	Exposure Time	Point Distance	Pulsing	U	ΔH	90° Strut		60° Strut		45° Strut		30° Strut		15° Strut	
(W)	(us)	um		(m/s)		Width (mm)	S.D. (mm)	Width (mm)	S.D. (mm)	Width (mm)	S.D. (mm)	Width (mm)	S.D. (mm)	Width (mm)	S.D. (mm)
50	30	30		0.833											
100	30	30		0.833	167.422	0.162	0.020	0.142	0.013	0.152	0.011	0.148	0.020		
150	30	30		0.833	251.133	0.170	0.018	0.168	0.018	0.177	0.016	0.179	0.011		
200	30	30		0.833	334.844	0.210	0.027	0.197	0.011	0.203	0.008	0.196	0.018	0.248	0.018
50	90	30		0.313	136.699	0.164	0.013	0.163	0.020	0.180	0.019	0.183	0.015	0.210	0.025
100	90	30		0.313	273.399	0.199	0.009	0.207	0.009	0.232	0.020	0.240	0.026	0.266	0.022
150	90	30		0.313	410.098	0.262	0.015	0.258	0.016	0.276	0.017	0.288	0.019	0.333	0.017
200	90	30		0.313	546.798	0.280	0.038	0.316	0.016	0.330	0.016	0.331	0.021	0.400	0.021
50	30	60		1.429											
100	30	60		1.429											
150	30	60		1.429	191.806	0.165	0.018	0.172	0.019	0.187	0.015	0.173	0.009		
200	30	60		1.429	255.741	0.174	0.020	0.178	0.022	0.181	0.017	0.172	0.014		
50	90	60		0.588											
100	90	60		0.588	199.272	0.137	0.012	0.164	0.019	0.160	0.015	0.180	0.016	0.238	0.010
150	90	60		0.588	298.908	0.161	0.013	0.209	0.011	0.211	0.014	0.216	0.012	0.274	0.016
200	90	60		0.588	398.544	0.184	0.008	0.236	0.014	0.246	0.025	0.269	0.021	0.314	0.024

SS316 Contour Strategy Raw Data

References

[1] Y.S. Touloukian, D.P. DeWitt, Thermophysical properties of matter-the tprc data series. volume 7. thermal radiative properties-metallic elements and alloys, THERMOPHYSICAL AND ELECTRONIC PROPERTIES INFORMATION ANALYSIS CENTER LAFAYETTE IN, 1970.

[2] R. Wauthle, S.M. Ahmadi, S. Amin Yavari, M. Mulier, A.A. Zadpoor, H. Weinans, J. Van Humbeeck, J.-P. Kruth, J. Schrooten, Revival of pure titanium for dynamically loaded porous implants using additive manufacturing, Materials Science and Engineering: C 54 (2015) 94-100.

[3] Y. Touloukian, R. Powell, C. Ho, M. Nicolaou, Thermophysical Properties of Matter-The TPRC Data Series. Volume 10. Thermal Diffusivity, Thermophysical and Electronic Properties Information Analysis Center Lafayette In, 1974.

[4] S. Amin Yavari, R. Wauthle, J. van der Stok, A.C. Riemslag, M. Janssen, M. Mulier, J.P. Kruth, J. Schrooten, H. Weinans, A.A. Zadpoor, Fatigue behavior of porous biomaterials manufactured using selective laser melting, Materials Science and Engineering: C 33(8) (2013) 4849-4858.

[5] R. Wauthle, J. van der Stok, S. Amin Yavari, J. Van Humbeeck, J.-P. Kruth, A.A. Zadpoor, H. Weinans, M. Mulier, J. Schrooten, Additively manufactured porous tantalum implants, Acta Biomaterialia 14 (2015) 217-225.

[6] Y.L. Zhou, M. Niinomi, T. Akahori, Effects of Ta content on Young's modulus and tensile properties of binary Ti–Ta alloys for biomedical applications, Materials Science and Engineering: A 371(1) (2004) 283-290.

[7] W.E. King, H.D. Barth, V.M. Castillo, G.F. Gallegos, J.W. Gibbs, D.E. Hahn, C. Kamath, A.M. Rubenchik, Observation of keyhole-mode laser melting in laser powder-bed fusion additive manufacturing, Journal of Materials Processing Technology 214(12) (2014) 2915-2925.

[8] S. Tsopanos, R.A.W. Mines, S. McKown, Y. Shen, W.J. Cantwell, W. Brooks, C.J. Sutcliffe, The Influence of Processing Parameters on the Mechanical Properties of Selectively Laser Melted Stainless Steel Microlattice Structures, Journal of Manufacturing Science and Engineering 132(4) (2010) 041011-041011.

9 Appendix B – Stochastic Porous Structure Raw Data & Further Optimisation Graphs

The raw data for all mechanical testing is presented in the following appendix. Plots displaying the relationship between compressive yield strength, fatigue strength, apparent modulus and build time to relative density are shown for all laser parameters, scanning strategies and materials explored.

B.1 Raw Data and Laser Parameters

Notation:

Laser Power-Exposure Time/Off Time[1]-Point Distance x(number of repeated exposures)[1]

OC = Contour

[1] For pulsing strategy only

[a] Laser parameter used for Ti64 optical microscopy and SEM microstructure images and for the EBSD specimens in Section 4.2.4

[b] Parameter used for material comparison SEM Images in Section 5.2.2.4

[c] Parameter used for material comparison microscopy images in Section 5.2.2.4

Ti64

Sample Name	Density	Density S.D.	Modulus (MPa)	Modulus S.D.	Yield Stress (MPa)	Yield Stress S.D.
Points						
50-400-50	8.75%	0.10%	0.303	0.006	3.636	0.094
50-600-50	10.43%	0.09%	0.813	0.020	11.017	0.149
50-800-50	11.86%	0.02%	1.196	0.024	16.358	0.293
50-1200-50	14.88%	0.15%	1.900	0.016	26.557	0.501
50-1600-50	17.62%	0.06%	2.577	0.037	35.411	0.752
50-2000-50[a]	20.69%	0.24%	3.502	0.060	48.323	1.723
50-2400-50	22.63%	0.05%	4.198	0.014	57.970	0.452
50-2800-50	23.47%	0.06%	4.306	0.058	57.035	1.173
200-30-50	10.06%	0.05%	0.469	0.027	5.471	0.172
200-50-50	14.96%	0.27%	1.382	0.051	16.969	1.312
200-70-50	15.33%	0.21%	1.824	0.009	21.575	0.245
200-80-50	18.35%	0.24%	2.747	0.057	35.527	0.747

200-100-50[a]	19.93%	0.00%	3.199	0.092	42.107	0.894
200-120-50	19.19%	0.07%	3.173	0.020	40.345	0.461
200-150-50	21.76%	0.12%	4.469	0.097	58.985	0.590
200-200-50	21.93%	0.34%	4.608	0.112	59.035	0.940
Outer Contour						
OC_50-100-50	9.64%	0.09%	0.731	0.005	10.193	0.078
OC_50-400-100	10.97%	0.18%	1.128	0.030	16.119	0.316
OC_50-200-50	12.46%	0.14%	1.374	0.025	19.798	0.119
OC_50-400-50	15.96%	0.01%	2.284	0.026	32.815	0.286
OC_50-600-50[a]	19.87%	0.11%	3.330	0.037	48.548	0.291
OC_50-800-50	23.08%	0.20%	4.398	0.066	63.392	1.162
OC_200-30-50	8.09%	0.17%	0.512	0.009	6.609	0.085
OC_200-50-100	8.83%	0.15%	0.580	0.020	7.470	0.227
OC_200-40-50	10.35%	0.09%	0.997	0.020	14.171	0.205
OC_200-50-50	14.49%	0.04%	1.861	0.020	25.799	0.048
OC_200-100-100	18.53%	0.14%	2.978	0.040	40.205	0.368
OC_200-60-50	20.39%	0.17%	3.709	0.047	49.807	0.355
OC_200-70-50	23.27%	0.28%	5.670	0.083	78.781	0.713
Pulsing						
50-50/50-50 x5	5.95%	0.11%	0.109	0.004	0.821	0.140
50-50/50-50 x8	8.01%	0.24%	0.325	0.008	4.002	0.134
50-50/50-50 x15	10.75%	0.23%	0.766	0.008	10.598	0.165
50-50/50-50 x20	12.27%	0.10%	0.958	0.007	13.517	0.160
50-200/200-50 x2	7.56%	0.18%	0.350	0.012	4.562	0.063
50-200/200-50 x5	11.77%	0.07%	1.084	0.060	15.934	0.555
50-200/200-50 x10	18.00%	0.35%	2.098	0.050	28.625	0.975
50-200/200-50 x15	23.08%	0.42%	2.687	0.006	34.394	1.454
50-200/200-50 x20[a]	27.19%	0.06%	3.464	0.055	41.308	2.614
200-20/20-50 x2	6.86%	0.18%	0.014	0.002	0.129	0.017
200-20/20-50 x5	10.05%	0.12%	0.687	0.017	7.794	0.133
200-20/20-50 x10	13.24%	0.20%	1.593	0.025	20.491	0.876
200-20/20-50 x15	17.26%	0.19%	2.649	0.031	36.016	0.865
200-20/20-50 x20	17.50%	0.27%	3.192	0.062	41.179	1.072

Ti64 Mechanical and Material Testing Raw Data

Specimen	Density	Internal Porosity
Points		
50-400-50	7.98%	0.00%
50-800-50	11.58%	0.01%
50-1600-50	15.50%	0.01%
50-2000-50[a]	21.70%	0.09%
200-30-50	10.32%	0.02%
200-50-50	14.08%	0.20%
200-80-50	17.68%	0.34%
200-100-50[a]	19.19%	0.34%
Contour		
OC_50-100-50	9.22%	0.01%
OC_50-200-50	12.57%	0.01%
OC_50-400-50	15.79%	0.01%
OC_50-600-50[a]	19.65%	0.02%
Pulsing		
50-200/200-50 x2	8.20%	0.01%
50-200/200-50 x5	13.30%	0.04%
50-200/200-50 x10	16.18%	0.11%
50-200/200-50 x20[a]	27.75%	0.23%

Ti64 Micro-CT Results

SS316

Sample Name	Density	Density S.D.	Modulus (MPa)	Modulus S.D.	Yield Stress (MPa)	Yield Stress S.D.
Points						
50-600-50	7.59%	0.03%	0.7	0.0	2.6	0.03
50-800-50	8.61%	0.01%	1.1	0.0	4.0	0.03
50-1200-50	10.27%	0.01%	1.8	0.0	6.0	0.02
50-1600-50	12.04%	0.02%	2.4	0.1	7.8	0.04
50-2000-50	13.54%	0.04%	2.9	0.1	9.6	0.20
50-2400-50	14.64%	0.04%	3.4	0.1	11.4	0.04
200-50-50	10.71%	0.10%	0.9	0.0	3.7	0.09
200-70-50	11.39%	0.11%	1.1	0.0	4.5	0.14
200-100-50	14.72%	0.10%	2.8	0.0	10.1	0.12
200-120-50	14.40%	0.06%	2.6	0.0	9.3	0.17
200-150-50	16.88%	0.03%	4.5	0.0	15.3	0.17
200-200-50	17.70%	0.21%	4.8	0.1	16.3	0.25
Outer Contour						
OC_50-100-50	6.30%	0.04%	0.5	0.0	2.3	0.03
OC_50-200-50	8.29%	0.01%	1.1	0.0	4.2	0.04
OC_50-400-50	10.65%	0.05%	1.9	0.0	6.6	0.06
OC_50-600-50	12.77%	0.05%	2.7	0.0	9.1	0.02
OC_50-800-50	14.36%	0.01%	3.5	0.0	11.1	0.04
OC_200-30-50	6.08%	0.02%	0.3	0.0	1.4	0.02
OC_200-40-50	8.20%	0.09%	1.0	0.0	3.8	0.06
OC_200-50-50	11.42%	0.11%	2.0	0.0	7.2	0.12
OC_200-60-50	15.46%	0.06%	3.6	0.0	13.0	0.12
OC_200-100-50	22.47%	0.19%	8.1	0.2	29.8	0.40
Pulsing						
50-200/200-50 x4	7.54%	0.03%	0.8	0.0	3.0	0.03
50-200/200-50 x5	8.25%	0.01%	1.0	0.0	3.7	0.02
50-200/200-50 x8	10.05%	0.06%	1.5	0.0	5.3	0.03
50-200/200-50 x10	10.84%	0.06%	1.9	0.0	6.2	0.04
50-200/200-50 x15	13.10%	0.10%	2.5	0.1	8.2	0.05
50-200/200-50 x20	15.19%	0.04%	3.1	0.0	10.1	0.03
200-20/20-50 x8	9.40%	0.14%	1.1	0.0	4.1	0.13
200-20/20-50 x10	10.34%	0.06%	1.5	0.0	5.5	0.10
200-20/20-50 x15	13.13%	0.19%	2.6	0.0	9.2	0.11
200-20/20-50 x20	14.58%	0.26%	3.6	0.1	12.0	0.30

SS316 Mechanical and Material Testing Raw Data

Specimen	Density	Internal Porosity
Points		
50-600-50	7.68%	0.00%
50-800-50	9.12%	0.00%
50-1600-50	12.68%	0.00%
50-2400-50	15.02%	0.00%
200-50-50	11.50%	0.08%
200-70-50	12.22%	0.13%
200-120-50	14.87%	0.17%
200-150-50	16.72%	0.76%
Contour		
OC_200-30-50	6.80%	0.03%
OC_200-40-50	8.62%	0.13%
OC_200-50-50	11.92%	0.23%
OC_200-60-50	16.70%	0.48%
Pulsing		
200-20/20-50 x8	9.80%	0.14%
200-20/20-50 x10	10.90%	0.26%
200-20/20-50 x15	13.54%	0.50%
200-20/20-50 x20	14.61%	0.70%

SS316 Micro-CT Results

Biomaterial Comparison Testing Raw Data

	Specimen	Density	Modulus (MPa)	Modulus SD	Yield Stress (MPa)	Yield Stress SD	Fatigue Strength (10^6)	Fatigue Strength S.D.
Ti64	50-400-50	8.75%	303.3	6.0	3.6	0.1	0.5	0.1
	50-800-50	11.86%	1195.9	24.4	16.4	0.3	2.5	0.2
	50-1600-50	17.62%	2577.0	36.8	35.4	0.8	5.3	0.5
	50-2000-50	20.69%	3502.1	59.8	48.3	1.7	6.6	0.7
	200-30-50	10.06%	469.4	27.3	5.5	0.2	0.8	0.1
	200-50-50	14.96%	1381.6	51.0	17.0	1.3	2.5	0.2
	200-80-50	18.35%	2746.7	57.1	35.5	0.7	5.3	0.5
	200-100-50	19.93%	3198.9	92.3	42.1	0.9	6.3	0.6
	OC_50-100-50	9.64%	730.7	5.1	10.2	0.1	1.5	0.1
	OC_50-200-50 [b]	12.46%	1374.0	24.8	19.8	0.1	3.0	0.3
	OC_50-400-50	15.96%	2283.5	26.5	32.8	0.3	4.9	0.5
	OC_50-600-50 [c]	19.87%	3329.9	36.8	48.5	0.3	7.3	0.7
	50-200/200-50-x2	7.56%	349.5	12.4	4.6	0.1	0.6	0.1
	50-200/200-50-x5	11.77%	1084.0	60.2	15.9	0.6	2.4	0.2
	50-200/200-50-x10	18.00%	2097.9	49.7	28.6	1.0	4.3	0.4
	50-200/200-50-x20	27.19%	3464.4	55.3	41.3	2.6	7.2	0.6
Ta	OC_200-40-50	7.93%	979.64	38.96	8.72	0.16	2.5	0.1
	OC_200-50-50 [b c]	9.30%	1533.91	5.12	13.96	0.12	4.2	0.2
	OC_200-70-50	13.93%	3373.25	49.79	30.14	0.48	9.0	0.4
	OC_200-90-50	16.39%	5091.53	92.17	44.24	0.65	13.8	0.6
Cp-Ti	OC_50-100-50	7.60%	530.89	9.30	4.26	0.03	1.3	0.1
	OC_50-200-50	9.63%	979.92	6.03	7.97	0.02	2.4	0.1
	OC_50-400-50 [b c]	12.78%	1715.26	29.87	13.60	0.20	4.1	0.2
	OC_50-600-50	15.18%	2435.97	7.01	18.96	0.02	5.9	0.3
	OC_50-850-50	18.13%	3370.91	21.21	27.27	0.36	8.5	0.4
TiTa	OC_50-100-50	7.71%	535.47	8.89	6.28	0.03	1.3	0.1
	OC_50-200-50	10.53%	995.86	11.09	12.33	0.09	2.6	0.2
	OC_50-400-50 [b c]	13.85%	1593.13	14.50	21.14	0.07	4.2	0.3
	OC_50-600-50	16.84%	2268.79	14.79	30.13	0.11	6.0	0.4
	OC_50-950-50	20.62%	3112.32	70.48	41.31	0.43	8.3	0.6

Material Comparison Raw Test Data (Chapter 5)

B.2 Further Optimisation Plots

The following figures display the relationships between yield strength, modulus, fatigue strength and build time with relative density for variations in laser parameters, scanning strategy and base material.

Notation:

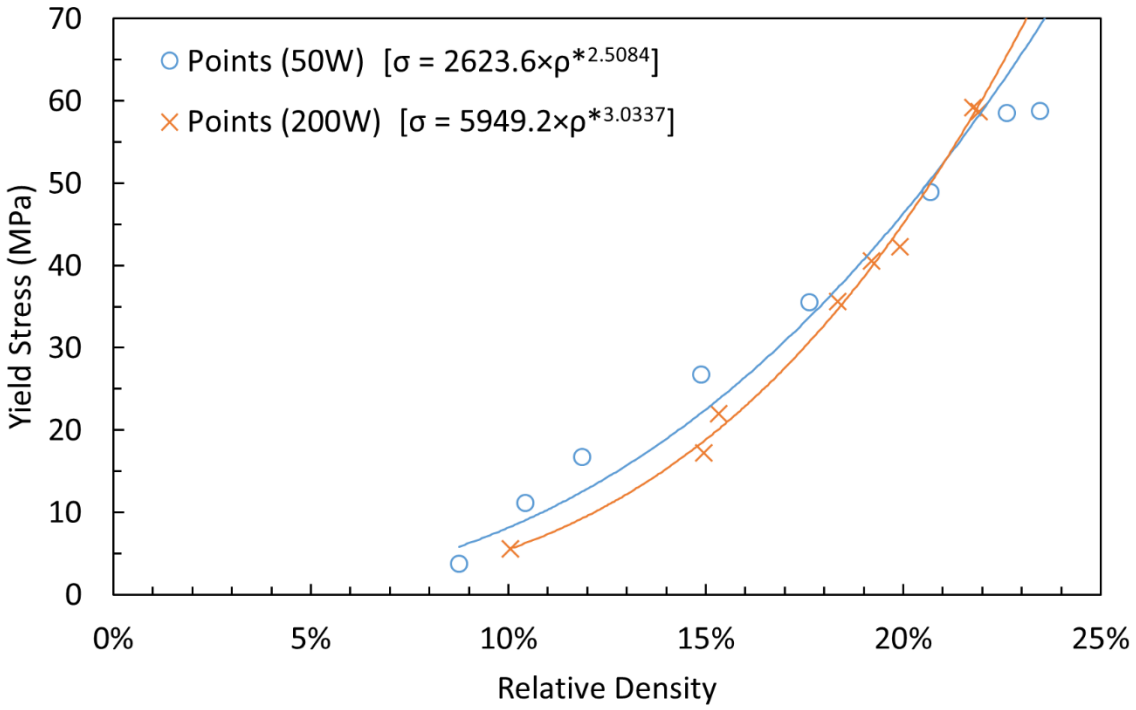
ρ* - Relative Density

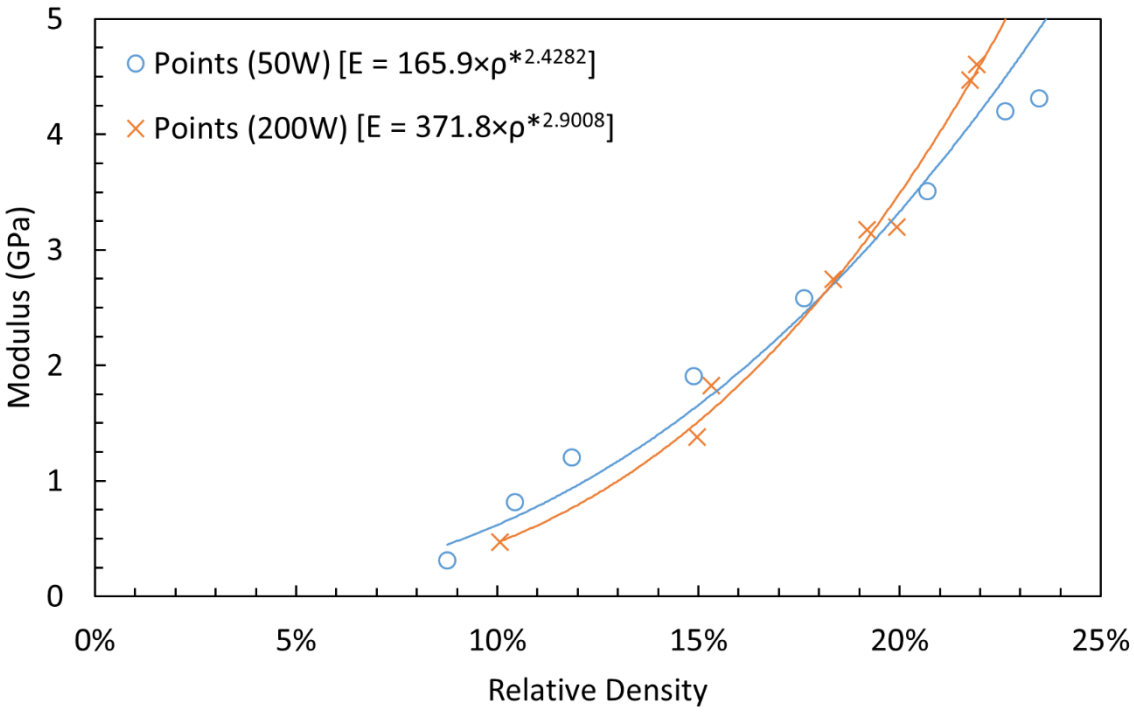
σ – Yield or Fatigue Stress

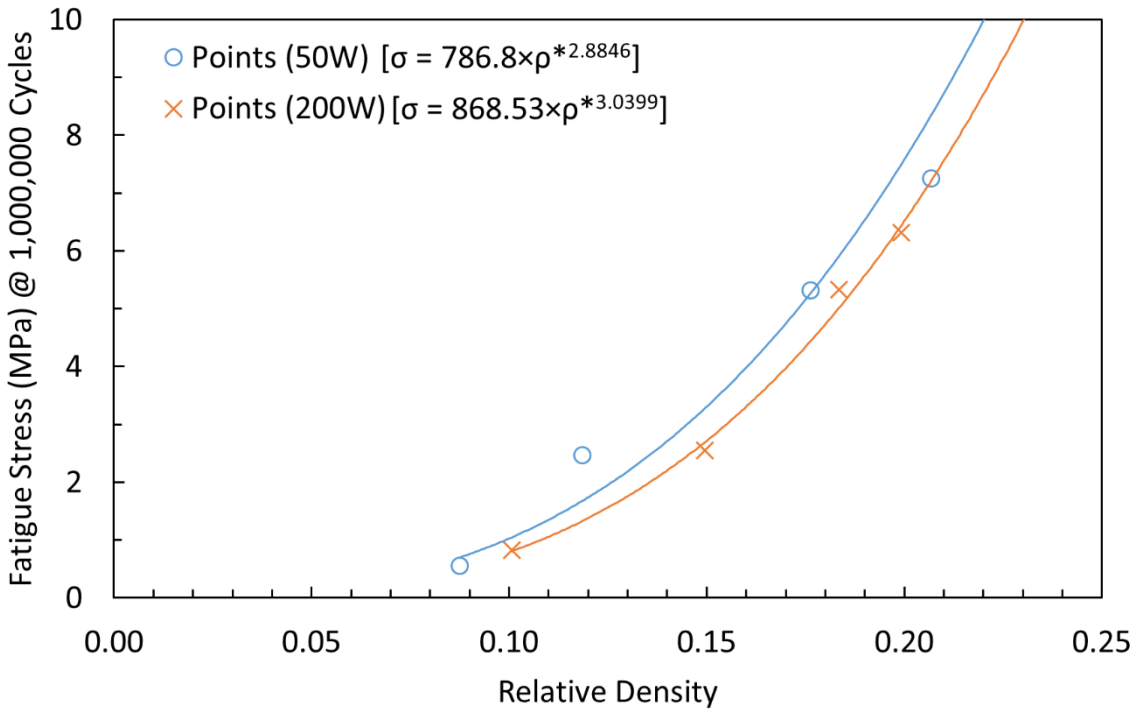
E - Modulus

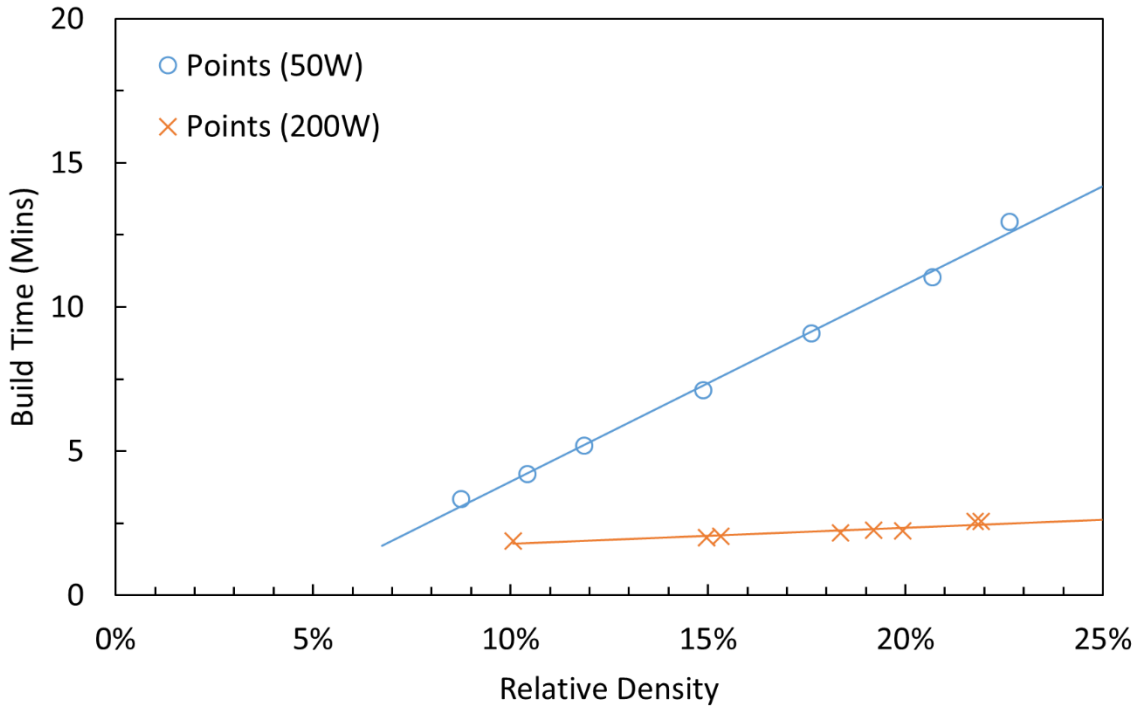
Laser Parameter Optimisation

Ti64

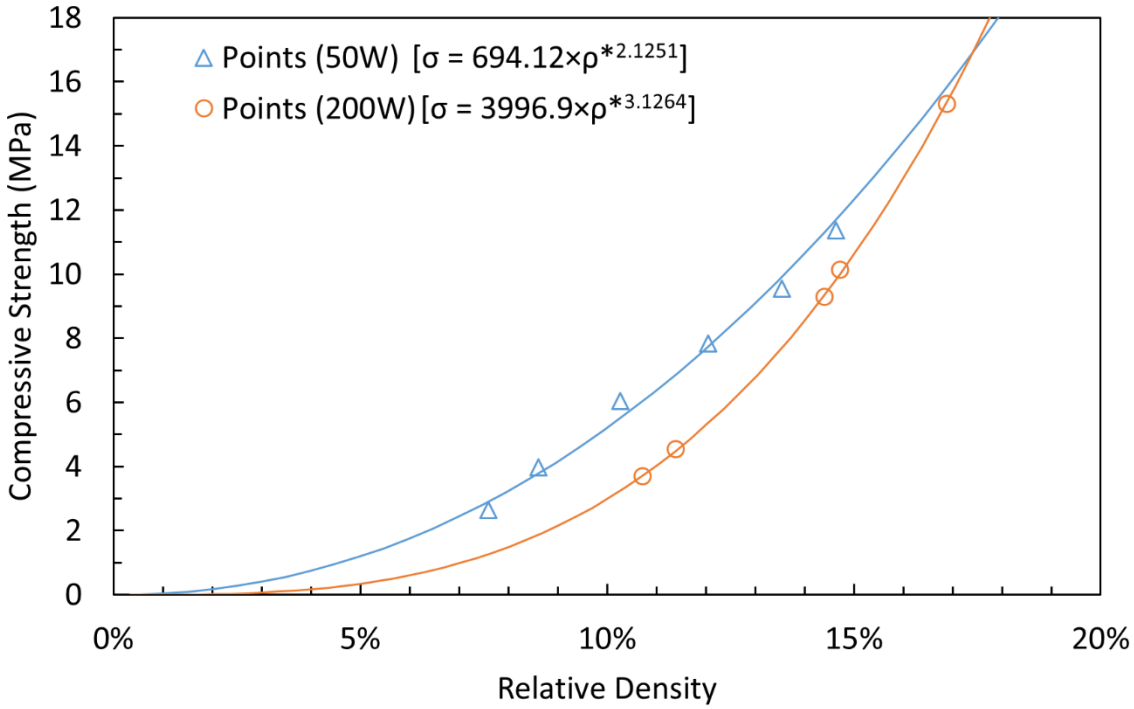


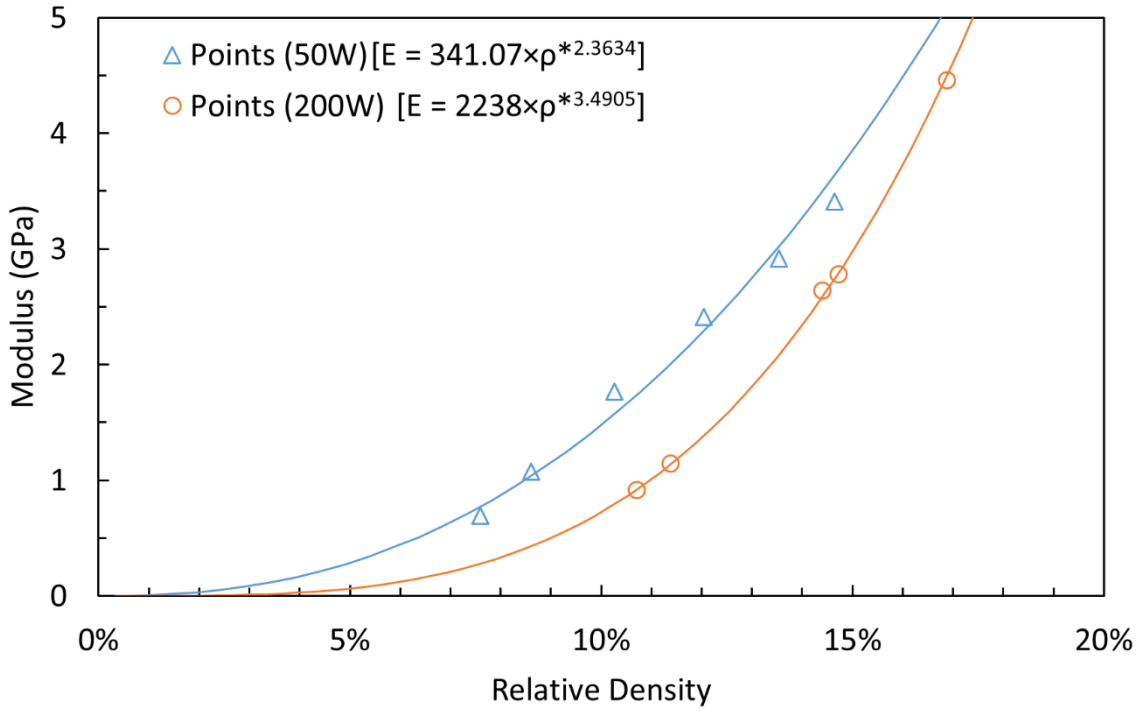

Points (50W) [E = 165.9×ρ*2.4282]
Points (200W) [E = 371.8×ρ*2.9008]
Modulus (GPa)
0
1
2
3
4
5
0%
5%
10%
15%
20%
25%
Relative Density


Points (50W) [σ = 786.8×ρ*2.8846]
Points (200W) [σ = 868.53×ρ*3.0399]
Fatigue Stress (MPa) @ 1,000,000 Cycles
0
2
4
6
8
10
0.00
0.05
0.10
0.15
0.20
0.25
Relative Density


Points (50W)
Points (200W)
Build Time (Mins)
Relative Density
0
5
10
15
20
0%
5%
10%
15%
20%
25%

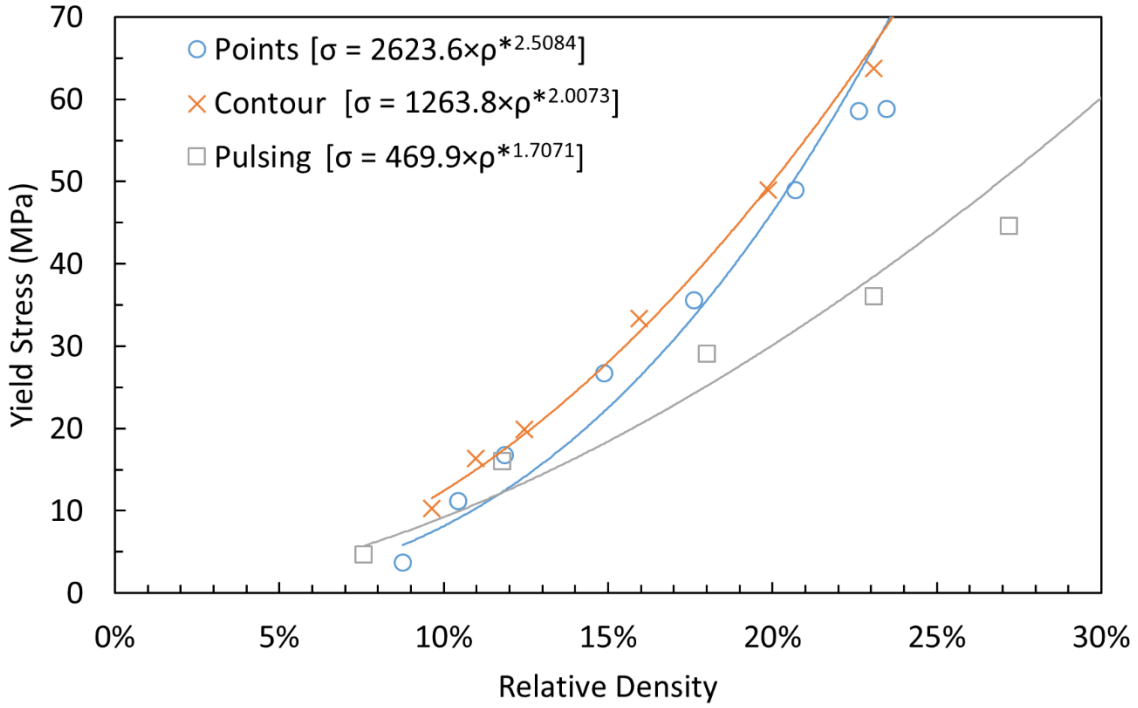
SS316

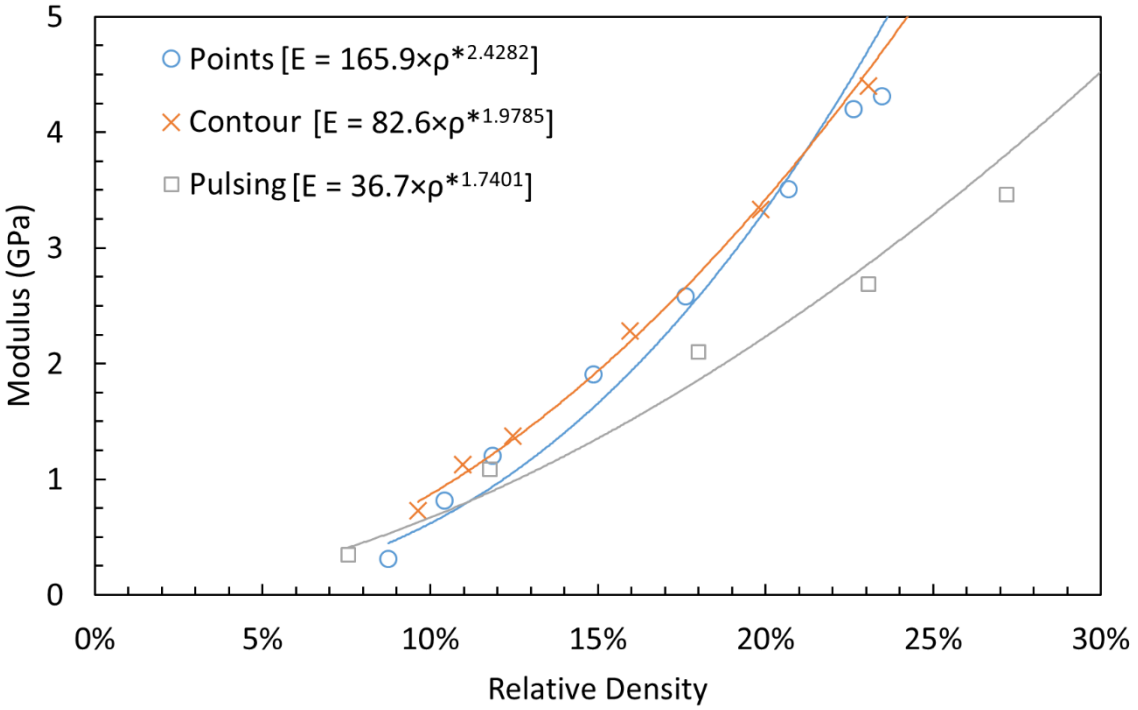

Points (50W) [σ = 694.12×ρ*2.1251]
Points (200W) [σ = 3996.9×ρ*3.1264]
Compressive Strength (MPa)
Relative Density
0
2
4
6
8
10
12
14
16
18
0%
5%
10%
15%
20%

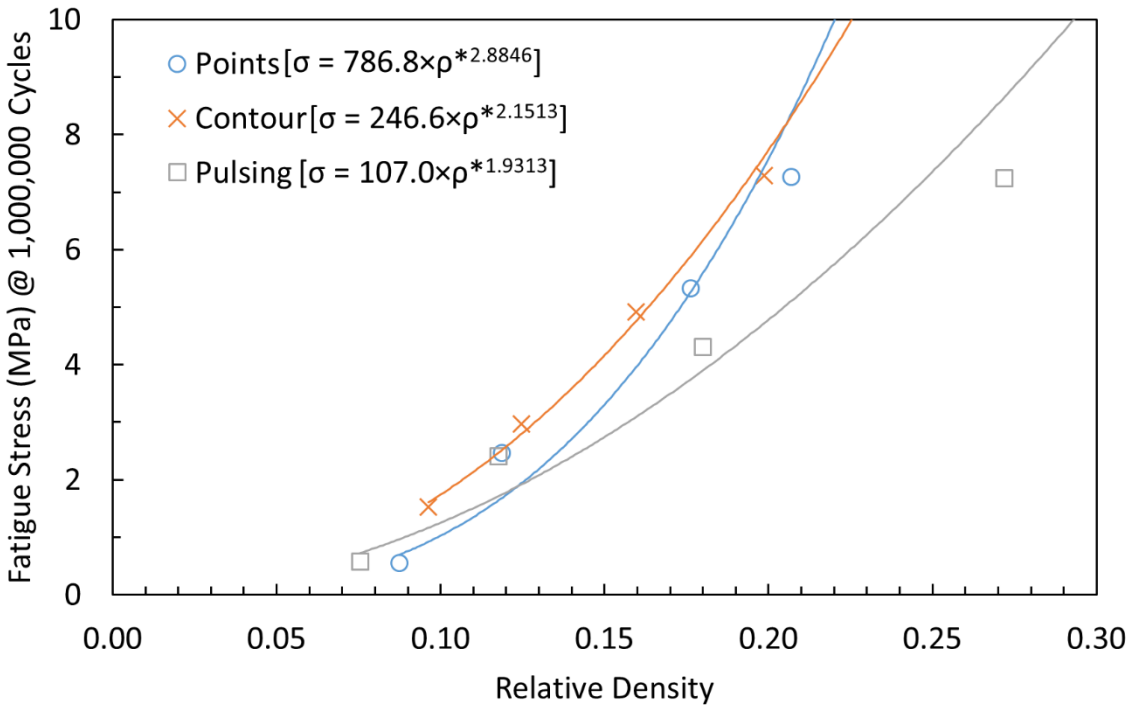

Points (50W) [E = 341.07×ρ*2.3634]
Points (200W) [E = 2238×ρ*3.4905]
Modulus (GPa)
Relative Density
0
1
2
3
4
5
0%
5%
10%
15%
20%

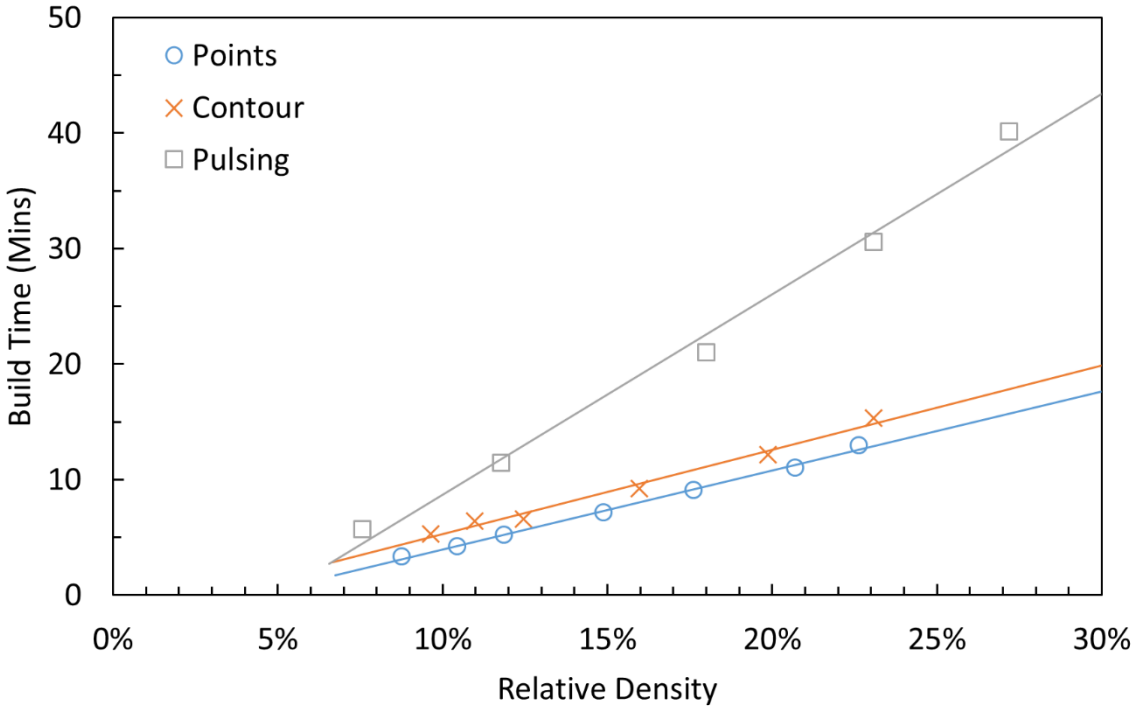
Scanning Strategy Optimisation

Ti64

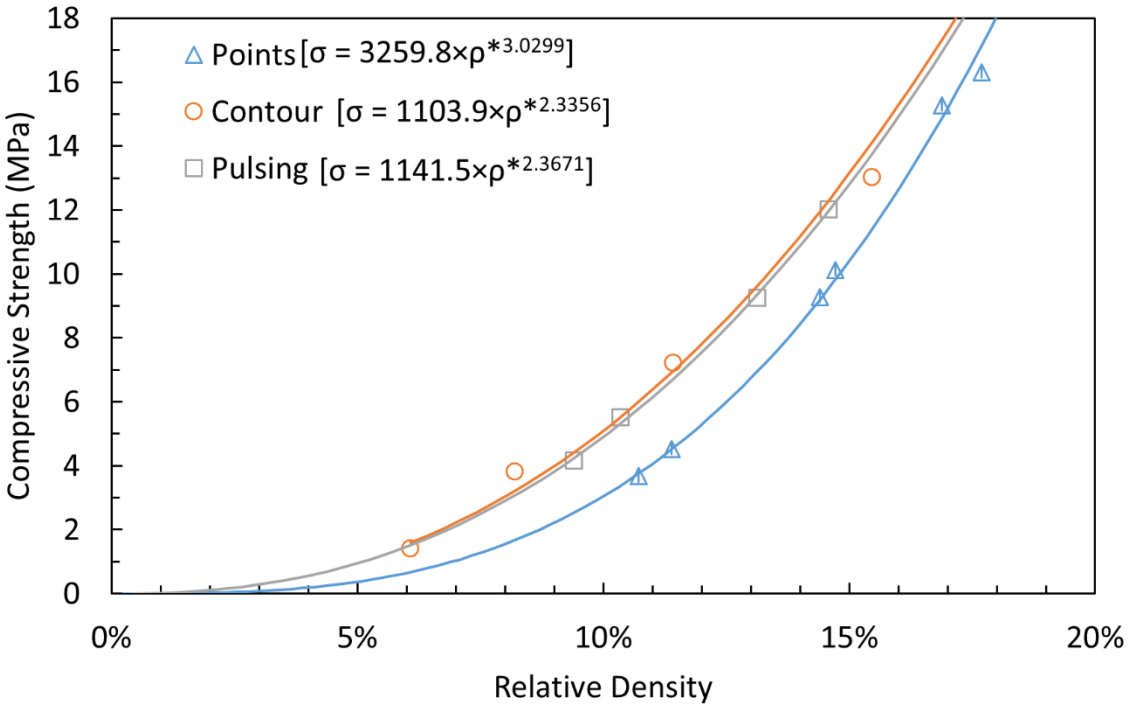


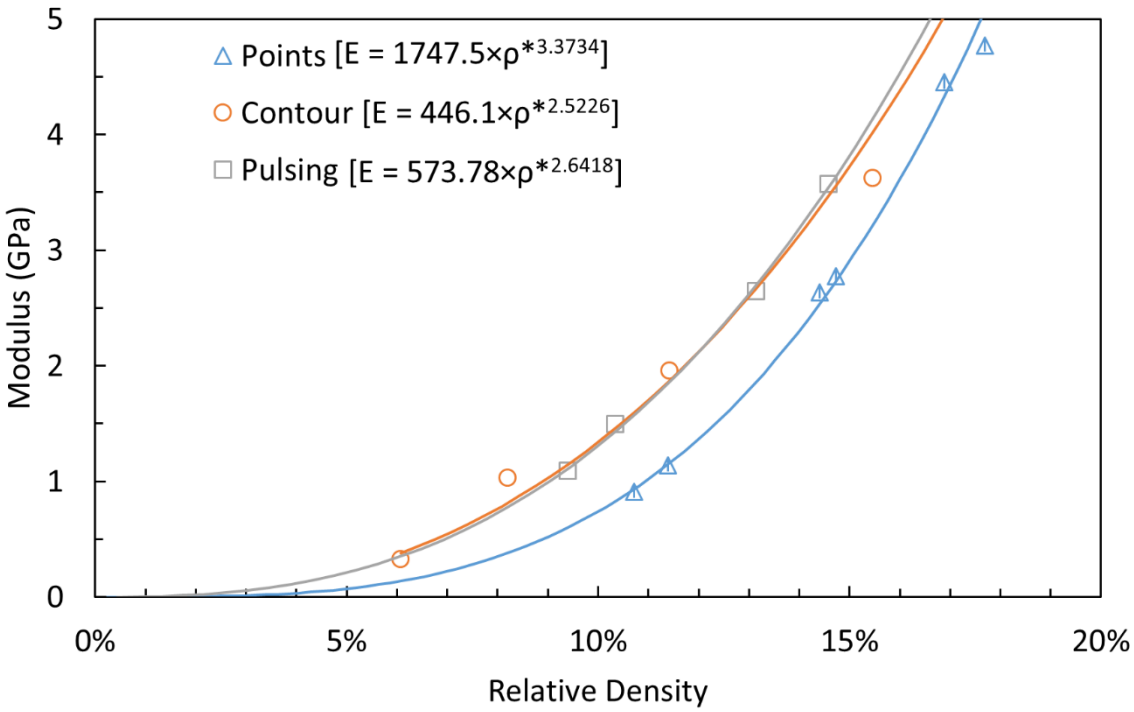



Points [σ = 786.8×ρ*2.8846]
Contour [σ = 246.6×ρ*2.1513]
Pulsing [σ = 107.0×ρ*1.9313]
Fatigue Stress (MPa) @ 1,000,000 Cycles
Relative Density
0
2
4
6
8
10
0.00
0.05
0.10
0.15
0.20
0.25
0.30

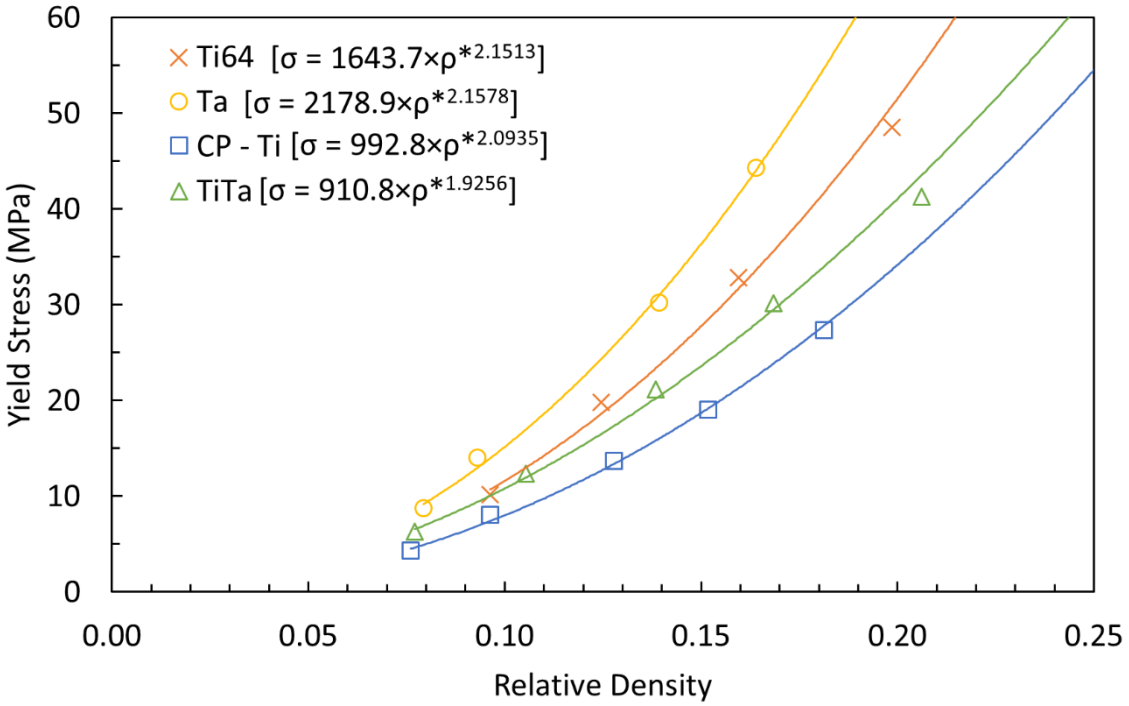

Points
Contour
Pulsing
Build Time (Mins)
Relative Density
0
10
20
30
40
50
0%
5%
10%
15%
20%
25%
30%

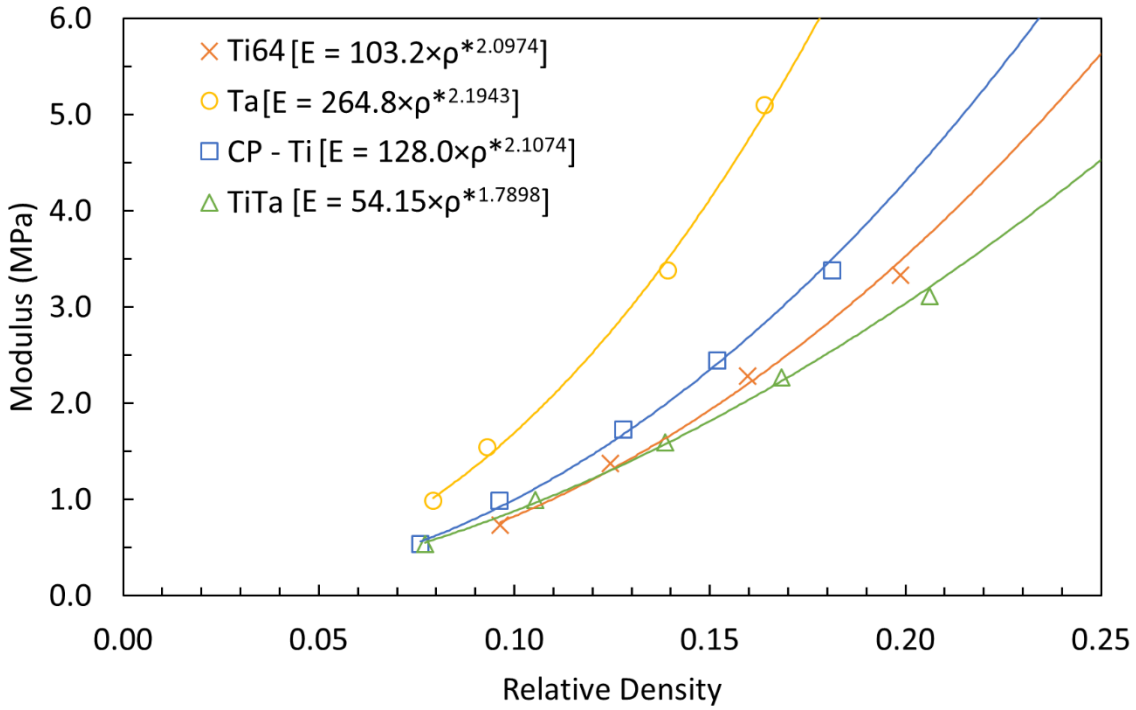
SS316

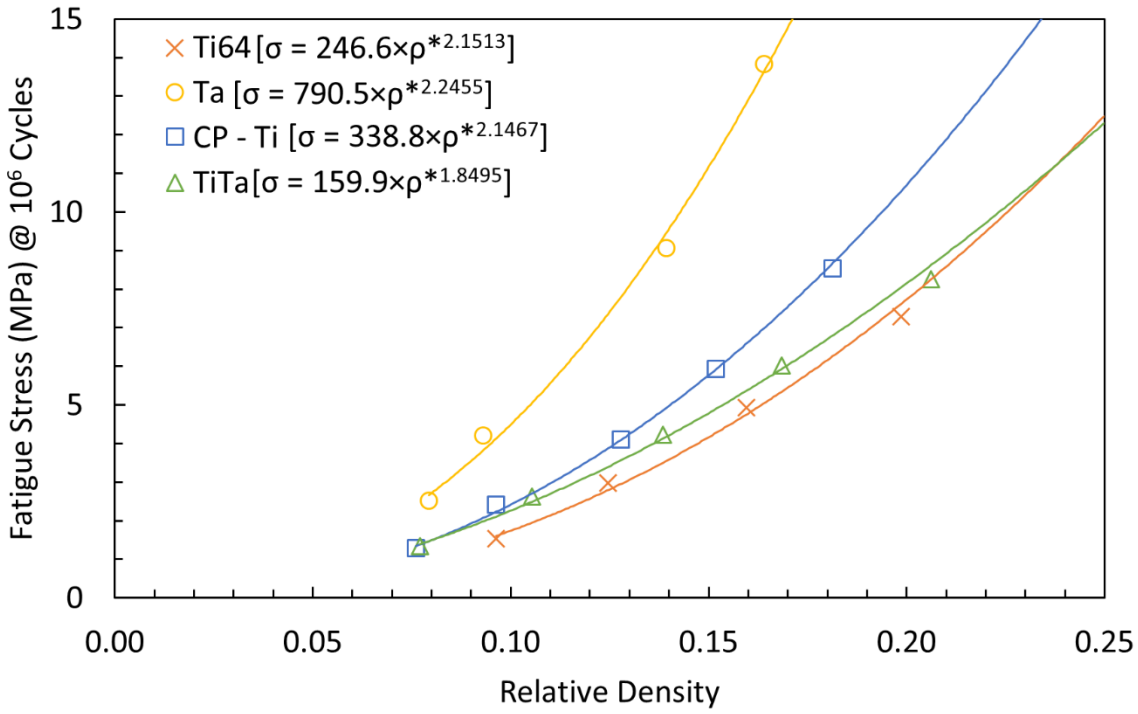

Points [σ = 3259.8×ρ*3.0299]
Contour [σ = 1103.9×ρ*2.3356]
Pulsing [σ = 1141.5×ρ*2.3671]
Compressive Strength (MPa)
Relative Density
0
2
4
6
8
10
12
14
16
18
0%
5%
10%
15%
20%


Points [E = 1747.5×ρ*3.3734]
Contour [E = 446.1×ρ*2.5226]
Pulsing [E = 573.78×ρ*2.6418]
Modulus (GPa)
Relative Density
0
1
2
3
4
5
0%
5%
10%
15%
20%

Material Optimisation

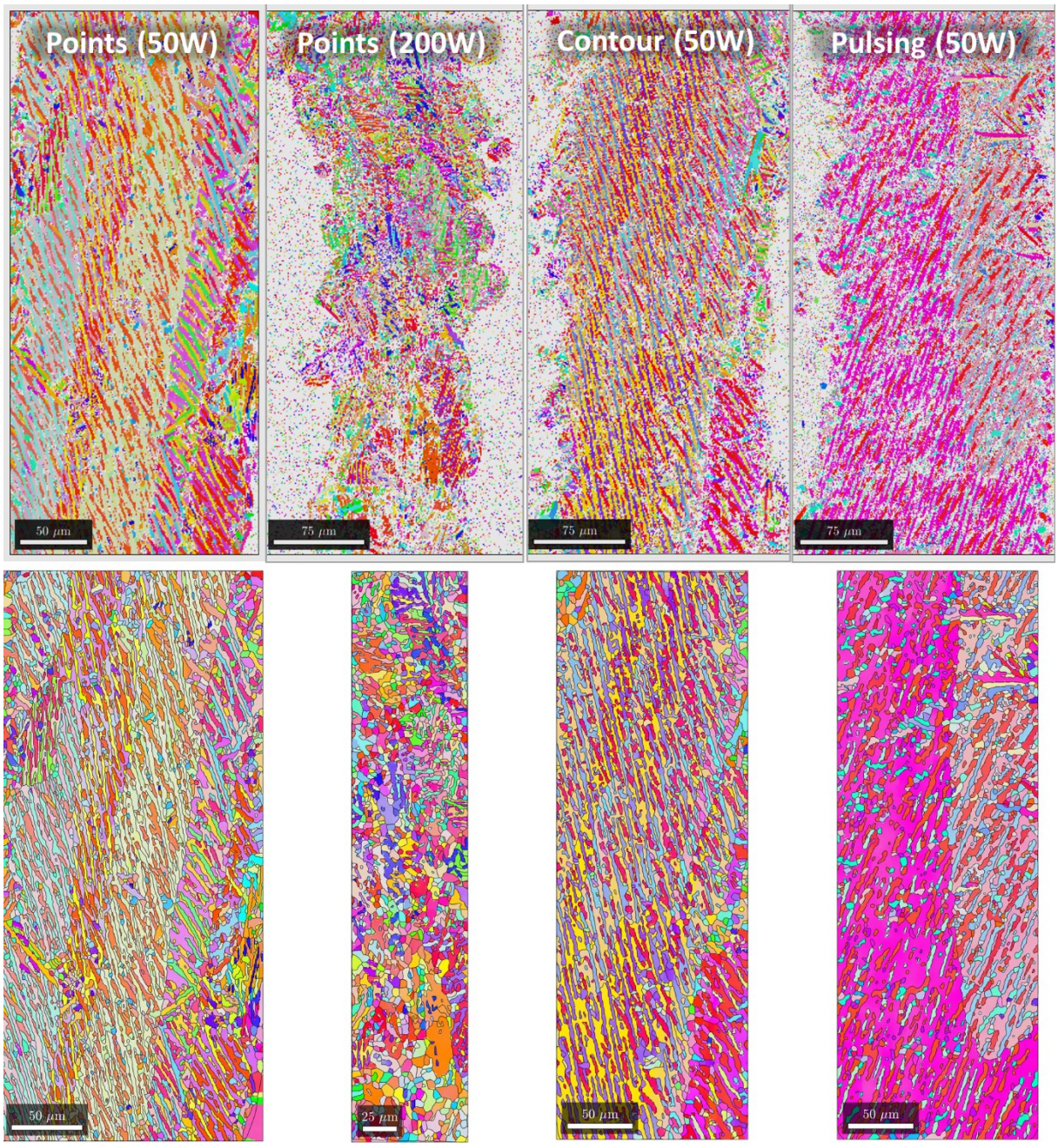




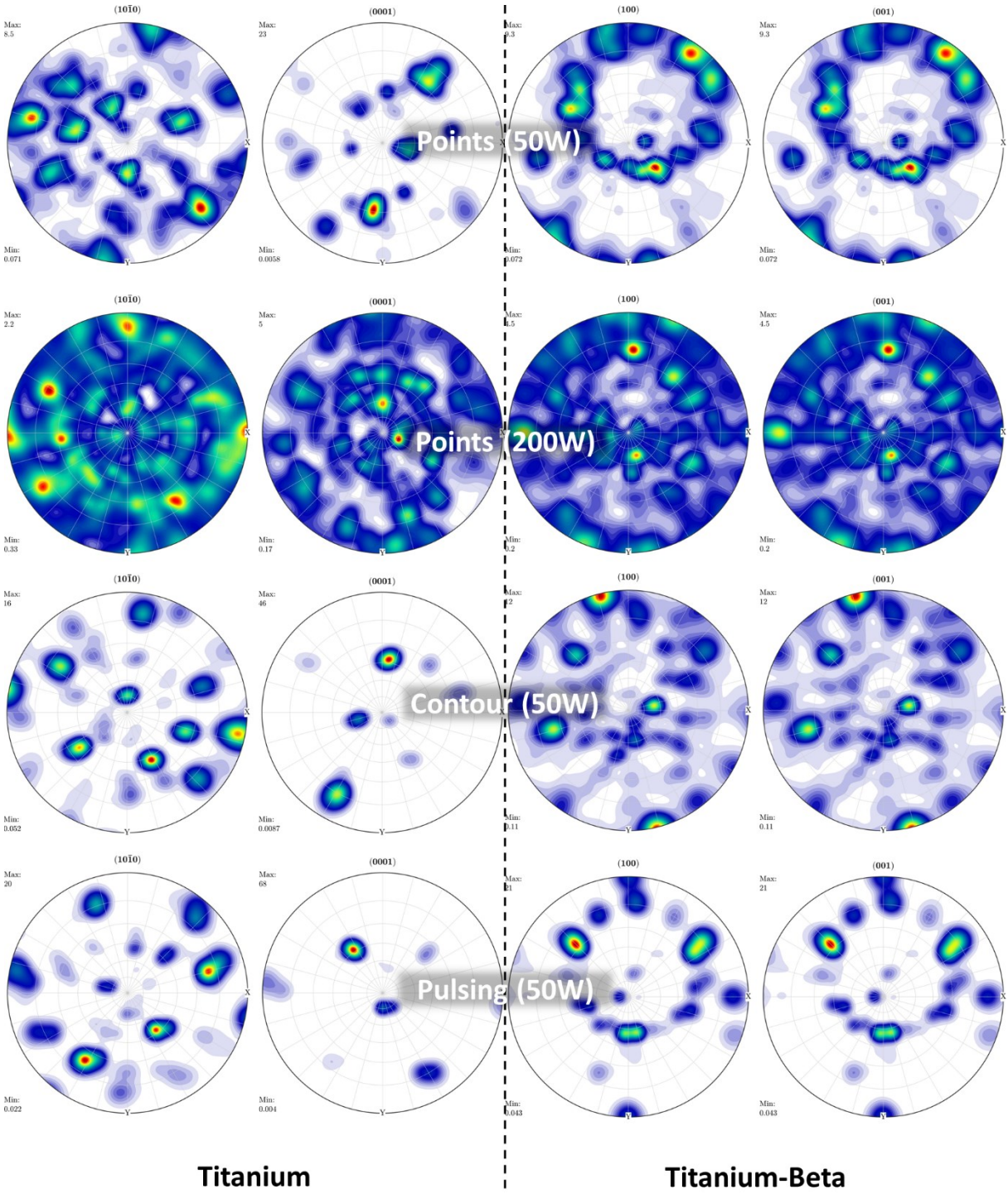

Ti64 [σ = 246.6×ρ*2.1513]
Ta [σ = 790.5×ρ*2.2455]
CP - Ti [σ = 338.8×ρ*2.1467]
TiTa[σ = 159.9×ρ*1.8495]
Fatigue Stress (MPa) @ 10^6 Cycles
Relative Density
0
5
10
15
0.00
0.05
0.10
0.15
0.20
0.25

10 Appendix C – EBSD Data

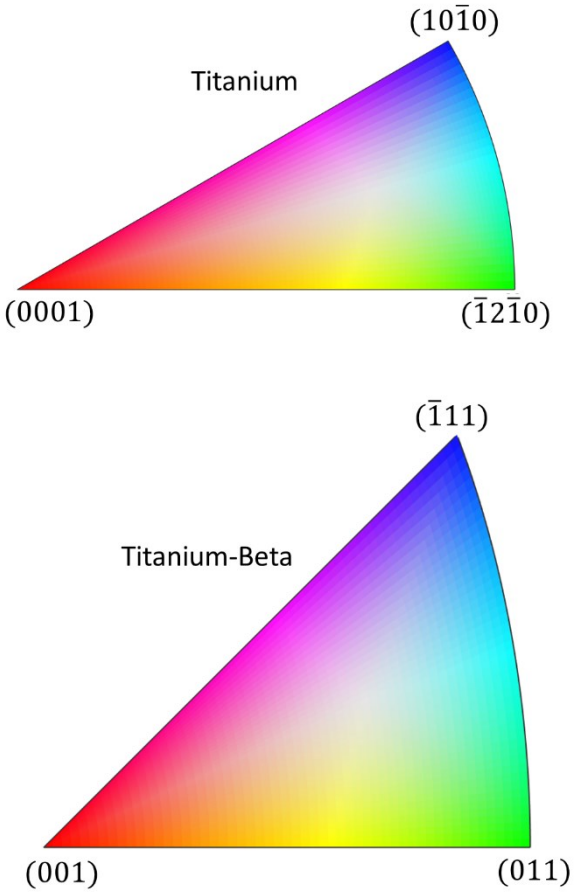
The following appendix presents all the EBSD data gathered, including orientation maps, grain maps, pole figures, phase maps as well as grain size, grain angle and grain aspect ratio distributions. Note: EBSD imaging had a relatively low hit rate (on average ~80%), thus results are only presented in Appendix C due to lack of confidence.



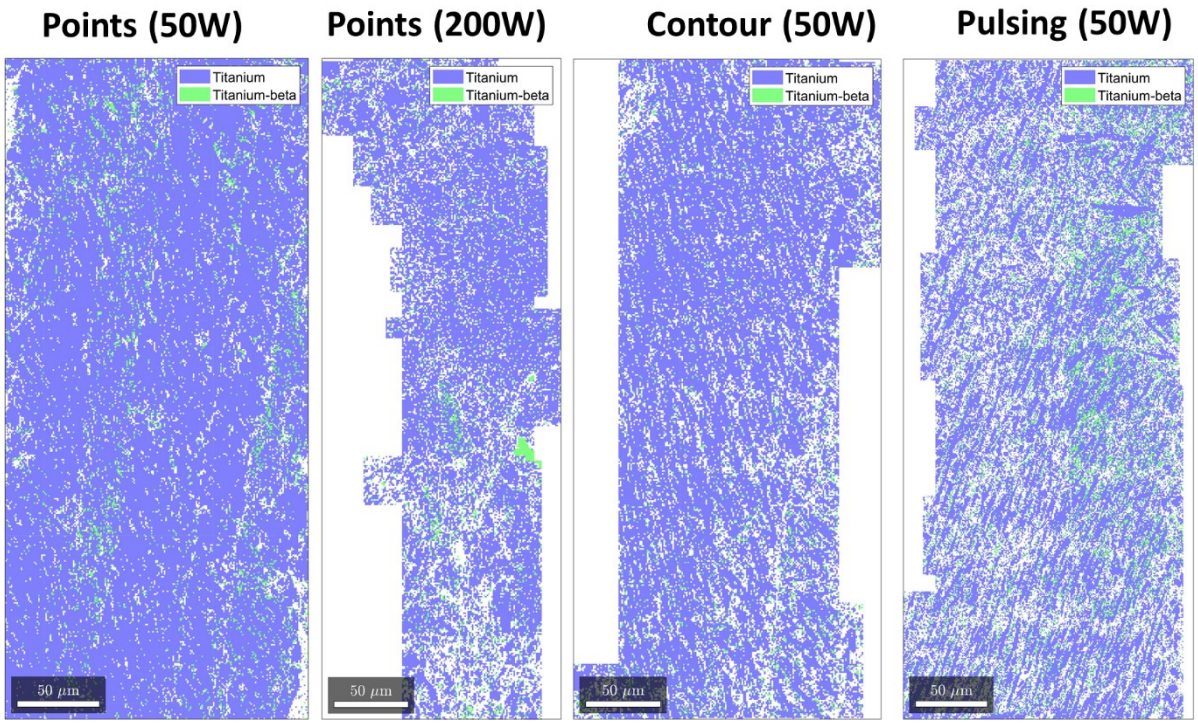
EBSD orientation maps (Top) and grain maps (bottom – restricted to just the struts and not including any mounting material) for varying laser parameters and scanning strategies, coloured according to crystal orientation figure below



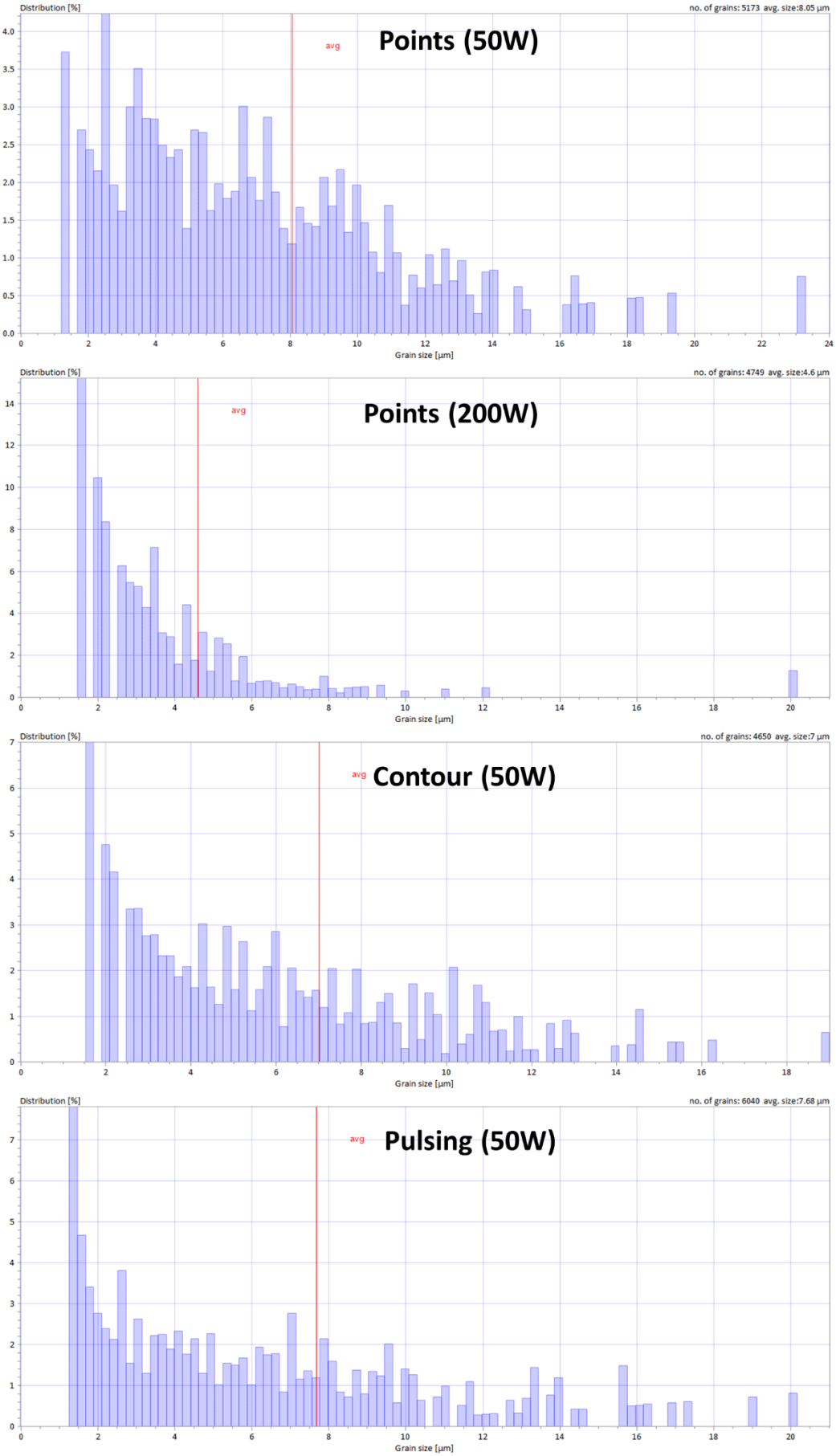
EBSD Pole Figures for Titanium (left) and Titanium-Beta (Right) with varying laser parameters and scanning strategies. Coloured according to Titanium and Titanium-Beta, coloured according to crystal orientation figure below



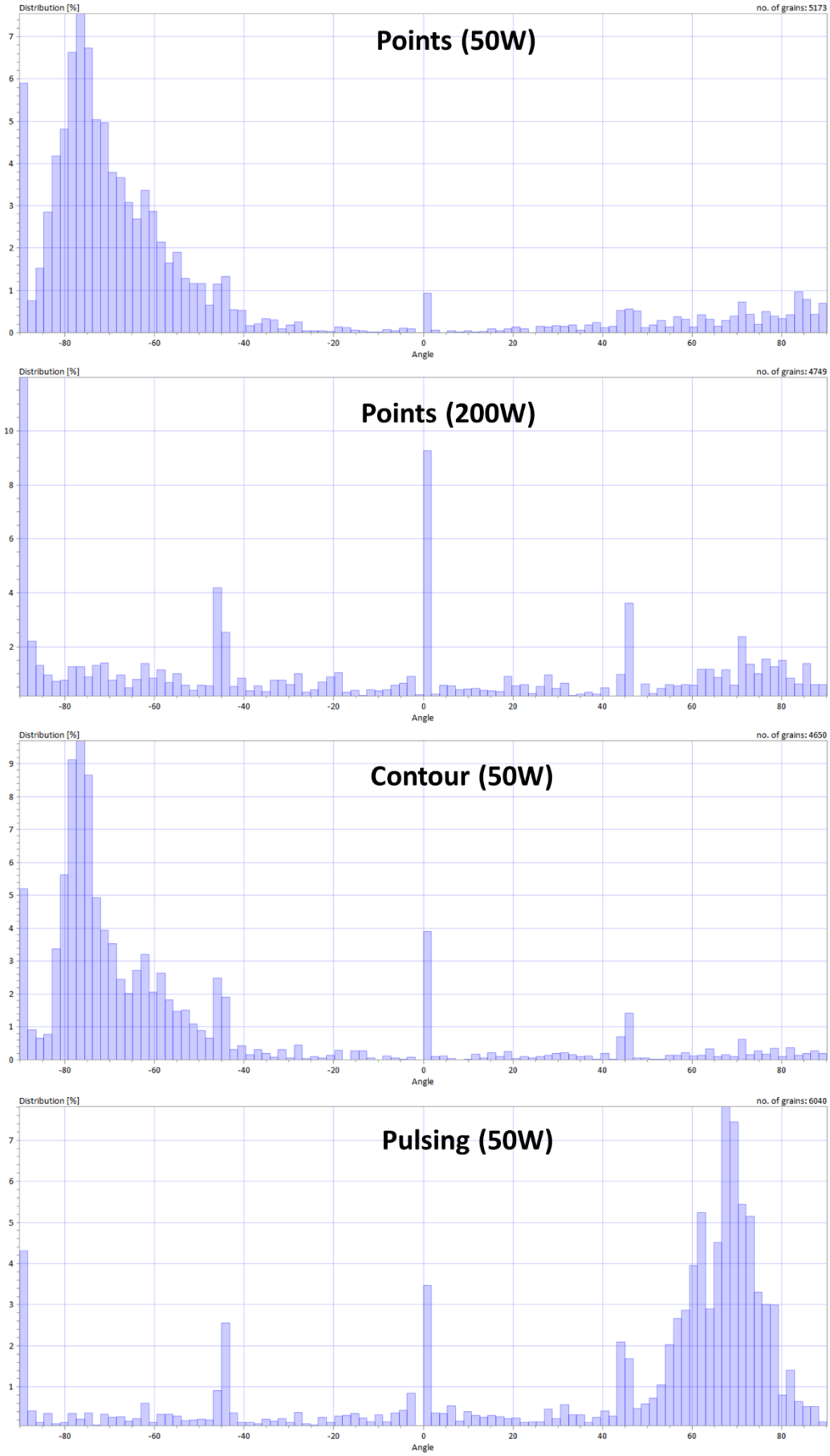
Crystal orientation colour code for Titanium and Titanium-Beta



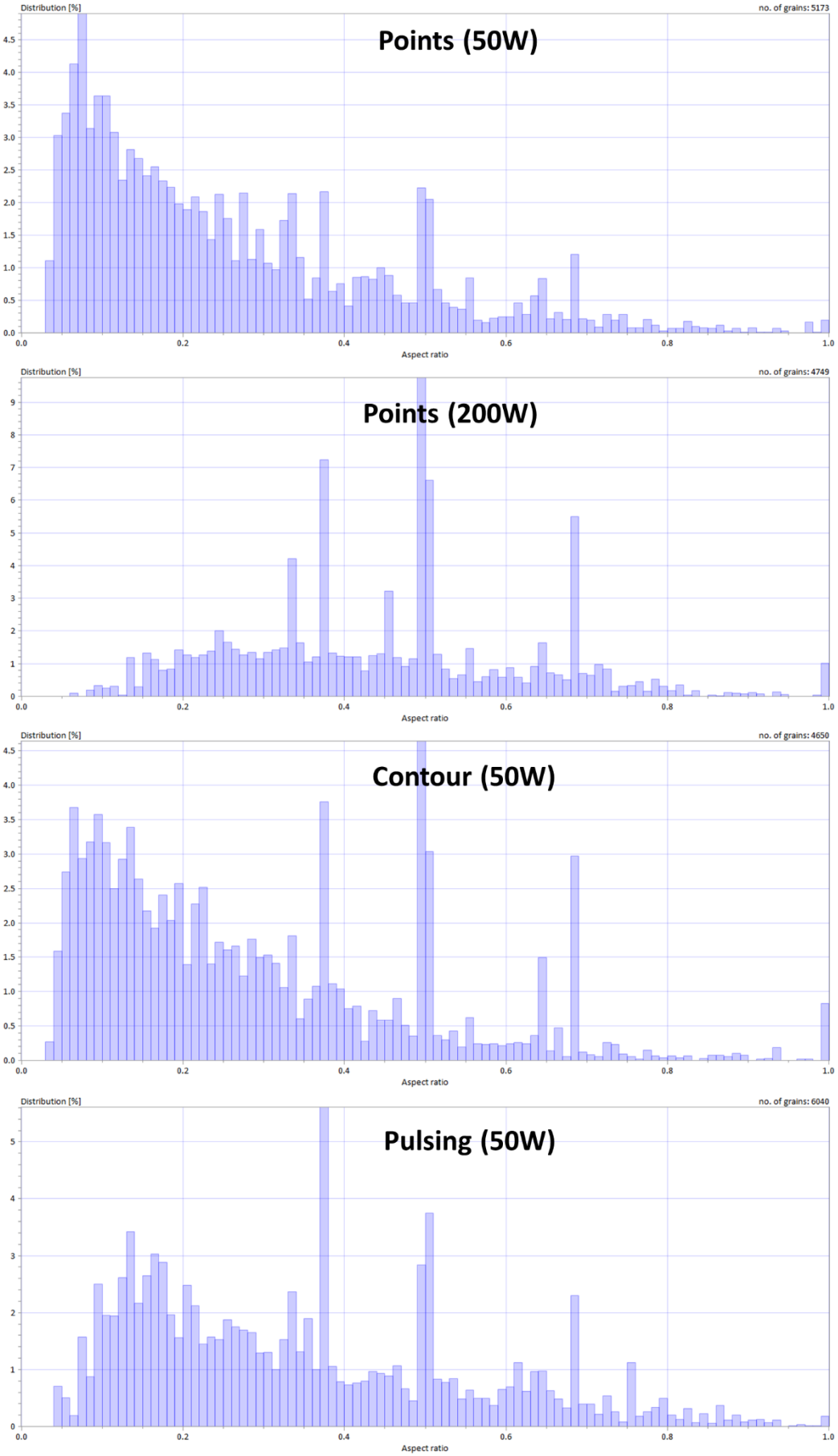
EBSD Phase Maps (maps are restricted to just the struts) for varying laser parameters and scanning strategies



Grain Size Distribution



Grain Angle Distribution



Grain Aspect Ratio Distribution

11 Appendix D – Ex-vivo Sheep Bone Raw Data

Specimen	Core	Apparent Density (g/cm^3)	Modulus (MPa)
1	**1**	0.379	515.0
1	**2**	0.241	134.3
1	**3**	0.322	123.5
1	**4**	0.210	56.5
2	**1**	0.621	1681.3
2	**2**	0.491	649.9
2	**3**	0.511	1039.1
2	**4**	0.364	722.4
3	**1**	0.651	1306.1
3	**2**	0.549	1512.4
3	**3**	0.499	825.6
3	**4**	0.412	663.4
4	**1**	0.531	1467.8
4	**2**	0.544	949.6
4	**3**	0.604	911.4
4	**4**	0.404	503.7
5	**1**	0.799	2737.7
5	**2**	0.635	1253.7
5	**3**	0.709	1701.1
5	**4**	0.449	1050.6
6	**1**	0.657	2001.1
6	**2**	0.679	1165.6
6	**3**	0.516	939.4
6	**4**	0.375	858.1
7	**1**	0.720	2318.9
7	**2**	0.501	1217.9
7	**3**	0.511	1660.3
7	**4**	0.343	606.3

Mechanical Test Data of ex-vivo ovine bones

Location	Pilot	1R	2R	3L	4R	5R	6L	7L
111	0.51	0.24	0.63	0.56	0.48	0.76	0.61	0.68
112	0.47	0.34	0.69	0.69	0.69	0.88	0.70	0.76
113	0.70	0.38	0.89	0.73	0.90	0.88	0.78	0.85
121	0.45	0.31	0.60	0.51	0.45	0.60	0.54	0.60
122	0.35	0.49	0.77	0.66	0.61	0.75	0.64	0.60
123	0.58	0.50	1.23	0.62	0.72	0.74	0.68	0.69
131	0.46	0.28	0.63	0.49	0.36	0.37	0.59	0.62
132	0.37	0.38	0.57	0.65	0.51	0.52	0.46	0.42
133	0.46	0.42	0.92	0.63	0.65	0.53	0.52	0.66
211	0.43	0.19	0.53	0.49	0.64	0.74	0.51	0.55
212	0.43	0.28	0.60	0.60	1.01	0.81	0.60	0.60
213	0.58	0.42	0.78	0.67	0.89	0.88	0.76	0.71
221	0.28	0.16	0.52	0.45	0.40	0.58	0.46	0.53
222	0.28	0.30	0.61	0.59	0.69	0.65	0.51	0.53
223	0.43	0.40	0.83	0.56	0.78	0.67	0.52	0.58
231	0.30	0.15	0.45	0.39	0.31	0.22	0.37	0.35
232	0.22	0.27	0.50	0.51	0.42	0.41	0.36	0.32
233	0.31	0.33	0.77	0.42	0.54	0.35	0.32	0.36
311	0.44	0.34	0.49	0.55	0.50	0.71	0.55	0.47
312	0.41	0.47	0.76	0.49	0.61	0.65	0.56	0.51
313	0.55	0.59	0.88	0.64	0.90	0.77	0.68	0.62
321	0.29	0.20	0.47	0.45	0.47	0.53	0.46	0.49
322	0.27	0.44	0.54	0.46	0.51	0.54	0.46	0.48
323	0.41	0.48	0.87	0.48	0.70	0.64	0.49	0.57
331	0.17	0.10	0.37	0.33	0.39	0.11	0.30	0.38
332	0.21	0.23	0.38	0.40	0.45	0.28	0.30	0.34
333	0.29	0.26	0.54	0.33	0.55	0.26	0.24	0.40

Density variation in g/cm^3 for the 8 CT-scanned ovine femora. Location notation: XYZ, X: Posterior-Anterior, Y: Medial-Lateral, Z: Inferior-Superior; all going 1-3 respectively.

Location	Pilot	1R	2R	3L	4R	5R	6L	7L
111	946.4	153.0	1615.5	1209.7	839.3	2518.9	1470.9	1945.8
112	775.6	340.0	2052.6	2044.1	2005.6	5317.2	2090.2	2589.4
113	2094.3	456.6	5439.0	2339.4	5940.9	5314.3	2703.9	4113.2
121	707.3	269.8	1419.3	947.5	698.0	1443.0	1093.1	1408.8
122	386.8	878.0	2664.0	1790.3	1508.1	2450.0	1651.8	1436.1
123	1302.7	926.4	16734.3	1544.9	2251.4	2414.5	1974.9	2004.6
131	727.0	214.2	1592.3	860.5	396.4	423.2	1378.1	1528.5
132	429.9	469.1	1264.8	1710.8	971.5	1000.3	754.0	600.2
133	724.0	592.5	6503.6	1583.9	1732.1	1049.8	1008.6	1791.4
211	633.0	79.6	1073.3	847.0	1660.5	2378.9	954.6	1138.4
212	632.6	220.1	1412.2	1438.5	9547.3	2773.0	1455.7	1447.1
213	1339.7	598.1	2767.3	1859.7	5659.8	5081.2	2571.2	2183.7
221	216.0	52.1	981.4	696.0	537.9	1287.5	721.5	1040.7
222	217.6	251.5	1499.7	1357.6	2048.7	1769.0	974.0	1029.8
223	611.9	529.3	3677.4	1221.5	2687.8	1878.7	1020.4	1320.8
231	256.6	44.2	688.1	500.8	272.6	114.2	437.5	364.1
232	121.0	192.4	916.5	966.3	588.4	568.6	403.1	295.1
233	283.5	329.7	2624.1	606.8	1122.1	364.6	298.4	400.0
311	680.6	355.7	883.4	1153.8	891.2	2187.6	1168.1	770.4
312	573.9	771.8	2600.3	863.3	1464.5	1747.5	1211.8	947.0
313	1162.4	1347.2	5361.3	1660.0	5782.8	2609.4	1951.4	1558.7
321	232.2	92.4	796.5	712.0	768.1	1046.6	722.5	883.4
322	192.3	653.1	1119.4	755.0	933.8	1095.1	740.1	811.0
323	559.8	820.0	5047.2	812.4	2116.0	1705.9	848.7	1278.0
331	59.7	16.4	426.8	332.3	506.4	23.5	262.4	470.3
332	100.8	137.8	458.3	532.9	709.1	217.4	248.6	348.9
333	235.3	185.2	1091.9	329.0	1135.7	184.8	141.1	537.8

Modulus (E) variation in MPa for the 8 CT-scanned ovine femora, where $E=5041.2\rho^{2.4695}$. Location notation: XYZ, X: Posterior-Anterior, Y: Medial-Lateral, Z: Inferior-Superior; all going 1-3 respectively.

12 Appendix E – Rights and Permissions

For all images not reproduced under Creative Commons Attribution Licenses the following permissions have been obtained.

Order Date	Article Title	Publication	Type Of Use	Order Status	Order Number
27-Sep-2018	Additive manufacturing of strong and ductile Ti–6Al–4V by selective laser melting via in situ martensite decomposition	Acta Materialia	reuse in a thesis/dissertation	Completed	4437260502261
27-Sep-2018	Analysis of defect generation in Ti–6Al–4V parts made using powder bed fusion additive manufacturing processes	Additive Manufacturing	reuse in a thesis/dissertation	Completed	4437250831928
27-Sep-2018	Anisotropy and heterogeneity of microstructure and mechanical properties in metal additive manufacturing: A critical review	Materials & Design	reuse in a thesis/dissertation	Completed	4437260452752
27-Sep-2018	Balling behavior of stainless steel and nickel powder during selective laser melting process	The International Journal of Advanced Manufacturing Technology	Thesis/Dissertation	Completed	4437231084900
27-Sep-2018	Compression fatigue of a cellular Al alloy	Materials Science and Engineering: A	reuse in a thesis/dissertation	Completed	4437250611193
27-Sep-2018	Deformation characteristics of metal foams	Journal of Materials Science (full set)	Thesis/Dissertation	Completed	4437250488678
27-Sep-2018	Effects of Ta content on Young's modulus and tensile	Materials Science and Engineering: A	reuse in a thesis/dissertation	Completed	4437260630940

Order Date	Article Title	Publication	Type Of Use	Order Status	Order Number
	properties of binary Ti–Ta alloys for biomedical applications				
27-Sep-2018	Mechanical loading histories and cortical bone remodeling	Calcified Tissue International	Thesis/Dissertation	Completed	4437220684018
27-Sep-2018	Mechanobiological Models for Bone Tissue. Applications to Implant Design	Wiley Books	Dissertation/Thesis	Completed	4437220802232
27-Sep-2018	Morphology and properties of CoCrMo parts fabricated by selective laser melting	Materials Science and Engineering: A	reuse in a thesis/dissertation	Completed	4437230522163
27-Sep-2018	Optimisation of process parameters to address fundamental challenges during selective laser melting of Ti-6Al-4V: A review	International Journal of Machine Tools and Manufacture	reuse in a thesis/dissertation	Completed	4437260397076
27-Sep-2018	Optimisation of process parameters to address fundamental challenges during selective laser melting of Ti-6Al-4V: A review	International Journal of Machine Tools and Manufacture	reuse in a thesis/dissertation	Completed	4437240459904
27-Sep-2018	Optimisation of process parameters to address fundamental challenges during selective laser melting of Ti-6Al-4V: A review	International Journal of Machine Tools and Manufacture	reuse in a thesis/dissertation	Completed	4437231167440

Order Date	Article Title	Publication	Type Of Use	Order Status	Order Number
27-Sep-2018	Optimisation of process parameters to address fundamental challenges during selective laser melting of Ti-6Al-4V: A review	International Journal of Machine Tools and Manufacture	reuse in a thesis/dissertation	Completed	4437230439983
27-Sep-2018	Revival of pure titanium for dynamically loaded porous implants using additive manufacturing	Materials Science and Engineering: C	reuse in a thesis/dissertation	Completed	4437260570191
27-Sep-2018	Stiffness and strength tailoring of cobalt chromium graded cellular structures for stress-shielding reduction	Materials & Design	reuse in a thesis/dissertation	Completed	4437230161976
27-Sep-2018	The mechanical behaviour of cancellous bone	Journal of Biomechanics	reuse in a thesis/dissertation	Completed	4437221047130
27-Sep-2018	The mechanical properties of human tibial trabecular bone as a function of metaphyseal location	Journal of Biomechanics	reuse in a thesis/dissertation	Completed	4437220897180
27-Sep-2018	Topological design and additive manufacturing of porous metals for bone scaffolds and orthopaedic implants: A review	Biomaterials	reuse in a thesis/dissertation	Completed	4437211261029